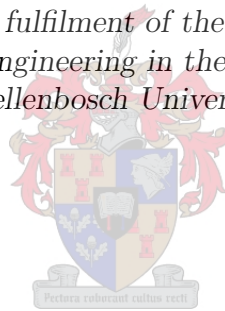


A Fundamental Analysis on Additive Manufacturing of a Cemented Tungsten Carbide

by

Andries Coetzee van Staden

*Thesis presented in partial fulfilment of the requirements for the degree
of Master of Industrial Engineering in the Faculty of Engineering at
Stellenbosch University*



Department of Industrial Engineering,
University of Stellenbosch,
Private Bag X1, Matieland 7602, South Africa.

Supervisors:

Dr. G.A. Oosthuizen Prof. N. Sacks

March 2016

Declaration

By submitting this thesis electronically, I declare that the entirety of the work contained therein is my own, original work, that I am the sole author thereof (save to the extent explicitly otherwise stated), that reproduction and publication thereof by Stellenbosch University will not infringe any third party rights and that I have not previously in its entirety or in part submitted it for obtaining any qualification.

Date:

Copyright © 2016 Stellenbosch University
All rights reserved.

Abstract

A Fundamental Analysis on Additive Manufacturing of a Cemented Tungsten Carbide

A.C. van Staden

Department of Industrial Engineering,

University of Stellenbosch,

Private Bag X1, Matieland 7602, South Africa.

Thesis: MEng (Ind)

December 2015

Cemented tungsten carbide tools, specifically tungsten carbide based alloys, have found a wide range of application fields that includes manufacturing, agriculture, and mining. These tools are used for their ability to resist the detrimental effects of several wear mechanisms, and have been developed specifically for each industrial application. Therefore, industry is consistently developing process technologies to produce customised tooling solutions using cemented tungsten carbide alloys. Additive manufacturing is chosen as a novel manufacturing process due to its superior material and process flexibility. Its flexibility in material applications, as well as its ability to produce highly complex geometries, makes additive manufacturing technologies a viable solution to the stringent requirements set by industries using cemented tungsten carbide tools. This study investigates the capability of an available selective laser melting (SLM) process to successfully produce single material layers from a cemented tungsten carbide powder. Specifically, the capability of the SLM process to fuse a tool grade cemented tungsten carbide material is investigated. The laser power, scan velocity, and hatch spacing are varied in a design of experiments. This is done in order to determine the optimum parameter combination (or processing region) to minimise the maximum surface height of each sintered layer. Samples, each produced using different parameter sets, are sintered onto a steel baseplate in an Argon environment. For each set of parameters the resultant single layer samples are analysed using microscope imaging, surface and roughness profile analyses, scanning electron microscopy (SEM) imaging and energy dispersive spectroscopy (EDS) analyses, as well as statistical analysis using the maximum surface height of each sample. The results are compared to a benchmark sample produced using a standard material and process parameter set that has been optimised to produce functional components. The results show that uniform single layers can be produced from the tool grade cemented tungsten carbide material and that the optimal parameter combination is one of high laser power, low scan velocity, and high hatch spacing.

Uittreksel

'n Fundamentele Analise op Laagvervaardiging van Wolframkarbied

("A Fundamental Analysis on Additive Manufacturing of a Cemented Tungsten Carbide")

A.C. van Staden

*Departement Bedryfsingenieurswese,
Universiteit van Stellenbosch,
Privaatsak X1, Matieland 7602, Suid Afrika.*

Tesis: MIng (Bed)

Desember 2015

Wolframkarbied gereedskap het 'n wye toepassingsveld waaronder vervaardiging, landbou, en mynbou enkele voorbeelde is. Die gereedskap word gebruik vir hul vermoë om erosie en korrosie te weerstaan. Vir elke toepassing word die gereedskapstuk doeltreffend om optimale uitvoering van die taak te bewerkstellig. Soos die aanvraag na doeltreffende wolframkarbied gereedskap toeneem, versuim tradisionele vervaardigingstegnieke om die aanvraag te bevredig. Innoverende vervaardigingstegnieke moet ondersoek word om doeltreffende oplossings aan industrieë te verskaf wat maklik aanpasbaar is vir elke toepassingsveld. Laagvervaardiging staan uit bo tradisionele vervaardigingstegnieke vir die wye keuse van materiale, asook die buigsaamheid van die tegnieke wat tans beskikbaar is. Laagvervaardiging het reeds bewys dat komplekse geometrieë vervaardig kan word en dat hierdie komponente sonder aanpassing gebruik kan word in die afsonderlike toepassingsvelde. Dit word voorgestel dat laagvervaardiging 'n potensiële oplossing kan bied na die aanvraag vir doeltreffende wolframkarbied gereedskap. Hierdie studie ondersoek die vermoë van 'n beskikbare laagvervaardigingstegnologie om 'n gereedskapsgraad wolframkarbied materiaal te konsolideer in 'n enkele laag. Die moontlikheid hiervan word gemeet teen die minimum oppervlakhogte haalbaar tydens konsolidering. Sestien 35x35mm monsters word vervaardig met verskillende vervaardigingsparameters. Hierdie monsters word gekonsolideer op 'n staal basisplaat in 'n Argon omgewing, en die laser krag, skandering spoer spasiëring, en skanderingspoed word in parameterstelle verander. Elke vervaardigingsparameterstel se monster word ondersoek met mikroskopiese fotos, oppervlak- en grofheidsprofiel analyses, SEM foto en spektrum analyses, asook statistiese analise. Die resultate toon daarop dat laagvervaardigingstegnologie daartoe in staat is om gereedskapsgraad wolframkarbied materiaal in enkele, uniforme lae te konsolideer. Verder is dit vasgestel dat die optimale parameter kombinasie ooreenstem met hoë laser krag, hoë skandering spoer spasiëring, en lae skanderingspoed.

Acknowledgements

I would like to express my sincere gratitude to the following people and organisations:

My family and loved ones for their unwavering support and encouragement.

My supervisors, Dr Tiaan Oosthuizen and Prof Natasha Sacks, and fellow researchers, Ms Zen-Mari Olivier, Mr Francois Conradie, Mr Pieter Conradie, and Mr Philip Hugo for their input, guidance and support.

The Industrial Engineering Department of Stellenbosch University.

The DST-NRF Centre of Excellence in Strong Materials.

Stellenbosch University.

Witwatersrand University.

Dedications

Hierdie tesis word opgedra aan my ouers en my broer, sonder wie ek nie hier sou wees nie.

This thesis is dedicated to my parents and my brother, without whom I would not be where I am.

Contents

Declaration	i
Abstract	ii
Uittreksel	iii
Acknowledgements	iv
Dedications	v
Contents	vi
List of Figures	ix
List of Tables	xiv
Nomenclature	xvi
1 Background	1
1.1 Additive Manufacturing	1
1.2 Additive Manufacturing in South Africa	4
1.3 Cemented carbide tooling	5
2 Problem Statement and Research Objectives	9
2.1 Problem statement	9
2.2 Research questions	9
2.3 Research objectives	10
3 Literature	12
3.1 Introduction	12
3.2 Additive Manufacturing technologies	14
3.2.1 Additive Manufacturing technology overview	16
3.2.1.1 Liquid based processes	16
3.2.1.2 Solid based processes	17
3.2.1.3 Powder based processes	17
3.2.2 Forming mechanisms in sintering processes	21
3.3 Cemented carbide materials in additive manufacturing	25
3.4 Considerations in cemented carbide tooling	27

3.4.1	Mechanical and material properties of cemented carbides . . .	27
3.4.2	Cemented carbide applications	31
3.4.3	Component wear and tool life in cemented carbides	33
3.5	Additive manufacturing of cemented carbides	36
3.5.1	Influences on achievable part properties	37
3.5.1.1	Material	38
3.5.1.2	Process	39
3.5.1.3	Energy source	41
3.5.1.4	Other	42
3.5.2	Phenomena in additively manufactured cemented carbides . .	44
3.6	Experimentation	47
4	Experimental methodology	51
4.1	Introduction	51
4.1.1	Basic principles of statistical methods	52
4.1.2	Screening experiments	55
4.1.3	Fractional factorial design	55
4.1.4	Full factorial design	56
4.2	Experimental procedure	57
4.2.1	Experimental setup and design	58
4.2.2	Single layer sample production	58
4.2.3	Material analysis	60
4.2.3.1	Composition analysis and SEM micrographs	61
4.2.3.2	Particle size distribution and shape analysis	62
4.2.4	Single layer sample analysis	63
4.2.4.1	Microscope image analysis	64
4.2.4.2	Profilometer analysis	65
4.2.4.3	SEM sample analysis	67
4.2.4.4	Statistical analysis	68
4.3	Benchmark part analysis	72
5	Experimental results and discussion	74
5.1	Material analysis	74
5.1.1	Material composition	74
5.1.2	SEM micrographs	75
5.1.3	Laser Diffraction Analysis	78
5.2	Single layer sample analysis	79
5.2.1	Microscope image analysis	80
5.2.1.1	Protrusion formation	81
5.2.1.2	Balling	81
5.2.1.3	Shrinkage	84
5.2.1.4	Scan track formation	87
5.2.1.5	Cracking	88
5.2.2	Profilometer analysis	89
5.2.2.1	Surface profile	89
5.2.2.2	Roughness profile	98
5.2.3	SEM sample analysis	101

<i>CONTENTS</i>	viii
5.2.4 Statistical analysis	107
5.3 Process windows	114
6 Conclusions	118
7 Recommendations and future work	121
List of References	123
Appendices	130
A Laser Diffraction Analysis report	131
B Concept Laser CL20ES data sheet	138
C Profilometer analysis - equipment and software setup	141
D Screening experiment results - MODDE example	146
E Single layer microscope images	152
F HommelMap Basic Reports	159
G Hommel-etamic Turbo Wave V7.53 reports	176
H MODDE analysis results	195
I COMA'16 conference article	205

List of Figures

1.1	Graphic representation of general inputs and outputs associated with AM technologies.	2
1.2	Illustration of the general powder-on-bed, metal based AM process. . . .	3
1.3	Process chain of conventional powder metallurgy part production. Adapted from Colton (2009).	5
1.4	Cold compaction process to form a metal bushing. Adapted from Colton (2009).	7
3.1	Additive manufacturing evolution time line. Adapted from Cotteleer <i>et al.</i> (2013).	14
3.2	Technology classification structure as proposed by Levy <i>et al.</i> (2003). . .	19
3.3	Manufacturing technology capability profile. Adapted from Levy <i>et al.</i> (2003).	20
3.4	A visual demonstration of necking in SSS. Adapted from Kruth <i>et al.</i> (2005) and Kruth <i>et al.</i> (2007).	23
3.5	A visual demonstration of necking in LPS. Adapted from Kruth <i>et al.</i> (2005).	24
3.6	Microdentritic structure of individual pre-alloyed cobalt-based powder particles. Adapted from Murr <i>et al.</i> (2012).	29
3.7	SEM images of WC powders with different particle sizes: a) 0.4, b) 1.3, c) 2.4, and d) 4.3 μ m. Adapted from Kim <i>et al.</i> (2004).	30
3.8	SEM images of sintered, binderless WC powders with different particle sizes: a) 0.4, b) 1.3, c) 2.4, and d) 4.3 μ m. Adapted from Kim <i>et al.</i> (2004).	30
3.9	SEM images of WC-9wt.%Co parts showing debris accumulation on the sample surface. Adapted from Kumar (2009).	34
3.10	Process windows established by a) Kruth <i>et al.</i> (2005), b) Li <i>et al.</i> (2010), c) Zhang <i>et al.</i> (2010), and d) Zhang <i>et al.</i> (2012b).	41
3.11	Temperature gradient mechanism illustrated by a) thermal expansion followed by b) contraction. Adapted from Kruth <i>et al.</i> (2004) and Kruth <i>et al.</i> (2012).	46
4.1	The number of experiments required by different DOE methods. Adapted from Cavazzuti (2013).	53
4.2	A graphical process flow of the experimental methodology in this work.	58
4.3	A possible scan pattern for a single layer.	60

4.4	A single layer test sample at a) 1.25 and b) 3.20 times magnification. (P=100W, v=100mm.s ⁻¹ , h=0.15mm)	64
4.5	Single layer sample parameter set corresponding to h=0.15mm and 1.25 times magnification.	65
4.6	Roughness profile evaluation lengths as determined by ISO Standard 4287.	66
4.7	Roughness profile parameters as determined by ISO Standard 4287.	67
4.8	Graphic illustration of the cross section sample area analysed using a Zeiss Evo MA15VP SEM.	68
5.1	Material composition as analysed using a ZEISS EVO MA15VP SEM.	75
5.2	Material composition mapping as analysed using a ZEISS EVO MA15VP SEM; a) titanium, b) cobalt, and c) tungsten.	76
5.3	SEM image of the material sample taken using a LEO 1450VP SEM at 200 times magnification.	77
5.4	SEM image of the material sample taken using a LEO 1450VP SEM at 500 times magnification.	77
5.5	SEM image of the material sample taken using a LEO 1450VP SEM at 1000 times magnification.	78
5.6	Particle size by volume frequency percentage present in material sample - tests one to three.	79
5.7	Particle size by volume frequency percentage present in material sample - averaged.	80
5.8	Single layer sample images corresponding to E13-E16 in Table 4.2.	82
5.9	Single layer sample images corresponding to E1-E4 in Table 4.2.	83
5.10	Single layer sample images corresponding to E9-E12 in Table 4.2.	84
5.11	Single layer sample images corresponding to E5-E8 in Table 4.2.	85
5.12	Single layer samples exhibiting localised shrinkage at island edges.	86
5.13	Failed WC-12wt.% Co sample production showing delamination as the cause of failure. (First experiment).	86
5.14	Failed WC-12wt.% Co sample production showing delamination as the cause of failure. (Second experiment).	87
5.15	3D surface profile for benchmark sample. ($P = 180W, v = 800mm.s^{-1}, h = 0.105mm$)	91
5.16	3D surface profile for experiment sample E5. ($P = 100W, v = 100mm.s^{-1}, h = 0.150mm$)	92
5.17	3D surface profile for experiment sample E7. ($P = 200W, v = 100mm.s^{-1}, h = 0.150mm$)	93
5.18	Roughness parameter histogram for a low scan speed and low laser power combination.	94
5.19	Surface parameter histogram for a low scan speed and low laser power combination.	94
5.20	Roughness parameter histogram for a low scan speed and high laser power combination.	95
5.21	Surface parameter histogram for a low scan speed and high laser power combination.	96
5.22	Roughness parameter histogram for a high scan speed and low laser power combination.	96

5.23	Surface parameter histogram for a high scan speed and low laser power combination.	97
5.24	Roughness parameter histogram for a high scan speed and high laser power combination.	97
5.25	Surface parameter histogram for a high scan speed and high laser power combination.	98
5.26	Roughness profile for benchmark sample.	99
5.27	Roughness profile for experiment sample E5.	100
5.28	Roughness profile for experiment sample E7.	101
5.29	Sample sites from trial-and-error experiments using a WC-12wt.% Co powder.	102
5.30	Descriptive SEM image of a cross section from sample E5.	103
5.31	Cross section comparison of a) sample E5 and b) sample E7 - wide angle.	103
5.32	Cross section comparison of a) sample E5 and b) sample E7 - close up.	104
5.33	Descriptive SEM image of a surface protrusion cross section and temperature diffusion pattern.	105
5.34	Analysed cross section sample composition for E5.	105
5.35	Analysed cross section sample composition for E7.	106
5.36	Analysed cross section sample composition for SLM layer E7.	106
5.37	Coefficients plot, for response variable R_{z-max} , before term exclusion.	108
5.38	Coefficients plot, for response variable R_{z-max} , after term exclusion.	108
5.39	Replicates plot for R_z -Average - MODDE analysis.	109
5.40	Histogram of the response variable, R_z -Average.	110
5.41	Model summary for R^2 and Q^2 statistics after adjustment.	110
5.42	Residual normal probability plot for response variable R_z -Average.	111
5.43	Observed versus predicted plot for response variable R_z -Average.	111
5.44	4D contour plot combining laser power, scan speed, hatch spacing and response variable R_z	112
5.45	Combined factor effect plot for all experiment factors and response variable R_z	114
5.46	4D response contour plot with selected setpoint for all factors and response variable R_z	115
5.47	Combined microscope images of single layer sample parameter sets, according to hatch spacing.	116
5.48	Roughness profile trend histograms according to different $P - v$ combinations.	117
C.1	Process monitoring interface for the measurement software.	142
C.2	Probe selection and measurement range setup.	142
C.3	Measuring conditions selection interface for the measurement software.	143
C.4	Topography settings in the program sequence for the measurement software.	143
C.5	Profilometer equipment setup.	144
C.6	Probe set specifications plaque.	144
C.7	Sample profile measurement example.	145
D.1	4D contour plot.	146
D.2	4D contour plot indicating the optimal setpoint.	147

D.3	4D contour plot of defect per million opportunities (DMPO) for the given setpoint.	147
D.4	Factor distribution plot.	148
D.5	Response distribution plot.	148
D.6	Factor effect plot for the SulfKet [mol/mol] factor, provided in a 95% confidence band.	149
D.7	Yield percentage prediction plot for three factors, provided in a 95% confidence band.	149
D.8	Observed versus predicted yield percentage plot used in regression analysis.	150
D.9	Summary plot showing the Replicates, Summary of fit, Coefficients, and Residuals normal probability plots.	150
D.10	Optimisation output summarising evaluated setpoints.	151
E.1	Single layer sample E1 at 1.25 and 3.20 times magnification.	153
E.2	Single layer sample E2 at 1.25 and 3.20 times magnification.	153
E.3	Single layer sample E3 at 1.25 and 3.20 times magnification.	153
E.4	Single layer sample E4 at 1.25 and 3.20 times magnification.	154
E.5	Single layer sample E5 at 1.25 and 3.20 times magnification.	154
E.6	Single layer sample E6 at 1.25 and 3.20 times magnification.	154
E.7	Single layer sample E7 at 1.25 and 3.20 times magnification.	155
E.8	Single layer sample E8 at 1.25 and 3.20 times magnification.	155
E.9	Single layer sample E9 at 1.25 and 3.20 times magnification.	155
E.10	Single layer sample E10 at 1.25 and 3.20 times magnification.	156
E.11	Single layer sample E11 at 1.25 and 3.20 times magnification.	156
E.12	Single layer sample E12 at 1.25 and 3.20 times magnification.	156
E.13	Single layer sample E13 at 1.25 and 3.20 times magnification.	157
E.14	Single layer sample E14 at 1.25 and 3.20 times magnification.	157
E.15	Single layer sample E15 at 1.25 and 3.20 times magnification.	157
E.16	Single layer sample E16 at 1.25 and 3.20 times magnification.	158
H.1	Contour plot combining laser power, scan speed, and response variable R_z .	196
H.2	Contour plot combining laser power, hatch spacing, and response variable R_z	196
H.3	Contour plot combining scan speed, hatch spacing, and response variable R_z	197
H.4	Predictive factor distribution plot for laser power.	198
H.5	Predictive factor distribution plot for scan speed.	199
H.6	Predictive factor distribution plot for hatch spacing.	199
H.7	Predictive response distribution plot for response variable R_z	200
H.8	Factor effect plot for laser power.	200
H.9	Factor effect plot for scan speed.	201
H.10	Factor effect plot for hatch spacing.	201
H.11	Response contour plot with selected setpoint for laser power and scan speed.	202
H.12	Response contour plot with selected setpoint for laser power and hatch spacing.	202

LIST OF FIGURES

xiii

H.13 Response contour plot with selected setpoint for scan speed and hatch spacing.	203
---	-----

List of Tables

3.1	Mechanical part properties of cemented carbides by cobalt weight percentage. Adapted from Wang <i>et al.</i> (2013).	31
3.2	Hardness and fracture toughness of cemented tungsten carbides by cobalt weight percentage. Adapted from Wang <i>et al.</i> (2013).	31
4.1	Summary of DOE methods and associated applications. Adapted from Cavazzuti (2013).	54
4.2	Single layer sample production DOE.	59
4.3	DOE model factors and associated interaction terms as determined by MODDE.	70
4.4	MODDE Optimiser factor setup summary.	70
4.5	MODDE Optimiser response setup summary.	71
4.6	Optimal process and material parameters for production of CL20ES parts using SLM.	73
5.1	Volume distribution arithmetic statistics of the material sample analysed by Laser Diffraction Analysis.	79
5.2	Surface parameters for benchmark sample. ($P = 180W$, $v = 800mm.s^{-1}$, $h = 0.105mm$)	89
5.3	Surface parameters for single layer sample E5. ($P = 100W$, $v = 100mm.s^{-1}$, $h = 0.150mm$)	91
5.4	Surface parameters for single layer sample E7. ($P = 200W$, $v = 100mm.s^{-1}$, $h = 0.150mm$)	92
5.5	Roughness parameters for benchmark sample. ($P = 180W$, $v = 800mm.s^{-1}$, $h = 0.105mm$)	99
5.6	Roughness parameters for experiment sample E5. ($P = 100W$, $v = 100mm.s^{-1}$, $h = 0.150mm$)	100
5.7	Roughness parameters for experiment sample E7. ($P = 200W$, $v = 100mm.s^{-1}$, $h = 0.150mm$)	100
5.8	Selected setpoint summary - factors.	113
5.9	Selected setpoint summary - response.	113
H.1	Extended setpoint summary for experiment factors.	197
H.2	Extended setpoint summary for response variable R_z	197
H.3	Alternate setpoints as determined by the MODDE Optimiser.	198
H.4	MODDE model predictions based on experimental parameter values.	203
H.5	Descriptive worksheet statistics.	204

LIST OF TABLES

xv

H.6 Descriptive model statistics. 204

Nomenclature

Accronyms and Abbreviations

3D	Three dimensional
3DP	Three dimensional printing
AM	Additive manufacturing
AMT	Ammonium meta tungstate
APT	Ammonium paratungstate
BIS	Beam interface solidification
BPM	Ballistic particle manufacturing
CAD	Computer aided design
CMB	Controlled metal build-up
CO	Carbon monoxide
CO ₂	Carbon dioxide
Cr ₃ C ₂	Chromium carbide
CT	Computed tomography
CUT	Central University of Technology
DMD	Direct metal deposition
DOE	Design of experiments
DSLS	Direct selective laser sintering
EDM	Electrical discharge machining
ES	Electrosetting
FDM	Fused deposition modelling
FGC	Functionally graded composites
GARPA	Global Alliance of Rapid Prototyping Associations
GPD	Gas phase deposition
HIP	Hot isostatic pressing
HIS	Holographic interface solidification
HSC	High speed cutting
LC	Laser cladding
LDA	Laser diffraction analysis
LENS™	Laser Engineered Net Shaping
LM	Laser melting

LMD	Liquid metal deposition
LOM	Laminated object manufacturing
LPS	Liquid phase sintering
LS	Laser sintering
LTP	Liquid thermal polymerisation
M ₆ C	eta phase
MAM	Metal additive manufacturing
MIM	Material incremental manufacturing
MMC	Metal matrix composites
MRI	Magnetic resonance imaging
NbC	Niobium carbide
NC	Numerical control
Nd:YAG	Neodymium-doped yttrium aluminium garnet
PCBN	Polycrystalline cubic boron nitride
PCD	Polycrystalline diamond
PM	Powder metallurgy
PMD	Precision metal deposition
PSD	Particle size distribution
RAPDASA	Rapid Product Development Association of South Africa
RP	Rapid prototyping
RSM	Response surface methodology
SA	South Africa
SDM	Shape deposition modelling
SEM	Scanning electron micrograph
SGC	Solid ground curing
SLA	Stereolithography
SLM	Selective laser melting
SLPS	Supersolidus liquid phase sintering
SLS	Selective laser sintering
SMS	Selective metal powder sintering
SSS	Solid state sintering
SU	Stellenbosch Univeristy
TaC	Tantalum carbide
TiC	Titanium carbide
TRS	Transverse rupture strength
US	United States
UV	Ultraviolet
VC	Vanadium carbide
VFP	Volume Frequency Percent

VUT	Vaal University of Technology
WC	Tungsten carbide
WC-Co	Tungsten carbide-cobalt alloy
WC-Ni	Tungsten carbide-nickel alloy
W-Cu	Tungsten-copper alloy
WHAs	Tungsten heavy alloys
W-Ni-Cu	Tungsten-nickel-copper alloy
W-Ni-Fe	Tungsten-nickel-iron alloy
wt.%	Weight percentage
XRD	X-ray diffraction

Variables

A	Surface profile sample area	[mm ²]
d	Layer thickness	[μ m]
θ	Incident light angle	[degrees]
Df	Degrees of freedom	[]
E_d	Single track energy density	[J.mm ⁻²]
γ	Island orientation angle	[degrees]
h	Hatch spacing	[mm]
I_{in}	Intensity of incident light source	[W.mm ⁻²]
I_{sc}	Intensity of scatter pattern	[W.mm ⁻²]
k	Number of factors (or parameters)	[]
L	Number of levels in a DOE	[]
λ	Incident light wavelength	[mm]
λ_c	Roughness profile cutt-off length	[mm]
l_c	Surface profile cutt-off length	[mm]
l_n	Evaluation length	[mm]
l_r	Sampling length	[mm]
l_t	Transverse length	[mm]
N	Number of experiments in a DOE	[]
n	Material or substance refractive index	[]
P	Laser power	[W]
p	Fractional factorial <i>word</i> or <i>generator</i>	[]
Q^2	Model prediction precision	[]
R	DOE design resolution	[]
R^2	Model fit significance	[]
R_a	Arithmetic mean profile roughness	[μ m]
R_z	Maximum profile height	[μ m]
S_a	Arithmetic mean surface height	[μ m]

S_p	Maximum surface peak height	$[\mu\text{m}]$
S_q	Root mean square of surface profile deviation	$[\]$
S_v	Maximum surface valley height	$[\mu\text{m}]$
S_z	Absolute sum of surface peak and valley heights	$[\mu\text{m}]$
v	SLM process scan velocity	$[\text{mm}\cdot\text{s}^{-1}]$
VED	Volumetric energy density	$[\text{J}\cdot\text{mm}^{-3}]$
v_t	Surface and roughness profile scan velocity	$[\text{mm}\cdot\text{s}^{-1}]$
x	Particle size	$[\mu\text{m}]$

Chapter 1

Background

The South African manufacturing industry is confronted with a specific set of challenges, namely a relatively limited market - as compared to the European and US industries - and, recently, competition from Eastern sources (e.g. China's tooling industry) using low manufacturing input costs. In the South African context there is a rising need for customised industrial application solutions. The use of customised, application-based tools is a step towards achieving a competitive advantage thus allowing South Africa to compete on a global scale. Example areas of customisation include tool geometry and material composition. These materials include, but are not limited to, carbon and alloy steel, stainless steels, cast iron, aluminium and titanium alloys, polymers, ceramics, tungsten carbide alloys, cermets, and other composites. Tools used in a wide range of industrial applications - such as mining, agriculture, and manufacturing - rely on the superior wear resistance and hardness of hardmetals, such as tungsten carbide (WC). It follows that for specialist applications of WC material in the tooling industry, South African players need to exploit market niches where local conditions define a unique product. If South African players in these industries can be provided with rapid prototyping (RP) capability, using WC materials, new opportunities could develop for them. Tool design, with the ability to define it specifically, as well as the ability to iteratively adapt the tool to conform to the local requirements, is therefore required.

1.1 Additive Manufacturing

Additive Manufacturing (AM) has distinguished itself globally as a technology capable of producing highly complex parts using a variety of materials such as tool steel, titanium alloys, polymers, and other materials (Santos *et al.*, 2006; Damm and du Preez, 2009). A significant focus is being placed on the use of metal materials in AM processes. Several of these processes, capable of manufacturing parts using metal powders, have been established as industry-accepted technologies for metal part production and have been the subject of extensive research (Kruth *et al.*, 2003).

A schematic illustrating the inputs and outputs associated with general AM processes are shown in Figure 1.1 on page 2. Every AM process requires as input a material (or combination of materials), a CAD model data containing the original 3D part as well as the 2D part slices required to build the part, and finally the laser

control algorithm(s) used to control the laser and ultimately build the final part. The outputs associated with the general AM process is a final part that is either ready to use or requires post processing treatment. These parts are intended for use in multiple industries under different application areas including prototyping, reverse engineering, and direct part manufacturing, among others.

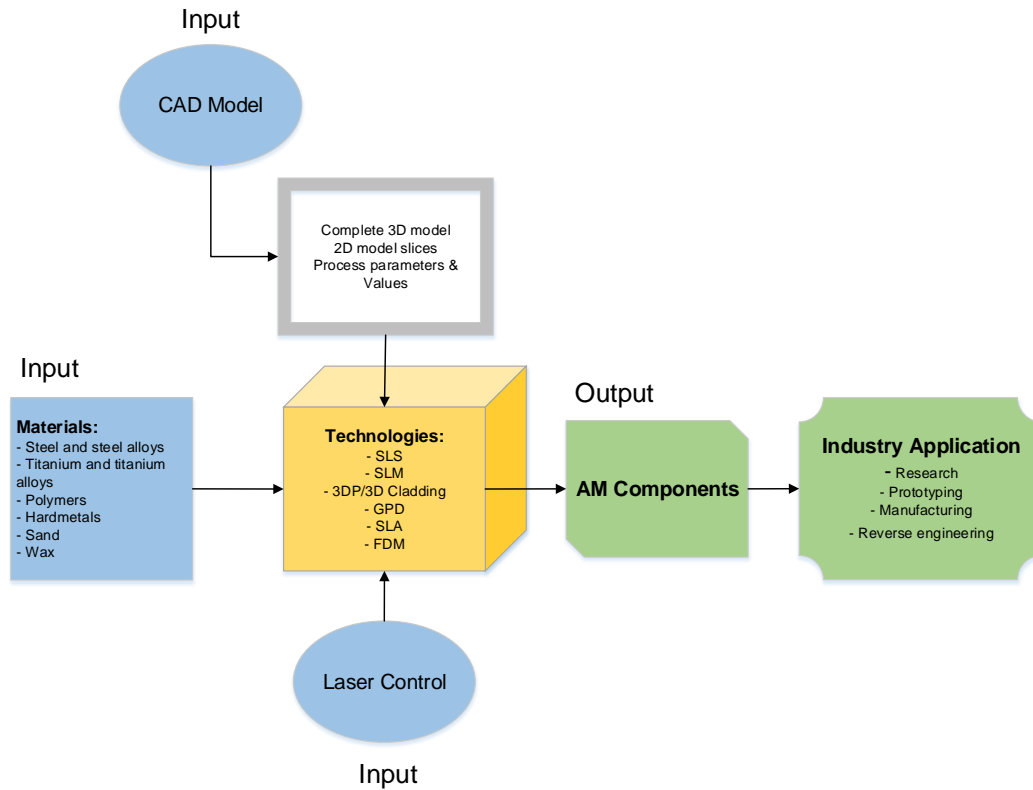


Figure 1.1: Graphic representation of general inputs and outputs associated with AM technologies.

The process used to build parts using metal powders is illustrated in Figure 1.2 on page 3. Parts are built by joining powder grains together using a laser and/or a separate binding material. The layer manufacturing (LM) technology has two pistons on which a build platform and powder delivery platform is mounted. The powder delivery platform is raised by a predetermined thickness, a scraper deposits a powder layer onto the build platform, the laser scans the corresponding part cross section as determined from the CAD model, the build platform is lowered, and the process repeats (Kruth *et al.*, 2003; Santos *et al.*, 2006). This process continues until the entire part has been successfully built.

Several LM machines exist, each employing different (or similar) building methods. These include three dimensional printing (3DP), fused deposition modelling (FDM), laminated object manufacturing (LOM), selective laser sintering (SLS), selective laser melting (SLM), and three dimensional (3D) laser cladding, among others. The primary manufacturing processes involving the use of powdered material

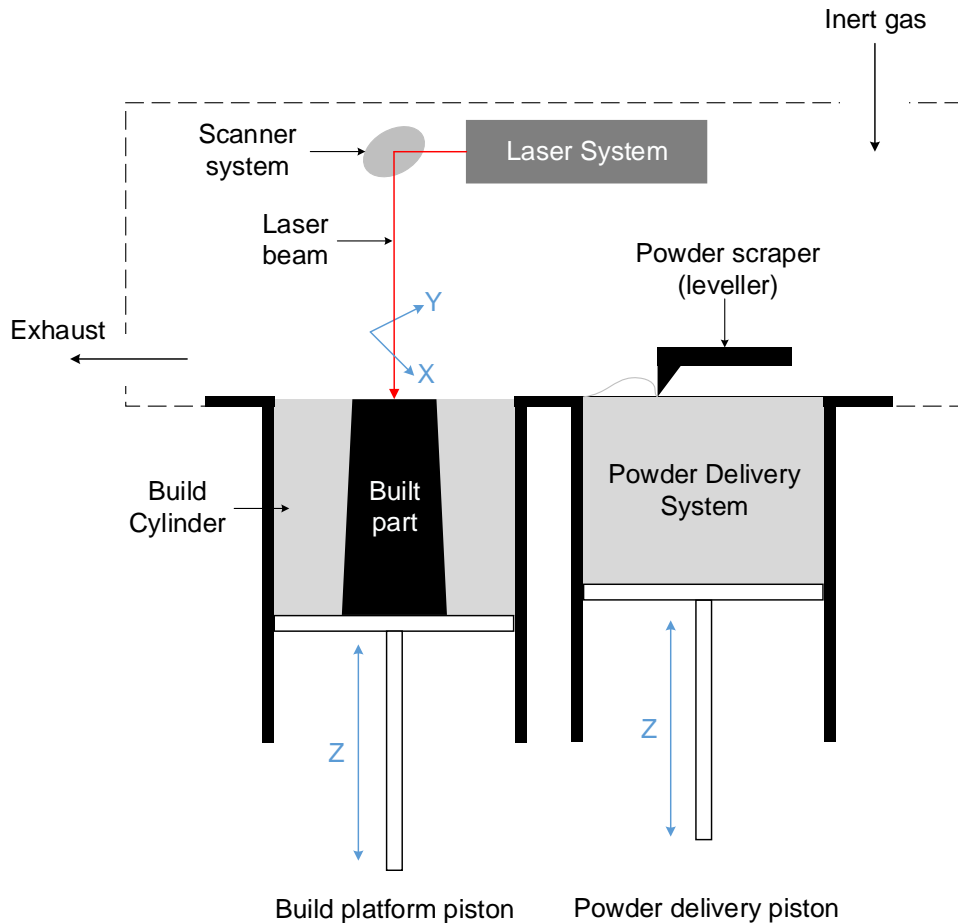


Figure 1.2: Illustration of the general powder-on-bed, metal based AM process.

includes SLS, SLM, gas phase deposition (GPD), and 3DP. Much like stereolithography (SLA), SLS and SLM use a laser beam to scan and fuse successive layers of raw material. In the case of SLS, the raw material is a bulk powder material that has been preheated to a temperature slightly below its melting point (Kruth, 1991). In some processes, however, preheating of the powder material is not required to achieve favourable results.

According to Pham and Gault (1998) any material that can be pulverised may be used for SLS/SLM. Materials include nylon, nylon composites, sand, wax, metals, and polycarbonates (Levy *et al.*, 2003). Kruth *et al.* (1998) furthered the argument by stating that notable progress has been achieved in developing new or better materials and methods for the use of AM processes. Metals such as bronze, steel, and hardmetals (e.g. tungsten carbide or cobalt) can be processed using SLS/SLM (Wang *et al.*, 2002).

The development of AM has recently concentrated on performance improvement in the use of injection-mould tooling. Some of these performance improvement concepts, such as conformal cooling channels, involves the use of AM to achieve results otherwise impossible with machined tooling (Wohlers and Gornet, 2012). A par-

ticular benefit for AM processes is the production of near net shaped parts from materials that are conventionally difficult to machine, such as hardmetals, ceramics, and composites (Kruth *et al.*, 1998; Chua *et al.*, 2003). In forming industries a reduction in production costs and machining time after process completion has been focused on by net or near-net shape manufacturing (Kim *et al.*, 1997). A typical example of an AM process, involving near net shape manufacturing, is Laser Engineered Net Shaping (LENSTM). This technology uses direct deposition of the metal powder onto the build platform as the material is being fused to the previous layer. A fundamental difference in the process control is that the build platform is moved in the X and Y axes, as opposed to the laser being moved to scan the part cross section (Atwood *et al.*, 1998).

As with any manufacturing system or technology, AM has its drawbacks. Parts created using AM systems tend to have inferior surface finishes and part accuracies as opposed to traditional manufacturing or machining processes (Chua *et al.*, 2003). Machined tools will have a higher quality surface finish than additively manufactured parts, and in most manufacturing applications a high quality surface finish is desirable. Depending on the specific field of application, however, a rough surface finish could be beneficial. For some applications, such as heat transfer, a rough surface finish has been found to be beneficial (Wohlers and Gornet, 2012).

1.2 Additive Manufacturing in South Africa

Despite the early introduction of AM technology to the rest of the world, South Africa (SA) experienced a late start in this particular area of technology adoption. Lagging behind by almost a decade, the first AM system was introduced in 1991 and had only tripled by 1994 (De Beer, 2011). By the end of 2011 total AM investments, both foreign and domestic, amounted to approximately US\$9.5 million for the year (Wohlers and Gornet, 2012). By observing the manufacturing industry and the emerging trends in the technology used, it becomes clear that SA is taking on a strong position in the AM industry. With government initiatives such as “Fab Lab” and association involvement from the Rapid Product Development Association of South Africa (RAPDASA) and the Global Alliance of Rapid Prototyping Associations (GARPA), SA has the resources to develop highly advantageous applications of AM in its industrial areas (Campbell *et al.*, 2011). De Beer (2011) found that the AM industry in SA is not limited to industrial areas of application and suffers a drawback in the form of a very wide and diverse range of application fields. These fields include anthropological studies, medical visualisation, industrial design models, architectural models, low volume tooling, and rapid manufacturing of functional parts, among others (De Beer, 2011).

Extensive research is being carried out at multiple research institutions across SA, with the majority of the research being concentrated on by universities. Specifically, the Vaal University of Technology, the University of Stellenbosch, and the Central University of Technology are on the forefront of AM research and technology adoption. Primarily, research was focused on the development of SLA and SLS, however the latest trend in the world of AM and academics is to shift the focus to the production of functional metal parts without the need for post process treatment.

The ability for an end-user to define a part or product that is tailored to his or her needs, have it produced in a fraction of the conventional lead time, and have it ready to be used or tested without the need for post process treatment is the end goal of most research efforts in this area of interest.

Considering the significant potential contained within the AM industry worldwide, a focused approach is needed in furthering the already flourishing applications of AM in the South African context. With government initiatives being focused on bolstering the manufacturing and mining industries, an area of particular interest is emerging in the industrial tooling sector. As stated previously the tooling industry relies on the superior hardness of metals such as WC. It therefore stands to reason that SA can benefit from the development of AM applications in the production of WC cutting tools, specifically aimed at providing customised industrial tooling solutions.

1.3 Cemented carbide tooling

Conventional powder metallurgy processes used to produce cutting inserts, drill buttons, and/or other tools differ greatly from additive manufacturing. A similarity, however, lies in the material's behaviour under sintering conditions.

Traditionally, tools made from cemented carbide powder (e.g. WC-Co) are produced by compressing the raw powder material into a desired shape and subsequently sintering the part in an oven. Martins *et al.* (2011) described their process thoroughly, from material production to the final sintering phase. This is illustrated in Figure 1.3 on page 5.

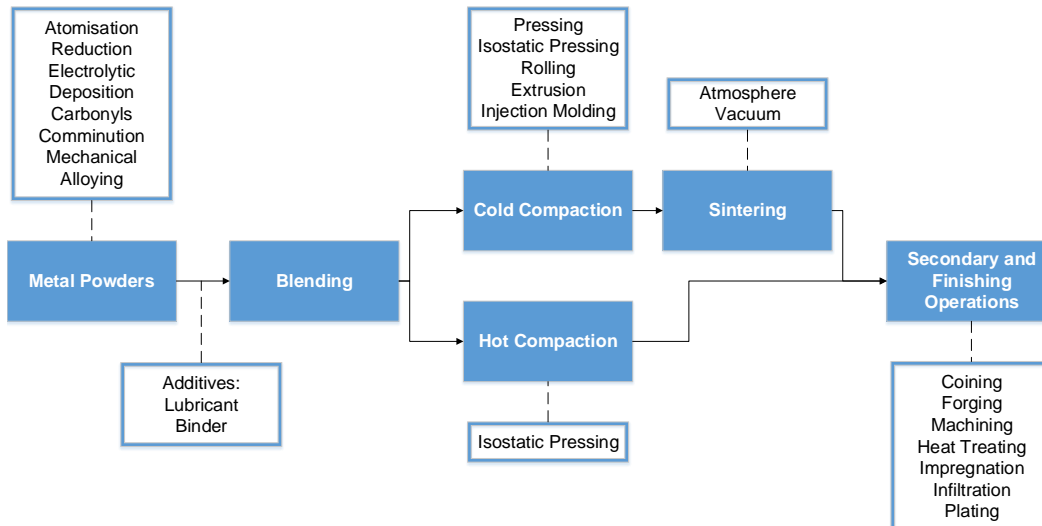


Figure 1.3: Process chain of conventional powder metallurgy part production. Adapted from Colton (2009).

The first step is material preparation. Depending on the application, a specific composition is required to obtain favourable mechanical and metallurgical properties once the part is completed. Often other carbide forming elements, such as titanium,

tantalum, vanadium, or niobium are added to the powder mixture to change grain growth activity during sintering. Also, different binder metals, such as nickel, are added to enhance the corrosion resistance or other properties of the tool (Martins *et al.*, 2011). Conventionally, WC-Co powder is produced by three steps (McCandlish *et al.*, 1992):

1. Reduce ammonium paratungstate (APT) powder to tungsten (W) powder.
2. React the W powder with carbon powder at 1600°C to obtain tungsten carbide (WC) powder.
3. Ball mill WC powder with high purity (>99%) cobalt (Co) powder.

Of course, many different processes now exist with which homogeneous WC-Co powder can be produced, such as the carburisation of tri(ethylenediamine) cobalt tungstate ($\text{Co(en)}_3\text{WO}_4$) or the atomisation of aqueous solutions of ammonium meta tungstate ($(\text{NH}_4)_6(\text{H}_2\text{W}_{12}\text{O}_{40}) \cdot 4\text{H}_2\text{O}$) and cobalt chloride (CoCl_2) (McCandlish *et al.*, 1992).

The application of one of these methods to produce WC-Co powder depends on the available compounds from which the powder is to be produced, as well as the intended application. This follows since each material production process will produce different compositions having different particle size distributions as well as different particle shapes.

The next step involves the addition of additives to the powder mixture, followed by blending. Typically this includes lubricants and binders. The binders are added to provide the part with green strength after the compaction process. Green strength allows a porous, unsintered part to be handled and prepared for sintering without falling apart.

Thereafter, the powder is compacted by means of two processes: 1) cold compaction or 2) hot compaction. Cold compaction may be done in various ways, including pressing, rolling, or extrusion. Typical compacting pressures can be as low as 70MPa for aluminium and as high as 800MPa for iron (Colton, 2009). Cemented carbides are compacted with pressures ranging from 140MPa to 400MPa. Figure 1.4 on page 7 illustrates the four steps in compacting a bushing. First a powder feed shoe deposits powder into die cavity. Next, the upper and lower punches apply pressure from the top and bottom, compacting the powder into the desired shape. The compacted shape is then ejected from the die and pushed from the mechanical press. Hot compaction is limited to isostatic pressing, which involves placing the powder to be sintered under high pressure and simultaneous high temperature for a certain period of time. Parts produced by hot isostatic pressing (HIP) do not need to undergo a separate sintering process.

The green parts produced by cold compaction are sintered in either a vacuum or inert atmosphere. This is done to limit the presence of oxygen in the sintering atmosphere which, for most metals, will form oxides at high temperatures. During sintering the binder is burned out of the green part resulting in a 100% dense, metal part. Typical sintering temperatures range from 760-900°C for copper, brass, and bronze and up to 2400°C for tantalum (Colton, 2009). Tungsten carbides are usually sintered between 1430°C and 1500°C for approximately 20-30 minutes. In work

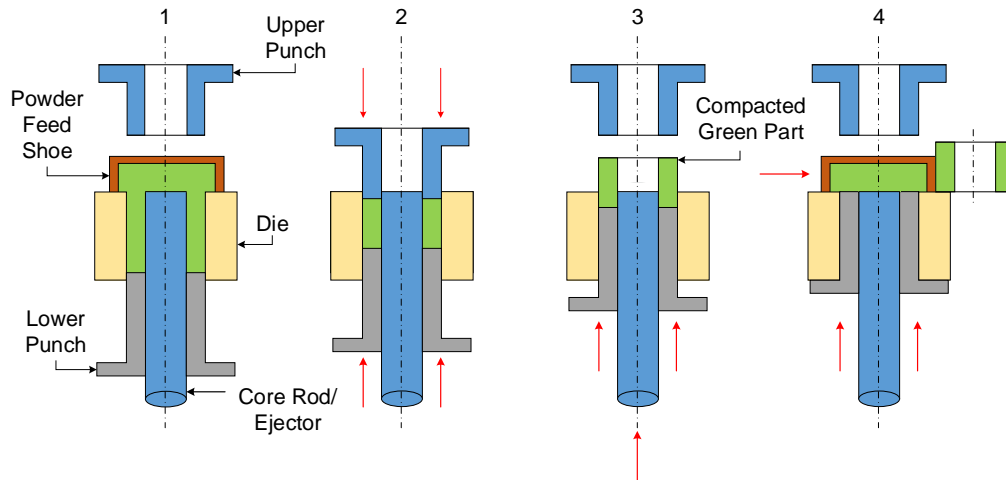


Figure 1.4: Cold compaction process to form a metal bushing. Adapted from Colton (2009).

carried out by Martins *et al.* (2011) WC-Co composites were produced at sintering temperatures ranging from 1360°C to 1450°C, depending on the composition. McCandlish *et al.* (1992) produced test samples by cold compaction and sintering at 1400°C. Here the material used is nanostructured WC-Co powder and dense structures were achieved after sintering at this temperature for only 30 seconds. This illustrates the significant influence particle size distribution can have on the production process and final part properties.

Prolonged exposure to high temperatures may have the undesirable effect of initiating and sustaining grain growth or increasing hardness (and subsequently decreasing toughness) through tempering. These effects can be controlled through careful selection of additional elements in the original powder mixture or through precise control of sintering temperatures and duration. For cemented carbides, this implies that there are three dominant influences on the ultimate hardness-toughness relationship in the final sintered parts: 1) the addition of grain growth inhibitors, 2) binder content, and 3) sintering conditions (Schubert *et al.*, 1998).

A frequent argument is made to increase the binder content in alloys with a given hardness, thereby increasing the toughness required in wear resistant parts. The use of a more ductile binder should increase the part's toughness. This relationship, however, is disputed by Schubert *et al.* (1998) wherein they show that alloys with similar hardness values and increasing binder contents exhibited no upward trend in toughness, as expected. Of course, this holds only for alloys with similar hardness values and is subject to the effect of many metallurgical processes, such as successful particle rearrangement, binder flow, and grain growth.

The hardness-toughness relationship in cemented carbides is further influenced by the addition of grain growth inhibitors. Typical additions include vanadium carbide (VC), tantalum carbide (TaC), titanium carbide (TiC), niobium carbide (NbC), and chromium carbide (Cr₃C₂) (Schubert *et al.*, 1995, 1998). TaC, TiC, and NbC are classified as cubic refractory alloy carbides and are designated as the γ -phase in WC-Co cemented carbides (Upadhyaya, 1998). These 'tool grade' cemented carbides are

typically used for machining of steels due to its resistance to diffusion wear. The sintering temperature for tool grade cemented carbides is generally higher than for straight grades.

Finally, the sintering conditions affect the hardness-toughness relationship in cemented carbide alloys. This follows since the conditions need to be altered to account for the powder/carbon/inhibitor system to be sintered. For example, a Cr-doped system will require lower sintering temperatures as opposed to a VC-doped alloy (Schubert *et al.*, 1998).

Considering the rising need in SA to find alternate solutions to manufacturing challenges that require custom solutions, it is imperative to explore the possibility of producing functional components, such as cutting inserts or through spindle cooled drill bits, using AM. The superior flexibility in material used as well as geometries produced makes AM an excellent candidate to meet these challenges. Furthermore, the sintering behaviour exhibited by cemented carbides in conventional PM processes is mimicked to a certain extent in AM, thereby offering comparable results in the end products. The following chapter presents the problem statement and associated research questions pertinent to the themes discussed here and defines the objectives to be met in this work.

Chapter 2

Problem Statement and Research Objectives

This chapter presents the problem statement for this study. The associated research questions are presented that this study attempts to answer. Furthermore, the research objectives for this study are presented. The objectives for this study are chosen to, when successfully accomplished, answer the research questions and present a solution to the problem statement.

2.1 Problem statement

The South African tooling industry faces multiple challenges, of which the capability to produce custom parts with complex geometries, using hardmetal alloys, is prominent. Furthermore, the rapid production of functional prototypes from these alloys presents a significant, and comparatively limiting, challenge to multiple industries. Additive manufacturing (AM) has proven to be capable of producing custom parts with complex geometries, as well as being capable of processing multiple materials, and combinations thereof. AM has also proven to be of particular use in the rapid production of functional prototypes.

There is a specific shortage of knowledge regarding the application of AM technology on cemented tungsten carbide (WC) alloy powders, aimed at industrial tooling applications. At present, tools produced using AM technology and WC-alloy powders have part densities that are too low for industrial application. Brittle tools have a higher probability of failure, as well as a higher rate of failure, as opposed to high density tools. Therefore, in order to exploit the flexibility of AM and the superior material properties of WC-alloys, a build strategy is required to successfully produce functional, highly dense WC-alloy tools for industrial application.

The following section presents the associated research questions pertaining to the problem statement presented here.

2.2 Research questions

The problem statement given in the previous section is investigated by answering the following research questions:

1. Can parts be additively manufactured from a cemented tungsten carbide alloy powder using an available AM process technology, namely selective laser melting (SLM) technology (i.e. LaserCusing[®])?
2. Does the powder particle size and structure influence the manufacturability (and subsequent achievable density) of WC-alloy parts?
3. What is the effect of alternate process, equipment, and material parameters on the manufacturability of WC-alloy powders using an AM technology?
4. Is the chosen AM process capable of creating high density (>95%) functional parts produced from WC-alloy powders?
5. Is the application of additive manufacturing feasible as a technology to improve manufacturing competitiveness where cemented tungsten carbide is the key material that determines the performance of the manufacturing process?

The research questions listed here are answered by completing the objectives presented in the following section.

2.3 Research objectives

The primary objective of this study is to develop a fundamental model that will serve as a guiding framework to successfully produce sintered single layers, free from surface defects or other undesirable characteristics that would hinder successful part production, using a SLM technology and a tool grade cemented tungsten carbide powder. The ability of the SLM technology to accomplish this objective is determined from an additive manufacturing perspective. That is, the produced sample layers must adhere to quality standards expected of any selectively laser melted metal layer, as opposed to production standards relating specifically to the material. Further to this objective, the following supporting objectives are completed towards answering the previously listed research questions:

- To evaluate whether uniform single layer samples can successfully be produced from a cemented tungsten carbide powder using an available SLM technology, i.e. LaserCusing[®].
- To determine the manufacturability of parts produced from a tool grade cemented tungsten carbide powder using an available SLM technology, i.e. LaserCusing[®].
- To determine how a change in process, equipment, and material parameters affects uniform single layer sample production in an available SLM process, i.e. LaserCusing[®].
- To determine what the optimal process combination is, in terms of combinations of process parameter values, to successfully produce single uniform layers from a cemented tungsten carbide material using an available SLM technology (i.e. LaserCusing[®]).

This chapter presented the problem statement, research questions, and research objectives for this study. By answering the research questions presented in the previous section, through the completion of the research objectives presented here, a viable solution to the problem statement for this study is achieved. The following chapter presents a comprehensive literature study pertaining to the research topic for this study.

Chapter 3

Literature

3.1 Introduction

Over the last 15 years extensive research has been focused on the high-end additive manufacturing (AM) processes. Of this research, special focus has been placed on the stereolithography (SLA) and selective laser sintering (SLS) technologies. According to Dimitrov *et al.* (2008) elements being investigated include process control issues as well as improvement of material properties. In South Africa (SA) a familiar trend of technology adoption is emerging, likened to that observable in first-world countries. Although technology adoption is behind by approximately 10 years, SA is gaining ground in the AM field through the acquisition of a variety of AM technologies. This is substantiated by the fact that the number of AM installations had grown to 450 machines in January 2012 (Wohlers and Gornet, 2012), with expected continuous growth for the foreseeable future. SA has looked to AM technologies as a way to revolutionise its industries, particularly the medical, automotive, aerospace, mining, and manufacturing industries, among others. The increased accessibility and variability in the AM technologies available has been a key enabler for the uptake of these technologies in SA, with close to 50% of South African universities having AM facilities in-house (Campbell *et al.*, 2011). According to a case study by the ZCorporation (2004) publications regarding findings on different material combinations and their effects on build accuracy, build volume, build time, and surface roughness, can contribute towards an improvement of the manufacturing industry in South Africa.

According to Campbell *et al.* (2011) universities such as Stellenbosch University (SU) and the Central University of Technology (CUT) are leading research teams into novel industrial applications where little to no research has been done. These novel applications include conformal cooling of wire drawing die sleeves (van Staden, 2013) and injection moulding (Moammer, 2011), drug delivery features in titanium-based hip replacements (Bezuidenhout, 2015), customised titanium cervical cage implants (Marcantonio, 2014), and dental modelling for external companies (Dimitrov *et al.*, 2008). Other industries, such as the architecture industry, have found benefits in AM applications as well. A SA based architectural firm, soundspacedesign (renamed Don Albert and Partners), commissioned SU to build a physical model of the Durban Millennium Tower for marketing and presentation purposes. The medical industry has also found benefits in the application of AM. Three dimensional (3D) models are

being constructed from computed tomography (CT) and magnetic resonance imaging (MRI) scans, enabling the examination of anatomy without surgery or dissection. Skill-intensive procedures and treatments can be planned and practiced ahead of time, to reduce the inherent risk and procedure time (ZCorporation, 2004). Dimitrov *et al.* (2008) concluded that the South African market is continuously experiencing moving boundaries in the AM industry. Given the correct combination of machines and supporting technologies, a competitive edge can be established and new market niches can be captured.

Companies, however, tend to resist adoption of rapid prototyping (RP) technology (such as 3D printing machines) due to a perception that the technology is too complex or the material might lack certain desirable qualities (ZCorporation, 2004). However, in terms of three dimensional printing (3DP), Dimitrov *et al.* (2008) suggests that the achievable dimensional accuracy ranges between 0.5mm and 1.0mm. Benefits realised through the application of 3DP include concept modelling and tooling production for prototyping. These prototypes are used for validation of designs, testing, and pre-production design checks (ZCorporation, 2004). Considering the application of this technology is largely aimed at prototyping, and not mass production, 3DP then offers a desirable advantage. 3DP has developed to a point where it provides vital, strategic benefits to organisations in a cost-effective manner (ZCorporation, 2004). According to Campbell *et al.* (2011) the number of RP machines sold by the end of 2008 amounted to approximately 136. Of these, 120 were 3D printers and the remaining 16 were high end AM machines. The significant amount of 3D printers collectively owned by industry and university establishments, as opposed to the ownership of high end AM machines, explains why there has been a slower development in the research regarding advanced applications such as tooling, direct digital manufacturing, or masters for investment casting.

Considering the degree to which industries in SA depend on the ability of a tool to resist wear and corrosion, as well as the desire for fast tool replacement in the event of tool failure or scheduled maintenance, it follows that there exists a need for wear resistant hardmetal tools that can be produced to specification in a shortened period of time. In the mining, agriculture, and power generation industries in SA, abrasion is a particular problem. In specifically designed experiments, Allen and Ball (1996) determined that wear rates can vary by up to 20 orders of magnitude in a typical agricultural application of heat treated steels. In power generation, it is found that ceramics and cemented carbides offer the ideal abrasive wear resistance required in the power station ash conditioners, wherein aggressive alumina silicate particles are mixed for subsequent processing (Allen and Ball, 1996). Significant attention must be paid to material design as well as production process choice when making tools intended for high wear condition use. AM processes have proven capable of producing tools fit for use in these conditions.

The adoption of AM technologies by the automotive and aerospace industries have been influenced by the increasing variety in available materials for application. This rapid adoption rate is further encouraged by the accuracy, surface finish, strength, and build speed achievable by AM technology. This, coupled with a relatively low cost, gives AM technologies a good price to performance ratio (Campbell *et al.*, 2011). As the need for faster response times rises and the necessity for specialised applications becomes more pressing, more and more tailored applications are

emerging that help set apart major players in the industries.

3.2 Additive Manufacturing technologies

Before the advent of additive manufacturing (AM) technologies new concept models had to be produced using standard machining operations and two dimensional (2D) engineering drawings (Pham and Gault, 1998). Skilled labourers were required to construct these models making resources limited thus prolonging the time required to produce the parts. Figure 3.1 on page 14 shows the evolution of AM, from the development of the first stereolithography system in 1985 to the advancement of materials processing capabilities. The evolution of AM over the years have enabled designers and manufacturers to develop physical models at a fraction of the conventional time and cost. Additive manufacturing technologies have been developed from rapid prototyping (RP) technologies. According to Pham and Gault (1998) RP technologies are described by two classes: those involving the addition of material and those involving the removal of material. Additive manufacturing describes a range of technologies which use CAD models to produce accurate parts, with little human intervention.

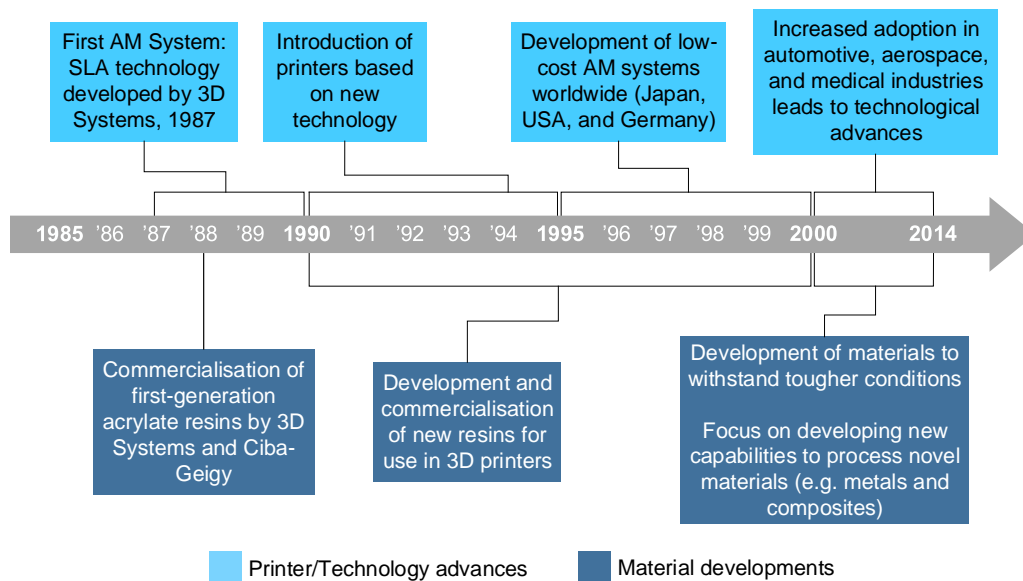


Figure 3.1: Additive manufacturing evolution time line. Adapted from Cotteleer *et al.* (2013).

Material removal processes are described by Kruth (1991) as processes that start with a larger amount of bulk material and thereafter removes all excess material. This may be accomplished either conventionally - i.e. turning, milling, grinding, etc. - or through use of non-traditional methods - i.e. electrical discharge machining (EDM), laser machining, and ultrasonic machining, among others (Kruth, 1991).

AM is based on a contrary forming mechanism as that of conventional material removal processes. That is, each part is built up by adding successive layers of

feedstock (usually powder materials) and subsequently fusing each new layer to the previous layer. Based on this principle any geometric shape imaginable could, theoretically, be manufactured using AM technology (Gu *et al.*, 2012). AM is considered to be a comprehensive integration of materials science, mechanical engineering, and laser technology. According to Pham and Gault (1998) and Kruth (1991) material addition can be done in one of three states: 1) liquid, 2) solid, or 3) powder. Dimitrov and De Beer (2014) classifies the different AM technologies according to three deposition processes, namely continuous printing, drop-on-drop printing, and drop-on-bed printing. The building material used in continuous or drop-on-drop printing, has to meet two requirements which limits the range of suitable materials. The first is related to the fluid printability, and the second is related to the intended application. In contrast to these material limits, drop-on-bed printing offers a much wider range of usable materials. According to Dimitrov and De Beer (2014) almost any material can be changed to a powder state, changing the task to finding a suitable binder to be used, for example in a selective laser sintering (SLS) process, instead of finding a suitable material.

AM is referred to in industry by many names, such as solid freeform fabrication, digital manufacturing, or e-manufacturing. Of all available AM techniques, stereolithography (SL), laminated object manufacturing (LOM), fused deposition modelling (FDM), three dimensional printing (3DP), and SLS were among the very first developed (Gu *et al.*, 2012).

Although a multitude of new possibilities are presented with the many manufacturing opportunities inherent to the use of AM technologies, AM is by no means a substitute for conventional manufacturing technologies and processes. The competitive advantages offered by AM are geometrical freedom and material flexibility (Levy *et al.*, 2003). Hopkinson and Dickens (2003) states that AM presents geometric freedoms not tolerated by other manufacturing processes, such as injection moulding. These freedoms include variable wall thickness and zero draft. Furthermore, geometric freedom is afforded to AM since specialised tooling is not required which would otherwise 'freeze' the production of parts. Hopkinson and Dickens (2003) further state that it is difficult to establish a complete scope for the use of such parts since part production in this manner is a very young practice.

According to Levy *et al.* (2003) AM faces several issues pertaining to material choice, part design, part accuracy, economic feasibility, and, finally, full technology adoption. Better base materials and the associated processing parameters are required, process accuracy needs to increase, part design approaches must be altered, and the available technology and materials need to become more cost effective if AM technology is to permeate the manufacturing industry and replace existing manufacturing processes. From a financial perspective, Pham and Gault (1998) reports cost reductions up to 70% when AM technologies are used. Time to market is also reduced by up to 90%. A possible explanation for this drastic reduction in cost and time to market is the ability of AM processes to minimize waste. This minimizes the total mass of materials needed for part production, as well as the cost associated with waste disposal since little waste is produced (Hopkinson and Dickens, 2003). Further cost reductions can be realised through the implementation of well structured recycling activities, wherein used materials are recovered, processed, and reused.

3.2.1 Additive Manufacturing technology overview

As stated previously, material addition can be done in one of three states: 1) liquid, 2) solid, or 3) powder. The following sections briefly describes each state and the associated AM technologies.

3.2.1.1 Liquid based processes

Manufacturing processes involving a liquid raw material state may be further classified as:

- Liquid polymers that form the base material and is subsequently solidified by light impact from either lasers or lamps (Stereolithography or Interference Solidification) or by heating (Thermal Polymerisation).
- Processes involving melting, deposition, and re-solidification of material. These processes include the use of metals (Shape Melting Technology), as well as resins and plastics (Fused Deposition Modeling and Ballistic Particle Manufacturing).

Stereolithography (SL) is an example of layer by layer manufacturing (Kruth, 1991). The process is reliant on a photosensitive monomer resin which forms a polymer and solidifies, when exposed to ultraviolet (UV) light (Pham and Gault, 1998). Liquid thermal polymerization (LTP) is similar to SL with the exception that the resin is thermoset using an infrared laser, rather than UV light (Pham and Gault, 1998). Beam interference solidification (BIS) involves resin polymerisation by two laser beams which are mounted at right angles. These lasers emit light at different frequencies which firstly excites the liquid and secondly polymerises the excited resin (Kruth, 1991; Pham and Gault, 1998). Solid ground curing (SGC), like SL and BIS uses polymerising liquids and light for part production. Layers from a computer aided drawing (CAD) file are made into masks, which are then placed over the liquid resin. The entire build surface is illuminated and any exposed resin solidifies (Pham and Gault, 1998). Holographic interference solidification (HIS) involves projecting a holographic image into a vat of photosensitive liquid monomer, which solidifies an entire three dimensional (3D) part rather than building it layer by layer (Kruth, 1991). The holographic image is generated from an entire CAD model, rather than layers of the CAD model (Pham and Gault, 1998).

Electrosetting (ES) involves printing electrodes onto a conductive material, such as aluminium. The completed layers are then stacked, immersed in an ES fluid, and energised. Any fluid between the metal layers solidifies to form the part (Pham and Gault, 1998). Ballistic particle manufacturing (BPM) is a process involving the solidification of molten metal. Parts are produced by droplets of molten metal being applied one on top of the other (Kruth, 1991). As the droplets hits the substrate it immediately cold welds to the part (Pham and Gault, 1998). Parts built using fused deposition modelling (FDM) are produced by deposition of a molten material - such as acrylonitrile butadiene styrene (ABS) or nylon - onto a base plate or previously solidified material (Kruth, 1991). Deposited material cold welds to previous layers or the base plate (Pham and Gault, 1998). Shape deposition modelling (SDM), according to Pham and Gault (1998), is a layered manufacturing process whereby molten

material is sprayed in a near net shape onto a base plate or substrate. Thereafter unwanted or excess material is removed using numerical control (NC) operations.

3.2.1.2 Solid based processes

Solid based additive manufacturing processes are limited. However, these processes have found useful applications such as part modelling and prototyping. The primary process using solids for parts fabrication is called laminated object manufacture (LOM). Parts are produced from stacks of build material which is cut from a roll (Kruth, 1991). Each layer is glued onto the previous layers using a hot roller which activates a heat-sensitive adhesive. Each layer's contour is cut with a laser which is modulated to cut to exactly one layer depth (Pham and Gault, 1998). With the development of more advanced AM technologies, LOM has become an outdated technology and is rarely used for its intended purposes.

3.2.1.3 Powder based processes

Powder based systems are arguably the most important and widely researched type of AM technology and is rapidly developing into cost effective alternatives to conventional production processes. In powder based AM technologies, parts are built by joining powder grains together using a laser or a separate binding material. The primary manufacturing processes involving the use of powdered material includes selective laser sintering (SLS), selective laser melting (SLM), gas phase deposition (GPD), and three dimensional printing (3DP). GPD relies on the solidification of reactive gas particles. The molecules of the reactive gas are decomposed using either heat or a light to render a solid. The resultant solid then adheres to the substrate which forms the part (Pham and Gault, 1998). 3DP involves the application of powder layers to a substrate (Pham and Gault, 1998). This is then selectively joined using a binder which is sprayed through a nozzle (or multiple nozzles). According to Kruth (1991) the process combines features of SLS and BPM. Prior to binder application the powder layer is misted with water droplets. This serves to avoid disturbance of the powder layer when the binder is applied (Pham and Gault, 1998). Much like stereolithography, SLS uses a laser beam to scan and solidify successive layers of raw material. In this case the raw material is a bulk powder material which has been preheated to a temperature slightly below its melting point (Kruth, 1991). According to Pham and Gault (1998) any material that can be pulverised may be used for SLS. Materials include nylon, nylon composites, sand, wax, metals, and polycarbonates.

According to Levy *et al.* (2003) the SLM process is described as a process characterised by the use of metallic powder material, applied in the form of a binderless metallic powder free of fluxing agents that is heated by a laser beam to melting temperature, forming a fully molten layer throughout the contact area of the incident laser beam. SLS and SLM are nearly the same process, using the same processing apparatus and procedures. The fundamental difference between these two processing techniques is that SLM is based on a complete melting and solidification of metallic powders (Gu *et al.*, 2012). Selective metal powder sintering (SMS) is defined to be a subclass of Stereolithography, focusing on the use metal material rather than

polymers. Like most additive manufacturing techniques, SMS builds a part layer by layer from a CAD file. Similar to SLS and SLM, SMS uses an unbound metal powder mixture as a basic material (Kruth *et al.*, 1996). Successive layers are deposited and spread thin, on the order of 0.4mm layer thickness, before being bound together using a focused energy source. Unlike laser melting techniques, SMS produces highly porous green parts that requires post-treatment in order to increase final component density.

According to Campanelli *et al.* (2010) the SLS process can be characterised as either direct or indirect. Indirect SLS uses polymer coated metal grains. The polymer is melted during the sintering process and subsequently fuses the metal grains together, resulting in a green part. Post-sintering processes (usually post-treatment in a high temperature oven) are thus required in order to remove the polymer to obtain a metal-metal link between adjacent metal grains.

Direct SLS (or DMLS) is similar to SLM in that a high melting temperature metal is fused together in subsequent layers through the use of a low melting temperature metal matrix. Here, the low melting temperature metal matrix (or binder) replaces the polymer used in indirect SLS.

Powder-based AM processes, like SLS, are highly dependent on the liquid-solid wetting characteristics of the chosen powder system. The wetting behaviour describes not only the wetting of the structural metal, but the wetting between the molten system and the solid pre-processed layer as well (Gu *et al.*, 2012). The most significant differences between SLS and SLM are as follows (Campanelli *et al.*, 2010):

- SLM has the ability to use powdered metal without the addition of a binder metal.
- SLM is capable of providing a higher incident energy density, thereby offering a higher final part density.

Metal-based AM technologies can be classified into two main categories: 1) Non-melting and 2) melting processes. A further sub-structure is proposed by Levy *et al.* (2003), thereby classifying the AM technologies according to the used material form, i.e. powder, foils, or wire. This classification structure can be seen in figure 3.2 on page 19. They also present a graphical representation of the capability profile associated with layer manufactured metal components as opposed to other conventionally manufactured metal components, referring to the achievable geometric complexity and economic build quantity. Figure 3.3 on page 20 indicates a high geometric complexity for layer manufactured objects, as well as a significantly low economic quantity. Campanelli *et al.* (2010) also states that a significant drawback to the use of SLS or SLM is the slow production rate, making it unsuitable for large production lots, and the resultant cost increase associated with powder production and procurement. Yasa and Kruth (2011) states that there are further drawbacks associated with the SLM process. These include inferior surface quality (as opposed to conventionally manufactured parts) and residual part porosity. In applications where high strength is necessary, such as machining or boring using WC-based tool bits, any residual porosity could lead to premature and catastrophic failure of the tool. Tool failure could result in costly damage to the machine tool, the processed part, and/or the machine operator.

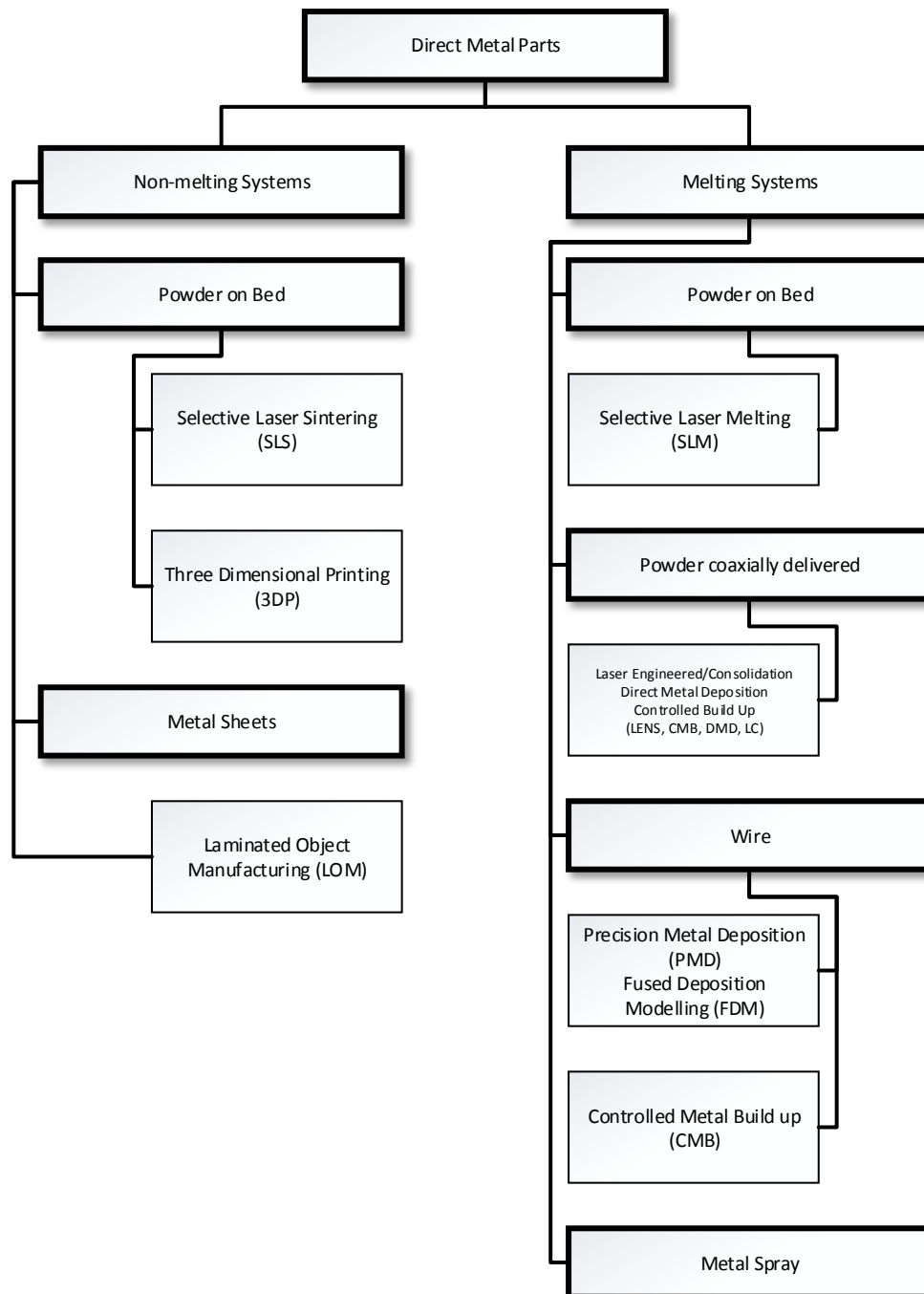


Figure 3.2: Technology classification structure as proposed by Levy *et al.* (2003).

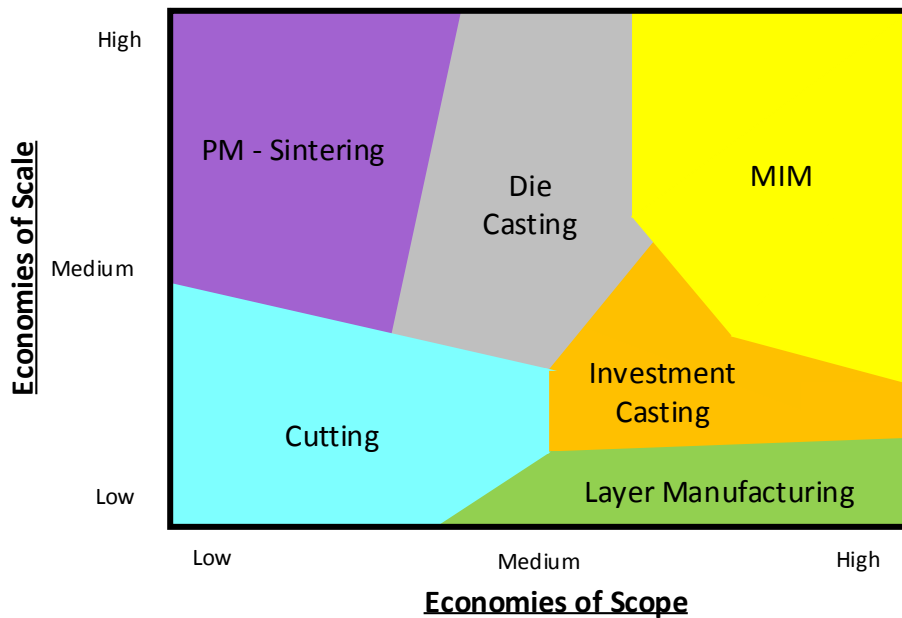


Figure 3.3: Manufacturing technology capability profile. Adapted from Levy *et al.* (2003).

This, however, is rapidly changing. SLM technology is capable of producing highly accurate parts, with Concept Laser GmbH reporting accuracy measurements below 0.04mm (Levy *et al.*, 2003). Zaeh and Ott (2011) claims that there are two main technological advances responsible for the growing success of selective laser melting production technology: 1) high process flexibility and the possibility of producing geometrically complex parts and 2) a wide range of different metal powders may be used with SLM. According to Levy *et al.* (2003) the most significant advantage associated with SLM is the independence associated with material selection. Theoretically, all typical metals and alloys may be considered candidate materials to be used in SLM. Presently regarded as the most versatile AM processes, SLS, SLM, and liquid metal deposition (LMD) are capable of processing a very wide range of metals, alloys, ceramics, and metal matrix composites (Gu *et al.*, 2012). Furthermore, other AM technology advancements, such as those achieved by the German company Voxeljet, have led to AM processes being capable of producing parts in an ‘assembly line fashion’.

Although many different nomenclatures for SLM are used in industry today (e.g. direct metal laser sintering or LaserCusing[®]), each is distinguishable from the other based on the selection of workable materials available, as well as the individual scanning strategies employed (Zaeh and Ott, 2011). A notable drawback associated with all of these technologies is that the microstructural features and the resulting mechanical properties are difficult to tailor for a specific material, given any of the aforementioned AM technologies (Gu *et al.*, 2012). Here, microstructural features include grain size, grain shape, and texture, among others. Mechanical properties include strength, hardness, and residual stresses, among others.

Based on the principles of selective laser melting (SLM), LaserCusing[®] technology is based on the fusion of metallic powder materials using a laser. Almost all

metallic materials may be used and parts are constructed on a layer-by-layer basis (Sinirlioglu, 2009). According to Yasa and Kruth (2011) SLM distinguishes itself from other layer manufacturing processes by being able to produce parts that have comparable mechanical properties to those of bulk materials of the same composition. Ductility, however, is significantly reduced (Levy *et al.*, 2003). This may be addressed through selection of appropriate materials and the associated weight percentage distribution.

Theoretically, 100% part densities are achievable through use of LaserCusing[®] technology. Sinirlioglu (2009) claims that such a dense structure yields mechanical properties as high as (or higher than) conventionally machined parts. In this respect, LaserCusing[®] technology differs from other SLM based technologies. An inherent benefit associated with this technology is the possibility to reuse unfused powders after processing is complete. No fresh powder materials are required to be added after each production (Sinirlioglu, 2009). This, however, seems counter intuitive as some powder will be lost to the completed part and subsequent builds may require more powder material than what is left over in the build chamber. From an investigation into the production of dental bridges, Sinirlioglu (2009) concludes that LaserCusing[®] technology allows for easier, cheaper, and faster part production having 100% dense microstructures and high mechanical properties.

Of the abundant AM processes and technologies available, it is clear that powder based systems offer the greatest benefits in terms of material selection, achievable part properties, and final part quality. Furthermore, the capability of powder based systems to reuse un-fused powders makes it an economically viable solution to the challenges facing the manufacturing industry. The following section describes the forming mechanisms associated with, primarily, SLS and SLM processes using cemented carbide powder systems.

3.2.2 Forming mechanisms in sintering processes

In order to develop processing parameters for additively manufacturing cemented carbide parts, having very high densities and desirable mechanical properties, a thorough understanding of the forming mechanisms associated with sintering of cemented carbides is required. Upadhyaya (2001) found that, in sintering of WC-Co powders, rapid densification of the carbide particles occurs as a result of interfacial diffusion that form close packed boundaries in the cobalt-rich regions. This leads to localised densification of carbide particles. Increasing the cobalt content increases the areas of localised densification (or aggregation of carbide particles) that increases the initial densification behaviour. Final part density is dependent on the temperature evolution during the sintering process. In additive manufacturing, sintering is achieved through the use of a laser. Frequently, built parts appear rigid and porous after a laser sintering process which poses a significant obstacle to producing functional parts using an AM process.

Kruth *et al.* (2005) introduced the term 'selective metal powder sintering (SMS)' as a collective term for SLS and SLM processes using metal powders. Furthermore, they investigated the different binding mechanisms prevalent in SMS. Two approaches exist for the consolidation of metallic powders using these processes: 1)

sintering, and 2) melting. Melting implies that a continuous feed of powder is required in the molten pool in order to compensate for thermal shrinkage. If no powder is applied, shrinkage will lead to the formation of pores (Kruth *et al.*, 1996).

In the case of a hard carbide phase sintered in a soft binder metal, shrinkage of the processed components are attributed to the spreading of the liquid binder on the carbide particles, as well as the rearrangement of the carbide particles that are dissolved in the liquid binder (Allibert, 2001). The use of a binder alters the mechanical properties associated with the carbide particles, specifically the hardness and toughness. This results in the need for a trade-off between hardness and toughness, typically determined by the intended application of the part (Andren, 2001). Wang *et al.* (2013) states that WC-Co composite components benefit greatly from a higher level of wear resistance provided by the WC particles. However, sufficient cobalt is needed in order to deter crack initiation and propagation, brittle fracture, or catastrophic failure of the components. This then suggests the existence of an inverse relationship between fracture toughness and wear resistance. The trade-off is dependent on the composition between WC and cobalt. Pores present in the built SMS component may lead to unpredictable and undesirable mechanical properties. This follows, since neither the size nor the location of the pores can be known within the components.

Porosity elimination is hindered by the rapid solidification of the molten pool or layer. This occurs due to the shrinkage of the powder-liquid mixture experienced during the cooling stage. Although porosity elimination is not accomplished completely, final part density is still higher than the apparent powder density.

Sintering distinguishes between solid state sintering (SSS) and liquid phase sintering (LPS) (Kruth *et al.*, 1996). Zhang *et al.* (2010) confirmed from their experiments that there are two dominant forming mechanisms present in the SLM process: 1) LPS, where full melting of the Ni and Fe particles occurred with no melting of the W particles and 2) SSS where full melting of the W particles occurred. SSS is driven by the diffusion of metal atoms from one particle to another. This process is slow and presents a significant drawback for SMS. More than 50% of densification occurs before the eutectic temperature is reached in the pseudobinary WC-Co system. As a result of surface tension forces, surface diffusion occurs between the binder (i.e. cobalt) as well as agglomeration between the metal and WC particles. It is important to note that any trace of reactive elements present in the powder mixture will influence solid state sintering (Upadhyaya, 1998).

Reduction of oxygen present during the SSS stage is essential, as the escape of carbon monoxide (CO) is difficult when temperatures are increased and pore cavities close up. At lower temperatures the cobalt diffuses out to the carbide surfaces and agglomeration of the carbides starts at these temperatures. A further increase in temperature results in the finer carbides dissolving and the binder being alloyed with the tungsten and carbon.

LPS is much more attractive, from a production point of view, as it results in much faster sintering and densification without the application of external pressure. Enhanced atomic diffusion enables faster sintering. This occurs in the presence of the formed liquid phase, ultimately facilitating material transport. The basic material consists of two metal powders, one with a high melting point and another with a low melting point. LPS densification occurs in three stages: 1) initial fluid flow, 2)

subsequent solution-precipitation, 3) and final coalescence by way of solid state sintering. A set of minimum criteria exists to achieve LPS: 1) a low temperature, 2) solid phase solubility in the liquid phase, and 3) successful liquid wetting of the solid, hard phase (Upadhyaya, 1998). In the WC-Co system, sintering produces a liquid phase that satisfies these basic conditions to achieve LPS. Traditionally, cobalt is the most widely used binder due to its excellent wettability and the solubility of WC.

Both SSS and LPS involves a phenomenon called necking, wherein two powder particles are fused together by partial melting or metal diffusion of the particles (Agarwala *et al.*, 1995; Levy *et al.*, 2003; Tolochko *et al.*, 2003, 2004; Kruth *et al.*, 2005, 2007). In LPS, the main driving force is the lowering of free energy (Upadhyaya, 1998). A vacancy gradient forms wherein the vacancy concentration in the neck goes from high to low as a flux of atoms towards the neck occurs.

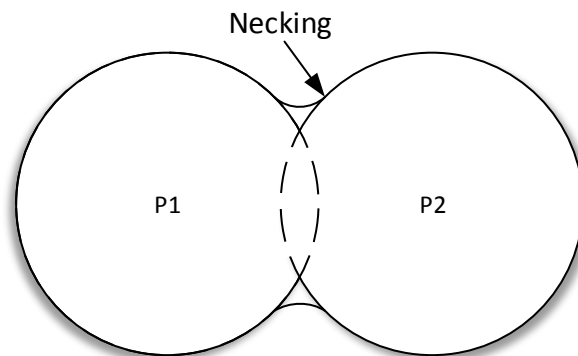


Figure 3.4: A visual demonstration of necking in SSS. Adapted from Kruth *et al.* (2005) and Kruth *et al.* (2007).

Figure 3.4 on page 23 visually demonstrates the necking phenomenon present in SSS. P1 and P2 are powder particles. Solid state sintering occurs below the eutectic temperature. Some of the hard phases are dissolved in the solid binder, new phases may be formed, and porosity starts to decrease (Andren, 2001).

Figure 3.5 on page 24 visually demonstrates the necking phenomenon present in LPS. Again, P1 and P2 are powder particles. The final step in the manufacture of cemented carbides is LPS. In conventional powder metallurgy (PM), this occurs at 1400-1500°C. The material is heated to, and maintained at, this temperature for several hours. Here, further dissolution of hard phases occurs, new phase precipitation continues, and density increases to nearly 100%. The process of sintering cemented carbides subjects the material to persistent LPS when all the basic conditions are met, i.e. 1) sintering at a low temperature, 2) liquid wetting of the solid grains, and 3) solubility of the solid particles in liquid (Upadhyaya, 1998, 2001). As stated previously, the main driving force behind densification behaviour during LPS is the minimisation of the total surface energy present in the system. Kruth *et al.* (2005) states that lowering the surface tension in the molten pool will enhance the wetting behaviour of the molten particles. Pores are eliminated during this process leading

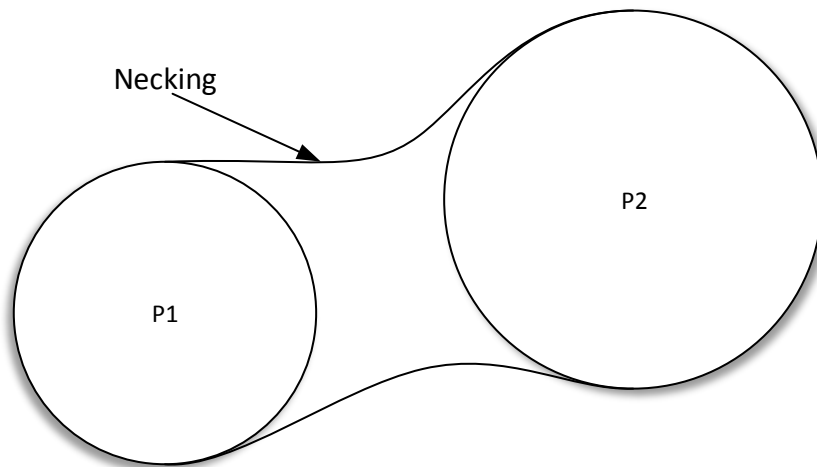


Figure 3.5: A visual demonstration of necking in LPS. Adapted from Kruth *et al.* (2005).

to improved mechanical properties. However, as solubility of the solid particles in liquid increases, initial densification will occur as a result of other processes as well. LPS is based on the fusion of a structural element (solid particles) and a binder material (liquid particles). According to Kruth *et al.* (2005) the binder and structural materials in LPS can be divided into three groups according to the type of powder grains used. These are 1) separate grains, 2) composite grains, and 3) coated grains.

According to Eso *et al.* (2005) typical cemented carbide manufacturing processes involve the use of liquid phase sintering as the dominant densification mechanism. They further explain that the flow of the liquid phase during sintering is a result of two mechanisms: 1) capillary forces drive liquid binder migration during sintering and 2) the inhomogeneity of local chemical composition causes local variations in liquid volume fraction during sintering.

In the experimental work carried out by Wang *et al.* (2002) the dominant sintering mechanism was LPS. Here the material to be sintered consisted of a mixture of a structural hardmetal, WC, and a softer binder metal, cobalt. In an investigation on SLM of W-Ni-Cu composite powders, Zhang *et al.* (2012b) observed two prevalent sintering mechanisms. The first occurred as a result of high laser energy input and full particle melting of the W, Ni, and Cu particles. Here particle bonding is realised through SSS. The second occurred as a result of lower energy input and full melting of the Ni-Cu component and no melting of the W particles. It was observed that the Ni-Cu solid phase functioned as a binder in the final part structure, whereas the W particles functioned as the structural skeleton. Li *et al.* (2010) investigated AM of W-Cu powder using SLM technology. During experimentation the morphological features of a single molten track was analysed and results showed LPS to be the dominant forming mechanism in the process. Here the Cu particles acted as binder for the structural W particles.

Upon heating of the powder bed the binder metal forms a liquid. This results in a rapid initial bonding, attributable to the strong capillary forces exerted on the

liquid. This is called the rearrangement stage in LPS (Upadhyaya, 1998). Part densification is found to increase as the particles rearrange to accommodate the different particle shapes. During the intermediate stage of LPS, shape accommodation and densification occur simultaneously (Upadhyaya, 2001). Further densification occurs during the second (solution-precipitation) and third (solid phase sintering) stages. During solution-precipitation particles are packed closer together. Solid phase sintering occurs as a result of a slower densification rate. These final two stages require longer sintering times. As laser contact is very brief during SLS and SLM, leading to a shortened liquid phase in the binder material, lower density parts are produced by this technology than by conventional PM technology (Wang *et al.*, 2002).

Complete densification in cemented carbide systems is achieved during the first two stages of LPS. More importantly, high density is obtained at the first stage of sintering. Prolonged exposure to sintering conditions will lead to microstructural changes, including particle growth in the solid (Upadhyaya, 1998). Excessive particle growth can be detrimental to the mechanical properties of the sintered part. Important factors, including particle size, the amount of liquid present, the solubility of the solid in the liquid, and contact angle, influences the maximum achievable densification.

Although the forming mechanisms in sintering processes are well understood, AM processing of cemented carbides is a relatively new field of research. Forming mechanisms will differ for different powder systems and a wide field of knowledge needs to be established to ensure successful sintering is possible. The following section presents a discussion on cemented carbides used in additive manufacturing processes.

3.3 Cemented carbide materials in additive manufacturing

Alloys have made up the majority of metals used for AM purposes. The weak nature of pure metals (such as the limited mechanical properties and poor anticorrosion/anti-oxidisation capabilities), as well as the unsuccessful attempts at producing functional components using laser sintering (LS) and pure metals, places the focus of AM technology on alloyed metals. To illustrate, LS processed titanium exhibits three different microstructural regions:

- Unmelted grain cores;
- Melted grain surfaces;
- Residual pores.

Gu *et al.* (2012) presents a categorisation of metallic powder systems available for use with LS systems: 1) a structural/binder metal powder combination with significant difference in melting temperatures, 2) multi-element metal powders without a significant difference in melting temperatures, and 3) intermetallics from elemental constituents. Transition metal carbides, such as WC, have been a topic of interest in

many research studies since its discovery. Properties such as high hardness, high electrical and thermal conductivities, and high melting temperatures make these metals suitable for use in applications that demand excellent mechanical properties (Kim *et al.*, 2004). Allibert (2001) concluded that the good hardness-toughness combination required by the applications of, for example, WC-Co components are achieved with dense mixtures of WC structural particles and cobalt binder. In cemented carbide applications, WC is found to be the most important carbide. It has a very high melting point (a peritectic melting temperature of 2785°C) and a high hardness. Most commonly, commercial grades of WC-Co composites contain between 4wt.% and 30wt.% cobalt and have grain sizes ranging from 0.5µm to 10µm (Paul and Khajepour, 2008). In a study on functionally graded composites (FGCs) Eso *et al.* (2005) used WC-Co powders with 6wt.% and 16wt.% cobalt content, with a grain size distribution of 1µm and 5µm. The use of finer grain sizes results in significant improvements in mechanical properties of metallic, intermetallic, and ceramic materials (Kim *et al.*, 2004).

Kumar (2009) suggests that other alloying metals, such as iron and nickel, may be used to replace the cobalt binder element. Zaeh and Ott (2011) also states that the wide range of powders available for processing using SLM systems include aluminium, copper, titanium, tool steel, and metal matrix composites (MMCs), among others (Zaeh and Ott, 2011). According to Andren (2001) the raw material used for the production of cemented carbides is pure or pre-alloyed powders such as WC, titanium carbide (TiC), cobalt, iron, and nickel. These powders are typically ball milled in alcohol to obtain a typical grain size of 1-3µm. Gu *et al.* (2012) found that research efforts focussed on AM of titanium, nickel, and iron based alloys have entered a mature phase of practical application. Conversely, research aimed at the use of WC based alloys in AM is still in its infancy, and creating high density parts has yet to be accomplished. Zaeh and Ott (2011) states that more refractory materials must be investigated in order to expand the list of available materials to be processed using SLM technology.

MMCs are traditionally produced by mechanically alloying different powder components. Usually, this is a mixture of a metal matrix and ceramic powders (Gu *et al.*, 2012). Generally speaking, MMCs created in this way can be considered a multi-component system consisting of a combination of structural and binder elements. Here, the matrix metal acts as the binder and the ceramic reinforcement acts as the structural material. Of the wide range of MMCs available, WC-Co is the most extensively studied. The poor wettability between the metal matrix and the ceramic reinforcement can be reduced by encapsulating the ceramic particles with a metal coating (i.e. the metal matrix). This effectively modifies the interfacial structure and promotes wettability. Pre-alloyed powders exhibit melting behaviour different from pure metals in that there exists a zone between the liquidus and solidus temperatures wherein liquid and solid phases coexist during melting and solidification process. The challenge here is to find the processing parameters that creates a supersolidus phase, i.e. a semisolid system. This gives rise to the term supersolidus liquid phase sintering (SLPS) (Gu *et al.*, 2012).

An important consideration, when choosing which powder material parameters is to be used, is the flowability of the bulk material. Powder flowability greatly affects the process of placing the powder selectively, or merely scraping over a new layer

as in powder bed based systems. Ott and Zaeh (2010) states that spherical powder grains, with a size distribution between 20 μm and 53 μm , has a high ease of flow. Consequently, spherical WC-Co powders with a wide range of weight composition and grain size is used during experimentation. Research regarding the manufacture and use of WC-Co has dramatically improved the material's mechanical properties and performance, and these remain the most important and widely used cemented carbides. Andren (2001) states that WC-Co powder systems are most often used due to the excellent wetting ability related to the cobalt binder.

It is clear that a large collection of cemented carbide material systems have been the subject of research for use in AM processes. There persists, however, a specific knowledge gap regarding the application and use of these materials in AM processes, when compared to conventional AM metals such as tool steel. Furthermore, there are several considerations that must be taken into account - such as the mechanical properties of the material before and after sintering - that will influence the choice in material. The following section describes these considerations.

3.4 Considerations in cemented carbide tooling

Since industrialisation occurred machining has been the predominant manufacturing activity using specialised tooling. Operations such as milling, drilling, turning, sawing, reaming, and tapping make use of hardmetal tools to achieve the desired end results. Although the main application of machining principles are aimed at metallic materials, other materials such as wood, ceramics, plastics, and composites can be processed in a similar fashion. The processing of these materials under different conditions often lead to extensive heat and wear development. This results in the need to develop better tooling solutions, ultimately leading to advanced material combinations and tooling geometries. Cemented carbides offer a superior combination of strength, wear resistance, and toughness, making it a popular choice as a tool material for industrial applications.

3.4.1 Mechanical and material properties of cemented carbides

The high demand for cemented carbide tools stems from the inherent material and mechanical properties associated with these tools. This includes superior hardness, toughness, and cutting ability, as well as its ability to resist corrosion and erosion, amongst other wear mechanisms. These properties make cemented carbides ideally suited for applications such as cutting, milling, turning, boring, and drilling amongst others (see section 3.4.2 on page 31 for more on cemented carbide applications).

A distinction is made between cermets and cemented carbides by way of composition. Cemented carbides do not include cermet materials, as cermets are made up of nitride or carbo-nitrides rather than carbides. The term 'hardmetal' is frequently used to include both cermets and cemented carbides. Newer cermet grades, wherein cobalt replaces nickel, approaches cemented carbides in composition, therefore the term 'cemented carbide' is also often taken to include cermets (Andren, 2001). Cemented carbides can be described as tough, very hard tool materials made

up of micrometer-sized carbide grains embedded in a metallic binder matrix. Typically, these carbides are fabricated by liquid phase sintering (LPS) at approximately 1300-1500°C. According to Prakash (1995) the grain size of the structural element varies from 0.3µm to 40µm. Also, the binder content generally ranges from 3wt.% to 30wt.%. Finer grained cemented carbides are characterised by higher abrasive wear resistance and hardness with lowered ductility. Made up of a carbide (e.g. WC, TiC, etc.) and a binder metal (cobalt, nickel, etc.), cemented carbides obtain its superior wear resistance from the carbide and its toughness and ductility from the binder and other alloying metals.

In an investigation by Wentzel and Allen (1997) to determine the erosion-corrosion resistance of WC hardmetals, different cemented carbides were selected for testing. These consisted of different combinations of cobalt, nickel, and chrome. It was found that nickel rich binders are softer than cobalt rich binders, leading to accelerated wear rates in functional components. In experiments undertaken to assess the performance of certain materials under erosive conditions, Allen and Ball (1996) found WC-Co alloys gave the best results. It was found that erosion of a WC-9.5wt.% Co alloy occurred mainly as a function of brittle fracture of the WC skeleton. Under erosive conditions by particles carried in a liquid stream, materials such as tungsten carbide-nickel (WC-Ni) and WC-Co showed the most erosion resistance. It is concluded that, when all other factors are equal, fine-grained homogenous materials are expected to show the best resistance to microfracturing. Prakash (1995) concluded that the impact strength of cemented carbide alloys are, however, limited.

Prakash (1995) further states that tungsten carbide and cobalt are the main constituents of cemented carbides. The WC imparts the necessary hardness, strength, and wear resistance whereas the cobalt imparts the desired toughness and ductility. Kumar (2009) presents the following reasons for the preference of combining WC and cobalt over other cemented carbide combinations:

- Cobalt is not soluble in WC, thereby requiring less cobalt to act as a binder.
- At 1275°C, cobalt forms a liquid phase with WC, dissolving 10wt.% of WC.
- Dissolved WC reprecipitates on solidification which increases part strength.
- Cobalt has a high melting temperature (1493°C) and exhibits high thermal strength.

According to Andren (2001) the WC-Co microstructure consists of hard WC grains embedded in a tough, cobalt-rich binder phase. The WC phase is stoichiometric and does not dissolve any cobalt, but the cobalt phase dissolves tungsten and carbon in equal proportions during LPS. During the cooling process the tungsten and carbon re-precipitates into WC until temperatures are too low for any diffusion to continue. It follows that during SLM of these powders this re-precipitation will occur rapidly, due to the rapid heating and cooling experienced by the material during the SLM process.

The final WC-Co microstructure is described as follows: the WC grains form a continuous, hard skeleton in which cobalt is present as grain boundary segregation. With large cobalt grain sizes, both the structural metal and the binder metal are

continuous throughout the bulk material. The final microstructure will be dependent on the raw powder used. Pre-alloyed powders will demonstrate several differences in microstructure, and thus differences in material and mechanical properties, as that of mixed-composition powders (i.e. powder compositions created by merely mixing two or more different powders). As an example Murr *et al.* (2012) demonstrates the microdendritic structure of individual powder particles that have been pre-alloyed using cobalt-based particles. This can be seen in figure 3.6 on page 29.

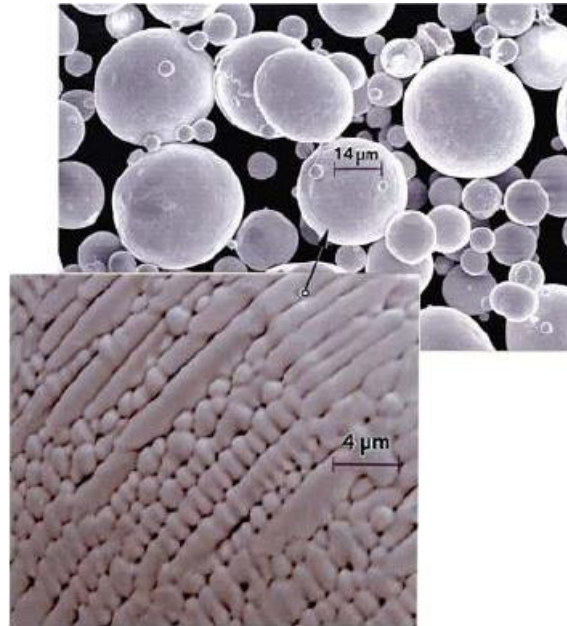


Figure 3.6: Microdendritic structure of individual pre-alloyed cobalt-based powder particles. Adapted from Murr *et al.* (2012).

In comparison, Kim *et al.* (2004) presents scanning electron microscopy (SEM) images of binderless WC powders of differing particle sizes. The difference in particle shape, as well as distribution in size, is apparent and can be seen in figure 3.7 on page 30. Furthermore, Kim *et al.* (2004) presents SEM images of sintered samples using these binderless powders and it is clear from figure 3.8 on page 30 that the particle size and shape has a definite influence on the achievable microstructure, which directly influences the mechanical properties. An important subject for study, concerning cemented carbides, is the elevated temperature strength behaviour of the material. Maximum material strength is influenced by several variables, such as the carbide grain size. The elevated temperature transverse rupture strength (TRS), on the other hand, depends on material composition as well as particle grain size. According to Paul and Khajepour (2008) TRS is defined as a combination of shear strength, tensile strength, and compressive strength and is generally used to measure the toughness of cemented carbides. The addition of certain materials, such as chromium carbide

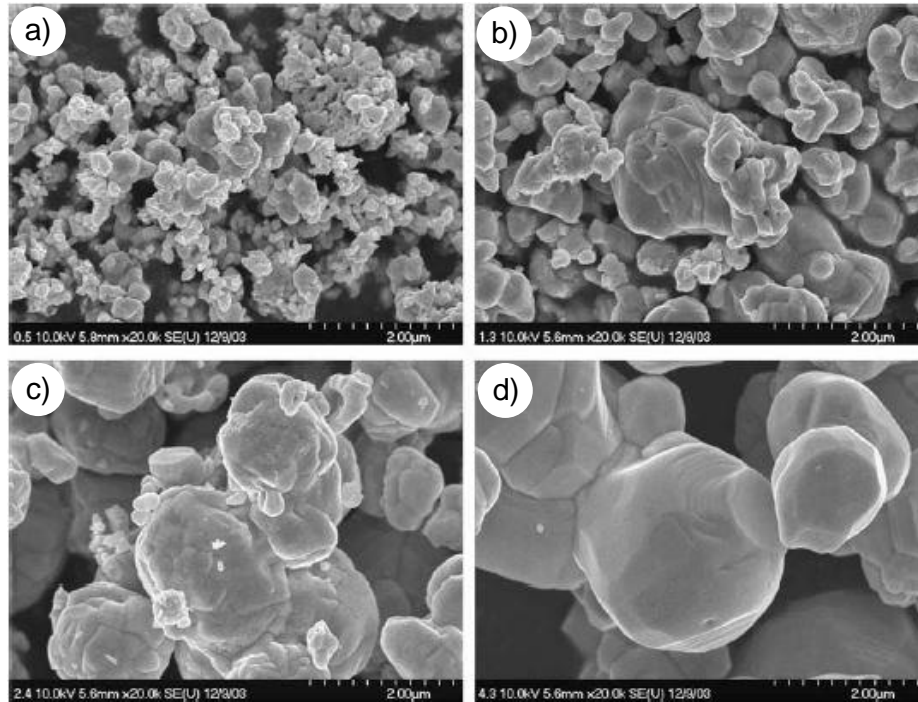


Figure 3.7: SEM images of WC powders with different particle sizes: a) 0.4, b) 1.3, c) 2.4, and d) 4.3 μm. Adapted from Kim *et al.* (2004).

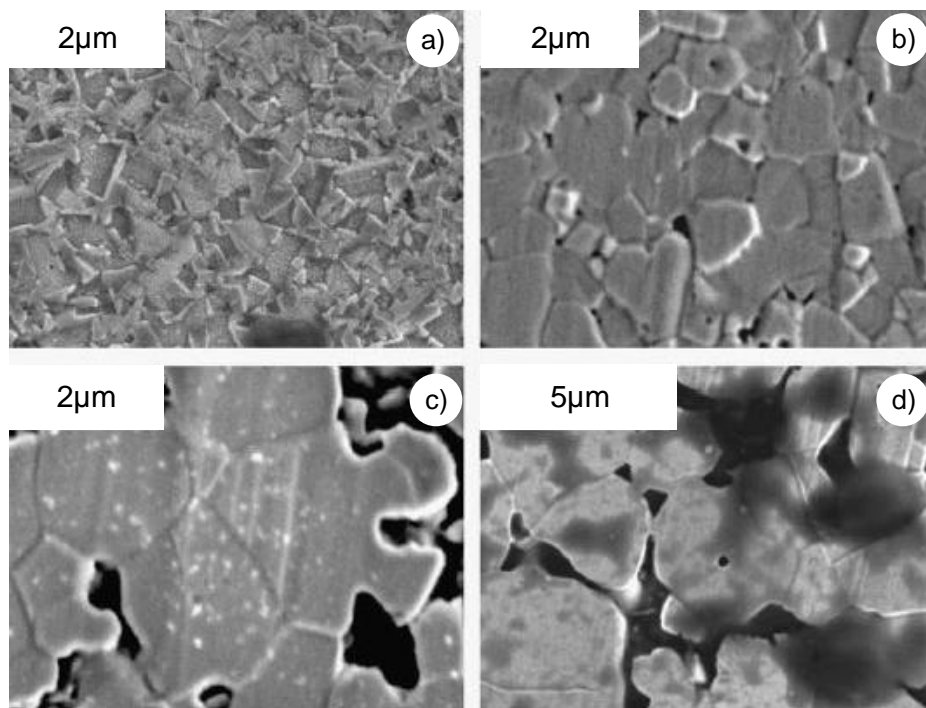


Figure 3.8: SEM images of sintered, binderless WC powders with different particle sizes: a) 0.4, b) 1.3, c) 2.4, and d) 4.3 μm. Adapted from Kim *et al.* (2004).

(Cr₃C₂), increases the elevated temperature TRS (Upadhyaya, 2001). In tables 3.1 and 3.2 on page 31, Wang *et al.* (2013) summarises the mechanical properties associated with cemented carbide parts with two different cobalt weight percentages.

Table 3.1: Mechanical part properties of cemented carbides by cobalt weight percentage. Adapted from Wang *et al.* (2013).

Sample (Co wt.%)	Static Compressive Strength [MPa]	TRS [MPa]	Wear Resistance [cm ⁻³]
10	11800	3144.9±78.2	2.7±0.2
16	9800	3099.4±60.2	4.7±0.2

Table 3.2: Hardness and fracture toughness of cemented tungsten carbides by cobalt weight percentage. Adapted from Wang *et al.* (2013).

Sample (Co wt.%)	Hardness [HV ₁]	Fracture Toughness [MPa.m ^{0.5}]
10	1242±9	15.3±0.5
16	1052±9	17.7±0.1

Based on differing cobalt weight percentages, the mechanical properties will increase and decrease accordingly. Cemented carbides are specifically tailored for each application by varying the amount of carbide and binder (or other alloying metals) present in the material composition (Prakash, 1995). As stated, cemented carbides offer a multitude of useful properties including high hardness, high melting temperatures, high thermal and electrical conductance, and a high chemical stability (Kim *et al.*, 2006).

3.4.2 Cemented carbide applications

High hardness and high strength are characteristics associated with cemented carbides. These components exhibit a high wear resistance and toughness and is therefore widely used in applications requiring these traits. According to Masuda *et al.* (1993) sintered diamond tools are superior to the wide variety of commercial tools available; however cemented carbides (such as WC-Co tools) are preferred due to the high cost of sintered diamond tools. Given the high hardness and fracture resistance, as well as the resistance to erosion and corrosion, cemented carbide alloys are a primary choice for industrial applications. Cemented carbides have found a wide variety of applications which include rock and earth drilling (Andren, 2001), forming dies, cutting tools, and wood machining and shearing/cutting blades (Prakash, 1995), among other speciality high wear applications (Wang *et al.*, 2013; Paul and Khajepour, 2008; Masuda *et al.*, 1993). Sintered cemented carbides are used extensively in earth-boring bits due to its wear resistance and increased earth-disintegrating capabilities (Kumar and Peltz, 1994; Prakash, 1995).

The application of cemented carbides in metal machining stems from the superior compressive strength and abrasive wear resistance of the material, allowing tools to be produced with sharp cutting edges and large rake angles (Prakash, 1995). These carbides are sintered into solid solution using transition metals as a binder matrix for the carbide particles. As stated, cemented carbides offer a combination of hardness and toughness, currently unparalleled by other materials. This is especially true of submicron cemented carbides.

In some applications wear is an advantageous occurrence during a manufacturing process, such as polishing and cleaning. Wear and corrosion can however lead to ineffective operation, as well as susceptibility to sudden failure of a functional component (Allen and Ball, 1996). The performance of cemented carbide tools, in long-life applications, is largely influenced by the wear resistance properties of the material selected. Coupled with the requirement for wear resistance and toughness in the cutting tools, a good surface finish also requires the cutting tools to have a sharp cutting edge. These requirements make cemented carbides ideal candidates for this application.

In an effort to determine the best combination of cemented carbide and binder phase compositions, researchers investigate the effective wear rates of the materials. Sudden breakdown, inefficiencies, and significant financial losses are but a few consequences associated with the wear of tools used on machinery found in industrial applications, such as agriculture, mining, and energy production (Allen and Ball, 1996). According to Wentzel and Allen (1997) cemented carbides are also used to process wood and wood-based materials, composites, plastics, ferrous and non-ferrous metals, and are used in several other processing applications. These include cutting tools, sandblasting nozzles, mining bits, and other wear resistant applications. Saw blades, milling cutters, and wood working routers are a few examples of tools in the wood machining application that make use of cemented carbides. Due to the inhomogeneity of natural wood grains the tools often experience high impact forces, thus the requirement for high levels of toughness in the cutting tools (Prakash, 1995).

Almost every industry uses submicron cemented carbides to combat the erosive and corrosive wear effects prevalent under certain operating conditions. However, cemented carbide tools with a large carbide grain size are more readily available for cutting materials that exhibit high abrasive action during cutting operations (Masuda *et al.*, 1993).

Most cemented carbide alloys used in the above mentioned applications are tailor-made, proving the need for tailored solutions in specific application areas. These application areas include mud and paint nozzles, textile knives, glass cutters, and high pressure pistons, among others.

Research presented by Ott and Zaeh (2010) shows that single layer cemented carbide recoating can be applied to functional components, in order to enhance the wear resistance properties. For example, wear resistant coatings can be applied to multiple material surfaces and be tailored to fit a specific application, such as the inside of pipes conveying abrasive materials. Specific applications of specialised tooling includes high speed cutting (HSC) and dry machining. Dry machining results in significant cost reductions but also in performance reductions. With dry drilling, for example, achieving the same tool life as with conventional drilling requires much

slower production rates (Cselle and Barimani, 1995).

An important factor for consideration, then, is the achievable tool life and the associated wear rates of cemented carbide tools for specific applications. The following section discusses component wear and tool life in cemented carbides.

3.4.3 Component wear and tool life in cemented carbides

According to Allen and Ball (1996) wear can be classified into three major categories, namely 1) abrasive wear, 2) adhesive wear, and 3) erosive wear. Abrasion is identified by phenomena known as gouging, ploughing, scoring, and cutting, among others. It is characterised by relative motion of abrasive particles on a metallic surface. Arsecularatne *et al.* (2006) describes abrasive wear to be a result of the presence of microscopic hard abrasives in the work material, as well as dislodged abrasive grains from the tool, abrading the tool.

Rawat and Attia (2009) states that abrasive wear is the dominant wear mechanism associated with drilling operations using WC-Co drill bits. This abrasive action is characterised as either hard abrasion or soft abrasion. Hard abrasion relates to crack initiation and propagation in the WC grains, leading to WC grain pull-out by brittle fracture. Soft abrasion relates to the wear of the cobalt binder. As the binder is worn deeper, larger areas of the WC grains are exposed and fracture by fatigue is accelerated.

According to Masuda *et al.* (1993) the primary causes of wear associated with machining carbon materials are as follows: 1) abrasive action caused by hard carbon particles and 2) the ejection of carbide particles due to brittle fracture. Rawat and Attia (2009) concluded that fracture during drill initiation, abrasion, and potentially adhesion are the three dominant wear mechanisms associated with drilling carbon fibre composites, using WC-Co drill bits.

Masuda *et al.* (1993) found that cutting tools containing larger carbide grains and less cobalt were preferred and showed the least amount of wear development during testing. Furthermore, a larger fracture toughness corresponds to a larger tool hardness. This results in a reduction in the tool wear rate. The dominant wear mechanism present during tooling is dependent on the prevalent cutting conditions as well as the tool and work materials used. Arsecularatne *et al.* (2006) states that tool life is dependent on several variables that includes the machine tool, the tool geometry and material, the work material, and the cutting conditions. Arsecularatne *et al.* (2006) presented work based on the wear mechanisms present in tooling operations, focusing on WC, polycrystalline cubic boron nitride (PCBN), and polycrystalline diamond (PCD) tools. Some of the major complexities found in establishing adequate machine theory relating to tool life of these alloys in cutting operations are as follows:

- Highly complex machining operations involving extreme conditions of high strains, high strain rates, and high temperatures.
- A significant lack of suitable data.

The combination of these extreme conditions and the lack of valuable insight leads to increased tool wear rates, thereby diminishing tool life.

The dominant wear mechanisms affecting tool life in cutting operations, using for example WC cutting tools, were found to be either diffusion or mechanical abrasion. The deciding factor is contained in the cutting conditions (high versus low cutting speed, high versus low cutting force, etc.) as well as the work material (steels, metal matrix composite alloys, etc.). In experiments carried out by Kumar (2009) the wear resistance of SLS processed parts were measured by fretting wear tests. Furthermore, bend and strength tests were performed to characterise the built parts. The final microstructures, as well as the fretting wear test results, were analysed using SEM. It was found that the sample surface had not been worn out, however the counterbody had been abraded leaving debris on the sample. The SEM images in figure 3.9 on page 34 shows the debris accumulated on the sample surface without any significant wear present. Although this tool surface experiences nearly no wear, debris accumulation

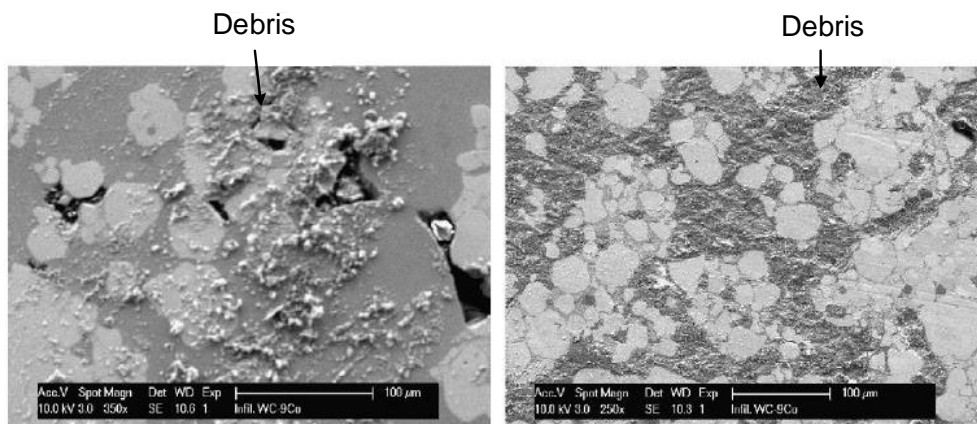


Figure 3.9: SEM images of WC-9wt.%Co parts showing debris accumulation on the sample surface. Adapted from Kumar (2009).

will lead to diminished surface finish as a result of surface ploughing. This means that the work surface will start to experience abrasive wear as opposed to the tool surface. The tool, therefore, experiences a different form of tool life deterioration. Results observed from tests performed by Masuda *et al.* (1993) lead to the characteristics of tool failure in WC-Co tools to be described as follows:

- WC particles experience systematic wear, whereas the cobalt binders wear in a very short time.
- WC grains experience cracking and fracturing and fall away after a certain cutting time.
- Carbon particles hardly adhere to the rake and clearance face of the cutting tool.

Adhesive wear occurs as a result of two contacting surfaces, moving relative to each other, under a normal load. It includes fretting, scuffing, galling, and surface fatigue. Erosive wear is damage caused by particle impact entrained in a gas or liquid stream. This type of wear can have serious deteriorating effects in engineering systems, such as pipelines.

Tool wear affects the tool change schedules, the end-product quality, and the productivity of the industrial application, amongst others. Arsecularatne *et al.* (2006) states that during turning operations it is crucial that catastrophic tool failure be avoided. Component damage to the cutting tool, the work piece, and the turning machine will interrupt the machining process significantly. It is therefore necessary to determine when a tool is nearing the end of its useful life. Rawat and Attia (2009) confirms that defects caused by the wear of tools, such as drill bits, has a significant economic impact on the machining process.

Tool wear determines what the optimal operating parameters must be in order to obtain the longest tool life, thereby incurring the minimum production costs and achieving the highest productivity. Typically, flank and crater wear is measured to determine when a tool is likely to fail, with flank wear being the dominant indicator.

According to Kim *et al.* (1997) the theory of wear can be classified according to the contact conditions. Amongst wear theories the abrasive-wear theory is generally applied to cold-forming processes and the tool-wear mechanism associated with it (Kim *et al.*, 1997; Lee *et al.*, 2012). Several factors are related to wear in mutual metal contacting: contact surface temperatures, contact surface roughness, hardness of the tool material, the normal pressure acting on the tool surface, the length of contact between the contacting metals, and lubrication conditions (Kim *et al.*, 1997). An important consideration in tool wear is friction. Friction poses the threat of accelerating tool wear.

The nature of frictional forces may be explained in a number of ways. In particular, the nature of frictional forces on dry contact surfaces is most popularly explained by the welding theory. According to Shaw *et al.* (1970) the welding theory is explained by the junction formation between the asperities of stationary contacting surfaces. These junctions weld under high local pressures. Friction is explained as the breaking of these junctions, together with a certain degree of surface ploughing (Shaw *et al.*, 1970).

An observation is made regarding the effects of binder composition in WC-alloy tools. It has been found that the binder phase, present in cemented carbides created using a binder metal, is more susceptible to corrosion and oxidation than the carbide phase. This is due to the binder phase's inferior chemical characteristics, as opposed to the carbide phase (Kim *et al.*, 2006).

Material removal, i.e. tool wear, occurs as a mechanism of binder loss closely followed by WC grain pull-out (Wentzel and Allen, 1997). It follows that the success of a binder is measured by its ability to resist removal, either by improved mechanical properties or better corrosion resistance. According to Kumar and Pelty (1994), depending on the material composition, cemented carbides, such as tungsten carbide-cobalt (WC-Co), are used for its various superior mechanical properties including wear resistance. It was found that cemented carbide alloys containing cobalt and nickel elements yielded the best results for earth-boring bit applications. Wentzel and Allen (1997) found that a higher weight percentage binder phase (e.g. cobalt)

present in the functional tool will lead to prolonged removal of the binder phase, thus taking longer to reach the possibility of WC grain pull-out. Conversely, Human and Exner (1997) found that material removal rates will increase with an increase in binder phase content since the fraction of corroding phase is increased.

Upadhyaya (2001) concluded that the processing, properties, and performance of any functional cemented carbide component used in industry is highly dependent on the nature of the component, i.e. the presence of both hard carbide and soft metal binder phases. Depending on the application of the functional component, the amount of binder phase present will vary resulting in differing wear rates.

This section presented several important considerations in cemented carbide tooling, namely the mechanical and material properties of the tools, the intended applications, as well as the wear mechanisms associated with the application. The following section presents literature regarding the use of cemented carbides in additive manufacturing processes.

3.5 Additive manufacturing of cemented carbides

The current literature available on AM of cemented carbides is limited. Specifically, the current knowledge on SLM of tungsten carbide powders are limited. The bulk of the literature available focuses on AM of tungsten-based alloys, with a limited focus on WC alloys. These alloys consist of WC powder and some binder element, such as cobalt, nickel, chrome, or iron. A similar selection of alloying metals are used in AM of tungsten-based powders. For the purpose of this study, processing of both tungsten-based alloys as well as WC-based alloys are investigated in order to establish a fundamental foundation and understanding of the prevalent sintering mechanisms, as well as processing parameters, pertinent to AM of these alloys. Amongst the wide range of AM technologies available, SLM has distinguished itself as being capable of producing metal components directly from metal powders. Deprez *et al.* (2013) found the major advantages involved in the use of AM technology to be the associated fast production rates and the possibility of producing novel geometries ordinarily impossible to produce using conventional techniques. Butler (2011) presents several advantages associated with the use of SLS:

- Reduced part count;
- Reduced post-production processing;
- Reduced requirement for inspection and the associated documentation;
- Higher design flexibility;
- Reduced engineering analysis and (stringent) specification requirements;
- Cost reductions in design, inspection, production, and finishing; and
- Reuse of non-sintered powder.

The associated advantages of SLM are the same as for SLS, with the addition of being capable of producing functional metallic components. According to Li *et al.* (2010) and Zhang *et al.* (2012b) SLM offers a high flexibility in its feedstock that enables it to produce complex final parts without conventional shaping methods that tend to be cost-intensive. Material versatility and final quality has yet to be extensively explored. Wang *et al.* (2002) investigated the use of direct selective laser sintering (DSLS) to build functional components using WC-Co powders. According to the results, production of sintered carbide or hardmetal parts using DSLS is feasible. The associated advantages include the production of highly complex 3D parts in shortened production times and at lowered production costs. According to Li *et al.* (2010) tungsten-copper (W-Cu) composite alloys have significant potential in electrical and thermal applications. The forming processes associated with this composite are, however, limited in its capabilities. Conventional powder metallurgy (PM) techniques, such as powder compaction and sintering, are being used to manufacture functional components using W-Cu powders. These techniques are not suited for production of complex shapes and are thus constrained in its applications.

According to Zhang *et al.* (2012b) tungsten is a very hard and brittle material, making it especially difficult to machine into complex shapes using conventional machining methods. However, with properties such as a high melting temperature, a high oxidation resistance capacity, a high density, and good electronconductivity, tungsten has a wide range of applications. These include industrial and even military applications. Tungsten-nickel-copper (W-Ni-Cu) alloys, for example, form part of the tungsten heavy alloys (WHAs). WHAs have excellent mechanical properties, high densities, and good corrosion resistance. SLM is used to produce complex shapes due to its high flexibility in feedstock, but due to the high melting temperature of tungsten (3,420°C) the process, and ultimately the achievable part density, is limited (Zhang *et al.*, 2012b).

The following sections presents a discussion on the influences on part production, and the resultant properties of these parts, in additive manufacturing. Furthermore, the phenomena observable in these parts (such as cracking, warping, and delamination) are discussed.

3.5.1 Influences on achievable part properties

In any additive manufacturing process there are several variables that influence the achievable part properties. For powder based AM systems, these include the material being used, the process being used, and the energy source used to consolidate the powders. Process related parameters include single layer thickness, scan velocity, hatch spacing, and scan strategy. Laser specific parameters include laser power, spot diameter, wavelength, and energy per laser pulse. Material specific parameters include type, particle size, particle distribution, particle shape, and percentage composition. The following sections explain the influences these aspects have on the achievable part properties.

3.5.1.1 Material

The mechanical and material properties associated with additively manufactured parts are directly correlated to part density. As porosity increases in these parts, the mechanical properties diminish making it unsuitable for industrial applications. According to Zaeh and Ott (2011) an important difficulty associated with SLM is the limitation of pore formation. Porous parts have diminished mechanical properties and lower overall part quality. Therefore, the achievable part density in additively manufactured parts is of particular interest. Porosity formation is noted to be a result of two processes: 1) bubble motion present in the molten pool and 2) pore coalescence as a result of the bubble motion. It is observed that the initial air content in the loose powder bed significantly affects the final part porosity (Zhang *et al.*, 2012b). According to Exner *et al.* (2008) the initial density of the powder bed can be increased by applying a higher rake pressure during the powder feed process. This is, however, dependent on the AM technology being used.

As the initial powder density increases the final part density increases as well. A further advantage to higher initial powder density is better control over the heating process. A more stable molten pool of liquid is achieved because of more constant dissipation of the absorbed laser energy into the powder material. As stated previously, material specific parameters influencing the achievable part properties in an AM process include type, particle size, particle distribution, particle shape, and percentage composition. Murr *et al.* (2012) suggests that spherical or near-spherical powders, consisting of a distribution of particle sizes, optimises efficient material flow, layer packing, and melt uniformity.

According to Li *et al.* (2010) the correct powder mixture is essential to the final part properties. The use of homogeneous powder mixtures accelerates liquid wetting of the non-melted particles, as well as particle rearrangement. For sintering of sub-micron WC composites, Gu *et al.* (2006) states that particle rearrangement is the dominant sintering mechanism for large carbide particles and dissolution precipitation is dominant for the finer carbide particles. Zhang *et al.* (2010) found that a homogenous powder mixture promotes laser energy absorption, improving the material flow behaviour during the SLM process, potentially accelerating the liquid wetting properties and particle rearrangement. This then leads to improved densification behaviour during the SLM process. According to Wang *et al.* (2002), in order to improve upon the achievable properties of parts created using DSLS and hardmetal powders, the influence of laser power, scan speed, scan interval, powder mixture ratio, and particle shape and size needs to be investigated. The investigation carried out by Wang *et al.* (2002) was limited to the effect of varying laser power and scan speed. Zhang *et al.* (2012a) found that uniform and smooth surfaces of the SLM parts could be obtained under the proper forming parameters, using tungsten powder. Furthermore, it was found that full melting of the tungsten particles formed nano-sized grains during the SLM process. Particle shape and size was found to influence the final sintered product in a significant way.

Polygonal shaped particles facilitate higher coordination numbers and particle rearrangement during processing. Also, finer powders provide a larger specific area. This aids in higher laser energy absorption that increases particle temperatures and melting activities.

According to Yasa and Kruth (2011) insufficient surface quality could lead to increased part porosity. High surface roughness, exhibiting high peaks and deep valleys, could create pores during the application of a new powder layer. As the new layer is scanned, these pores are trapped thereby increasing the porosity. Yasa and Kruth (2011) also states that unmelted powder can become trapped if the surface layer is too thick in some areas. Trapped powders will have a significantly lower density than the surrounding, melted material which leads to higher part porosity.

3.5.1.2 Process

Porosity formation is not only dependent on the associated material properties or characteristics. Gu *et al.* (2012) states that, considering the elements that govern the metallurgical phenomena present in AM processing, in order to achieve favourable microstructural and mechanical properties, significant emphasis is required on the design strategy of powder materials as well as the laser control processes. Furthermore, they state "...a comprehensive review on the materials design, process control, property characterisation and metallurgical theories for laser sintering, laser melting, or laser metal deposition of a wide variety of metallic powders is particularly necessary."

This suggests that a specifically tailored approach, in terms of process control (among other), is required for a specific material. In any given AM process, certain parameters can be altered in order to obtain high density parts. These parameters are associated with the process itself, the laser technology being used, as well as the materials being used (Campanelli *et al.*, 2010). As stated previously, process parameters include single layer thickness, scan velocity, hatch spacing, and scan strategy.

Kruth *et al.* (1996) concluded from their experiments that two parameters are crucial to the dimensional control of the scan tracks: 1) scan speed and 2) laser power. Scan speed determines track width, while laser power affects track thickness given a specific scan speed. According to Li *et al.* (2010) investigation of single layer formation during the SLM process could establish a foundation for defining processing parameters for the powder material under investigation. A particular characteristic defining the relationship between the crucial parameters in AM processing is the associated energy density, E_d . Campanelli *et al.* (2010) and Glardon *et al.* (2001) states that the energy density of a single track can be calculated by the following equation:

$$E_d = \frac{P}{vd} \quad (3.5.1)$$

Where E_d is the single track energy density [$kJ.mm^{-2}$], P is the laser power [$Watt$], v is the laser scan speed [$mm.s^{-1}$], and d is the layer thickness [mm]. An integrated factor called 'volumetric energy density' or VED [$kJ.mm^{-3}$] is also defined (Simchi, 2006; Gu and Shen, 2009; Gu *et al.*, 2012; Ciurana *et al.*, 2013). This differs from the single track energy density by including the hatch spacing h [mm] of the build parameters, as per Equation 3.5.2:

$$VED = \frac{P}{vhd} \quad (3.5.2)$$

where P , v , h , and d are as defined previously. According to Gu *et al.* (2012) laser melting (LM) is capable of producing high density parts (>99.5%) using pure metal powders. However, in order to achieve such a high density, full melting of the powder layer is required. That is, a high volumetric energy density is required. This requires an optimised combination of high beam quality, high laser power, a small spot size diameter, and a thin layer thickness. The use of a thin layer thickness, however, has the undesired outcome of prolonging build time.

According to Kruth *et al.* (2005) a process window needs to be established experimentally for any new material in order to avoid scan track instabilities (such as spheroidisation) and excessive part porosity. Single layer experimentation using W-Cu powders, carried out by Li *et al.* (2010), led to the establishment of process windows, identifying four process regions (or melting states), namely 1) over melting, 2) moderate melting, 3) spheroidisation (or “balling”), and 4) insufficient melting. The process window is established by varying both scan speed and laser power. In a similar experiment as those of Zhang *et al.* (2010) and Li *et al.* (2010), Zhang *et al.* (2012b) evaluated the possibility of forming W-Ni-Cu parts using SLM and established similar process windows to determine the particle melting behaviour by also varying laser power and scan speed. The corresponding process windows are 1) no melting, 2) slight melting, 3) spheroidisation, and 4) appropriate melting. Figure 3.10 on page 41 shows four process windows established by varying the laser power and scan speed in AM processes using hardmetal powders.

Spheroidisation is defined as the formation of isolated metal spheres with a diameter equalling the diameter of the incident laser beam (Gu *et al.*, 2012; Campanelli *et al.*, 2010). This occurs as a result of the molten metal’s inability to fully wet the substrate due to increased surface tension. The formation of these spheres hinders subsequent powder deposition and results in a decrease of the final part density (Campanelli *et al.*, 2010).

To avoid spheroidisation during laser melting, Gu *et al.* (2012) suggests that careful selection of both laser processing and powder deposition parameters are necessary in order to find a suitable processing window. This is necessary to maintain a moderate temperature field and avoid overheating of the laser melting system.

An important phenomenon was observed by Zhang *et al.* (2010) during their experimentation. During the SLM process, powder temperatures exceeded the vaporisation points of the nickel and iron particles leading to vaporisation of the partial nickel-iron liquid phase. The SLM process uses high energy densities to heat the powder particles to its melting temperature. A further increase in temperature (to approximately double the metal’s melting temperature) will cause evaporation of the powder. This causes an accelerated expansion of evaporated particles, resulting in overpressure in the melted zone. This ultimately causes material ejection from the powder bed (Campanelli *et al.*, 2010). This occurrence could become prevalent if complete melting of the hardmetal component in a hardmetal alloy is desirable.

Metallurgical phenomena present during AM processing is material and process dependent. It is governed by both powder characteristics and processing parameters (Gu *et al.*, 2012). As previously stated, powder characteristics refer to chemical constituents, particle shape, particle size and distribution, loose packing density, and powder flowability. Processing variables refer to laser and process related parameters that includes laser type, spot size diameter, laser power, scan speed, hatch spacing,

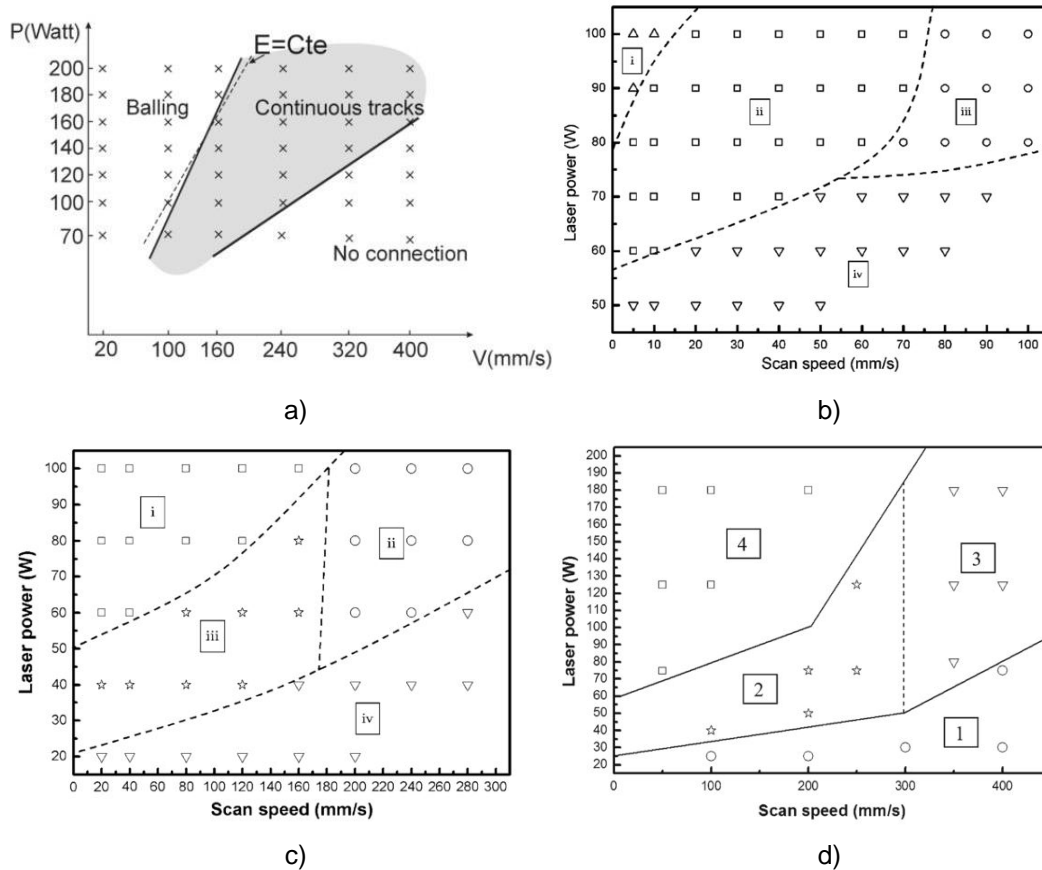


Figure 3.10: Process windows established by a) Kruth *et al.* (2005), b) Li *et al.* (2010), c) Zhang *et al.* (2010), and d) Zhang *et al.* (2012b).

and powder layer thickness.

3.5.1.3 Energy source

In any powder-based additive manufacturing process, consolidation (or sintering) of the material is dependent on many factors, of which the energy source used is one. Typically, the energy source is a laser. As stated previously, laser specific parameters include laser power, spot diameter, wavelength, and energy per laser pulse.

Butler (2011) noted a specific problem associated with the laser focal point on the powder bed. When perpendicular to the powder bed the focal point is round. This facilitates accuracy during the sintering process and promotes uniform heat distribution in the molten pool. When angled, such as at the edge of the powder bed, the focal point experiences elliptical deformation. This occurrence leads to problems associated with part density and dimensional accuracy. Zhang *et al.* (2012a) found that a smaller laser beam diameter could lead to higher laser energy absorption in the powder bed, if coupled with a large laser power. Furthermore, using a smaller laser beam diameter could offset the negative effects associated with elliptical deformation. Campanelli *et al.* (2010) concluded from their work that part feature

accuracy diminishes as the feature dimensions reach 0.4mm since the nominal size gradually approaches the laser spot diameter.

Laser choice in laser sintering (LS) is an important factor determining the consolidation of powders. This is attributed to 1) laser energy absorptivity of materials being dependent on the laser wavelength and 2) powder densification being dependent on the incident laser energy on the powder bed (Gu *et al.*, 2012). Furthermore, the laser beam contact time will determine the amount of laser energy transmitted to the powder bed. Laser beam contact time in a LS/LM process is typically between 0.5 and 25ms. This is determined by the combination of the spot size diameter and the scan speed. Due to the short exposure time, fully molten powder particles cannot be achieved. This renders solid state sintering infeasible (Gu *et al.*, 2012).

Concerning the choice in laser source, a high powered carbon dioxide (CO₂), a neodymium-doped yttrium aluminium garnet (Nd:YAG), or a fibre laser is required to yield a favourable bonding mechanism (Santos *et al.*, 2006; Gu *et al.*, 2012). According to Zaeh and Ott (2011) a high energy density is required for the consolidation of metal powders. In their experiments, in order to achieve this high energy density, a Nd:YAG fibre laser is used.

An important factor for consideration, relating to the choice in laser energy source, is the reflectivity of the material. Different alloys will have different reflective properties based on the materials used to create the alloys and the effect thereof will be dependent on the laser wavelength used during the sintering process. As an example, Cu exhibits high reflectivity at a laser wavelength of 1064nm. This high reflectivity could lead to poor absorption of the laser energy, resulting in insufficient sintering of the Cu particles (Exner *et al.*, 2008).

3.5.1.4 Other

Apart from the main influences on the achievable part properties discussed in sections 3.5.1.1 - 3.5.1.3, other influences include the presence of surface oxides, residual stresses, and grain growth during sintering, among others.

Defects, such as spheroidisation, can be attributed to the presence of oxide layers between the powder particles and the previously processed layer. A reduction of surface oxides is necessary to form direct metal/metal interfaces (Gu *et al.*, 2012). This will ensure good wetting behaviour in the powder system. Gu *et al.* (2012) also suggests that AM processes must be conducted in inert environments, such as Argon gas, in order to mitigate the detrimental effects of oxidation. Most metals will form oxides at the respective melt temperatures, even under extremely low partial pressure of oxygen.

Results from experiments carried out by Kruth *et al.* (1996), obtained from sintering the WC-30wt.% Co powder, revealed that the WC particles are well embedded in the Co matrix, giving it typical hardmetal characteristics. However, a high degree of oxidation in the Co matrix resulted in brittle samples. It is suggested that processing in an inert environment may resolve this issue. In experiments carried out by Li *et al.* (2010) analysis of the final W-Cu samples produced by SLM showed lower part densities than for conventional PM. This can be attributed to the non-melting of the W particles and limited liquid phase content under the investigated processing

parameters. It is suggested that part densities can be increased by decreasing scan speed and increasing the laser power (Li *et al.*, 2010).

According to Zhang *et al.* (2012b) an increase in laser power, a narrower scan interval, and a reduction in the scan speed are potential approaches to increasing part density. However, even though SLM is capable of producing high part densities, the process develops residual stresses in the material, derived from the high thermal gradients induced in the material. This leads to part distortion, cracking, or delamination (Campanelli *et al.*, 2010; Zaeh and Ott, 2011; Gu *et al.*, 2012). The formation of thermally induced stress cracks in high density parts occurs as a result of insufficient opportunity for stress relief, which aims to reduce the stress present in the formed layers (Exner *et al.*, 2008). According to Gu *et al.* (2012) residual stresses are smaller along the scan direction than perpendicular to it.

In conventional PM these stresses are reduced through a prolonged sintering process. In AM, an argument is made for the use of partial melting systems over full melting systems, since the lowered sintering temperature will limit the formation of thermal stresses, thereby limiting the resultant part deformation, delamination, and crack formation (Gu *et al.*, 2012).

Grain growth, among other thermodynamic adjustments in microstructure, can be achieved by re-melting each completed layer. In addition to this, the laser beam and other processing parameters may be adjusted to allow for re-heating activity to anneal the processed layer (Murr *et al.*, 2012). Re-heating of processed layers could achieve similar stress relief to that of prolonged sintering in conventional PM techniques.

Another approach to achieve a reduction in residual stress levels and distortions within the built parts is heating of the build platform to slightly below the metal's melting temperature. Pre-heating of the metal powder holds several advantages for the sintering process and final parts (Campanelli *et al.*, 2010):

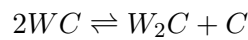
- Minimisation of laser power requirements;
- Improved laser energy absorption;
- Prevention of part warping due to non-uniform thermal expansion and contraction;
- Reduction of temperature gradients; and
- Improved wetting properties of the metal matrix.

It has been found that the residual stress profile present in AM processed components consists of large tensile stresses at the top and bottom of a LS or LM part, as well as intermediate compressive stress in between (Gu *et al.*, 2012). The magnitude and shape of the profile is dependent on:

- Geometric height of the part;
- Material properties; and
- Chosen laser scanning strategy and processing conditions.

Residual stresses present in the built parts also holds potential benefits. According to Wang *et al.* (2013) introduction of a functional gradient in cemented carbide composites holds the potential to induce compressive stresses in the surface during processing. Compressive surface stresses inhibits WC grain pull out, thereby slowing crack initiation and propagation. These stresses could also close crack tips, further halting crack propagation.

Due to the significant difference in melting temperatures for the structural and binder elements, solid particles have a tendency to debond along particle boundaries, yielding inherent intercrystalline weaknesses (Gu *et al.*, 2012). Debonding along the particle boundaries significantly lowers the mechanical properties of the components processed by partial melting, especially the tensile strength. During sintering of WC powders, the decarburisation process (due to the presence of surface oxides on the initial powder particles) forms W_2C which causes a decrease in the final part density (Andren, 2001; Kim *et al.*, 2004). According to Paul and Khajepour (2008) excessive heating of the WC particles in a WC-alloy composite results in a carbon deficiency due to the precipitation of carbon as graphite. The chemical reaction is described as:



The graphite reacts with atmospheric oxygen, forming carbon monoxide (CO) and carbon dioxide (CO₂). This often results in the formation of gas porosities in finished WC-alloy components. The addition of excess carbon is suggested to reduce the formation of this phase, however this enhances grain growth during sintering (Andren, 2001).

The control of grain growth during processing of fine grained cemented carbide powders poses a significant obstacle in AM of these powders. Grain growth may be managed through careful control of the consolidation parameters, such as temperature and sinter time (Andren, 2001). The mechanical properties of AM processed components is determined by the solidification microstructure and the associated grain sizes. For example, functionally graded composites (FGCs) such as a WC-Co composite, typically exhibits a gradient in WC grain size. Also, a gradient in cobalt composition is apparent, resulting in varying mechanical and material properties across the microstructure (Eso *et al.*, 2005).

Due to the rapid heat conduction through the substrate during sintering, rapid solidification microstructures are formed (Gu *et al.*, 2012). These microstructural phases exhibit specific mechanical properties related to its composition. During sintering of WC and cobalt powder mixtures, there is a fine composition range wherein the two-phase mixture of WC-Co may be generated. According to Allibert (2001) even a slight departure in tungsten or carbon concentration in this composition range will result in the formation of graphite and eta (M_6C) phases. These phases are detrimental to the mechanical properties of the processed components and must be prevented from forming (Paul and Khajepour, 2008).

3.5.2 Phenomena in additively manufactured cemented carbides

There are numerous phenomena observable associated with additively manufactured part, specifically those produced using powder bed technology. This includes curling, warping, delamination, displacement and uprooting, shrinkage, and cracking.

Kumar (2009) presents a discussion on five dominant manufacturing problems faced when producing functional components by SLS. Since SLM shares similarities with SLS, these problems can occur in an SLM process as well. The first, curling, is an upward bending of a sintered layer when the centre of the layer remains attached, either to the previous layer or the base plate. The second, warping, is the protrusion of the centre of a sintered layer when the peripheries remain attached, either to the previous layer or the base plate. The third, delamination, is defined as partial detachment of a sintered layer, or a collection of sintered layers, from an adjacent layer. This occurs due to a change in process parameters, resulting in stronger interlayer bonds between some layers, as opposed to others. The fourth, displacement, occurs when unfinished samples are moved on the base plate by the roller. This is due to a very poor bond between the first sintered layer and the base plate, as well as roughness or protrusions that develop on the sample surface. Lastly, uprooting occurs when a sample is tilted, resulting in the inability of the laser to reach a desired surface. The cause is similar to displacement, however the roller force is inadequate to completely detach the sample from the base.

Crack formation in AM processed components may be classified under either microscopic or macroscopic cracks. Microscopic cracks form during rapid solidification and is termed hot cracking. Macroscopic cracks occur after solidification, due to low material ductility and stress induced part deformation, and is termed cold cracking (Gu *et al.*, 2012). Particle bonds are broken along grain boundaries and occur as a result of residual stress present in the built up layers. Crack formation is further ascribed to the temperature gradient mechanism (TGM). A steep temperature gradient develops due to the rapid heating of the upper surface by the incident laser energy and the slow heat conduction into the lower surface layers. Simultaneously, the material strength is reduced due to an increase in temperature. Increasing the surface layer temperature results in rapid expansion of the material which is converted into elastic and plastic compressive strains, owing to the fact that the surrounding material inhibits free expansion.

An increase in temperature lowers the associated material yield stress, and as this value is reached the top layers become plastically compressed. As the scanned layer cools (and subsequently shrinks) the upper layers become shorter than the bottom layers and a bend moment towards the laser beam develops.

The underlying layers are exposed to a similar temperature gradient each time a new powder layer is melted on top. Due to the stresses generated as a function of the TGM, the underlying layers attempt to bend the consolidated layers towards the laser beam. This causes distortion and part failure by way of delamination and cracking. This observation is confirmed by the work presented by Kumar (2009) and Kruth *et al.* (2012).

Figure 3.11 on page 46 illustrates the process described above. This continual cycle of thermal expansion and subsequent shrinkage produces cracks in the scanned layers.

Shrinkage is a commonly occurring phenomena not only in conventional sintering of cemented carbide powders (Kim *et al.*, 2006), but during SLS and SLM as well (Senthilkumaran *et al.*, 2009). During a conventional press and sinter process, parts can experience varying degrees of shrinkage, depending on the nature and properties of the material used (Kim *et al.*, 2004). Typically, during SLM, the material experi-

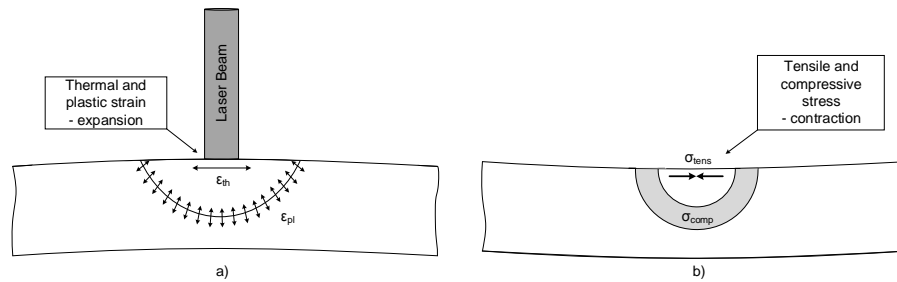


Figure 3.11: Temperature gradient mechanism illustrated by a) thermal expansion followed by b) contraction. Adapted from Kruth *et al.* (2004) and Kruth *et al.* (2012).

ences thermal expansion upon heating of the powder bed. As the melted tracks cool and solidify, shrinkage occurs due to rearrangement of the particles. The use of finer particle sizes leads to more rapid shrinkage (Allibert, 2001).

For each of the aforementioned difficulties associated with SLS, Kumar (2009) suggests solutions aimed at reducing the likelihood of it occurring. To avoid the occurrence of curling or warping, the use of a higher laser power could result in successfully sintering the deposited layer, as well as partially melting the previous layer. Kumar (2009) contradicts this by stating that warping and curling occurs due to a higher supply of laser energy.

To avoid delamination, process changes must be kept at a minimum. When parts are grown in a SLS or SLM process, the associated build parameters should remain constant throughout the entire process. This will ensure that interlayer bonds and stresses are equal throughout the entire part, thereby reducing the likelihood for delamination.

The approach to reducing, or completely avoiding, displacement and uprooting is threefold: 1) create the initial layers using higher laser power, 2) decrease laser power if protrusion becomes evident, and 3) increase laser power if insufficient sintering activity becomes apparent. The increase in laser power during the formation of the initial layers serves to ensure that the initial layers experience high melting activity, thereby securing these layers to the baseplate and avoiding displacement of the part. Thereafter, a decrease in laser power ensures the limitation of protrusion formation which could catch on the scraper blade, causing the part to detach from the baseplate and be displaced in the build environment. Finally, uprooting is avoided by increasing the laser power if insufficient sintering activity is noticed. This ensures that each layer is successfully sintered, thereby making it possible for the laser to reach a desired surface.

Another approach to avoiding displacement or uprooting is an increase in laser pulse frequency. Paul and Khajepour (2008) found during experimentation that an increase in laser pulse frequency lead to a higher energy density per unit length which allows the molten pool to remain liquid for an extended period of time. This approach resulted in the formation of a good WC-Co metal matrix. It was also found that a further increase in laser pulse frequency lead to overheating of the WC particles, leading to graphite precipitation. Therefore, there exists a threshold above which an increase in laser power or pulse frequency will lead to other, undesirable phenomena to develop in the built parts.

This section presented literature regarding the influences on achievable part properties, specifically influences related to the powder used, the AM process used, and the choice in energy source, among others. Furthermore, a discussion is presented on some of the most important phenomena observable in parts created using a powder-based additive manufacturing process and cemented carbides. The following section presents experiments performed in literature relating to powder-based additive manufacturing and powder metallurgy processes, using cemented carbide powders.

3.6 Experimentation

This section presents a discussion on literature related to research on the use of advanced manufacturing techniques and novel materials, such as cemented tungsten carbides. These processes include selective laser sintering (SLS), selective laser melting (SLM), and hot isostatic pressing (HIP), among others.

As mentioned in section 3.5.1 on page 37, there are quite a few parameters that may be altered in an AM process relating to the production technology, the materials used, and the energy source used. It is therefore necessary to establish which parameters are to be fixed variables and which are controlled variables.

There have been countless works published on the effects that changing processing parameter values in a SLM process has on the achievable part density and corresponding mechanical properties of the built parts. The work stems from the need to understand the material behaviour under production conditions, specifically for an unfamiliar material, in order to obtain favourable and desirable results with regard to the final part properties (i.e. high density, correct hardness/toughness relationship, necessary wear resistance, etc.).

Authors such as Agarwala *et al.* (1995), Yadroitsev *et al.* (2007a), Gu and Shen (2009), and Yadroitsev and Smurov (2010) have specifically focused on the effect that changing laser power, scan speed, and layer thickness in a SLS or SLM process has on the achievable single track, single layer, and multi-layer sample properties. Others investigate the effect that different hatch spacing values have on these different production phases (Yadroitsev *et al.*, 2007b; Badrossamay and Childs, 2007; Yadroitsev and Smurov, 2011). Similarly, work presented by Hauser *et al.* (2003), Simchi (2006), Mumtaz *et al.* (2008), and Yadroitsev *et al.* (2010) focuses on the use of SLS and SLM with different materials and what the effect in different material properties has on the achievable properties in single scan tracks and layers, as well as multi-layered samples. Other authors have focused on analysing the specific formation mechanisms associated with, for example, residual stress (Shiomi *et al.*, 2004; Kruth *et al.*, 2012) and balling (Tolochko *et al.*, 2004; Gu and Shen, 2007).

The work presented by these authors form the basis onto which research into the use of novel SLM technologies is built. The expected observable phenomena associated with high scan speed and laser power, for example, must be understood to draw valuable information from similar experiments using a novel material. In this case a tool grade cemented tungsten carbide.

In specific work on the use of cemented tungsten carbides, several boundary conditions are established for the experiments carried out by Zaeh and Ott (2011): 1) the

selected powder configuration is kept constant throughout experimentation, 2) the laser source is invariant, and 3) heating of the build platform is carried out by open loop control. In their experiments they found that the manufacture of hard materials can be optimised by increasing the build platform temperature. They also found that difficult to fuse materials, i.e. WC-Co, can be handled well. In another example, investigation on the potential improvement, or possible replacement, of the production processes involved in constructing complex collimators, having a high number of oblique pinholes, Deprez *et al.* (2013) used SLM to produce these components from pure tungsten powder. The material parameters were kept constant during the experimentation process. All conventional techniques used to produce these components are subtractive, labour-intensive, and ultimately cost-intensive. The results showed that parts can be successfully produced from pure tungsten powder using SLM.

In development tests performed by Sinirlioglu (2009) dental bridges were produced using a M1Cusing machine from the Hofmann Türk Company. In order to optimise the achieved part density, several laser parameters and scan strategies were investigated. The most important parameters were determined to be as follows:

- Laser power, P [Watt];
- Scan speed, v [$mm.s^{-1}$];
- Weld overlapping (hatch spacing), h [mm];
- Spot size diameter [mm]; and
- Layer thickness, d [mm].

Yasa and Kruth (2011) investigated the effect that altering some of these parameters have on the final part properties. It was found that an optimised combination of these parameters lead to higher density parts with better surface features. This investigation was limited in the number of parameters varied during experimentation, and it is suggested that a significant influence on part porosity may be held in those parameters not investigated (i.e. layer thickness and spot diameter). In the experiments carried out by Zaeh and Ott (2011) various configurations of volumetric energy density (VED) is evaluated by using Design of Experiments. In this way the parameters involved in determining VED (i.e. laser power, scan speed, hatch spacing, and layer thickness) can be varied to obtain the optimal combination of parameter values. According to Yasa and Kruth (2011) typical layer thickness for SLM parts are between $30\mu m$ and $70\mu m$. Typical layer thickness associated with LaserCusing[®] technology is between $20\mu m$ and $50\mu m$ (Sinirlioglu, 2009).

The parameters used during experimentation carried out by Yasa and Kruth (2011) are standard values optimised to achieve a maximum density, i.e. $v = 380[mm.s^{-1}]$, $P = 105[W]$, and $h = 125[\mu m]$. The material used during experimentation is AISI 316L stainless steel. From their experiments it was found that a higher part porosity is related to an excessive increase in the energy input into the substrate. Furthermore, with a higher hatch spacing part porosity is increased and scan speeds between $50mm.s^{-1}$ and $200mm.s^{-1}$ resulted in a decrease in porosity. Zaeh and Ott (2011) concluded from their experiments on AM of hardmetal parts

that the manufacturing of hard-materials can be optimised by increasing the build platform temperature. It was concluded that even materials that are difficult to fuse, such as tungsten carbide bound with cobalt, could easily be processed.

Campanelli *et al.* (2010) performed experiments wherein varied combinations of laser power and scan speed are explored, since these are the parameters responsible for the melting activity present during the sintering process and ultimately influences final part quality. Layer thickness was set to $30\mu\text{m}$, and an oxygen level of 0.8% was maintained. $15\times 15\times 10\text{mm}^3$ samples were used to analyse density, hardness, and microstructure. The material used is similar to a typical composition of maraging steels reinforced with cobalt. Specifically, a composition close to 18-Ni-Marage-300 steel was used, with spherical powder particles having an average particle size below $40\mu\text{m}$. The results obtained showed the highest part density corresponds to the highest energy density. This corresponds to the lowest scan speed and highest laser power (i.e. $180\text{mm}\cdot\text{s}^{-1}$ and 100W, respectively). An approximate porosity of 0.01% is obtained.

Paul and Khajepour (2008) presents experiments performed to find the set of optimal parameters for component-level fabrication. Components are subjected to dye-penetrant testing, three-point flexural testing, hardness measurement, optical and scanning electron microscopy (SEM), and X-ray diffraction (XRD) analysis. WC-Co powder with a particle size range of $10\text{-}45\mu\text{m}$ was used during experimentation. An inert environment was created using Argon gas. The authors start by fabricating a number of single tracks to determine the appropriate parameters required to obtain continuous and uniform tracks. It was found that an increase in laser pulse frequency lead to a higher energy density per unit length which allows the molten pool to remain liquid for an extended period of time. This approach resulted in the formation of a good WC-Co metal matrix. It was also found that a further increase in laser pulse frequency lead to overheating of the WC particles, leading to graphite precipitation.

Kumar (2009) presents work based on the production of functional parts using WC-9wt.%Co powders and a SLS process technology (100W DTM Sinterstation 2000). Fully functional parts could not be produced using only the SLS technology. Post-sintering infiltration using bronze was done to achieve fully dense, functional parts. The highest part density achieved is 96%. The experiments followed two stages: 1) pilot experiments, wherein the correct powder mixtures and process parameters were established and 2) final experiments, wherein the final parts were produced. After each stage, the built parts were characterised by measuring mechanical properties such as hardness, strength, and microstructure, among others. The aim of producing WC and cobalt composites, according to Kumar (2009), is to use as little cobalt binder in order to ensure a maximum hardness. Conventionally, the minimum amount of cobalt used is 6% by weight.

In a study on functionally graded composites (FGCs) Eso *et al.* (2005) used WC-Co powders with 6wt.% and 16wt.% cobalt content, with a grain size distribution of $1\mu\text{m}$ and $5\mu\text{m}$. Masuda *et al.* (1993) presents work on the effect of WC grain size and cobalt content on the tool wear rate, when machining carbon materials. The tools are sintered using a hot isostatic pressing (HIP) process, with the tools having a cobalt content from 5wt.% to 10wt.%. The mean WC grain size is $0.6\mu\text{m}$ to $9.0\mu\text{m}$. During experimentation, specific focus is placed on the wear patterns

developed during testing. The failure process is examined from a brittle fracture probability point of view. The main results show that an increase in WC grain size and a decrease in cobalt content decreases tool wear rate. Failure of the WC-Co tools was found to be due to a loss of WC particles. Paul and Khajepour (2008) noted that a particle size distribution of 0.1 μm to 10 μm is used in conventional sintering processes, achieving the maximum transverse rupture strength (TRS) at particle sizes of approximately 4 μm .

In an investigation undertaken by Zhang *et al.* (2010) tungsten-nickel-iron (W-Ni-Fe) alloy parts were manufactured using a SLM process. During this investigation the phase transformation, microstructure evolution, and processing behaviour of the material was studied. Functional components made up of this composition exhibit high densities, good corrosion resistance, and comprehensive mechanical properties. In experiments carried out by Kim *et al.* (2006) it was found that parts with a 98.5% density could be produced. Furthermore, an increase in total power output caused an increase in sintering temperature and therefore higher densification rates. It was also found that finer initial WC powders allowed for higher final part densities as well as better mechanical properties. The powder grain size used was 0.4 μm .

Yasa and Kruth (2011) explored an approach to reducing the limitations of the SLM process. This involved the use of layer re-melting, whereby each built up layer is scanned again (after solidification) to remove remnant porosity and improve the surface quality of the final parts. They concluded that laser re-melting, using suitable parameters, effectively eliminates residual porosity resulting in a dense microstructure. This, however, is only achievable at the cost of longer production times.

This section presented results and discussions from experimental work carried out focusing on the use of additive manufacturing and powder metallurgy processes using significant or novel materials. It was found that the parameters having the greatest effect on the achievable part properties is laser power, scan speed, hatch spacing, and layer thickness. The following chapter presents the experimental methodology followed in this work, presenting the material, equipment, and software used, as well as the analytical approach followed.

Chapter 4

Experimental methodology

This chapter presents literature on different experimental design methods, as well as the experimental methodology followed, the equipment and material used, and the comparative benchmark analysis methodology followed. The following section describes some different DOE methods and basic principles in order to choose the optimal approach to designing, carrying out, and analysing statistical experiments.

4.1 Introduction

Developed in the 1920's, Design of Experiments (DOE) stemmed from the work of Sir Ronald Aylmer Fisher. Fisher was a statistician and created the basis for modern statistical science. Thereafter came the second era in statistical experimental design. This began in 1951 with the work of Box and Wilson (Cavazzuti, 2013). They applied statistical experimental design to industrial experiments and developed the Response Surface Methodology (RSM). The primary idea behind RSM is to use sequentially designed experiments in order to obtain an optimal response. In the later 1980's, Genichi Taguchi had a significant impact in popularising statistical experimental design and emphasised the importance and impact it can have on total quality improvement and management.

Different DOE methods may be used for different purposes. The use of screening experiments, for example, is aimed at determining which factors in the experimental setup has the most significant effect on the response variable(s). Once known, these factors (and the associated response values) may be used to optimise the choice in factor values. This, for example, may be used to optimise the yield of a chemical process, such as the production of ammonium sulfate ($(\text{NH}_4)_2\text{SO}_4$).

Once screening is completed and the significant factors are known, optimisation experiments are often carried out. Values associated with the significant factors are varied and the response measured in order to determine an optimal range to achieve the most efficient and effective process. As with any optimisation problem, there is no one perfect solution. Much depends on the nature of the problem and the available time and resources. Applications (or problems) can range from optimising yields in chemical plants to speeding up grape packaging lines.

Some of the most significant DOE methods include Latin Squares, Full and Fractional Factorial, Central Composite, Box-Behnken, and Taguchi experimental

designs. The following section gives a brief overview of the basic principles of experimental design.

4.1.1 Basic principles of statistical methods

DOE refers to the planning, design, and analysis of experiments in order to draw objective conclusions effectively and efficiently. It is necessary to integrate both powerful and simple statistical methods into the design methodology in order to draw statistically sound conclusions from the experiments (Antony, 2003*b*). There are three basic principles of experimental design, namely randomisation, replication, and blocking (Antony, 2003*b*; Cavazzuti, 2013). These principles can be used in industrial experiments to improve the efficiency and effectivity of experimentation. The principles are applied in order to avoid or otherwise completely remove experimental bias and ensure objectivity. Wherever experimental bias is present, incorrect optimal settings could result or in some cases mask the effect of statistically significant factors (Antony, 2003*b*).

Replication is the process of repeating experimental trials in a randomised sequence, in order to obtain statistically accurate results (sample mean value or factor/interaction effect) and experimental error estimation (sample standard deviation) (Antony, 2003*b*; Cavazzuti, 2013). Replication can refer to the entire experiment, or merely a portion of it under more than one condition. Depending on the result of the experimental error, factor or interaction effects could be quite significant. However, with sufficient replicates satisfactory inferences can be made about the factor or interaction effects (Antony, 2003*b*). It should be noted that ‘replication’ and ‘repetition’ are, in a technical sense, not the same. For repetition, an experimenter may repeat any experimental trial condition numerous times before proceeding to the next trial.

Randomisation is relied on to reduce the effect that experimental bias can have on the outcome and refers to the random order in which experimental runs are performed (Antony, 2003*b*; Cavazzuti, 2013). This ensures that the conditions of the previous or next run, don’t affect the conditions of a current run. It assists in averaging out the effects that noise factors may have, if it is present in the process.

Blocking is a method that improves experimental design efficiency by eliminating the effects of extraneous variation caused by noise factors (Antony, 2003*b*). According to Cavazzuti (2013) it aims to isolate known systematic bias effects in order to prevent it from obscuring main effects. Experiments are arranged in groups (or blocks) that are similar in nature, thereby reducing variability and improving precision. Blocks can refer to, for example, batches of raw material, different vendors, or different operators, among others.

Although the underlying principles of DOE are similar for each method, the amount of DOE methods available to the experimental designer means there is no “best choice” when it comes to choosing which DOE method to use. The aim of the experiment, as well as the nature of the problem being investigated, will influence the choice in design method.

Cavazzuti (2013) describes the following items that need to be considered when deciding which DOE method is most applicable: First, the affordable number of experiments, N , that may be run must be considered. Here, an important consid-

eration is the time required for a single experimental run. In the case of computer simulations, results may be achieved in mere seconds; however, in the case of complex laboratory experiments, results could take days to be generated.

Second, the number of parameters (or factors), k , of the experiment must be considered. Typically, the number of experiments required, for any given DOE method, grows exponentially with an increase in parameters. This is graphically illustrated by Cavazzuti (2013) in Figure 4.1 on page 53. Here, using all parameters and the cheapest technique isn't necessarily the correct option. Cheap techniques lead to inaccurate results and limited design space exploration. It is suggested to use a limited number of parameters, known to have a significant influence on the response variable(s). Of course, choosing which parameters should be discarded can be a difficult issue. A solution is to use a cheap technique (such as the Plackett-Burman technique) as a preliminary study aimed at identifying significant variables.

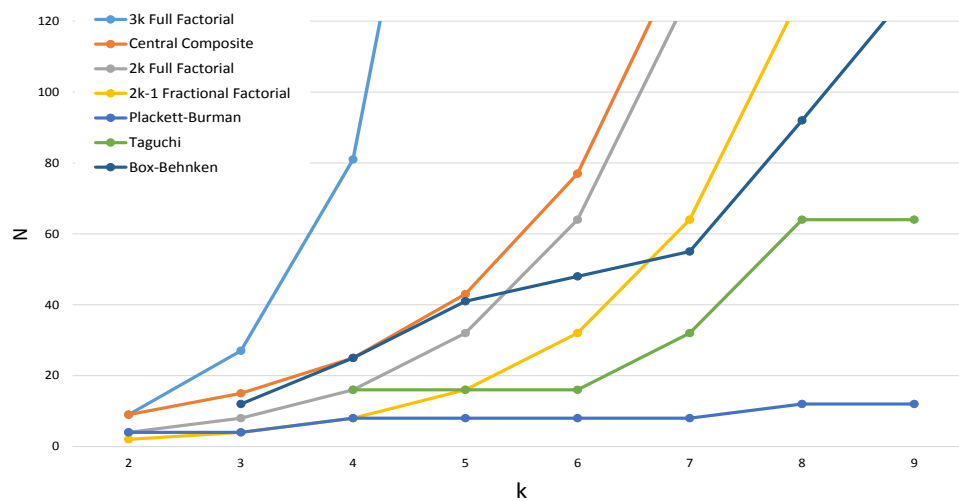


Figure 4.1: The number of experiments required by different DOE methods. Adapted from Cavazzuti (2013).

Third, the number of levels, L , assigned to each parameter must be considered. Just as parameters can increase the number of experiments, so too can the levels assigned to each parameter. A trade-off, however, is required as a small number of levels does not permit accurate interpolation of the design space. It is suggested that the number of levels must be limited when possible, and increased when irregular behaviour of the response variable is expected. It should be noted that a two-level DOE method will result in an approximately linear or bilinear response surface to be developed, whereas a three-level DOE method will result in an approximately quadratic or biquadratic response surface to be developed, and so on.

Finally, the aim of the DOE has a significant influence. Depending on the nature of the desired results, a Plackett-Burman method (suitable for rough estimates of the main effects) or a Full or Fractional Factorial method (suitable for more precise calculation of main and interaction effects) may be used. If the focus is on a primary

Table 4.1: Summary of DOE methods and associated applications. Adapted from Cavazzuti (2013).

Method	Number of Experiments	Suitability
Latin Squares	$N(L) = L^2$	Focusing on a primary factor, cheaply
Full Factorial	$N(L, k) = L^k$	Computing main/interaction effects, building response surfaces
Fractional Factorial	$N(L, k, p) = L^{k-p}$	Estimating main/interaction effects
Central Composite	$N(k) = 2^k + 2k + 1$	Building response surfaces
Box-Behnken	$N(k)$ from tables	Building quadratic response surfaces
Plackett-Burman	$N(k) = k + 4 - \text{mod}(k/4)$	Estimating main effects
Taguchi	$N(k_{in}, k_{out}, L) = N_{in}N_{out}, N_{in}(k_{in}, L), N_{out}(k_{out}, L)$ from tables	Addressing influence of noise variables
Random	Chosen by the experimenter	Building response surfaces
Latin Hypercube	Chosen by the experimenter	Building response surfaces

factor, Latin Square or Randomised Complete Block design would be more suitable. If noise variables are (or may be) present, a Taguchi method is suggested. For RSM analyses, a Full Factorial, a Box-Behnken, a Central Composite, or a Space Filling technique must be used. Cavazzuti (2013) presents a table (Table 4.1 on page 54) that summarises the different methods available, as well as the estimated costs in terms of the number of experiments and the associated aim of the method.

As mentioned previously, it may be beneficial to carry out a cheaper DOE technique in order to determine which parameters have a more pronounced effect on the response variable(s). This can be done when the number of parameters is rather large. In the case of part production using a SLM process, the number of parameters that influence single layer formation amounts to approximately 18. Of these, five have been identified as potentially significant parameters (see section 3.6 on page 47). These relate to process and laser specific parameters. This is still a rather large number, and in order to determine an optimal parameter-level combination this number needs to be reduced. Through extensive literature analysis, laser power (P), scan speed (v), and hatch spacing (h) are identified as the parameters holding the most significant influence on single layer formation and subsequent part production capability (Kruth *et al.*, 2005; Li *et al.*, 2010; Zhang *et al.*, 2010, 2012b; Campanelli *et al.*, 2010; Yasa and Kruth, 2011).

The above mentioned basic principles form the foundation of experimental design methods and have been used to develop both simple and complex experimental designs, such as Full and Fractional Factorial, Taguchi, Plackett-Burman, and Composite designs, among others. A discussion is presented in the following sections on some of the experimental design methods identified to hold the most relevance to this work.

4.1.2 Screening experiments

According to Mason *et al.* (2003) screening experiments are conducted to identify a limited number of predominant factors, with the intent of conducting a more extensive investigation using only these dominant factors. Cavazzuti (2013) states that, at the start of experimentation, there is no prior knowledge of the solution space. As such, it may occur that the initial region of interest excludes the optimum design. Screening experiments is therefore used to identify not only which parameters are the most significant, but to adjust the region of interest to include the optimum design. The optimum design region will be dependent on the chosen levels for each parameter. Usually the number of levels is the same for each parameter, however some DOE methods allow for differentiation of the number of levels for some or all parameters.

According to Mason *et al.* (2003), saturated Fractional Factorial Resolution III designs are commonly used in screening experiments. The reason for this is it allows the experimenter to estimate main and interaction effects with very few test runs. It has been found that these types of experiments often result in the identification of dominant factors without significant time or cost investment. See section 4.1.3 on page 55 for more on Fractional Factorial design methods.

A special two-level Fractional Factorial experimental design exists, often called a Plackett-Burman design, that has Resolution III when conducted as completely randomised. Plackett-Burman designs are frequently used for screening experiments. These types of experiments, however, are only applicable to experiments that have test runs equal to a multiple of four.

For this work, the Fractional Factorial design methodology has been identified from literature as a potential approach for a screening experiment design. Furthermore, based on the outcome of the screening experiments and the nature of the Fractional Factorial design method, the Full Factorial design method is identified from literature as the most intuitive and informative design method to be used in optimisation experiment design. However, restrictions in budget and time preclude the use of both screening and optimisation experimentation. Therefore, an alternative approach is identified and employed in this work. This is discussed further in section 4.1.4 on page 56. A short discussion on Fractional Factorial and Full Factorial design methods follows.

4.1.3 Fractional factorial design

Some experiments require the analysis of more than four factors. In this event, a Full Factorial design may be very time-consuming and costly to carry out. Fractional Factorial experimental designs are important alternatives to Full Factorial designs and could curtail budgetary, time, or experimental constraints and difficulties (Mason *et al.*, 2003). The basic principle of a Fractional Factorial design is to run a subset of the Full Factorial experiments. In so doing, it is possible to receive valuable information on the main effects and some information on the interaction effects. According to Cavazzuti (2013) the sample size of a fractional factorial design can be one-half, one-quarter, etcetera, of the Full Factorial design. These samples must be chosen carefully and should, in particular, be balanced and orthogonal. Here,

balanced refers to a sample space wherein each factor has an equal amount of samples for each of its levels.

Fractional Factorial designs are distinguished by the chosen design resolution (R). According to Antony (2003b) the design resolution summarises the patterns associated with confounding or aliasing of factor effects, be it main or interaction. Confounded effects are termed aliases. Simply put, the resolution indicates the degree to which the experimental design is confounded. A higher design resolution corresponds to better expected results (i.e. a lesser degree of confounding).

When conducting Fractional Factorial experiments, the goal is to ensure (through selective design) that the effects that are of primary interest are unconfounded with other effects. Confounding of higher order interactions is recommended, since these frequently don't exist or are negligible as opposed to the main effects or lower order interactions. Thus primary effects are designed to be confounded with effects that are not likely to have significant magnitudes. In short, efficient Fractional Factorial designs utilise planned confounding of factor effects in its construction (Mason *et al.*, 2003).

The term confounding refers to the attribution of the combined influence of two or more experimental effects on the response factor, as opposed to each effect's unique influence. Antony (2003b) states that factor effects and the associated interaction effects cannot be estimated independently.

He further states that the degree to which main effects are aliased with interaction effects (for two-factor or higher designs) is represented by the corresponding design resolution. Designs that have resolutions III, IV, or V are especially important. The order of the confounding of the main effects and their interactions are unique to each resolution and is an essential tool in determining which design is best suited for the problem. The following describes each resolution and the corresponding order of confounding (Antony, 2003b; Cavazzuti, 2013).

- Resolution III: Main effects aren't confounded with other main effects, but may be confounded with two-factor interactions and two-factor interactions with each other.
- Resolution IV: Main effects aren't confounded with other main effects or two-factor interactions, but two-factor effects are confounded with each other.
- Resolution V: Main effects aren't confounded with other main effects, two-factor interactions, or three-factor interactions; however two-factor interactions are confounded with three-factor interactions.

Therefore, depending on the amount of main factors present in the design, the amount of time and resources available, and the permitted level of confounding, a Fractional Factorial experimental design can be successfully utilised to delineate which factors have the most significant impact on the response factors.

4.1.4 Full factorial design

The most common and often most intuitive of design methods is the Full Factorial experimental design. It consists of all possible combinations of levels, for all factors.

The simplest form, the two-level Full Factorial, consists of k factors and $L = 2$ levels. Each combination of factors at different levels are called samples. Thus the total number of samples this experimental setup would yield is 2^k . Of course, Full Factorial experiments consisting of three or more levels can be designed and is designated as L^k factorial designs. According to Antony (2003a) the 2^k factorial design is particularly useful in early stage experimental work. This is especially true when the number of process or design parameters (or factors) is less than or equal to four. An important assumption made regarding factors at two levels is that the response is approximately linear over the chosen factor settings range.

For each factor in a 2^k design, two levels are chosen and typically called high and low values. Choosing any sample in the Full Factorial scheme as a starting point, the samples for which factors are changed one at a time still form part of the complete sample space. This allows for the effect of each factor on the response variable not to be confounded with other factors (Cavazzuti, 2013).

In some cases it is useful to include the central point of the design space in the sample space. The central point in the sample takes on the average between each factor's high and low values. The addition of three central points in the sample space serves to determine the robustness of the experimental design and to discern what the effect(s) of noise factors are, if any.

The primary advantage of a Full Factorial design is that it makes very efficient use of the data and confounding of the factor effects does not occur. It is therefore possible to evaluate main and interaction effects very clearly. The main disadvantage is that the sample size grows exponentially with the number of factors and levels chosen (Cavazzuti, 2013), as illustrated in Figure 4.1 on page 53.

Considering the nature of the investigation (i.e. the number of factors and corresponding possible levels), an adapted 2^k Full Factorial DOE is used to evaluate which production parameters have the most significant effect on the formation of single layers in AM of WC-6.6wt.% Co powder. This follows since Full Factorial design methods are used to ensure no confounding of any factor effects are present. In this work it is specifically aimed at determining which factors are significant to the statistical model. The factors being evaluated are scan speed (v), laser power (P), and hatch spacing (h). The experimental setup is explained in more detail in the following section, which presents the experimental procedure followed in this work.

4.2 Experimental procedure

The experimental procedure followed in this work is outlined in this section. The experimental setup is described, presenting the analysis software used as well as the parameter combinations used during experimentation. The equipment used for single layer sample production and analysis is briefly described. Also, the procedure followed to analyse the material used in this work is presented. Finally, the single layer analysis procedure is outlined. Figure 4.2 on page 58 outlines the experimental methodology graphically.

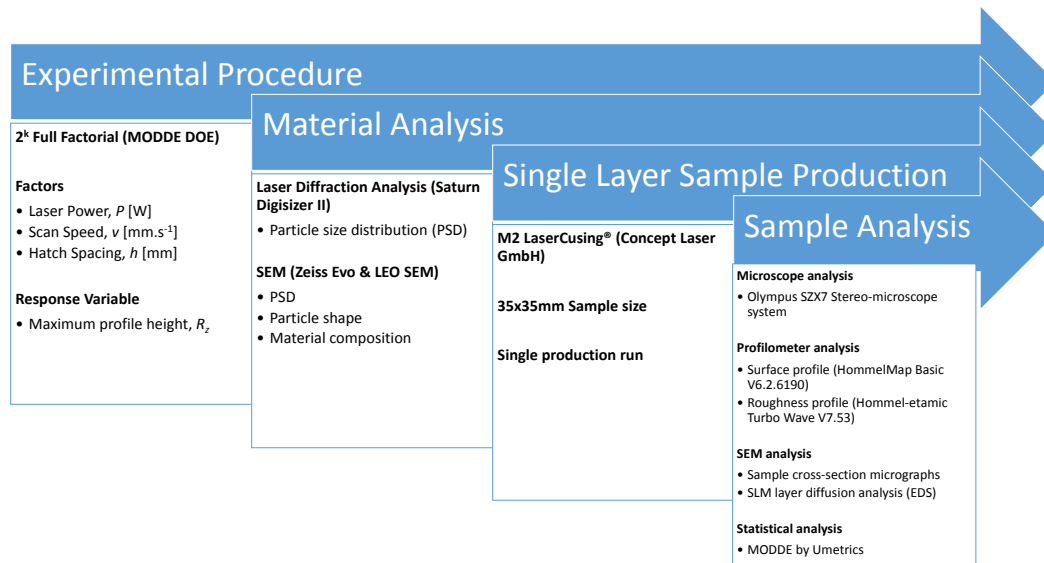


Figure 4.2: A graphical process flow of the experimental methodology in this work.

4.2.1 Experimental setup and design

The Design of Experiments (DOE) for this work is set up using MODDE by Umetrics. MODDE is a tool used by researchers to facilitate set up and subsequent data analysis of experiments. The software guides the analyst through the necessary steps to set up the initial design: 1) factor definition, 2) response and associated target value definition, 3) objective definition, and 4) choice in design method.

The software suggests the optimal design method associated with the number of factors and response variables defined, however the analyst is free to generate his/her own design based on the principles of a standard DOE method.

Using this, the experimental design as shown in Table 4.2 on page 59 is established. The run order is randomised as to eliminate (or at least limit) possible bias that may be present during experimentation. In this work, however, the run order will have no effect as all samples are produced in a single production run, on the same baseplate, with only the process parameters being different per sample. The table lists only the defined factors and associated levels. The response variable for this work is the maximum measured deviation in the z-axis, R_z , using a Hommel-etamic T8000 Profilometer, measured in micro-meters (μm). The objective for this DOE is chosen to be screening, which is aimed at finding the important factors as the first phase of the research process using linear and interaction models. The experimental design is chosen to be a 2^k Full Factorial interaction model.

4.2.2 Single layer sample production

The test samples for this work are created using a M2 LaserCusing[®] SLM machine from Concept Laser GmbH. The single layer test samples are 35x35mm squares. This geometry is chosen for simplicity and ease of analysis. The Computer Aided Design (CAD) model is prepared using Magics[®]. A simulated build environment is created

Table 4.2: Single layer sample production DOE.

Experiment Name	Run Order	Scan Speed [$mm.s^{-1}$]	Laser Power [$J.s^{-1}$]	Hatch Spacing [mm]	Layer Thickness [mm]
E1	15	100	100	0,1	0,15
E2	10	200	100	0,1	0,15
E3	16	100	200	0,1	0,15
E4	7	200	200	0,1	0,15
E5	14	100	100	0,15	0,15
E6	9	200	100	0,15	0,15
E7	11	100	200	0,15	0,15
E8	8	200	200	0,15	0,15
E9	5	100	150	0,125	0,15
E10	2	150	100	0,125	0,15
E11	6	150	150	0,125	0,15
E12	1	100	100	0,125	0,15
E13	12	125	125	0,075	0,15
E14	3	175	175	0,075	0,15
E15	13	175	125	0,075	0,15
E16	4	125	175	0,075	0,15

wherein the part is positioned, the build parameters are selected, and a specialised slicing algorithm is used to create the 2D slices that make up the 3D model. The 2D slice data are exported and loaded into the SLM machine. This is then used by the SLM machine to scan each layer, building the final 3D part. For this work, however, only a single layer is scanned.

Each sample is created by scanning the surface with a laser according to pre-configured build parameters listed in Table 4.2 on page 59. Each single layer is scanned using an island scan strategy patented by Concept Laser GmbH. The scan strategy divides the scanned area into square sections (or islands) (Kruth *et al.*, 2012). The scan sequence is chosen randomly by the machine to determine in what order each island is scanned. The slicing algorithm in Magics[®] enables the user to change the size and orientation (γ) of the islands, as well as shift the islands in the x- and y-direction between each layer. Figure 4.3 on page 60 demonstrates a possible scan pattern for a single layer, using 5x5mm islands and a 45°- γ orientation.

As mentioned previously, the parameters being varied are laser power (P), scan speed (v), and hatch spacing (h). Parts are grown on a tool steel baseplate, based on experiments carried out by Tolochko *et al.* (2003) and Kharanzhevskiy *et al.* (2015). The baseplate is prepared by first sandblasting the surface. This is done to ensure it has a slightly rougher surface finish and a dull appearance. The roughened surface ensures better adhesion of the melted powder to the build surface. The dull appearance ensures that the incident laser beam does not reflect back into the lens, thereby damaging the laser. Thereafter, the baseplate is demagnetised to ensure that no residual magnetisation is present that may negatively affect powder distribution during deposition and melt activity during processing.

A single, uniform layer is created by sieving the powder onto the build surface, to a thickness of approximately 150 μ m. This corresponds to a chosen layer thickness limit approximately three times the maximum particle size (as prescribed by the manufacturers). The machine is sealed and the build chamber flooded with argon gas to create an inert environment. Once the oxygen percentage present in the build

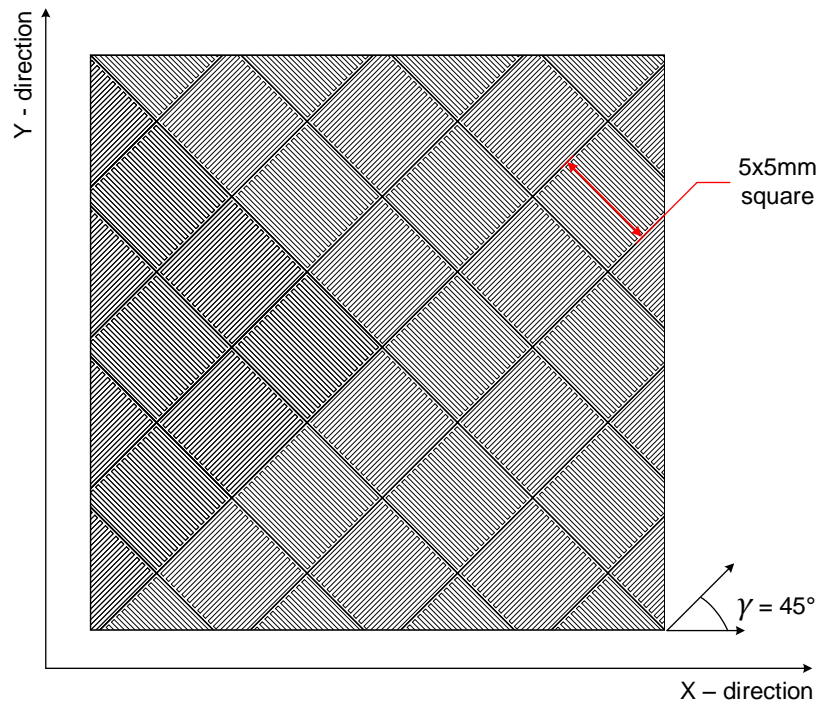


Figure 4.3: A possible scan pattern for a single layer.

chamber reaches 0.9% the scanning process may commence. Since each individual sample has the same layer thickness, and since the machine is capable of processing multiple build parameters for multiple parts, all 16 samples are created on the same build platform during a single production run.

4.2.3 Material analysis

Material analyses are carried out for a tool grade WC-6.6wt.% Co. The tool grade material is used in this study to determine the degree of usability of the powder in the chosen SLM process, based on successful single layer formations. The flowability of the tool grade powder presents significant obstacles for autonomous deposition of uniform powder layers on the build platform. Therefore, the study is limited to single layer formation under different process parameter values with the layer thickness being kept constant. The capability of an SLM process to produce functional parts from a tool grade cemented tungsten carbide holds great interest for the manufacturing industry.

The material used is a standard PI-25 spray dried powder supplied by Pilot Tools (Pty) Ltd. This specific material is conventionally used in press and sinter operations for the production of industrial tools (see section 1.3 on page 5). In order to provide the powder with the necessary green strength before sintering, the powder is produced containing a polymer binder. Since the focus of this work is on the production of parts using SLM, a polymer binder is not necessary and poses the risk of enhancing porosity formation and other layer defects during the SLM process. The polymer binder must be removed (i.e. the material must be debinded) (Kruth

et al., 2003). Therefore, the powder material is heated in an oven to 450°C for one hour, in order to burn out the polymer binder.

The final step in preparing the material is the removal of agglomerates that form as a result of the debinding process. As the polymer evaporates from the material, particles adjacent to one another remain in an agglomerated state (i.e. spherical agglomerates). Therefore, the powder is ball milled for 2 hours in WC cylinders using WC drill buttons. The powder to button weight ratio is approximately 3:1. This is done according to standard practices employed at Pilot Tools (Pty) Ltd.

Once the powder is in the desired state and consists of only metal powder particles, it is analysed for composition, particle size, and particle shape. The following sections describe these analyses.

4.2.3.1 Composition analysis and SEM micrographs

Both compositional analysis and micrograph imaging is done using a scanning electron microscopy (SEM). A SEM utilises a focused, high-energy electron beam that generates a variety of signals at the sample surface. Signals derived from sample interactions provide the analyst with information pertaining to the external surface morphology (texture) and the sample's chemical composition, as well as the orientation of the materials making up the sample and its crystalline structure. Generally, data are collected for a selected sample surface area generating a two-dimensional (2D) image displaying the spatial variation of these properties. Typical scanned areas range from 5µm to 1cm in width and can be imaged in scanning mode by conventional SEM techniques. Magnifications range from 20 to approximately 30,000 times and spatial resolutions range from 50 to 100nm.

A material's composition will influence the melting activity experienced for a specified set of scan parameter values. Higher binder content (e.g. cobalt) will lead to a tougher final part (Prakash, 1995; Andren, 2001) and often a higher part density. A lower binder content implies a higher content of structural element, thereby increasing the final part's hardness and diminishes its fracture toughness (Kumar, 2009). Elements, such as mixed crystals, are often added to a base material composition. This is aimed at changing grain growth phenomena during sintering or enhancing the final part's wear resistance. It is therefore important to analyse a material for composition to enable accurate replication of desirable results and to avoid undesirable results when repeating experiments.

The PI-25 cemented tungsten carbide powder, as supplied, has a weight percent composition of 85.5% WC, 6.6% cobalt, and 7.9% mixed crystals (TiC, TaC, NbC, and N). This composition is reported by Pilot Tools (Pty) Ltd. The powder is thus classified as a WC-6.6wt.% Co cemented tungsten carbide. The reported composition is a generalised measurement of multiple production batches. A material sample is analysed for individual elemental composition using a ZEISS EVO MA15VP SEM.

Furthermore, a sample of the PI-25 powder is analysed using a LEO 1450VP SEM. The sample is prepared by loading powder onto double-sided carbon tape, attached to the sample cartridge for the SEM. The sample is placed into the SEM and studied using the associated SEM software at 200, 500, and 1000 times magnifications.

4.2.3.2 Particle size distribution and shape analysis

Two particular material properties that have significant influences on the melting behaviour during SLM are particle size and shape. The material used for this work is analysed to determine the associated particle size distribution (PSD) using both Laser Diffraction Analysis (LDA) and SEM imaging.

A limitation imposed on the building parameters associated with the M2 Laser-Cusing[®] SLM machine used is the maximum allowable layer thickness. For this specific model, a maximum layer thickness of 50µm can be achieved using autonomous powder deposition. This particle size limit also corresponds to the optimal size distribution for the production of near full density (>99.9%) parts for some standard materials. This then implies that the powder material used must have a maximum particle size of 50µm in order to adhere to, as far as possible, the standard SLM material parameters. However, since the powder layer is created by manually sieving the material onto the baseplate, this constraint holds significance only to the particle behaviour under melt conditions. The PI-25 powder is analysed for particle size using two methods, namely Laser Diffraction Analysis and SEM imaging.

LDA is a light scattering analysis technique that is used to determine the size and shape of a particle (Hareland, 1994; Eshel *et al.*, 2004). Different particle sizing techniques measure certain parameters that are affected by the size of the particle, rather than measuring the particle size directly (Hareland, 1994). Some examples of these parameters include settling velocity, volume displacement of the particle, or the light scatter pattern produced by the particle (Webb, 2000).

Static light scattering techniques are based (generally) on either the 1) Mie theory of light scattering by particles or 2) the Fraunhofer model. Variations in each model's ability to measure particle size is negligible up to a PSD less than 10µm. A full Mie Theory model may be more appropriate for finer grained samples (Blott and Pye, 2006). According to Webb (2000) and Eshel *et al.* (2004) the Mie theory describes the characteristics of the scatter pattern that is produced by the interaction of a plane wave-front of monochromatic light with a spherical, isotropic particle suspended in a medium with known optical properties. The theory predicts the angle versus intensity relationship as a function of particle size for spherical particles (as opposed to irregular shaped particles) (Eshel *et al.*, 2004). This is dependent on all other system variables being known and held constant. These variables are the relative refractive index of the sample material and suspension fluid, as well as the wavelength of the incident light.

Mathematically, the intensity of the scatter pattern (I_{sc}) is a function of the incident light angle (θ), the wavelength (λ), the particle size (x), and the system's optical properties. That is:

$$I_{sc} = I_{in}(\theta, \lambda, x, n) \quad (4.2.1)$$

Specifically, the system's optical properties refer to the refractive index, n , of the material sample relative to the suspension medium.

Webb (2000) also notes that the Mie theory only accounts for light scattered by spherical particles. In some cases, however, sample particles exhibit entirely different morphologies than spherical. Light will, however, scatter according to physical laws governing the interactions between light and matter if the particle's refractive index

is different from the suspension medium. The associated issue with non-spherical particles is that the light scatter direction and intensity is not described by any known theory. Thus, the Mie theory merely provides an approximation for non-spherical particles. This, however, is still a reliable approximation since particles of a given shape, size, and index of refraction will scatter light in the same way each time the analysis is conducted. A spherical equivalent of the particles can thus be obtained to approximate the PSD.

The equivalent sphere assumption introduces error in the measurement of particle size. Through repetition of the same experiment, the same error is introduced. Therefore, the error has no effect on the repeatability, reproducibility, and resolution of the analysis. The same issue is present in essentially all particle sizing techniques, be it Mie theory, Stokes law, or SediGraph, among others (Webb, 2000). An important note on particle sizing is that no one technique offers the best or optimal solution for all sample types. There are, however, some techniques that consistently yields the best results depending on the nature (size range, material type, applications of concern, etc.) of the material being analysed.

The primary advantages associated with LDA for PSD determination includes a short time for analysis (± 5 -10min per sample), high repeatability, small sample size requirements (< 1 gram), and a large size distribution range into which the particles sizes may be classified (Eshel *et al.*, 2004).

A variety of instruments have been developed for the use of LDA, including Beckman-Coulter, Microtrac, Fritsch, Malvern, Retsch, Cilas, and Helos, among others (Blott and Pye, 2006). In this work, however, a Saturn Digisizer II from Micromeritics is used to analyse particle size. The instrumentation is developed (and operates) in accordance with ASTM Standards B822, C1070, and D4464, as well as ISO Standard 13320. This instrument measures PSD based on a full Mie Theory model. For the standard PI-25 powder used in this work, a sample is prepared in a solution of distilled water with a diffractive index of $n_{solution} = 1.331$. The refractive index of the sample is set to $n_{sample} = 1.768$. The sample is sonicated in order to break up any agglomerates present in the sample mixture. A monochromatic light source is scattered by the particles in the sample and a spherical approximation of the particle size is determined. The test is conducted three times and adjusted to produce an accurate model fit ($\ll R^2$).

4.2.4 Single layer sample analysis

Single layer test samples are produced according to the process outlined in section 4.2.2 on page 58. Each single layer test sample is studied using microscope imaging (Olympus SZX7 Stereo-microscope System). This is done to determine what, if any, observable trends exist in the formation of single layers using an available SLM technology and a WC-6.6wt.% Co material. The surface quality - i.e. the degree to which surface and subsurface defects are present on each sample and how these defects hinder subsequent powder layer deposition and consolidation - is used as the primary criteria to determine the success of the parameter set to produce single layer samples. In order to do this, each sintered layer is analysed using a Hommel-etamic T8000 Profilometer to determine the 2D and 3D profiles of the single layers developed during sintering. The data are used to determine the maximum deviation in the z-

axis, R_z , for each parameter set. The deviation data are used in a statistical analysis to determine which of the three identified parameters has the most significant effect on the formation of a single layer. Using the same data, an optimisation analysis is performed to determine what parameter set should, theoretically, yield the best result in terms of producing single material layers that are free of surface and subsurface defects. The optimisation objective is set to minimise the z-axis deviation. The following sections outline, in more detail, each of the analyses described here.

4.2.4.1 Microscope image analysis

Each single layer test sample is analysed using an Olympus SZX7 Stereo-microscope System. The analysis is aimed at determining what surface defects are present on each sample and to what extent these defects would hinder successful 3D part production. The software used with the equipment is Olympus Stream Essentials. Single layer images are captured at 1.25 and 3.20 times magnification. Figure 4.4 on page 64 shows a single layer sample, demonstrating the different magnifications. In order to compare the observable differences in single layer formation, as a result of different production parameter sets, the images are graphed according to high-low, low-high, low-low, and high-high combinations of power and scan speed. This is done for each hatch spacing value. An example of this is shown in Figure 4.5 on page 65. The graph heading indicates the corresponding hatch spacing for the sample set as well as the associated average volumetric energy density (VED).

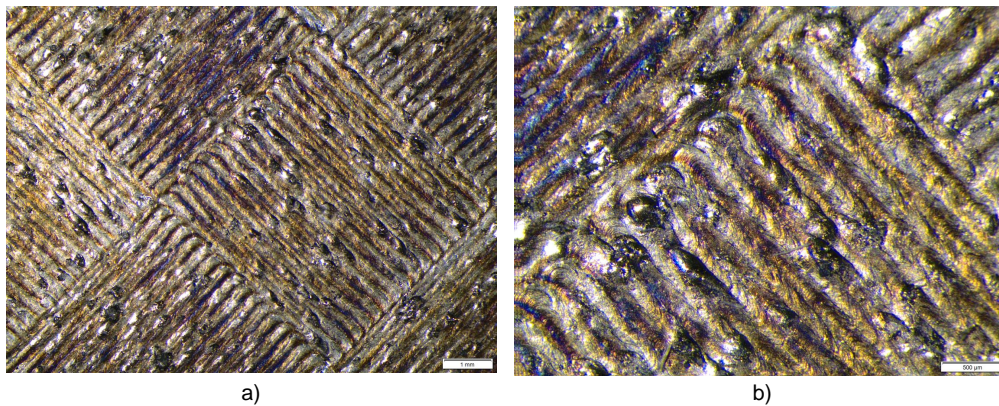


Figure 4.4: A single layer test sample at a) 1.25 and b) 3.20 times magnification. ($P=100W$, $v=100mm.s^{-1}$, $h=0.15mm$)

In Figure 4.5 the high values for scan speed and laser power are $P = 200W$, $v = 200mm.s^{-1}$ and the low values are $P = 100W$, $v = 100mm.s^{-1}$. The graphs are used to analyse observable trends in the formed layers as a result of the chosen parameter values. The primary focus is placed on the effect hatch spacing has on scan track formation, the associated peak and valley formation for high versus low scan speed and laser power, and the formation of surface defects for the combined parameter sets. The observable results are validated against existing literature, specifically sections 3.5.1 and 3.6 in Chapter 3.

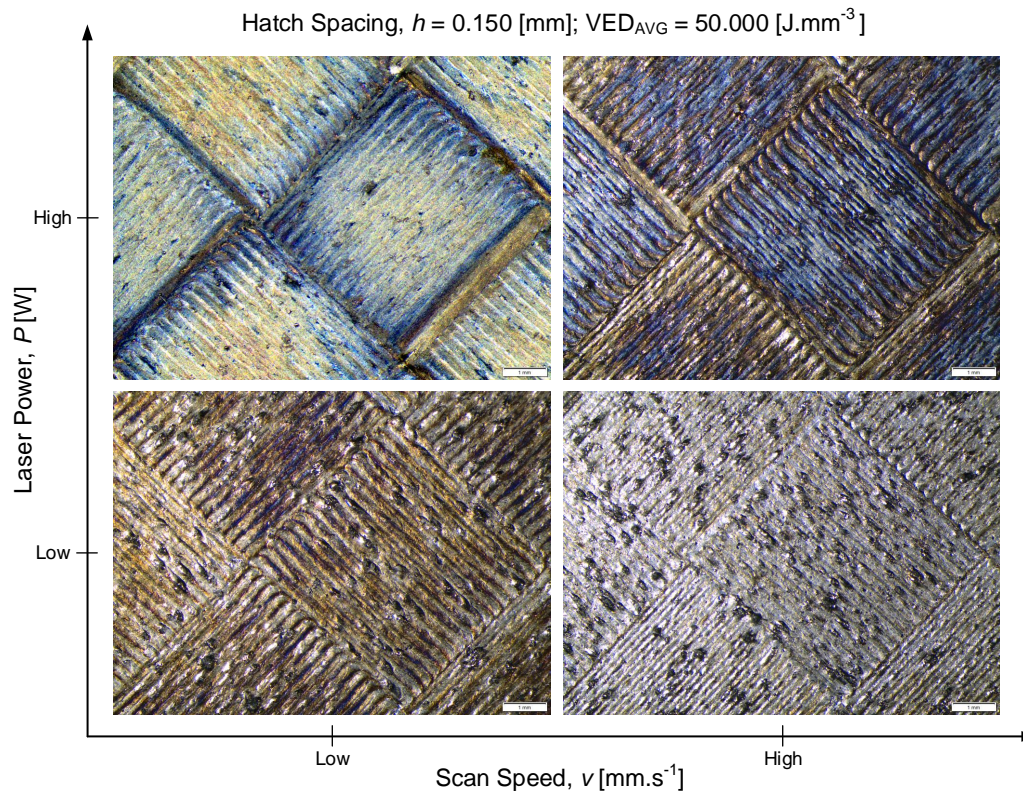


Figure 4.5: Single layer sample parameter set corresponding to $h=0.15$ mm and 1.25 times magnification.

4.2.4.2 Profilometer analysis

The surface profile of each single layer sample is analysed using a Hommel-etamic T8000 Profilometer by Jenoptik AG. Both a three-dimensional (3D) surface map and two-dimensional (2D) roughness profile is generated. The software used for the 3D mapping of each surface is HommelMap Basic V6.2.6190. The software used for the 2D roughness profile analysis is Hommel-etamic Turbo Wave V7.53.

Both the surface and roughness parameters are influenced by the choice in sampling area. The roughness profile (2D) parameters are defined either by sampling length, l_r , or the evaluation length, l_n . If a parameter is defined by l_r , it is calculated on each sampling length and a mean value is reported. The default number of sampling lengths is five, based on ISO Standard 4288. The cut-off length, λ_c , is equal to l_r and determines the limit between the waviness and the roughness of the profile.

For parameters defined by l_n or for a surface (i.e. areal parameters) the sampling and evaluation areas are still defined by ISO Standard 4288, however only a single sampling area is used per evaluation area (as opposed to five) (Blateyron, 2013).

Figure 4.6 on page 66 shows an example profile and indicates the evaluation length (l_n) and the sampling length (l_r). Furthermore, the image shows that the transverse length, l_t , consists of a start-up length, a run-off length, and five sampling lengths (by default, according to ISO Standard 4288). For this work the default

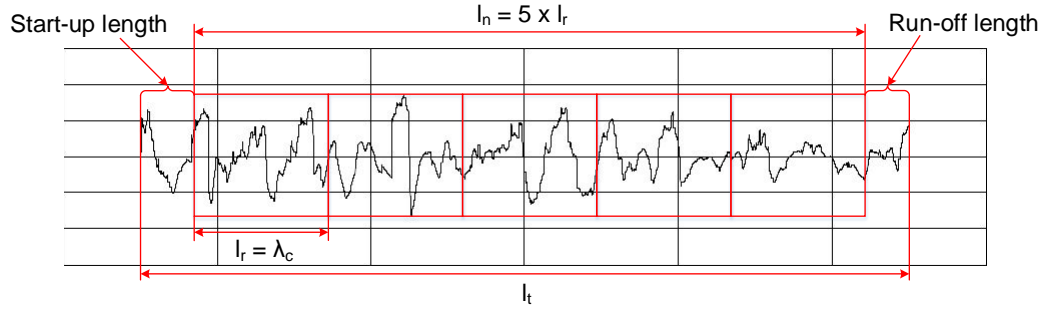


Figure 4.6: Roughness profile evaluation lengths as determined by ISO Standard 4287.

definitions are used during the single layer sample analysis.

The 3D surface for each sample is characterised by surface parameters, according to ISO Standard 25178 (for appropriate symbol use) and ISO Standard 4287 (for parameter definition). The surface texture parameters have a prefix that is a capital letter S and is followed by one or many lower case letters which forms the suffix (Blateyron, 2013).

The surface parameters, also referred to as the height parameters, measured and reported in this work is the root mean square height (S_q), the arithmetic mean height (S_a), the maximum peak height (S_p), the maximum pit height (S_v), and the maximum surface height (S_z). S_q is defined as the root mean square value of the surface deviations, $z(x, y)$, in the sampling area, A . This value is calculated as follows (Blateyron, 2013):

$$S_q = \sqrt{\frac{1}{A} \int \int_A z(x, y) dx dy} \quad (4.2.2)$$

S_a is defined as the arithmetic mean of the absolute value of the height in the sampling area, A . This value is calculated as follows (Blateyron, 2013):

$$S_a = \frac{1}{A} \int \int_A |z(x, y)| dx dy \quad (4.2.3)$$

Both these parameters are strongly correlated. The S_q parameter, however, is statistically more significant and indicates the standard deviation.

The S_z value for each surface is derived from the maximum peak and valley heights, S_p and S_v , and is determined as the sum of their absolute values (Blateyron, 2013), as per equation 4.2.4. That is:

$$S_z = |S_p| + |S_v| \quad (4.2.4)$$

Similarly, the 2D profile for each sample is characterised by profile parameters according to ISO Standard 11562 (for the $P-R-W$ profile filter) and ISO Standard 4287 (for parameter definition). The type of surface profile from which the profile parameters are calculated determines the prefix used in naming the parameters. For example, the R -parameters are calculated from the roughness profile (Blateyron, 2013). In this work a roughness profile is reported for each single layer sample.

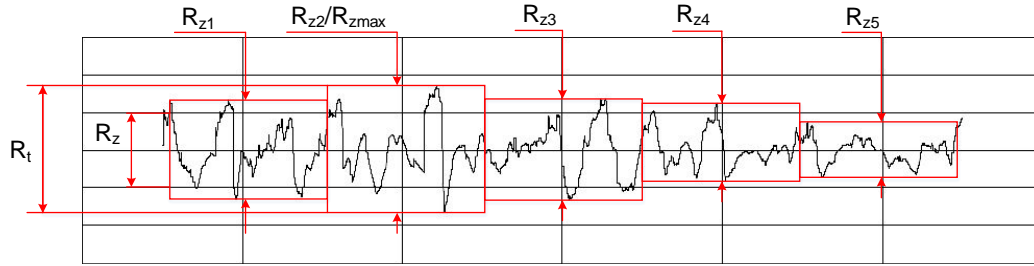


Figure 4.7: Roughness profile parameters as determined by ISO Standard 4287.

Figure 4.7 on page 67 shows how the roughness parameters are determined for each roughness profile, according to ISO Standard 4287. The R_z value indicates the height of the profile, and corresponds to the average of the five R_z values. These five values correspond to the sampling length, l_r , defined previously. The R_t value indicates the distance between the highest peak and lowest valley of the profile for the entire evaluation length, l_n . Finally, the R_{z-max} value indicates the largest R_z value from the five sampling lengths. Again, refer to Figure 4.6 on page 66 for a visual representation of the l -variables associated with the roughness profile.

In this work the R_z parameter is used to evaluate the capability of each experimental parameter set to successfully produce a single layer using the material described in section 5.1 on page 74. These values are used in the statistical analysis described in the following section. Furthermore, the R_a value (or arithmetic mean roughness value) for each sample is reported in the trend analysis in section 5.2.2 on page 89. The R_a value is calculated as follows:

$$R_a = \frac{1}{l_r} \int_0^{l_r} |z(x)| dx \quad (4.2.5)$$

It should, however, be noted that the R_a value does not differentiate between peaks and valleys and therefore has a comparatively weak information character as opposed to the R_z variable.

For both the 3D surface map and the 2D roughness profile a 25x25mm sample area is scanned using a TKU300 probe with a measuring range of 400 μ m, a scanning velocity $v_t = 0.50\text{mm}\cdot\text{s}^{-1}$, a transverse length $L_t = 25.00\text{mm}$, and a cut off length $L_c = 2.5\text{mm}$. The surface and roughness parameters are determined according to the standards and definitions reported previously. The profile analysis is used to verify, quantitatively, the observations and conclusions presented by the qualitative analysis of the microscope image analysis.

The images presented in Appendix C on page 141 shows the equipment and software setup as used during the analysis procedure.

4.2.4.3 SEM sample analysis

The two best samples from the sample set are selected for further scanning electron microscopy (SEM) analysis, based on the profilometer results obtained by following the methodology outlined in the previous section. Only the two best samples are

selected due to time and financial constraints precluding the analysis of all samples. Cross sections from the selected samples are wire cut using a AgieCharmilles CUT 30 P by GF Machining Solutions. The samples measure 12x33x3mm. Each sample is polished along the long edge according to the following polishing regime: 1) 20 minute grind using a 1000 grit sand paper and a metal polish paste (15-30% aliphatic hydrocarbons, 5-15% aromatic hydrocarbons, soap less than 5% anionic surfactants), 2) 10 minute grind using a 1200 grit sand paper and a metal polish paste (15-30% aliphatic hydrocarbons, 5-15% aromatic hydrocarbons, soap less than 5% anionic surfactants), 3) 5 minute polish using a polishing pad and a 1 μ m diamond paste, 4) 30 second final polish using dry finishing polish pad.

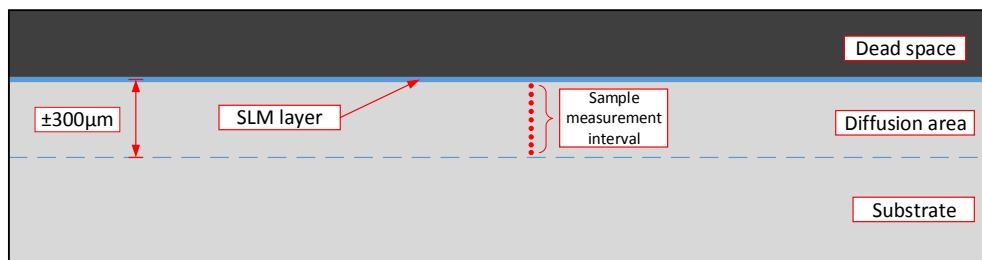


Figure 4.8: Graphic illustration of the cross section sample area analysed using a Zeiss Evo MA15VP SEM.

Each sample is mounted in a Zeiss EVO MA15VP SEM for energy dispersive spectroscopy (EDS) analysis and SEM imaging. The EDS analysis is done for the cross section of each sample to determine the degree of diffusion present from the WC-6.6wt.% Co layer sintered onto the steel substrate. A 9 point EDS analysis is carried out for each sample within the diffusion area, as indicated in Figure 4.8 on page 68. A final 9 point spectrum analysis is carried out at the SLM layer of the best sample, at higher magnification, to determine the material-substrate interface composition after sintering. Each sample cross section is imaged at different magnifications to discern visible signs of diffusion and/or the presence of layer defects after sintering.

4.2.4.4 Statistical analysis

The statistical data analysis is carried using MODDE by Umetrics. The software determines, based on the analysed factors and response values, what the best statistical model fit is. The fitted model is then analysed using functionalities embedded in the Design of Experiments (DOE) software. This can be defined in two parts: 1) evaluation of the raw data and 2) computation of the regression model. The regression model is used in the optimisation analysis wherein the theoretically optimal parameter set values (or setpoint) are determined. MODDE uses a six-step sequence to initialise model data analysis:

1. A Replicates plot;
2. A Distribution plot;
3. A Summary plot;

4. A Coefficient plot;
5. A Residuals plot; and
6. An Observed versus Predicted plot.

The Replicates plot shows the results for all experiments. It shows the variation in the measured data and is used for a quick raw data inspection. In the event where repeated experiments are present, the ideal outcome relates to very little variability in this repetition data. Any experimental data that deviates significantly from the rest is termed an outlier and must be investigated. Also, an indication of the model quality is provided in the form of an R^2 and Q^2 value. The R^2 value represents the model fit, which is indicative of its significance. A model with a low R^2 value (<0.5) has a rather low significance. The Q^2 value is an estimation of the model's future prediction precision. The Q^2 value should be greater than 0.1 for a significant model and greater than 0.5 for a good model. The model quality can potentially be improved in the coefficient plot, where insignificant terms (e.g. interaction terms) are excluded from the model.

The Distribution (or Histogram) plot is a visualisation of the response variable's values as a histogram. In order to determine a proper estimate of the distribution at least 11 observations are required. During this step in the analysis process a non-normal distribution may be transformed into a normal distribution by selecting an appropriate transformation. This is typically a log or negative log transformation, depending on the skewness of the distribution.

The Summary plot provides a summary of the basic model statistics. The statistics include the R^2 and Q^2 values, as well as Model validity and Reproducibility values. The model validity is a test of diverse model problems. Here, a value less than 0.25 indicates significant model problems which may include the presence of outliers, a transformation error, or an incorrect model. The reproducibility value indicates the variability of the replicates relative to the overall variability. A value greater than 0.5 indicates a good level of reproducibility. However, without the presence of centre points MODDE does not provide a measure of the model validity or reproducibility. In this work, no centre points are used and therefore these measures are not reported.

The Coefficient plot is a graphical representation of the significance of the model terms. It indicates which of the coefficients in the calculated model is insignificant and may be excluded from the model. In this step of the analysis insignificant terms are excluded in order to improve the Q^2 value. An important aspect of this step is that the model terms are linked to a hierarchy. This means that linear terms cannot be excluded from the model if higher order terms exist containing that factor.

At this point in the analysis it is beneficial to revisit the summary plot to re-evaluate the basic model statistics and determine whether a significant improvement has been achieved after excluding insignificant model terms.

The Residuals plot presents a graphical illustration of the residuals of a given response versus the normal probability of the distribution. The ideal result is a plot where all points appear in a straight line on the diagonal. This indicates that all residuals are normally distributed noise. Where points deviate significantly from a linear trend it is obvious that there exists a non-linear relationship between some

of the factors and the response variable. This plot also indicates the presence of outliers.

An important aspect to bear in mind here is that the minimum degrees of freedom (Df) of 5 is required to enable proper analysis of the residuals. Replicated centre points, if present, must be counted as one real Df .

The final plot, the Observed versus Predicted plot, is used to fit a regression line to the data. In this case, plots where the graphed points are close to the regression line indicates a good model. Here it is important to note that models having $Df < 3$ will implicitly give a perfect fit.

The model factors and associated interaction terms for this work are illustrated in Table 4.3 on page 70. This is the direct output from MODDE which describes the model to be evaluated.

Table 4.3: DOE model factors and associated interaction terms as determined by MODDE.

	Full Name	Abbreviation
Responses:	R_z -Average	z-Err
	Constant	Cst
1	Scan Speed	v
2	Laser Power	P
3	Hatch Spacing	h
4	Scan Speed*Laser Power	v*P
5	Scan Speed*Hatch Spacing	v*h
6	Laser Power*Hatch Spacing	P*h

R_z -Average (also referred to as R_z) is the response measured, the constant relates to a constant factor (in this case the layer thickness, d), and all the rest are as defined in the table.

Once the model analysis is carried out and a statistically significant model is obtained, the model is then used to predict the response based on variations in the factor values. MODDE enables the analyst to evaluate the model and determine an optimised result using the Optimiser function also embedded in the software. The analyst chooses the objective value and sets the factor ranges, sets the amount of simulations that must be run, and sets the confidence interval within which the results must be reported. The optimiser setup summary for this work is presented in Tables 4.4 and 4.5 on page 70 for the factors and response variable, respectively.

Table 4.4: MODDE Optimiser factor setup summary.

Factor	Role	Low limit	High limit	Precision	Unit
Scan Speed	Free	100	200	2,5	$mm.s^{-1}$
Laser Power	Free	100	200	2,5	Watt
Hatch Spacing	Free	0,075	0,15	0,00188	mm
Layer Thickness	Constant				mm

The factor ranges are chosen base on equipment constraints as well as production economy constraints. That is, the upper limit for the laser power corresponds to the maximum setting for the M2 LaserCusing[®] machine used. The lower limits for both the laser power and scan speed are chosen since any values below these limits are, from a production viewpoint, economically not viable. Finally, the lower limit of the hatch spacing is chosen since any value below this will have too high scan track overlapping and the upper limit corresponds to the highest possible value before scan tracks become isolated.

Table 4.5: MODDE Optimiser response setup summary.

Response	Criterion	Target	Max	Predicted Minimum	Predicted Maximum	Unit
R_z -Average	Minimize	0	150	46,7641	174,253	μm

The maximum allowable R_z value is set to 150 μm , with the target value set to zero as this is a theoretically perfect surface which would accommodate uniform layer formation and subsequent powder deposition during part production. This target value is chosen even though, due to process constraints and the typical sintering mechanisms and behaviour observable in SLM (see section 3.5.1), this is highly improbable. The Optimiser is set to run 10,000 simulations and report the results within a 95% confidence interval. Once the optimiser process is completed an extensive collection of analysis tools are used to analyse the experimental data. This includes:

- Response contour plots;
- Factor effect plots;
- Factor and response distribution plots;
- Prediction plots;
- Descriptive statistics;
- Predictive model tables;
- ANOVA analyses; and
- Setpoint analysis plots and tables.

Figure D.1 on page 146 (Appendix D) shows an example analysis used by MODDE to demonstrate a screening experiment result, based on the Willgerodt Kindler reaction studied by Torbjörn Lundstadt in 1986. The study was completed towards obtaining his PhD.

The figure illustrates the 4-dimensional (4D) contour plot analysis tool embedded in MODDE. The contour plot illustrates the effect that varying four factors has on the response variable. This is only possible if the analysis involves four or more factors. 2D and 3D contour plots can be generated in a similar fashion. From

this image it is possible to determine what the factor values should be to obtain a theoretically optimal response (in this case a 100% reaction yield). As stated, however, this is merely theoretical and system and factor constraints preclude the use of certain factor values and combinations.

Another 4D contour plot, showing the best result (i.e. the factor values resulting in the best response values), can be generated. An example of this is shown in Figure D.2 on page 147 (Appendix D). The four arrows in the centre of the graph indicate the optimal factor settings (also known as the setpoint) and the expected optimal yield percentage.

These outputs, and others shown and described in Appendix D, demonstrates the analysis carried out in this work pertaining to the minimisation of the deviation observable in the z-axis of single layers produced by SLM of the WC-6.6wt.% Co material. The tools listed previously embedded in MODDE is used to analyse the deviation data, within a 95% confidence band, to determine what the expected minimum achievable deviation is given a specified factor range. The objective of the analysis is set to minimize the measured R_z value, corresponding to the roughness profile analysis. The statistical analysis is carried out to verify and substantiate the results and discussions presented with respect to the microscope analysis.

4.3 Benchmark part analysis

Each single layer sample is compared to a single layer from a benchmark part built in a M2 LaserCusing[®] machine, using a standard stainless steel powder (CL20ES) supplied by Concept Laser GmbH. This material is chosen as the benchmark based on the proven track record for the successful production of single and multi-layered samples, using the standardised production parameters supplied by Concept Laser GmbH. This material has been successfully used to produce samples free from surface and subsurface defects and provides a good basis for comparison on the capability of the AM technology to sinter the chosen cemented tungsten carbide material. The data sheet for this material is shown in Appendix B on page 138 to supply the baseline material parameters typical of a standard SLM material. The part is produced according to standard parameters provided by Concept Laser, that has been optimised to achieve a near full density (>99.9%) and low defect/deviation presence. It should be noted that the optimal production parameters for this material may differ depending on the material and part properties desired of the final product.

Table 4.6 on page 73 presents each parameter and the corresponding optimised value to produce the benchmark. The benchmark single layer is analysed according to the same procedure outlined in section 4.2.4.2 on page 65. The results are used in a comparison to the single layers produced from the WC-6.6wt.% Co material. The test sample deviation measured in the z-axis, or R_z value, is compared to the benchmark to establish which parameter set produces the most favourable results. A comparative analysis and discussion is presented regarding the benchmark part and the best and second best single layer sample.

This chapter presented the methodology followed in determining the capability of a SLM process to successfully produce single layers from a WC-6.6wt.% Co ma-

Table 4.6: Optimal process and material parameters for production of CL20ES parts using SLM.

Parameter	Value	Unit
Laser Power (P)	180	Watt
Scan Speed (v)	800	mm.s ⁻¹
Hatch Spacing (h)	0,105	mm
Layer Thickness (d)	0,030	mm
Spot diameter	0,150	mm
Island hatching	5x5	mm ²
γ	45	°
Particle size	-45/+15	μm
Particle shape	Spherical	N/A

terial. The process to analyse the material, the production of the single layers, and the subsequent analysis of the sintered layers (using microscopic, profilometer, and statistical analyses) are described. The following chapter presents the results and discussion pertaining to the work described here.

Chapter 5

Experimental results and discussion

This chapter presents the results for this work obtained by following the methodology outlined in the previous chapter. Here, results pertaining to the material, microscopic imaging, profilometer, and statistical analyses are presented and discussed.

5.1 Material analysis

The results from the material analysis is presented here. Specifically, the material's composition, the scanning electron microscopy (SEM) images, and the laser diffraction analysis results are presented and discussed. An analysis of the material is required to determine its nature, which is suggested to have a significant influence on the achievable properties of parts produced from it (Wang *et al.*, 2002). As stated in literature, particle shape and size has been found to significantly influence the final sintered part (Zhang *et al.*, 2012a).

5.1.1 Material composition

The material composition is reported according individual elements present in the material. As the weight percentage composition of the mixed crystals (TiC, TaC, NbC, and N) are proprietary information held by Pilot Tools (Pty) Ltd. it cannot be reported here.

The results from the SEM analysis are shown in Figure 5.1 on page 75. The analysis shows a composition consisting of tungsten, tantalum, niobium, cobalt, titanium, and carbon. This agrees with the reported elemental composition for the as-received material.

The individual constituents are also mapped, corresponding to the most abundant elements. This is shown in Figure 5.2 on page 76. In each image the coloured areas correspond to the element distribution reported for each image. Figure 5.2a corresponds to the distribution of titanium in the sample, 5.2b corresponds to the distribution of cobalt in the sample, and 5.2c corresponds to the distribution of tungsten in the sample. These are the three primary elements present in the material,

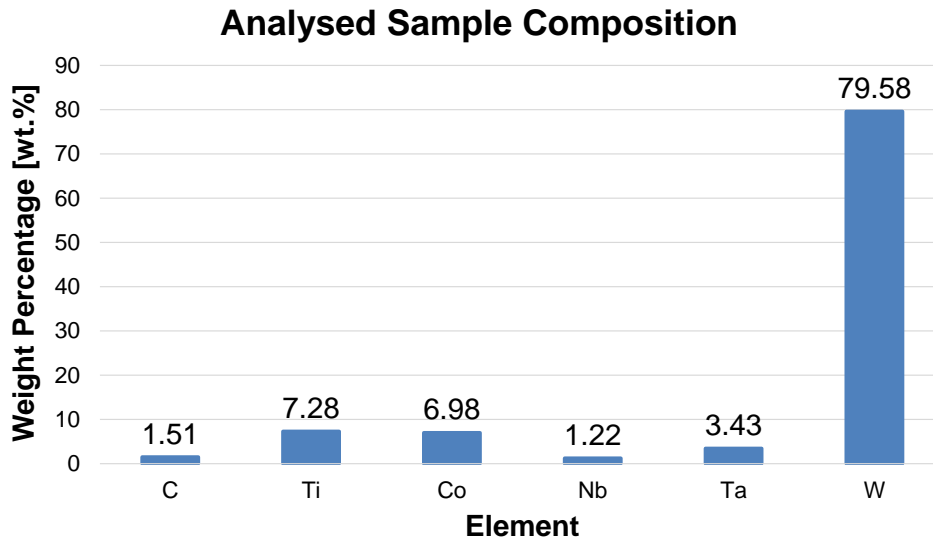


Figure 5.1: Material composition as analysed using a ZEISS EVO MA15VP SEM.

according to the SEM analysis. A colour scale, for red to green, indicates high to low concentrations of the reported element, respectively.

5.1.2 SEM micrographs

SEM micrographs are taken of a material sample to determine the associated particle size and particle shape of the material. The micrographs are shown in Figures 5.3 to 5.5 on page 77. The craters visible in Figure 5.3 are due to the carbon tape used to load the sample into the SEM.

Figure 5.3 shows the sample under 200 times magnification. The image clearly shows the individual powder particles present in the material sample. The agglomerated particles are present as a result from the debinding process, wherein the polymer binder is burned out of the material. As the polymer binder evaporates, the remaining material retains the spherical shape due to particle orientation, as well as the nature of the individual particles' shape and size. The inhomogeneous nature of the shape and size distribution inhibits flowability, resulting in the presence of the agglomerates.

The agglomerates are determined to be approximately 100-150 μm in size. This is far larger than the maximum allowable particle size (50 μm) as per the SLM machine specifications. Therefore, it is necessary to break up these agglomerates through a ball milling process. Furthermore, a reduction in the associated particle size distribution (PSD) encourages energy distribution and absorption during the SLM process. This is crucial since a higher energy density (E_d) in the melt pool enhances liquid wetting of the structural grains, increasing the associated layer density and decreasing the formation of single layer defects such as balling (Gardon *et al.*, 2001; Campanelli *et al.*, 2010; Gu *et al.*, 2012).

There are, however, negative consequences associated with breaking up the agglomerates. Flowability in spherical powders are far superior to other particle shapes.

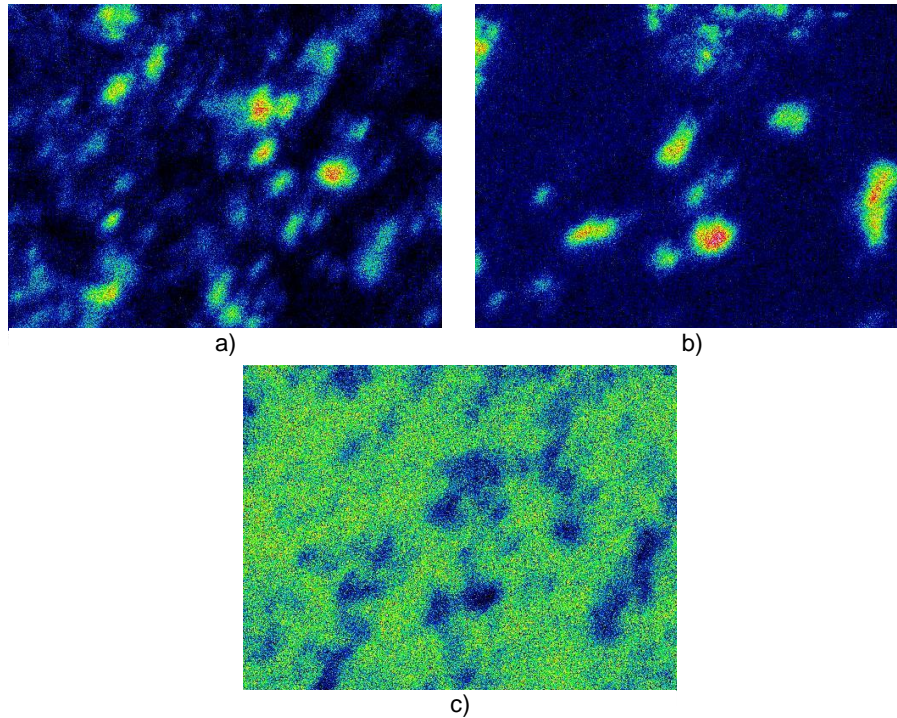


Figure 5.2: Material composition mapping as analysed using a ZEISS EVO MA15VP SEM; a) titanium, b) cobalt, and c) tungsten.

Since flowability is crucial to the successful autonomous deposition of a uniform powder layer in the SLM process, it follows that it is desirable to preserve the spherical nature of the material. As stated in literature, spherical or near-spherical powders optimises efficient material flow, layer packing, and melt uniformity (Murr *et al.*, 2012). However, even with the presence of spherical agglomerates in the material, the flowability is insufficient. This is explained by the surface morphology of each agglomerate.

Figure 5.4 shows the sample under 500 times magnification. This is an enlarged image of one of the agglomerates present in the sample. The image shows that each agglomerate is made up of fine, individual grains ($<7\mu\text{m}$). These fine grain do not exhibit any particular morphology and appears to have multi-faceted (or polygonal) surfaces. The nature of the particles' morphology creates a 'rough' agglomerated surface which inhibits ease of flow of the agglomerates past one another. In the event that these spheres were solid (i.e. exhibited a smooth surface), the material flow would enable autonomous material deposition. The particle shape, however, should facilitate higher coordination numbers and particle rearrangement during processing, according to Zhang *et al.* (2010).

Figure 5.5 is a further enlargement of the powder sample. This is the powder sample shown under 1000 times magnification. It shows that the sample is made up of a wide range of particle sizes, up to the nanoscale. This is ideal and is expected to promote single layer densification behaviour during processing (Murr *et al.*, 2012).

The SEM analysis shows an average particle size of approximately $4\mu\text{m}$, not counting the influence of the agglomerated particles. The material appears the same

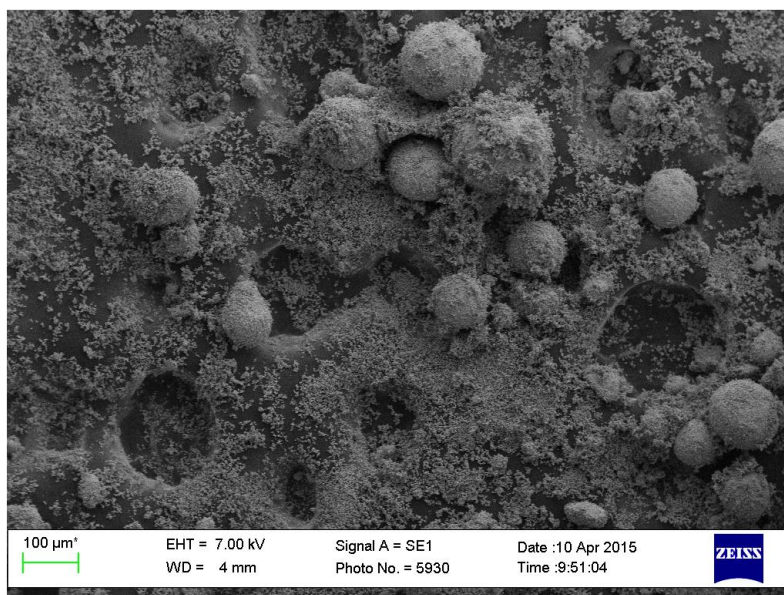


Figure 5.3: SEM image of the material sample taken using a LEO 1450VP SEM at 200 times magnification.

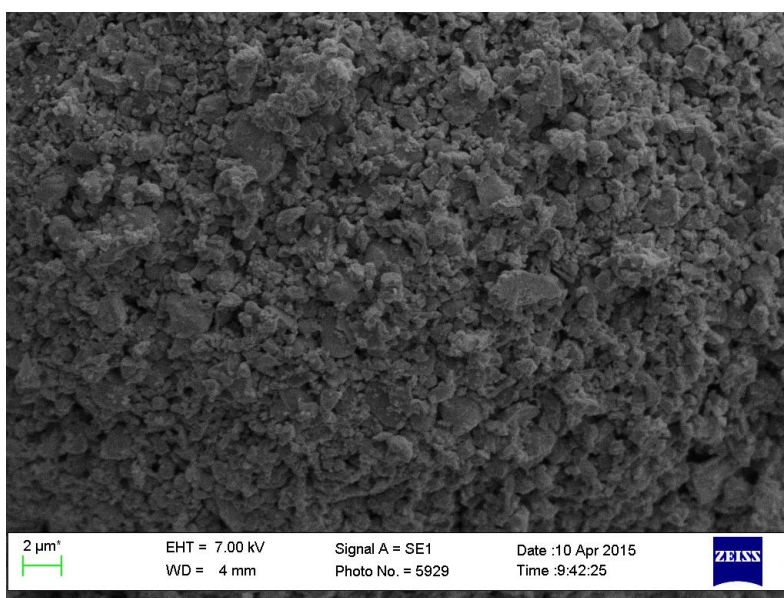


Figure 5.4: SEM image of the material sample taken using a LEO 1450VP SEM at 500 times magnification.

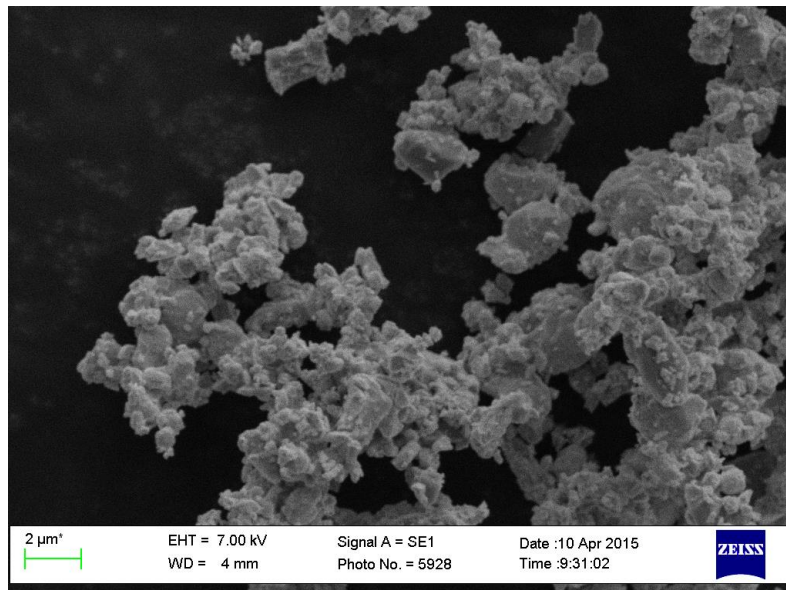


Figure 5.5: SEM image of the material sample taken using a LEO 1450VP SEM at 1000 times magnification.

as that shown in Figure 5.5, after ball milling, since the agglomerates are merely broken up and no other physical alterations are made to the material. The following section presents the results from the laser diffraction analysis.

5.1.3 Laser Diffraction Analysis

The laser diffraction analysis (LDA) is carried out according to the procedure outlined in section 4.2.3.2 on page 62. The LDA output includes a PSD, graphed according to the volume percentage each particle size makes up in the sample. Furthermore, a summary of the arithmetic statistics is provided for the distribution. Finally, a goodness of fit test is done to evaluate the significance of the model fitted to the particle size data obtained.

The LDA requires adjustments in the chosen model parameters during the test. This ensures that the best fit is obtained. To demonstrate, Figure 5.6 on page 79 shows a pronounced spike in the volume frequency percentage (VFP) around $26\mu\text{m}$. A subsequent adjustment in the model parameters identifies this as an anomaly. The second and third tests show little variation in the measurement data which indicates that the model should represent the actual PSD accurately. This is confirmed by analysing the goodness of fit of the final model (corresponding to test three), which is shown on page 6 of the LDA report, presented in Appendix A on page 131. The weighted residual is 0.23%, which indicates a statistically significant model.

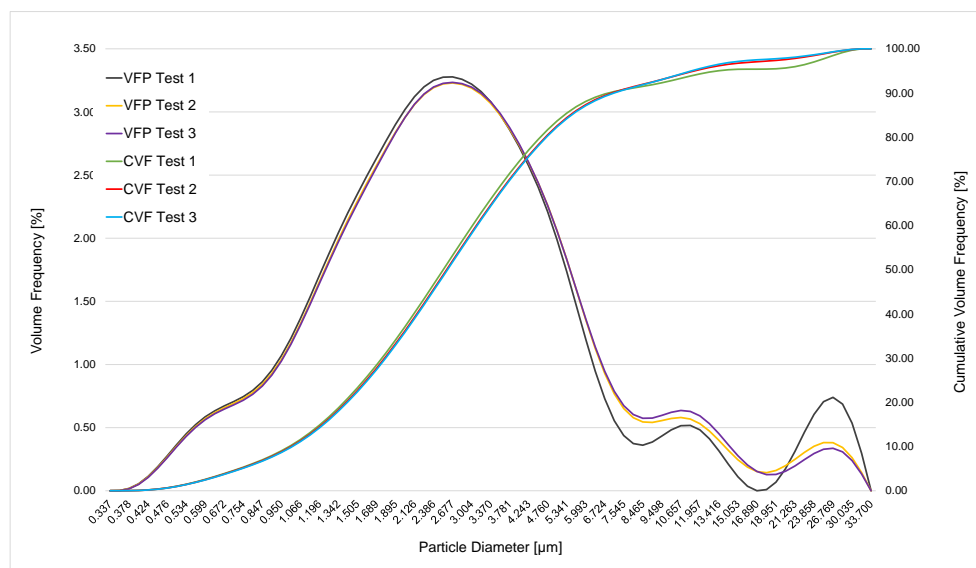
Table 5.1 on page 79 presents the volume distribution arithmetic statistics of the laser diffraction analysis. These are the averaged results for all three tests.

The analysis indicates a mean particle size of $3.9\mu\text{m}$. The mode (or most frequently occurring particle size) is $2.677\mu\text{m}$. Figure 5.6 on page 79 shows the volume

Table 5.1: Volume distribution arithmetic statistics of the material sample analysed by Laser Diffraction Analysis.

Statistic	Value [μm]	Standard Deviation
Mean	3.9	0.134
Median	2.671	0.036
Mode	2.677	0

percentage of the PSD in the sample, for all three tests, along with the cumulative volume percentage of the particle sizes.

**Figure 5.6:** Particle size by volume frequency percentage present in material sample - tests one to three.

The obtained results are averaged to obtain the arithmetic statistics presented in Table 5.1. The results are graphed and presented in Figure 5.7 on page 80. According to the results, 90% of the sample volume has a particle size smaller than 7.319 μm .

The average particle size observable in the SEM images and the results from the LDA agree on the PSD for the material used in this work. The fine grained particles are expected to enable favourable melting activity and subsequent layer formation. The following section presents the results obtained from the single layer sample analysis.

5.2 Single layer sample analysis

In this section the results from the microscope, profilometer, SEM, and statistical analyses are presented. The microscopic analysis results are used to examine the single layer formation process under different parameter value combinations. This is compared to the expected results, determined by the literature review presented

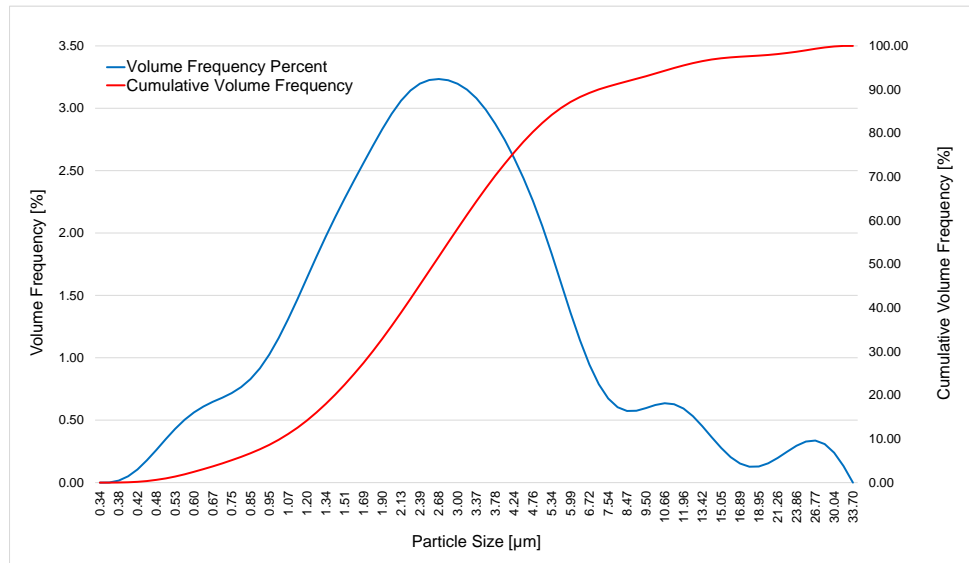


Figure 5.7: Particle size by volume frequency percentage present in material sample - averaged.

in Chapter 3 on page 12. Furthermore, the profilometer results are used to analyse observable trends in the surface and roughness parameters according to changes in the processing parameter values. The SEM sample analysis is used to determine what, if any, observable defects are present as a result of the sintering process, as well as the degree of diffusion present in the sample substrate. Finally, the statistical analysis is used to determine the optimal processing region with reference to the maximum surface height measured for each sample surface.

5.2.1 Microscope image analysis

Microscope images of each single layer sample are taken according to the procedure outline in section 4.2.4.1 on page 64. The resultant images are shown in Appendix E on page 152. Each single layer sample is shown at 1.25 and 3.20 times magnification. When viewed separately, a range of observable phenomena are immediately evident. These phenomena are classified according to:

1. Protrusion formation,
2. Shrinkage,
3. Scan track formation,
4. Balling, and
5. Cracking.

5.2.1.1 Protrusion formation

Almost every sample exhibits the formation of protrusions on the sample surface. The degree to which these protrusions form on a sample layer is dependent on the parameter values chosen.

The protrusion formation observable in the sample layers are explained by the near-excessive volumetric energy densities (VED) developed in the powder bed during processing. VED relates the laser power, scan speed, layer thickness, and hatch spacing into a single mathematical expression which describes the combined effect each of these parameters have on the formation of single layers. In this work, since the layer thickness is held constant and both laser power and scan speed have only two levels, the hatch spacing becomes the dominant factor in explaining the differences in the observable phenomena for each sample. Again, VED is calculated by (Gu and Shen, 2009; Gu *et al.*, 2012; Ciurana *et al.*, 2013):

$$VED = \frac{P}{vdh} \quad (5.2.1)$$

A high VED value is required to initialise melting activity in the powder bed. However, this should be limited to just above the material's melting temperature. Lower values of hatch spacing increases the VED (i.e. the temperature) developed in the powder bed. As stated in literature, increasing the temperature far beyond the melting temperature of the material will result in evaporation of the powder (Hauser *et al.*, 2003; Campanelli *et al.*, 2010). The rapid expansion of the evaporating particles generates an overpressure on the melted zone which results in material ejection from the powder bed. Since SLM is a rapid melting and solidification process, the ejected material is trapped on the surface of the sample by the non-ejected, solidifying material. As hatch spacing increases, the VED decreases. This corresponds to an observable decrease in the presence of protruding powder particles. This trend can be seen in Figure 5.8 on page 82 to Figure 5.11 on page 85. The protrusions appear as dark spots in the images. As hatch spacing increases, the amount of visible dark spots diminishes. Also noticeable is the decrease in the average VED as hatch spacing increases. This confirms the expected results, based on the literature reviewed. The measured height of the protrusions are presented and discussed in section 5.2.2 on page 89.

A further explanation for the formation of the protrusions in the samples is held in the theory behind spheroidisation (or "balling"). The following section discusses protrusion formation according to this phenomenon.

5.2.1.2 Balling

As stated in literature, balling is the formation of a series of small metal spheres along a scan track during the melting process. These spheres form as a result of the molten material's tendency to reduce the surface free energy (Li *et al.*, 2010; Zhang *et al.*, 2012b). This is noted to be a very undesirable process which could hinder subsequent layer deposition and lead to porosity formation in final parts, reducing the mechanical properties required by the intended part application (Tolochko *et al.*, 2004; Gu and Shen, 2007).

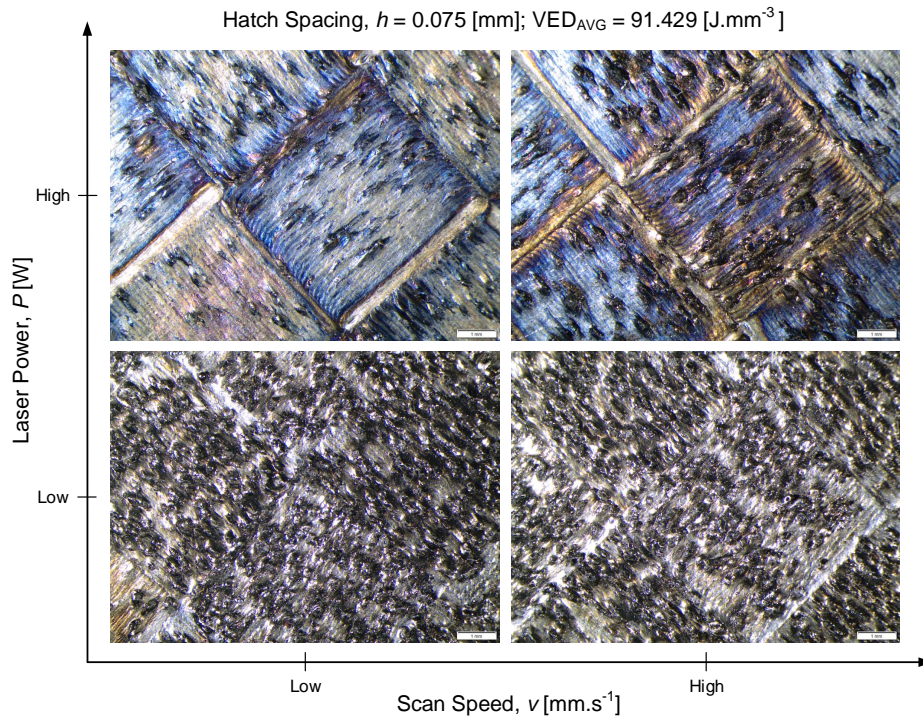


Figure 5.8: Single layer sample images corresponding to E13-E16 in Table 4.2.

The formation of the so-called protrusions (as presented in the previous section) can also be explained as the formation of these isolated metal spheres. As a track is scanned, insufficient liquid wetting of the particles and substrate, coupled with a high surface free energy, leads to balling. This can be seen for every sample produced in this work, with sample E7 (corresponding to $P = 200W$, $v = 100mm.s^{-1}$, and $h = 0.150mm$) showing the least amount of balling (or protrusion formation).

At high scan speeds, balling becomes more noticeable for both low and high laser power. The material is rapidly melted and subsequently cooled due to the rapid scan speed. This hinders successful wetting of the underlying layer and the tendency to reduce the surface free energy dominates the behaviour of the molten material, thus forming these spheres. Gu and Shen (2007) called this ‘shrinkage-induced balling’ and attributed it to a significant capillary instability effect. Of the three balling mechanisms identified (i.e. first line scan balling, shrinkage-induced balling, and self-balling) shrinkage-induced balling and self-balling corresponds with the work presented here. This suggests that lower scan speeds yield more favourable results.

The samples show a tendency to experience greater amounts of balling formation for lower hatch spacing values. This follows when one considers the definition of self-balling presented by Gu and Shen (2007). In their work, they explain that the binder material melts incongruently over a range of temperatures and will exhibit a higher degree of melt activity as the temperature increases above the solidus point. The excessive liquid formation is accompanied by a prolonged liquid lifetime (resulting from a higher energy input into the powder material) which leads to considerably lower melt viscosity. This yields a higher degree of superheat of the low melting phase, enhancing the Marangoni effect. This forms a large amount of individual

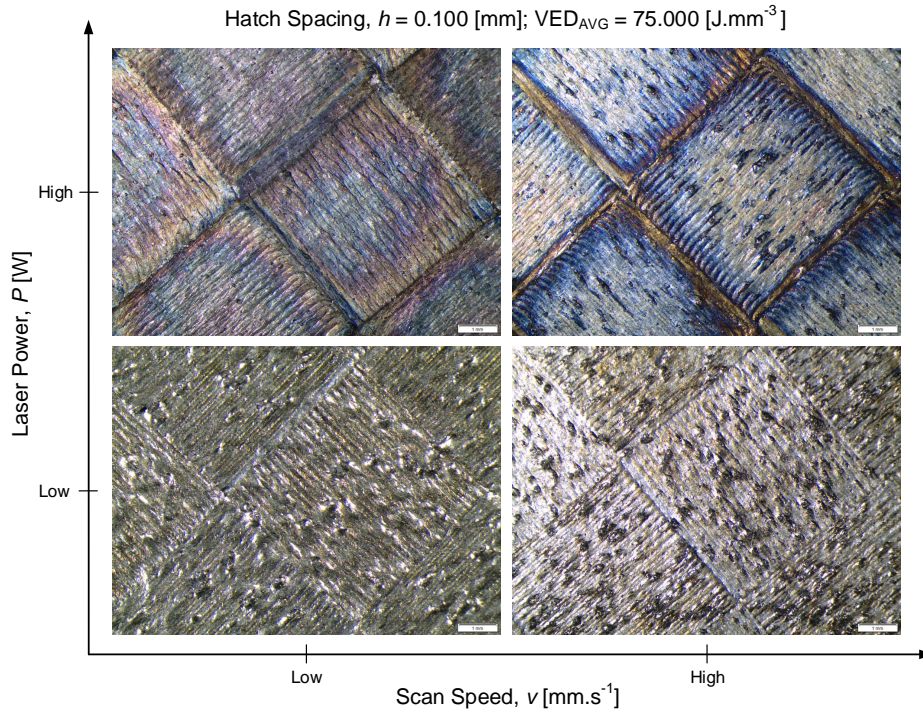


Figure 5.9: Single layer sample images corresponding to E1-E4 in Table 4.2.

balls (or spheres) with the associated diminishing surface energy. At lower hatch spacing values, the amount of thermal energy in the sample layer will be higher due to a larger concentration of laser energy per unit area, thus leading to the formation of individual balls according to the mechanisms described here. This suggests that high values for hatch spacing yield more favourable results.

A contrary observation to those presented by Tolochko *et al.* (2004) and Gu and Shen (2007) in these samples lies in the level of balling formation at high laser power levels. Their findings reported higher balling at parameter combinations with high laser power. In this work, however, at high laser power balling is notably less pronounced than for low laser power values. This, coupled with high hatch spacing values produces significantly better scan tracks showing less balling or defect formation. Parameter combinations with low laser power values show a higher concentration of balling (or protrusion) formation which, as stated previously, is an undesirable result.

These results suggest that parameter combinations of low scan speed, high hatch spacing, and high laser power will result in favourable single layer formation. Of course, there still exists the possibility of microscopic defect formation (such as micro-cracks and poor microstructure development during layer scanning) which requires further investigation. The following section discusses the observable shrinkage phenomena in the test samples produced in this work.

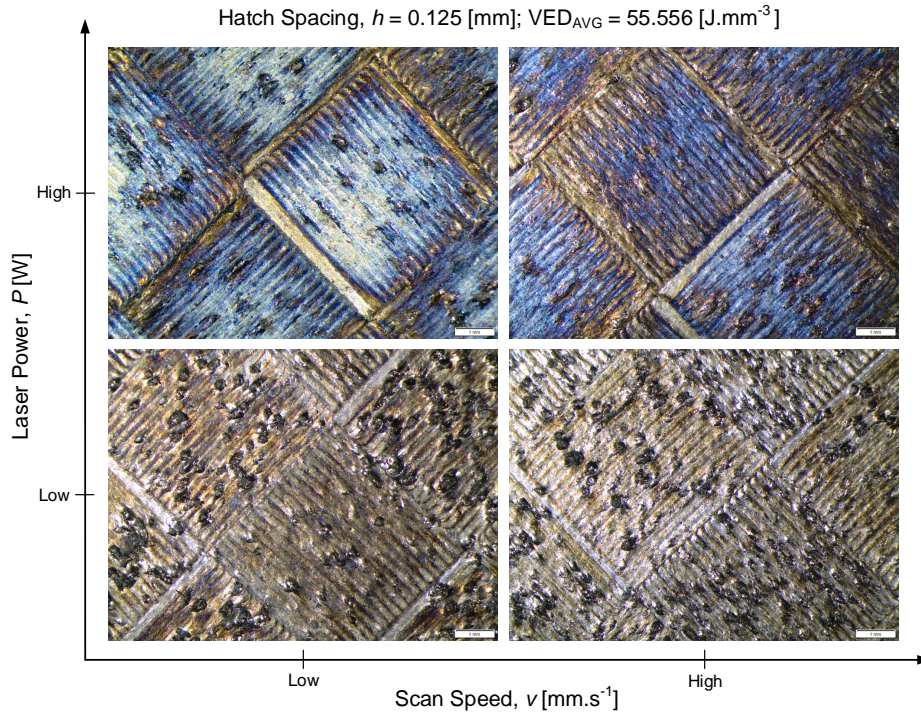


Figure 5.10: Single layer sample images corresponding to E9-E12 in Table 4.2.

5.2.1.3 Shrinkage

The single layer samples in this work exhibit localised shrinkage near the island edges. This is explained by noticing that the scan tracks at the island edges are rescanned when an adjacent island edge is scanned. As a scan track is rescanned, it undergoes another cycle of thermal expansion, particle rearrangement, and subsequent shrinkage. This process continues as the scan tracks are remelted and reaches a plateau once particle rearrangement is no longer necessary or possible. Figure 5.12 on page 86 shows several samples demonstrating the occurrence of shrinkage at the island edges. The broad bands (indicated in the figure) are formed by the rescanning of track-ends orientated perpendicular to the remelting track. This forms a melted area that appears as a single scan track. The resultant shrunken scan track holds negative implications for the intended final part.

It should be noted that areas exhibiting shrinkage do not appear uniformly across any specific sample surface. The width, length, relative shrinkage, and even placement of each area varies with the associated process parameter values for a given sample. This agrees with the work presented by Senthilkumaran *et al.* (2009). In some sample sets, the amount of observable shrinkage increases as hatch spacing and scan speed increases. Other influences, such as layer thickness and build platform temperature remain unexplored in this work.

The occurrence of shrinkage, specifically at localised regions on a single layer, has the undesirable effect of encouraging porosity formation. Where shrinkage is pronounced, a uniformly deposited powder layer will form a thicker layer. The incident laser energy may not penetrate deep enough into the powder layer, specifically

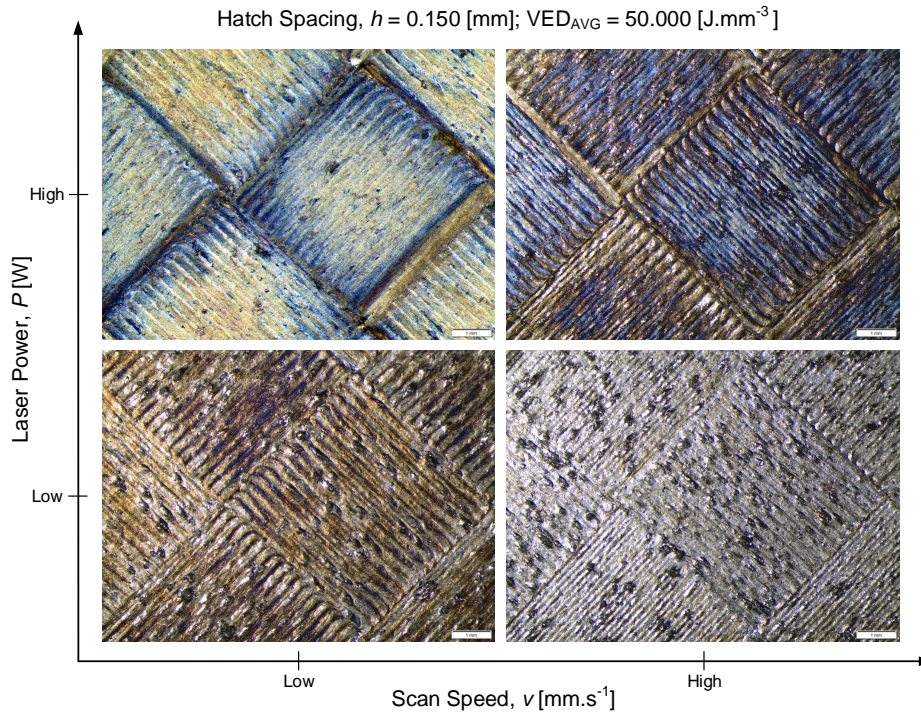


Figure 5.11: Single layer sample images corresponding to E5-E8 in Table 4.2.

where the powder is significantly thicker, which would result in unmelted powder being trapped beneath the melted layer. Unmelted powder has markedly lower densities as opposed to the bulk material, which alters the mechanical properties of the built part. This agrees with work presented by Kruth *et al.* (1996).

Furthermore, as unmelted powder is trapped between melted layers, unstable bonds are formed between these layers and delamination has a higher probability of occurring. This was observed in several trial-and-error based experiments using a straight grade WC-12wt.% Co material having a particle size distribution (PSD) of $-45/+10\mu m$ and a spherical particle shape. The nature of the material allows for autonomous deposition, thus enabling the production of multi-layer samples. After approximately 20 layers (having a thickness of $50\mu m$ each) delamination occurred and catastrophic failure of the process resulted. Figures 5.13 and 5.14 shows photographs of the trial-and-error experiments, illustrating the areas of delamination and the parts that were completely ripped from the build platform by the scraper blade during powder deposition. These experiments are presented as a concept illustrator and is therefore not formally reported in this work.

The occurrence of catastrophic process failure by delamination, where the scraper blade hits an elevated edge of a part, was extensively studied by Yasa *et al.* (2009). The parts produced here exhibited the same formation of elevated edge formation at both the island and part contours. It is understood as a consequence of surface tension. That is, a scan track tends to assume a form where surface tension is a minimum and its volume is at a maximum (i.e. a rounded cross section in a cylindrical shape). The first scan line is surrounded by unmelted powder particles having a very low thermal conductivity. As the melt pool shape changes, more

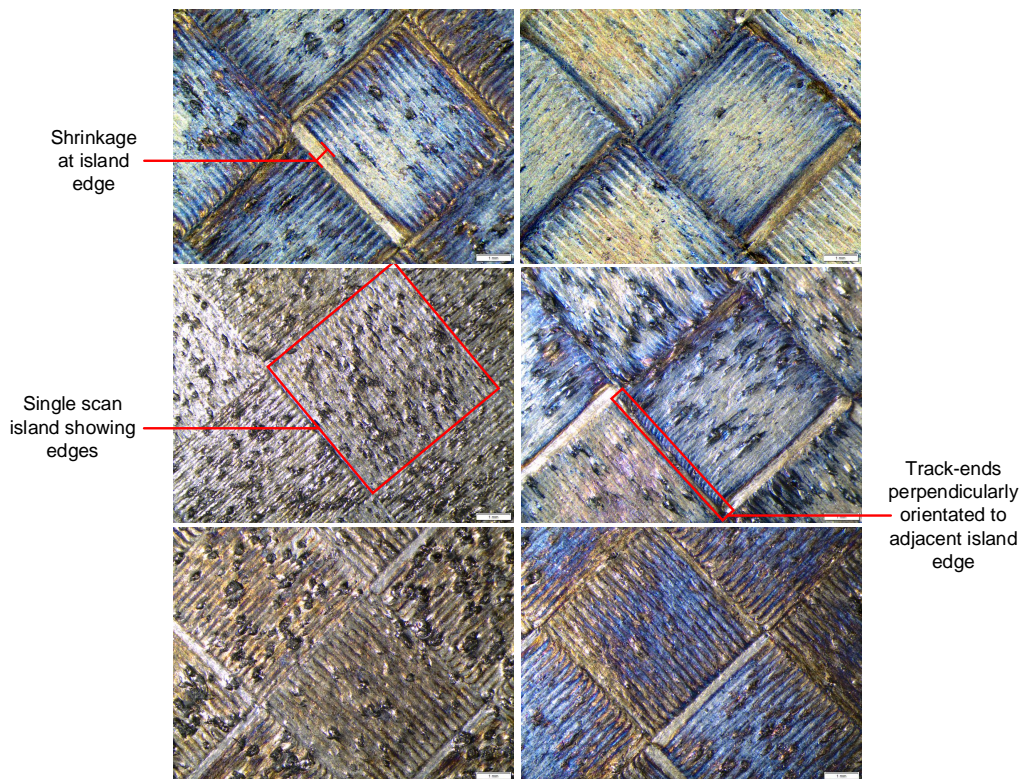


Figure 5.12: Single layer samples exhibiting localised shrinkage at island edges.

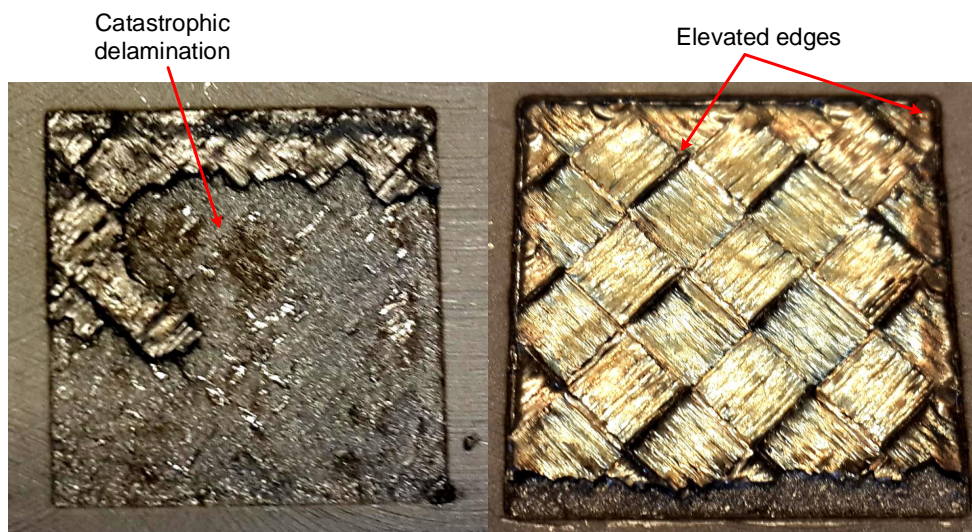


Figure 5.13: Failed WC-12wt.% Co sample production showing delamination as the cause of failure. (First experiment).

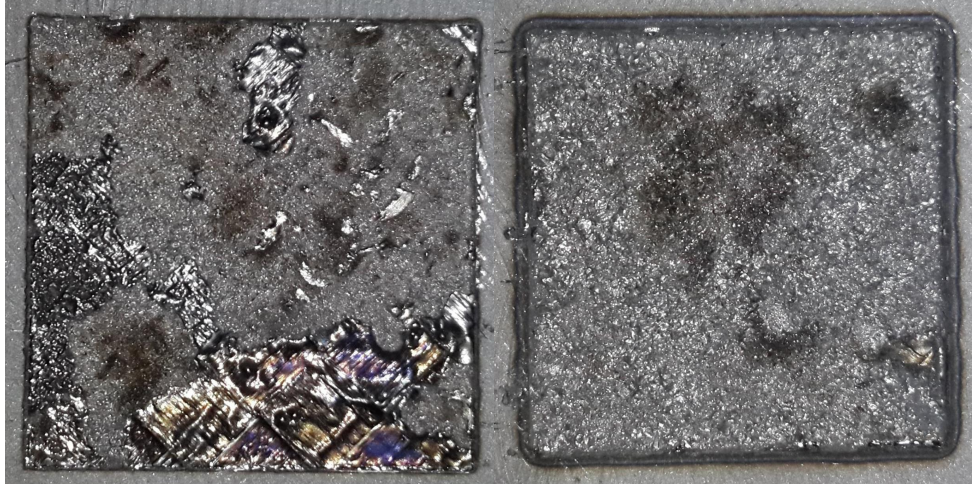


Figure 5.14: Failed WC-12wt.% Co sample production showing delamination as the cause of failure. (Second experiment).

powder particles are drawn towards the melt volume thereby increasing the melt pool and altering the solidification rate. This results in significantly lower amounts of powder available for subsequent scan tracks. The result is the formation of lower subsequent scan tracks. This phenomena is further discussed in the following section.

The single layer samples produced in this work exhibit similar, localised tendencies to form elevated edges at both island and part contours. This is explained according to the mechanisms outlined above and in the work presented by Kruth *et al.* (2007); Shiomi *et al.* (1999); Childs *et al.* (2005); Das (2003); DebRoy and David (1995). This, however, is limited and localised shrinkage is much more evident. The elevated edges produced during the trial-and-error based experiments are explained by noticing that as each layer is scanned onto the previous one, the substrate changes from the steel baseplate to a WC-Co substrate. The choice in substrate will have a significant influence in the powder consolidation behaviour during SLS or SLM. This follows since the thermal conductivity and coefficient of thermal expansion for a steel substrate will differ (often significantly) from the SLM material being melted.

The achievable single layers produced directly onto the steel baseplate, in this work, will therefore not demonstrate the pronounced shrinkage and deformation activity seen in samples produced consisting of multiple layers. This requires further investigation and does not form part of the scope of this work.

5.2.1.4 Scan track formation

Several mechanisms play a role in scan track formation. Hatch spacing, scan speed, and laser power have been found to be the dominant factors affecting how well an individual scan track is formed. Work presented by Pham and Gault (1998); Gu and Shen (2009); Yadroitsev *et al.* (2007a, 2010); Gu *et al.* (2012), among others, supports this statement.

In this work it is observed that an increase in hatch spacing results in better

defined scan tracks. This follows since an increase in hatch spacing decreases the percentage overlap between two adjacent scan tracks. Not only does increased hatch spacing lead to the isolation of individual scan tracks, it reduces the heat sink effect observable in single layer formation during SLM.

As successive tracks are scanned, the percentage overlap will determine how much laser energy is dissipated into the substrate as a function of substrate denudation, previous scan tracks, and the raw powder material (Badrossamay and Childs, 2007; Yadroitsev and Smurov, 2011). To demonstrate, a track width of $150\mu\text{m}$ (corresponding to the laser spot diameter) combined with a hatch spacing of $75\mu\text{m}$ will have a 50% overlap. The absorbed laser energy reheats the previously melted layer, as well as the substrate, and conducts the heat towards the unmelted powder. As a result of this effect, and substrate denudation (i.e. the reduction of the substrate surface), the second scanned track appears lower than the first and the powder consolidation zone diminishes. The occurrence of this phenomenon relates to, and partially explains, the shrinkage phenomena discussed in the previous section.

As stated, by increasing the hatch spacing this heat sink effect is reduced. The formation of individualised scan tracks promote the formation of a uniform single layer. This is necessary for part stability and corresponding increased part density, which affects the mechanical properties associated with the final part. This suggests, based on the experimental results observed here, that single layers with higher hatch spacing values ($>100\mu\text{m}$) yield more favourable results.

In samples with lower hatch spacing values some obvious defects are visible. These include pitting as a function of particle evaporation at low hatch spacing (see section 5.2.1.1), balling as a result of low hatch spacing and moderate to high scan speed, and cracking as a result of low hatch spacing and high power. The formation of cracking is discussed in the following section.

5.2.1.5 Cracking

Limited crack formation is visible in the single layers formed in this work. This is ascribed to the temperature gradient mechanism (TGM), as explained in work presented by Kruth *et al.* (2004). Again, the TGM describes material behaviour under sintering conditions, as noted in literature. A steep temperature gradient develops due to the rapid heating of the upper surface by the incident laser energy and the slow heat conduction into the lower surface layers. A further reduction in material strength, due to increased temperature, also occurs. The associated material yield stress is lowered, the top layers become plastically compressed, and a bend moment towards the laser beam develops. Similarly, the underlying layers experience a similar temperature gradient with each new sintered layer. The TGM stresses bend the consolidated layers towards the laser beam, causing distortion and part failure by way of delamination and cracking, as explained in literature.

Again, Figure 3.11 on page 46 illustrates the process described above. This continual cycle of thermal expansion and subsequent shrinkage produces cracks in the scanned layers. Other authors, such as Gu *et al.* (2012), describe this process according to hot and cold cracking mechanisms, as stated in the literature review presented in this work. The cold cracking mechanism accurately describes the process observed here. The macroscopic cracks appear after solidification as a result of low material

ductility (which is attributable to the low binder content in this material) and form along grain boundaries as a result of residual stresses present in the scanned layer. The cracks are also visible along scan track boundaries for high hatch spacing values. The low binder content, the addition of mixed crystals aimed at increasing hardness and reducing grain growth, and the tempering effect induced in the scanned layers increases the brittleness of each single layer which leads to a higher probability of crack initiation and propagation. Tempering is understood to be the process of hardening metal by raising the temperature of the metal high enough to cause microstructural changes, and subsequently cooling the metal to room temperature. This cooling process can occur rapidly or gradually, depending on the desired final microstructure.

From the discussion presented here, it is clear that differentiations in the laser power, scan speed, and hatch spacing values influence the formation of single layers quite significantly, leading to protrusion formation, balling, shrinkage, differences in scan track formation, and cracking. It is found that hatch spacing has the greatest observable effect on these phenomena. The following section presents the results obtained from the profilometer analysis carried out in this work.

5.2.2 Profilometer analysis

The surface and roughness profile analyses are carried out according to the methodology described in section 4.2.4.2 on page 65. The complete surface profile reports for each single layer sample are presented in Appendix F on page 159. Excerpts from the roughness profile analysis for each single layer sample is presented in Appendix G on page 176. A discussion of the results follows.

5.2.2.1 Surface profile

The surface profile of each single layer sample is characterised by a set of surface parameters. These parameter values are calculated according to ISO Standard 25178.

Table 5.2: Surface parameters for benchmark sample. ($P = 180W$, $v = 800mm.s^{-1}$, $h = 0.105mm$)

Parameter	Value	Unit
S_q	0,354	μm
S_{sk}	0,0126	<i>Dimensionless</i>
S_{ku}	3,21	<i>Dimensionless</i>
S_p	1,25	μm
S_v	1,23	μm
S_z	2,48	μm
S_a	0,278	μm

Table 5.2 on page 89 presents the surface parameter values recorded for the benchmark single layer. The S_q , S_a , S_p , S_v , and S_z parameters are used in a trend analysis to identify what the observable phenomena in surface formation are, given a specific process parameter set. S_a represents the arithmetic mean height of the

sampling area. For the benchmark surface this is equal to $0.278\mu\text{m}$, as reported in Table 5.2. This is a significantly low value, indicating a limited presence of surface protrusions, scan line balling, and/or elevated edges on the layer surface. This is to be expected since the parameters used to form this layer have been optimised to yield a favourable result in terms of subsequent layer formation.

The S_a parameter, however, has a lower statistical significance in comparison to the S_q parameter, which is the standard deviation associated with the height of the surface deviations. For the benchmark surface $S_q = 0.354\mu\text{m}$. This value is slightly higher than the mean height, however it is still significantly low and corroborates the theoretical optimal result associated with successful single layer formation, which is a zero deviation with a uniform surface. The highest peak ($S_p = 1.25\mu\text{m}$) and the lowest valley ($S_v = 1.23\mu\text{m}$), as well as the associated maximum height ($S_z = 2.48\mu\text{m}$) of the surface provides a good comparative guideline against which the single layer samples produced in this work may be evaluated. The best sample is expected to have a similar value distribution, however elevated, as the benchmark surface.

The dimensionless parameters, S_{sk} and S_{ku} , indicate the skewness and kurtosis of the surface profile, respectively. The skewness describes the shape of the topography height distribution. A symmetrical topography, associated with a surface with a random (or Gaussian) height distribution, has a skewness value of zero. This parameter, however, is strongly influenced by isolated peaks and/or valleys and cannot distinguish if the profile spikes are evenly distributed above or below the mean plane. For the benchmark sample the low S_{sk} value indicates that the surface height approximately follows a Gaussian distribution, having a symmetrical topography. This is a desired trait to ensure that uniform powder layers can be deposited onto previously sintered layers during SLM processing.

The kurtosis value is a measure of the sharpness of the surface height distribution. This is a strictly positive value, characterising the spread of the height distribution. This parameter detects whether the profile spikes are distributed evenly, as well as provides a measure of the spikiness of the sample area. A high kurtosis value indicates a spiky surface, whereas a low kurtosis value indicates a bumpy surface. A surface having a Gaussian height distribution will have a kurtosis value equalling three. For the benchmark sample, the kurtosis value confirms the approximate Gaussian height distribution indicated by the S_{sk} value. Since the S_{ku} value is slightly higher than three, the surface is more spiky than bumpy. This is expected of SLM surfaces, owing to the powder consolidation phenomena observable during SLM processing (Glarion *et al.*, 2001; Yadroitsev *et al.*, 2007a; Yasa *et al.*, 2009; Yasa and Kruth, 2011).

Figure 5.15 on page 91 shows the 3D surface profile measured using the TKU300 probe and the HommelMap Basic software. The surface has a sample area of $4.8 \times 10\text{mm}$. The figure shows elevated edges along the island edge intercepts and the highest peaks correspond to these edges. Furthermore, some pitting (or valley formation) is visible, corresponding to the lowest points on the surface. These valleys form along the island edges as a result of shrinkage, similar to that observed for the single layer samples produced from the WC-6.6wt.% Co material, reported in section 5.2.1.3.

After the data are analysed it is determined that experimental samples E5 and E7 produced the best results, closely matching the height parameter values associated

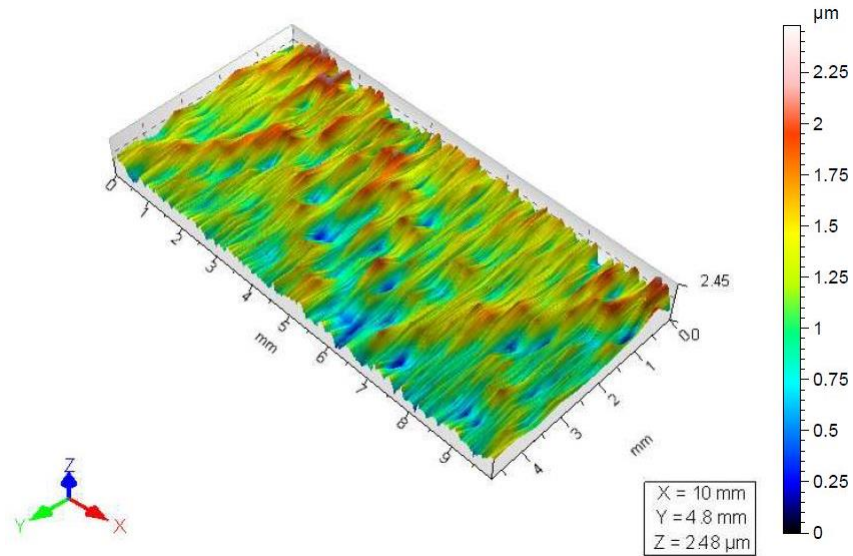


Figure 5.15: 3D surface profile for benchmark sample. ($P = 180W$, $v = 800mm.s^{-1}$, $h = 0.105mm$)

Table 5.3: Surface parameters for single layer sample E5. ($P = 100W$, $v = 100mm.s^{-1}$, $h = 0.150mm$)

Parameter	Value	Unit
S_q	0,478	μm
S_{sk}	1,21	<i>Dimensionless</i>
S_{ku}	6,56	<i>Dimensionless</i>
S_p	3,7	μm
S_v	1,04	μm
S_z	4,75	μm
S_a	0,362	μm

with the benchmark sample.

Table 5.3 on page 91 presents the surface parameter values for sample E5. The arithmetic mean surface height, S_a , is $0.084\mu m$ larger than the benchmark sample value and the standard deviation, S_q , is $0.124\mu m$ larger. These values, however, are rather small in comparison to the other experimental samples and indicates, based on surface parameters alone, that it is possible to produce a uniform single layer using SLM and a WC-6.6wt.% Co cemented tungsten carbide. The degree to which this layer will enable subsequent material deposition and consolidation is still uncertain and requires further research, focusing on the production of multi-layered samples.

The skewness and kurtosis parameters (S_{sk} and S_{ku}) indicate that the surface exhibits a largely spiky characteristic (corresponding to the high kurtosis value) and is a-symmetrical in its topography height distribution (corresponding to the positive skewness value). The positive S_{sk} value indicates that the bulk of the material lies beneath the mean line, also called a positive skew. Furthermore, it is clear that the

surface does not exhibit a Gaussian height distribution as is expected from a optimal process parameter set (according to the benchmark results).

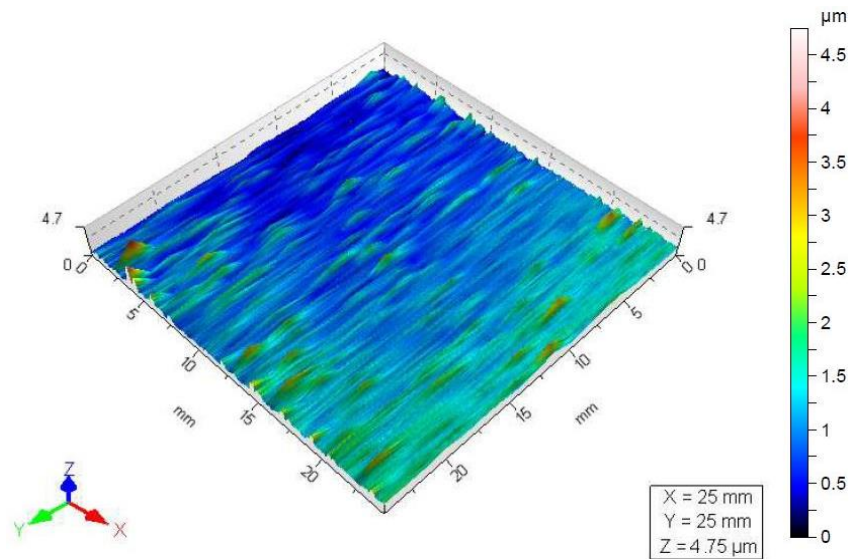


Figure 5.16: 3D surface profile for experiment sample E5. ($P = 100W$, $v = 100mm.s^{-1}$, $h = 0.150mm$)

Figure 5.16 on page 92 shows the 3D surface profile of experiment sample E5. It can be seen that there are isolated peaks present on the sample surface. This greatly affects the skewness parameter, as stated previously. It is also clear that a positive skew can be expected since the bulk of the material lies below the mean line (corresponding to the largely blue region on the surface). Furthermore, the large kurtosis value seems reasonable considering the amount of isolated spikes present.

Table 5.4: Surface parameters for single layer sample E7. ($P = 200W$, $v = 100mm.s^{-1}$, $h = 0.150mm$)

Parameter	Value	Unit
S_q	0,741	μm
S_{sk}	0,158	<i>Dimensionless</i>
S_{ku}	2,75	<i>Dimensionless</i>
S_p	2,54	μm
S_v	1,9	μm
S_z	4,45	μm
S_a	0,599	μm

Table 5.4 on page 92 presents the surface parameter values for sample E7. The arithmetic mean surface height, S_a , is $0.387\mu m$ larger than the benchmark sample value and the standard deviation, S_q , is $0.321\mu m$ larger. These values also indicate and verifies, based on surface parameters alone, that it is possible to produce a

uniform single layer using SLM and a WC-6.6wt.% Co cemented tungsten carbide. Again, it remains unclear whether this surface will enable subsequent layer deposition and consolidation. Further research is required that focuses on multi-layer accretion using SLM and a tool grade cemented tungsten carbide powder. It does, however, also confirm that more than one parameter set may be used to produce favourable results (in terms of single layer production), thereby affording flexibility to the production process.

The skewness and kurtosis parameters (S_{sk} and S_{ku}) indicate that the surface contains limited and isolated spikes. This corresponds to the relatively low S_{sk} value. Furthermore, the surface is predominantly symmetrical in its topography height distribution, also corresponding to the positive skewness value. It is clear that the surface exhibits an approximately Gaussian height distribution, which is expected from an optimal process parameter set (according to the benchmark results). This follows from the S_{ku} value, which is close to three.

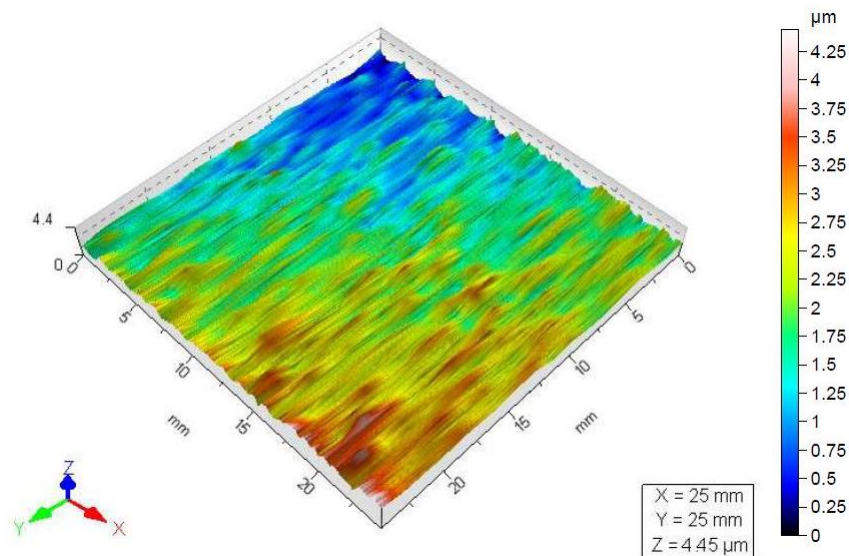


Figure 5.17: 3D surface profile for experiment sample E7. ($P = 200W$, $v = 100mm.s^{-1}$, $h = 0.150mm$)

Figure 5.17 on page 93 shows the 3D surface profile of experiment sample E7. It can be seen that there are isolated peaks and valleys present on the sample surface, located in opposite corners. However, the surface exhibits an even distribution throughout the sample area which could explain the favourable S_{sk} and S_{ku} values. Nonetheless, this is a good result and demonstrates the capability of a SLM process to produce uniform single layers from a tool grade cemented tungsten carbide.

It can therefore be concluded that although experiment sample E5 has both a lower average surface height and standard deviation than experiment sample E7, it does not demonstrate the desired properties associated with a uniform surface layer. The parameter set corresponding to experiment sample E7 results in the desired surface properties and is determined to be the best result.

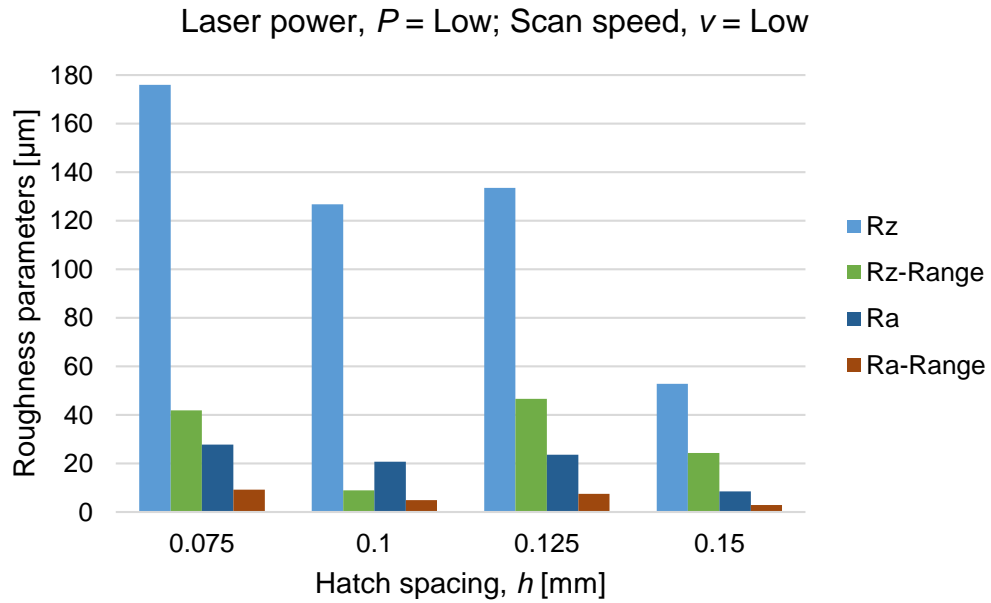


Figure 5.18: Roughness parameter histogram for a low scan speed and low laser power combination.

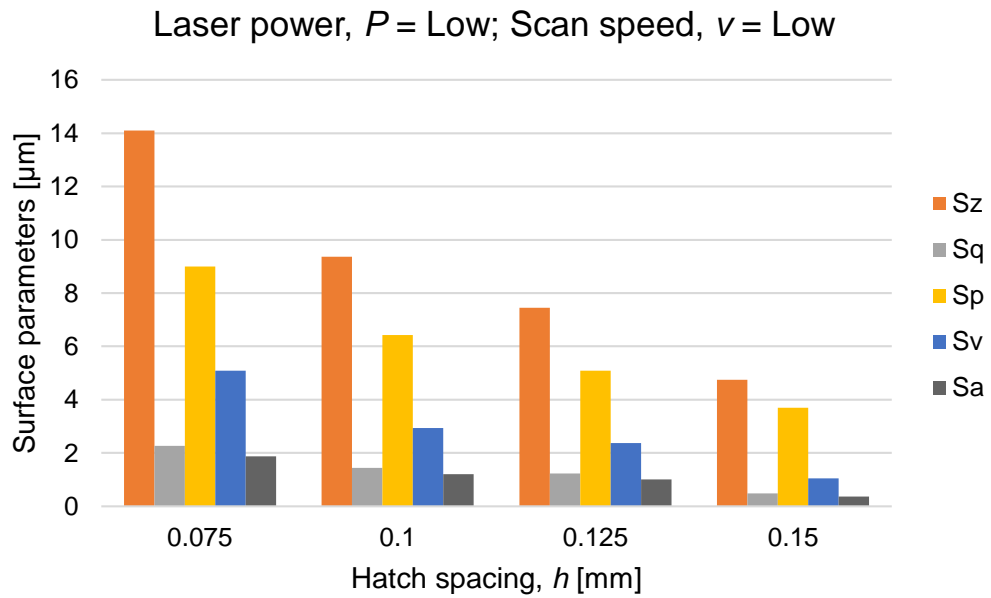


Figure 5.19: Surface parameter histogram for a low scan speed and low laser power combination.

An analysis to determine the observable trend in the single layer formation is carried out by graphing both the roughness and surface parameters according to each parameter set. That is, according to high/low combinations of laser power and scan speed corresponding to the four different hatch spacing values used in this work.

Figures 5.18 and 5.19 on page 94 presents the surface and roughness profile parameters, graphed for a low speed and low laser power combination according to each hatch spacing value, respectively. The trends exhibited here corresponds to experiment samples E1, E5, E12, and E13. The most favourable result (i.e. sample E5) corresponds to $h = 0.150mm$.

It is clear from Figure 5.19 that the surface parameter values decrease as hatch spacing increases. This corresponds to a reduction in surface protrusion formation, excessive balling, and the occurrence of elevated edges at the island intercepts and sample contours. Also, the occurrence of valley formation (i.e. shrinkage) diminishes as hatch spacing increases, corresponding to the reduced overlapping which causes thermal expansion and contraction, leading to shrinkage. These results are explained by, and subsequently corroborates, the results and discussions reported in section 5.2.1 on page 80.

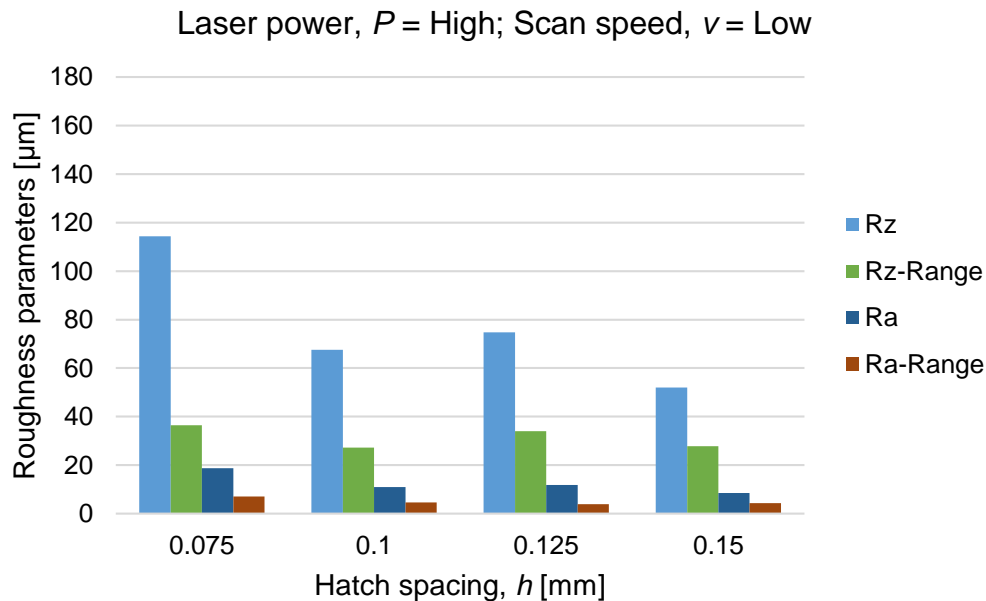


Figure 5.20: Roughness parameter histogram for a low scan speed and high laser power combination.

Figure 5.20 and 5.21 on page 95 presents the surface and roughness profile parameters, graphed for a low speed and high laser power combination according to each hatch spacing value. The trends exhibited here corresponds to experiment samples E3, E7, E9, and E16. The most favourable result (i.e. sample E7) corresponds to $h = 0.150mm$.

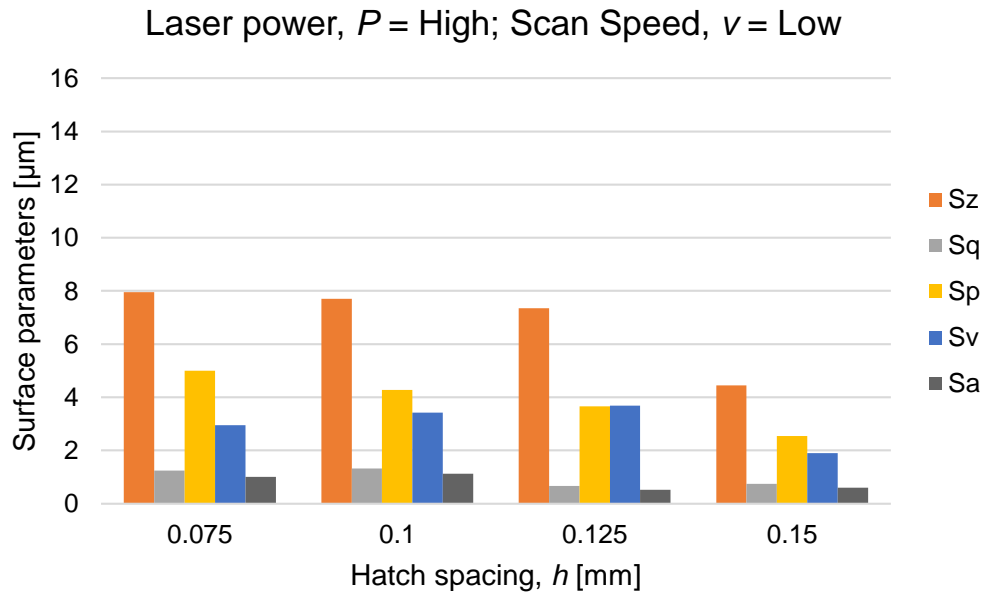


Figure 5.21: Surface parameter histogram for a low scan speed and high laser power combination.

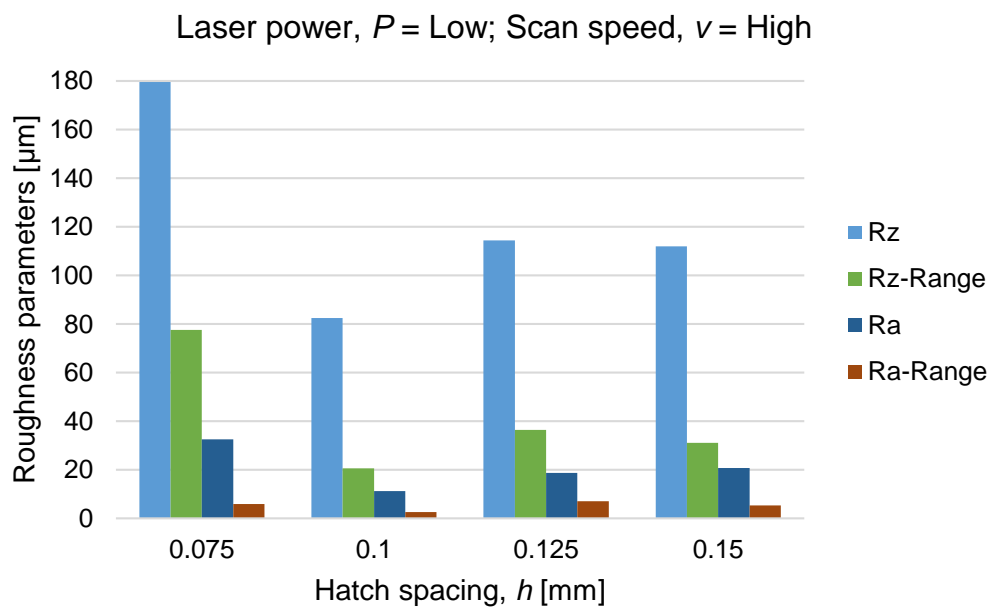


Figure 5.22: Roughness parameter histogram for a high scan speed and low laser power combination.

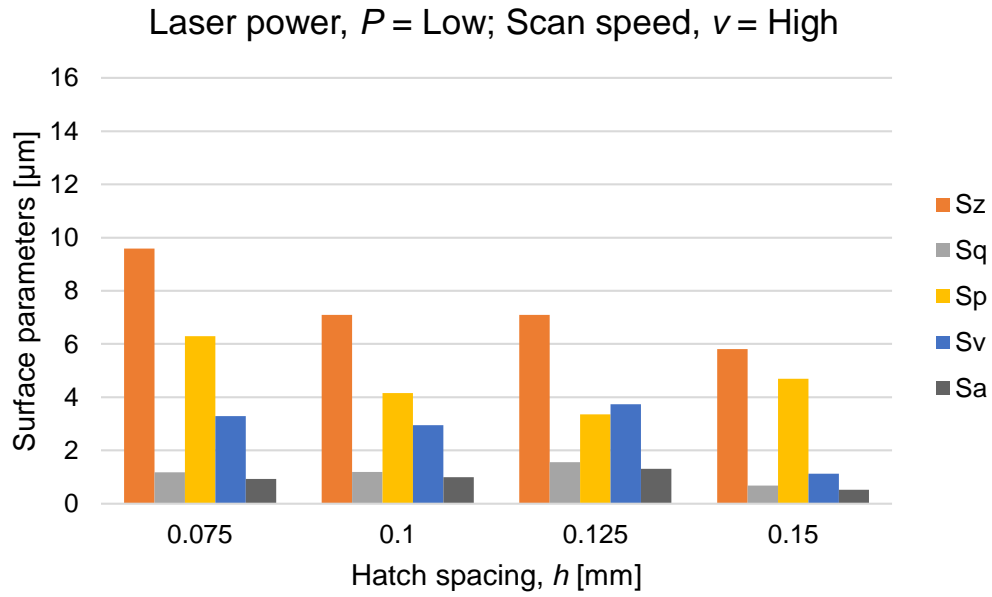


Figure 5.23: Surface parameter histogram for a high scan speed and low laser power combination.

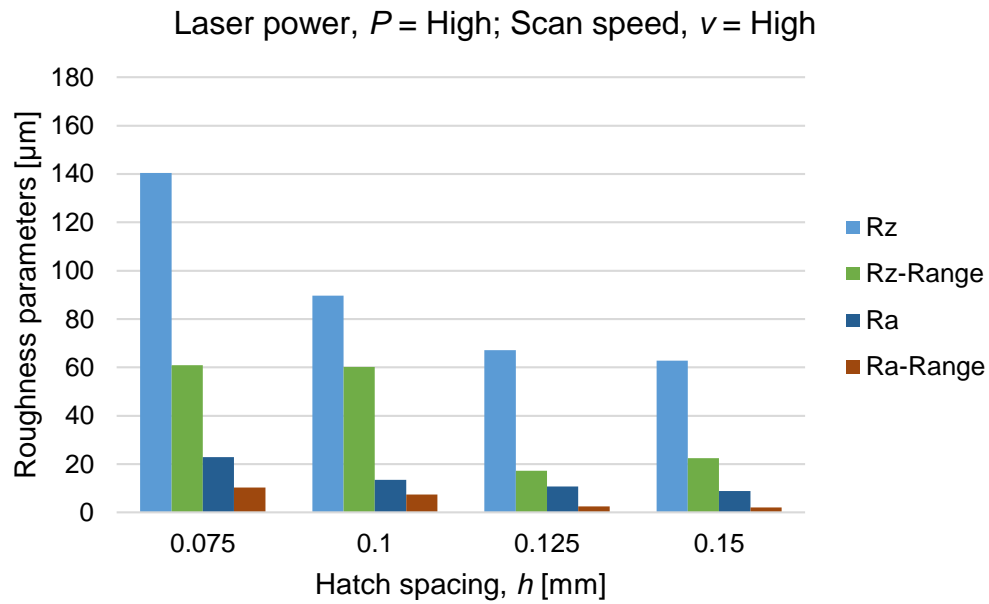


Figure 5.24: Roughness parameter histogram for a high scan speed and high laser power combination.

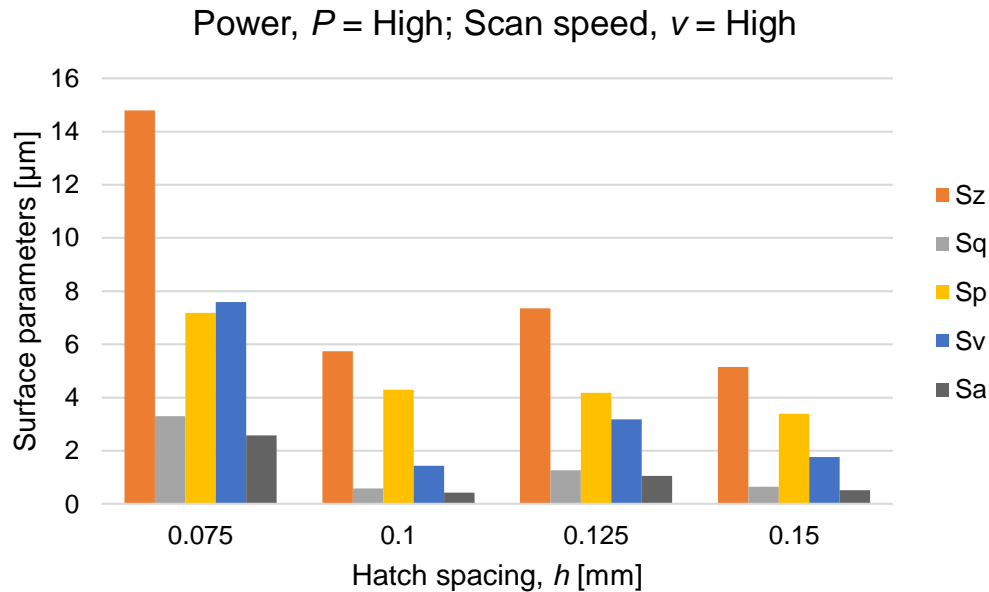


Figure 5.25: Surface parameter histogram for a high scan speed and high laser power combination.

Again it can be seen that the surface parameter values decrease as hatch spacing increases. Furthermore, it can be noticed that the overall values are lower for this parameter set (as opposed to the remaining three), regardless of hatch spacing. Figures 5.22 to 5.25 on pages 96 to 98 presents the trend analysis results (both roughness and surface histograms) for low laser power and high scan speed, and high laser power and high scan speed, respectively. By comparing all four process parameter regions it is clear that of the four combinations of laser power and scan speed, a high laser power and low scan speed produces the best results. This agrees with the reported optimal process windows (Kruth *et al.*, 2005; Li *et al.*, 2010; Zhang *et al.*, 2010, 2012b), and is explained by and corroborates the results and discussions presented in section 5.2.1 on page 80. Furthermore, analysing the effect that hatch spacing has on the parameter values shows that a high hatch spacing yields more favourable results in combination with high laser power and low scan speed.

5.2.2.2 Roughness profile

The roughness profile for each single layer sample, as well as the benchmark sample, is characterised by a set of roughness parameters. These parameters include the arithmetic mean roughness, R_a , the maximum height of the profile, R_z , and the maximum distance between the lowest peak and highest valley, R_{max} (also referred to as R_t). The roughness profiles are generated using a R-profile filter according to ISO Standard 11562, and is generated from the data captured during the surface profile analysis.

Table 5.5 on page 99 presents the roughness parameters, and associated values, for the benchmark sample surface. X_q represents the average value for the corre-

Table 5.5: Roughness parameters for benchmark sample. ($P = 180W$, $v = 800mm.s^{-1}$, $h = 0.105mm$)

Parameters	X_q	Range	S	X_{max}	X_{min}
R_a	11,04	3,9	1,27	12,96	9,06
R_z	59,53	21,14	6,8	69,69	48,55
R_{max}	77,86	16,62	6,47	85,52	68,9

sponding parameter, S is the standard deviation, X_{max} and X_{min} is the maximum and minimum occurring value for the corresponding parameter (respectively), and $Range$ is the difference between X_{max} and X_{min} .

The data in Table 5.5 indicates a low mean roughness with a significantly low standard deviation. However, since the R_a does not differentiate between peaks and valleys, and therefore has a relatively weak information character, the R_z value holds the greatest interest. For the benchmark sample, the average R_z value is $59.53\mu m$ with a range of $21.14\mu m$. A larger range will correspond with a larger standard deviation, and in this case it is 6.8. Therefore, the optimal experimental result will have a similar R_z value with a narrow range, hence a low standard deviation value. The values presented here form the comparative baseline against which experiment samples E5 and E7 are evaluated.

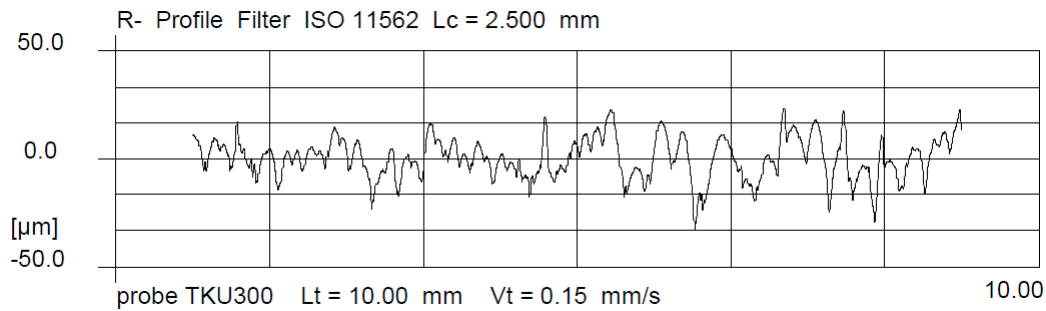
**Figure 5.26:** Roughness profile for benchmark sample.

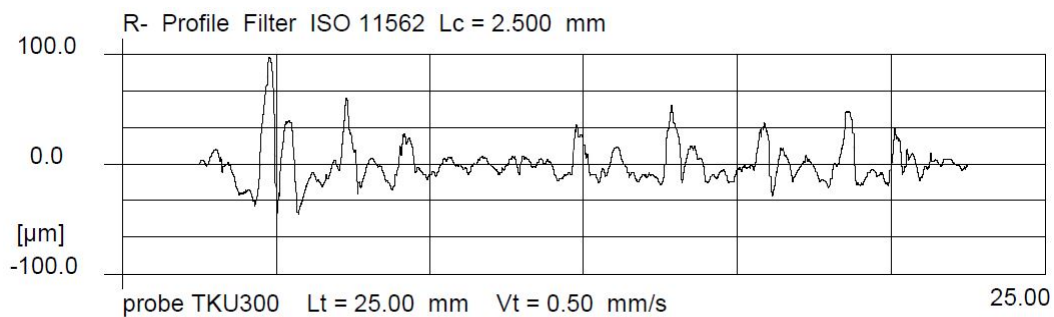
Figure 5.26 on 99 shows the roughness profile measured for the benchmark sample. The profile indicates a relatively uniform roughness profile with low peak and valley magnitudes. This is expected since the process parameters for this material (CL20ES) have been optimised to achieve the best results. It should be noticed, however, that the appearance of the pronounced valleys in the latter half of the profile indicates a limited amount of pitting still occurs even for optimised parameter combinations. This is expected based on the consolidation mechanisms and phenomena observed for the SLM process (see section 5.2.1).

Table 5.6 on page 100 presents the roughness parameters, and associated values, for experiment sample E5. The average roughness is lower than that of the benchmark sample with $R_a = 8.54\mu m$ and a standard deviation of 0.98. Furthermore, the average maximum height is also lower with $R_z = 52.85\mu m$ and a standard deviation of 8.65. Here, the range is larger which results in a larger standard deviation. This

Table 5.6: Roughness parameters for experiment sample E5. ($P = 100W$, $v = 100mm.s^{-1}$, $h = 0.150mm$)

Parameters	X_q	Range	S	X_{max}	X_{min}
R_a	8,54	2,82	0,98	10,18	7,36
R_z	52,85	24,26	8,65	63,08	38,82
R_{max}	82,77	39,54	12,17	102,15	62,61

corresponds a large R_{z-max} which indicates that there are isolated spikes present on the sample surface. This can also be seen in Figure 5.27 on page 100 which shows that there are several, rather large spikes distributed across the profile. Furthermore, the interval on the y-axis in Figure 5.27 has a wider range than the benchmark roughness profile, indicating that the peaks and valleys are far larger.

**Figure 5.27:** Roughness profile for experiment sample E5.

It seems reasonable to suggest, based on the R_a and R_z figures alone, that experiment sample E5 holds better results than the benchmark sample. However, taking into consideration the range and standard deviations of sample E5 with respect to the corresponding R_a and R_z values, sample E5 shows a poorer result.

Table 5.7: Roughness parameters for experiment sample E7. ($P = 200W$, $v = 100mm.s^{-1}$, $h = 0.150mm$)

Parameters	X_q	Range	S	X_{max}	X_{min}
R_a	8,44	4,38	1,45	11,05	6,67
R_z	52,02	27,74	9,38	66,75	39,01
R_{max}	72,24	49,23	16,79	92,52	43,29

A similar observation can be made for experiment sample E7. Table 5.7 on page 100 presents the roughness parameters, and associated values, for experiment sample E7. Here, the R_a and R_z values are lower than that of sample E5 (and therefore the benchmark sample) at $8.44\mu m$ and $52.02\mu m$, respectively. Again, however, both the range and standard deviations for both parameters are larger than that of the benchmark sample

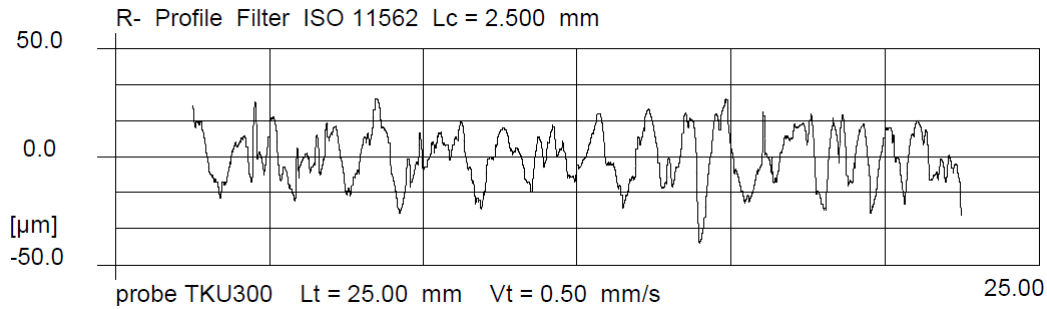


Figure 5.28: Roughness profile for experiment sample E7.

Figure 5.28 on page 101 presents the roughness profile for experiment sample E7. The y-axis for this graph has the same range as the benchmark sample profile, indicating lower peaks and valleys as opposed to sample E5. Also, the peaks and valleys are more evenly and uniformly distributed which would facilitate uniform powder deposition during processing, whereas the spikes in sample E5 could hinder it.

A trend analysis, similar to that for the surface parameters, is carried out for the roughness profile and associated parameters. The R_a and R_z values, as well as the corresponding *Range* values, are graphed according to high/low combinations of scan speed and laser power for all hatch spacing values. These results are shown in Figures 5.18 to 5.24 on pages 94 to 5.24. For each parameter set there is a clear downward trend for the roughness parameter values, indicating improved surface roughness profiles as hatch spacing increases. Also noticeable is that the best results are achieved for combinations of high laser power and low scan speed. This, again, affirms the conclusions drawn in sections 5.2.1 and 5.2.2.1, and is explained according to the discussions presented in section 5.2.1.

Therefore, it can be concluded that experiment sample E7, based on the surface and roughness profile analyses, presents the best results in comparison to the benchmark sample. A combination of high laser power, low scan speed, and high hatch spacing holds the greatest potential to successfully produce uniform single layers from a tool grade cemented tungsten carbide powder material. The following section presents the results obtained from the SEM analysis carried out for samples E5 and E7.

5.2.3 SEM sample analysis

Image analysis of the sample cross sections from single layer samples E5 and E7 revealed discernible defects such as voids and localised shrinkage in the substrate as well as a limited degree of material diffusion across the SLM layer/substrate boundary. Void formation in the substrate increases brittleness in the diffusion area, subsequently increasing the likelihood for catastrophic failure during SLM processing, as witnessed in several trial-and-error experiments (using a WC-12wt.% Co powder) wherein the material deposition mechanism (or scraper blade) caused delamination of the sintered layers from the substrate. Protrusions, formed on the SLM surface, is caught by the scraper blade during the powder deposition step and subsequently

breaks the bond between the accumulated SLM layers and the substrate. Further inspection of the part shards revealed a very brittle material structure that is prone to breaking under moderate force.

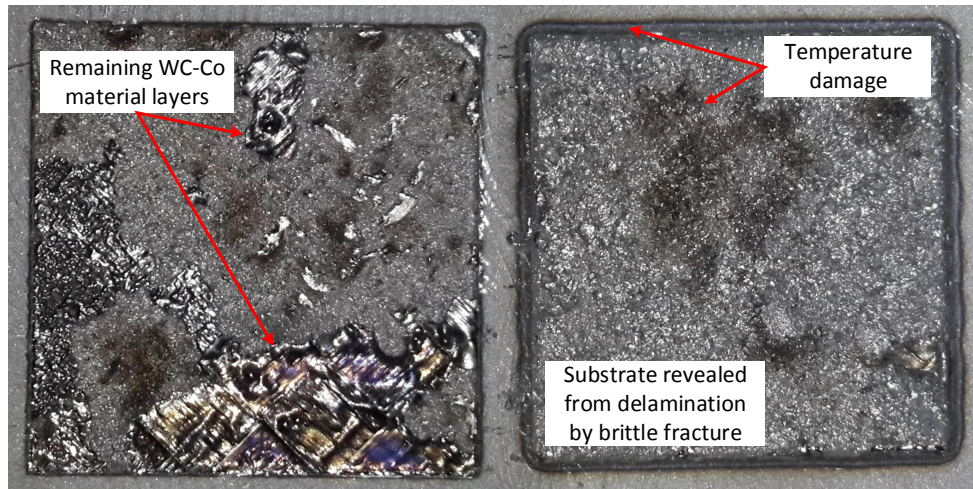


Figure 5.29: Sample sites from trial-and-error experiments using a WC-12wt.% Co powder.

Two sample sites from the trial-and-error experiments are shown in Figure 5.29 on page 102. The images indicate that brittle fracture, leading to part delamination, is the primary cause of process failure. Figure 5.30 on page 103 to Figure 5.32 on page 104 shows void formation that presents as black spots in the diffusion area and is the primary defect detectable. This is explained as a result of the excessive heat input into the powder layer which exposes the underlying material to the temperature gradient mechanism (TGM). Due to the stresses generated as a function of the TGM, the underlying layers attempt to bend the consolidated layers towards the laser beam. This causes distortion and part failure by way of void formation, leading to cracking and delamination.

Further inspection of the sample cross sections (from samples E5 and E7) revealed a localised increase in W and C concentrations corresponding to the white spots shown in the SEM micrographs (see Figure 5.30 to Figure 5.32). A localised increase in W and C elements corresponds to an expected increase in hardness, which relates to an increase in brittleness and a decrease in ductility. The decrease in ductility also corresponds to the limited degree of binder (cobalt) diffusion. This, coupled with the presence of voids, results in a fragile surface layer that is prone to brittle fracture and, ultimately, catastrophic failure by delamination.

Figure 5.31 demonstrates the level of defect presence in a) sample E5 and b) sample E7. As the image suggests, there is a comparatively lower degree of visible defect formation in sample E7 as opposed to sample E5. This supports the conclusions drawn from the surface and roughness profile analyses that the process parameter values corresponding to sample E7 presents optimised results for single layer production using a cemented tungsten carbide material and an available SLM technology.

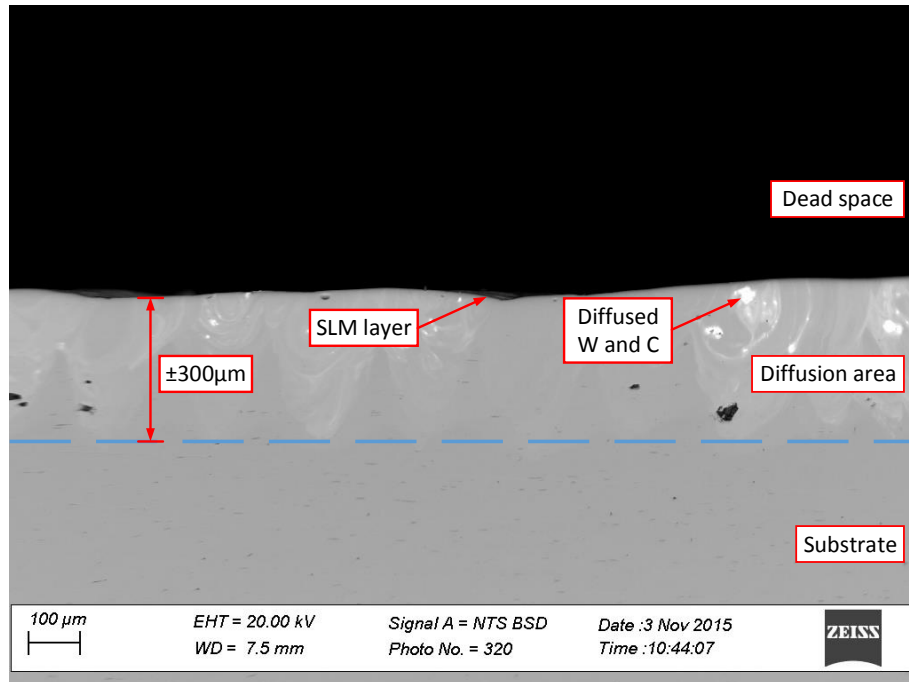


Figure 5.30: Descriptive SEM image of a cross section from sample E5.

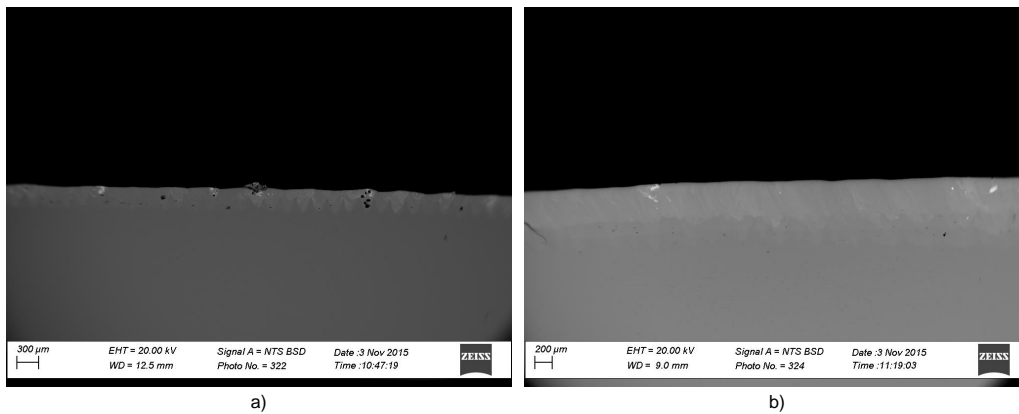


Figure 5.31: Cross section comparison of a) sample E5 and b) sample E7 - wide angle.

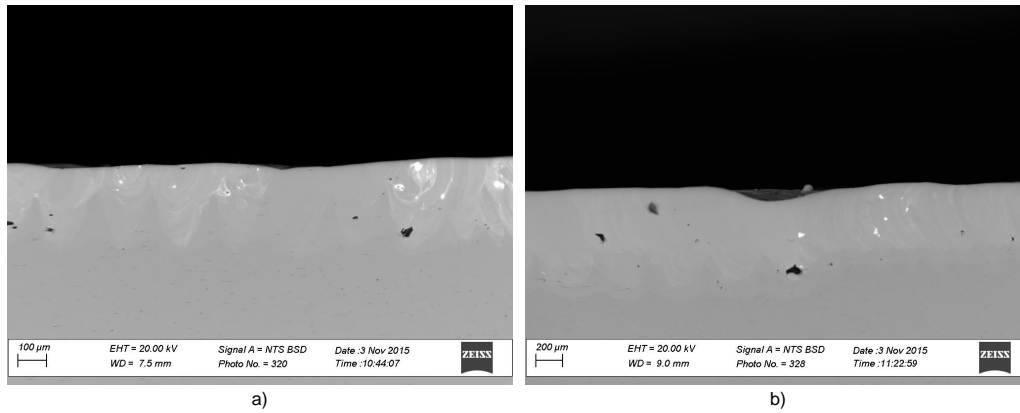


Figure 5.32: Cross section comparison of a) sample E5 and b) sample E7 - close up.

Figure 5.32 shows an enlargement of the diffusion areas shown in Figure 5.31, for a) sample E5 and b) sample E7. From the images alone it is unclear which sample shows a lesser degree of defect presence in the diffusion area. Both samples have voids present and Figure 5.32b shows some valley formation at the SLM surface. Protrusion formation can also be seen on the surface in Figure 5.32b. Refer to Figure 5.33 on page 105 for a SEM micrograph illustrating the cross section of a surface protrusion defect.

Further inspection of the cross sections reveal microstructural changes due to the tempering effect the incident laser beam has on the substrate. This is visible as v-shaped temperature diffusion patterns (indicated in Figure 5.33 with dotted lines) in the diffusion area corresponding to each scan track that makes up the build strategy.

As the laser traces the scanning pattern the laser energy diffuses into the substrate, causing microstructural changes due to the heat generated, resulting in an increase in localised hardness. As stated previously, tempering hardens the surface, increases brittleness, and increases the likelihood of catastrophic failure by delamination.

An energy dispersive spectroscopy (EDS) analysis is carried out to determine the material weight percentage that has diffused into the substrate during sintering. Figure 5.34 on page 105 presents the results from the EDS analysis for cross section sample E5. The dominant element present is iron (Fe), corresponding to the substrate material. The graph shows that a low concentration of W and C elements are present in the diffusion area. This is true of both samples. Figure 5.35 illustrates the results from the EDS analysis for cross section sample E7. A similar trend in the element concentrations is noticeable.

The presence of the mixed crystals (TaC, NbC, TiC, and N), as well as the binder element, cobalt, in the SLM layer and the diffusion area is also illustrated in the aforementioned figures. Very limited amounts of the mixed crystals and cobalt is present in the diffusion area, increasing in concentration closer to the SLM layer.

Figure 5.36 on page 106 shows the EDS results for the enlarged SLM-layer/substrate interface. The results clearly show an increase in W and C concentrations, as well as a corresponding decrease in iron concentration, in the SLM layer. A similar observation can be made for the mixed crystal and cobalt elements.

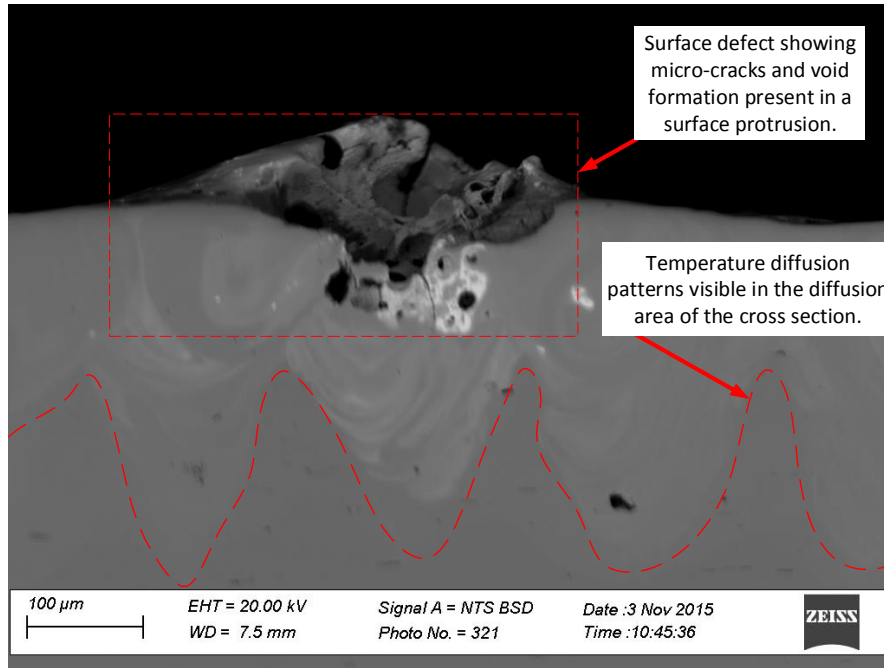


Figure 5.33: Descriptive SEM image of a surface protrusion cross section and temperature diffusion pattern.

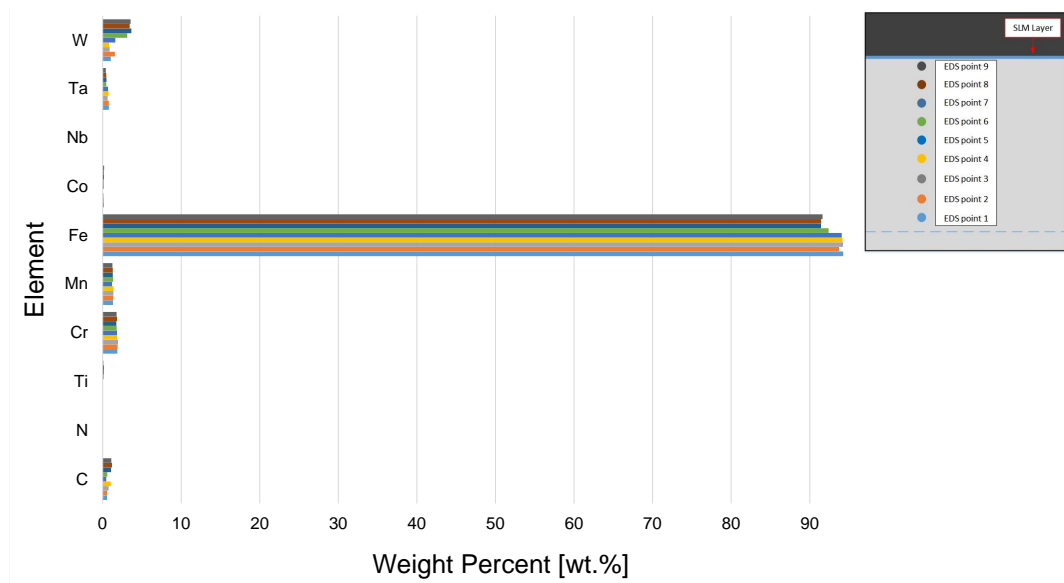


Figure 5.34: Analysed cross section sample composition for E5.

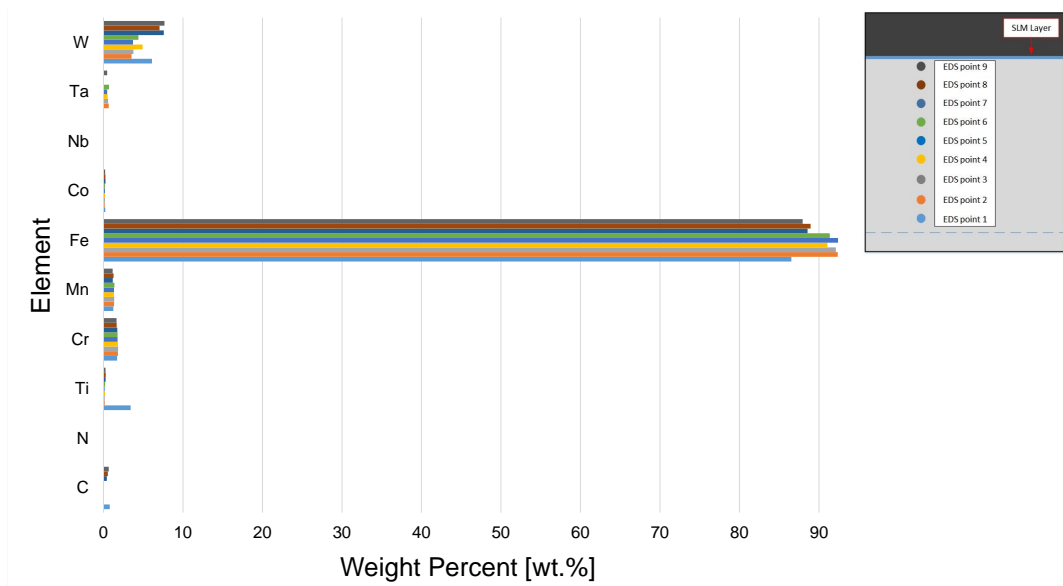


Figure 5.35: Analysed cross section sample composition for E7.

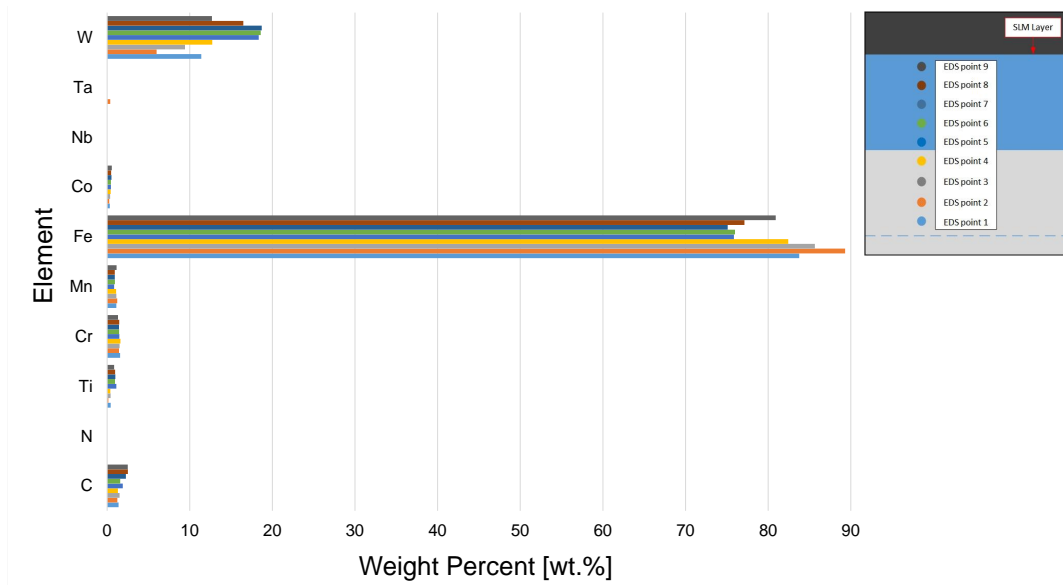


Figure 5.36: Analysed cross section sample composition for SLM layer E7.

These results suggest that a cemented tungsten carbide material layer can be sintered onto a steel substrate, resulting in limited diffusion and microstructural alterations in the substrate. It remains, however, unclear whether a SLM layer created in this way would suffice as the basis for building 3D components and further research into the microstructure is required.

The low levels of element concentrations in the diffusion areas could be attributable to only a single SLM layer being sintered onto the baseplate. It is expected that higher concentrations, of both the primary cemented carbide elements and the additional mixed crystals and binder element, should diffuse into the substrate (up to a limit) during continued deposition and subsequent sintering of the WC-6.6wt.% Co material. This, however, requires further investigation as a continued exposure to high laser power levels will continue the tempering process in the material layers and the baseplate, which could increase material brittleness and the likelihood of catastrophic failure by brittle fracture and delamination.

The EDS and SEM micrograph analyses thus reveal, to a certain degree, that SLM of a cemented tungsten carbide is possible and that favourable microstructures can be achieved, with the limiting factor being the amount of defect formation present as a result of tempering and over-exposure to laser energy. Taking into consideration these results, as well as the results presented in the previous section, it becomes apparent that the combination of process parameters corresponding to sample E7 is only optimal in so far as to create a uniform SLM layer from cemented tungsten carbide powder. It is entirely possible that a completely different set of process parameters might create the optimal microstructure, and it is suggested that further investigation into this subject is required to completely understand (and possibly predict) the material behaviour under optimal sintering conditions for multi-layer accretion. The following section presents the results obtained from the statistical analysis carried out for this work, that aims to optimise the process parameters required to create a uniform SLM layer from a cemented tungsten carbide powder.

5.2.4 Statistical analysis

The statistical data analysis is carried out according to the methodology outlined in section 4.2.4.4 on page 68. For each parameter set the resultant R_z value is recorded and entered into the MODDE analysis environment. The software performs a Multiple Linear Regression (MLR) analysis based on a 2^k Full Factorial interaction model. The resultant model is analysed according to the six step sequence described in section 4.2.4.4. However, the model is adjusted in step four when insignificant model terms are excluded. Therefore, the results from the fourth step is presented first and thereafter the sequence is presented as usual.

The model terms, before exclusion, is shown in Figure 5.37 on page 108. The graph shows how each model term affects the response variable. It should be noted that the error bars illustrated in the image indicates that the model as-is can be improved by excluding some interaction terms (or possibly the primary factors). Terms such as $P * h$ and $v * h$ are considered insignificant terms, according to the analysis guidelines provided in MODDE. These terms are selectively excluded from the model until the Q^2 value reaches a maximum, and any subsequent term exclusion will result in a drop in the Q^2 value.

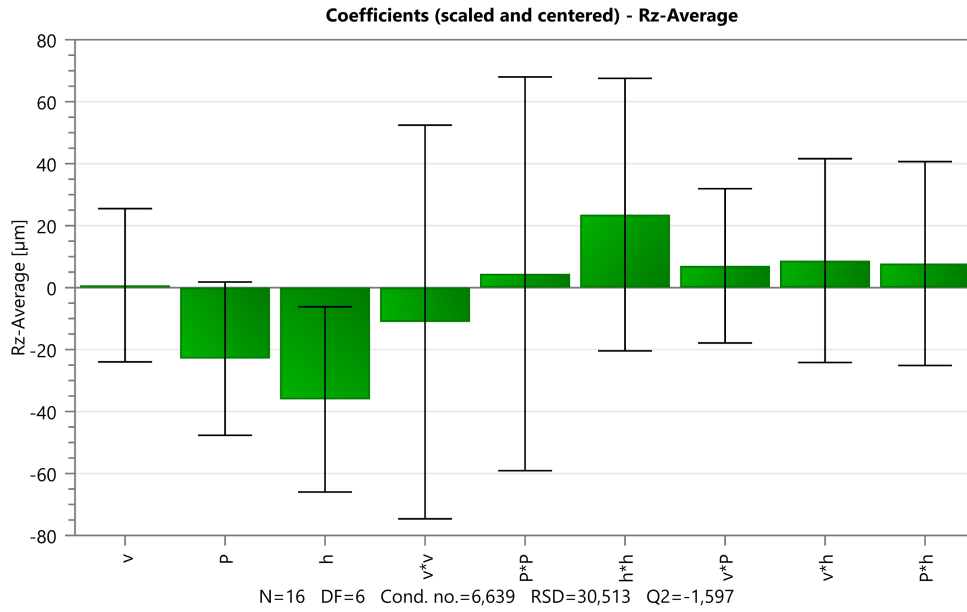


Figure 5.37: Coefficients plot, for response variable R_{z-max} , before term exclusion.

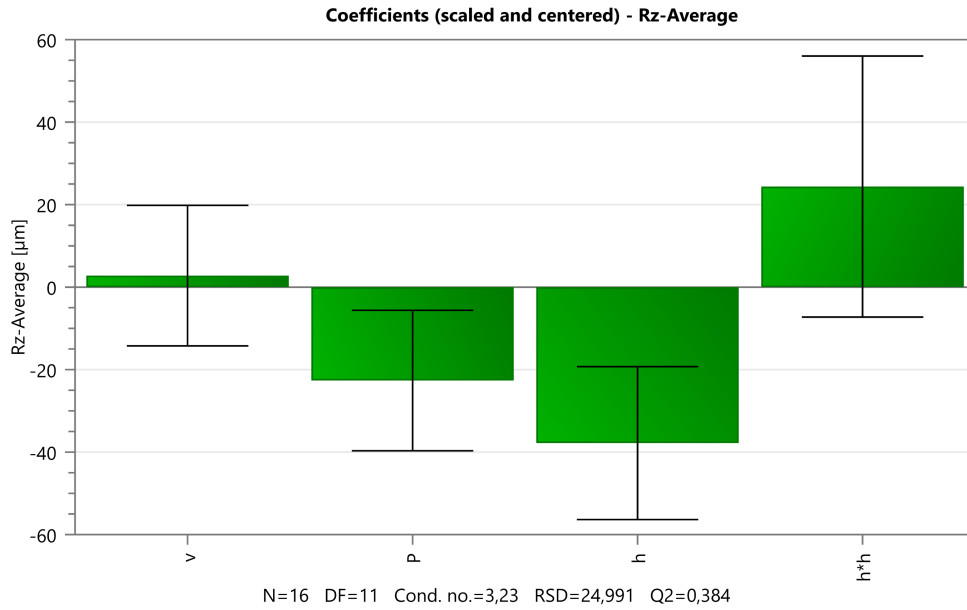


Figure 5.38: Coefficients plot, for response variable R_{z-max} , after term exclusion.

Figure 5.38 on page 108 shows the final model terms (after the exclusion of some interaction terms) and Q^2 value. These terms are used in any subsequent data analyses, such as optimisation and factor effect analysis. The image illustrates how the model-error for each factor has been reduced. As expected, the laser power, scan speed, and hatch spacing values primarily affect the R_z value for each sample layer, with a $h * h$ interaction term indicating that the hatch spacing is the determining factor in deciding which parameter set yields the optimal results. The model results analysed and graphed in steps 1-3 and 5-6 also show the Q^2 value that was maximised in this analysis step. The rest of the basic model analysis results, follow.

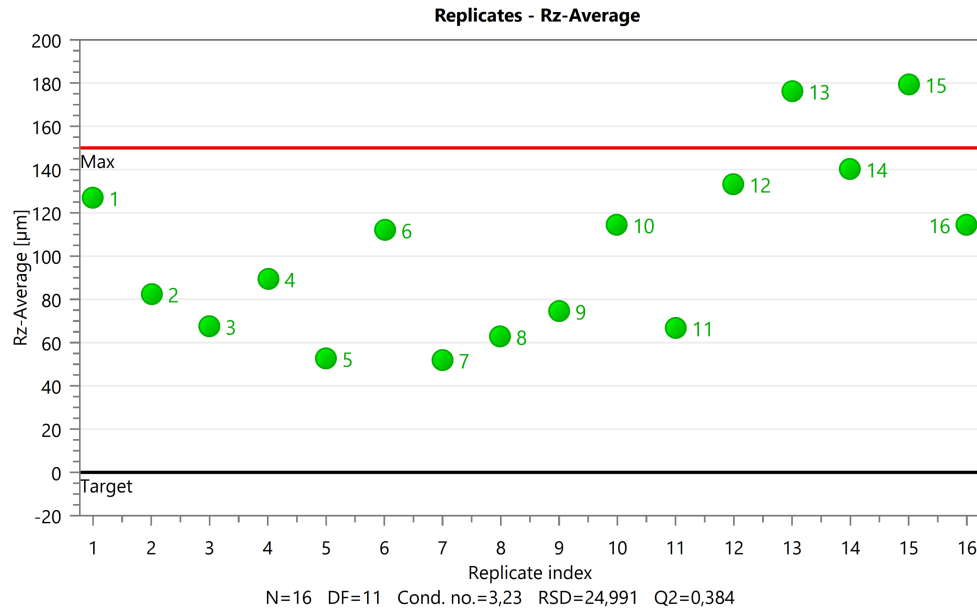


Figure 5.39: Replicates plot for R_z -Average - MODDE analysis.

Figure 5.39 on page 109 presents the replicates plot for the model data. Here it can be seen that all experiment samples except E13 and E15 lie beneath the maximum, which has been set to $150\mu\text{m}$. Also noticeable is that the majority of the results lie between $50\text{-}120\mu\text{m}$. Even though this is a fairly wide range, it indicates that the process is unbiased and performs consistently.

Figure 5.40 on page 110 shows the R_z values graphed as a histogram. In this step of the basic data analysis, the shape of the histogram is examined to determine if the data follows an approximately normal distribution. The results shown here confirm that the data follows an approximately normal distribution and therefore requires no transformation (i.e. log or negative-log transformations).

The summary of the model statistics Q^2 and R^2 is shown in Figure 5.41 on page 110. As indicated, $R^2 = 0.726$. This corresponds to a significant model with a good fit, since its value is greater than 0.5. Also, the $Q^2 = 0.384$ which is greater than 0.1, further indicating that the model is statistically significant.

Figure 5.42 on page 111 shows the residuals normal probability plot for the fitted model. The majority of the response values lie in a straight line on the diagonal,

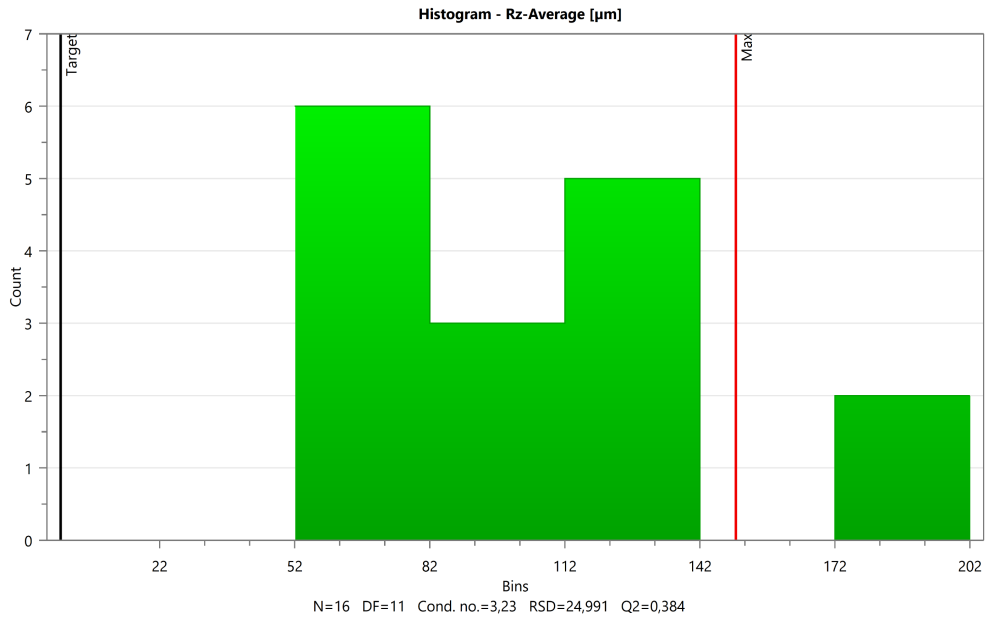


Figure 5.40: Histogram of the response variable, R_z -Average.

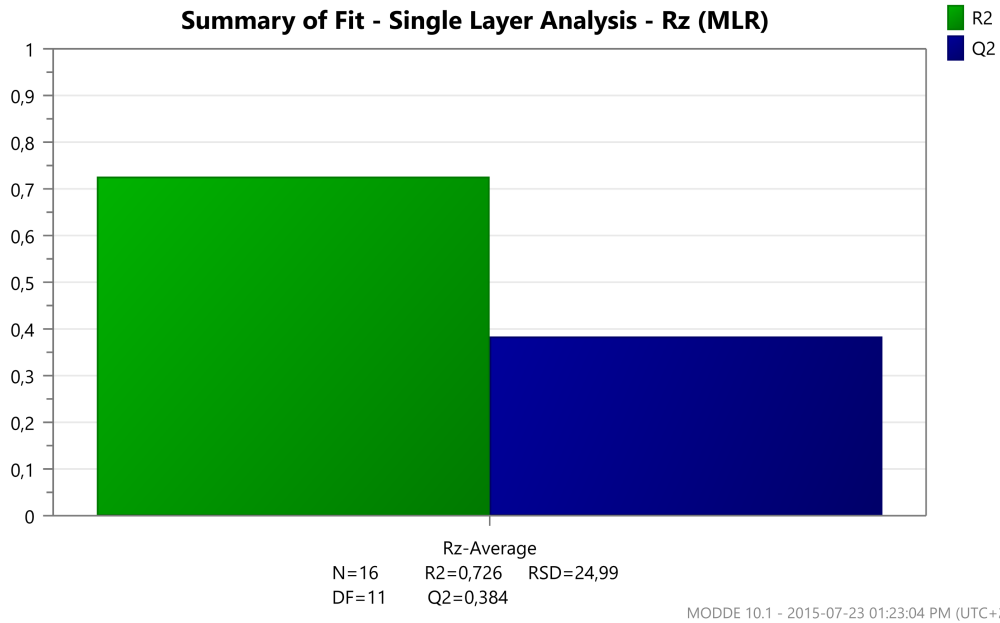


Figure 5.41: Model summary for R^2 and Q^2 statistics after adjustment.

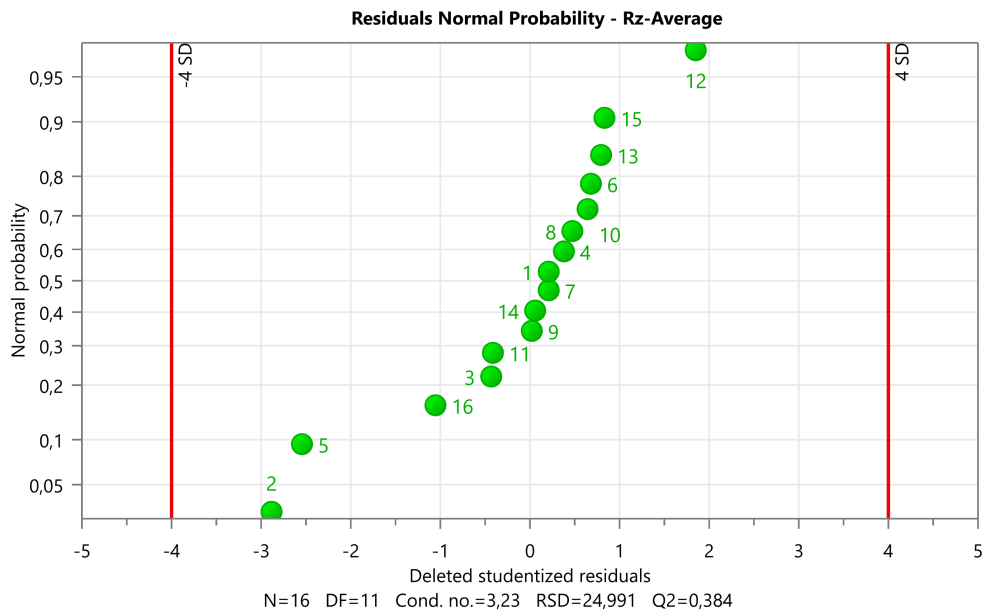


Figure 5.42: Residual normal probability plot for response variable R_z -Average.

however the response values for samples E2, E5, and E12 do not. In this case it can be concluded that there is a non-linear relationship between some of the factors and the response variable, R_z .

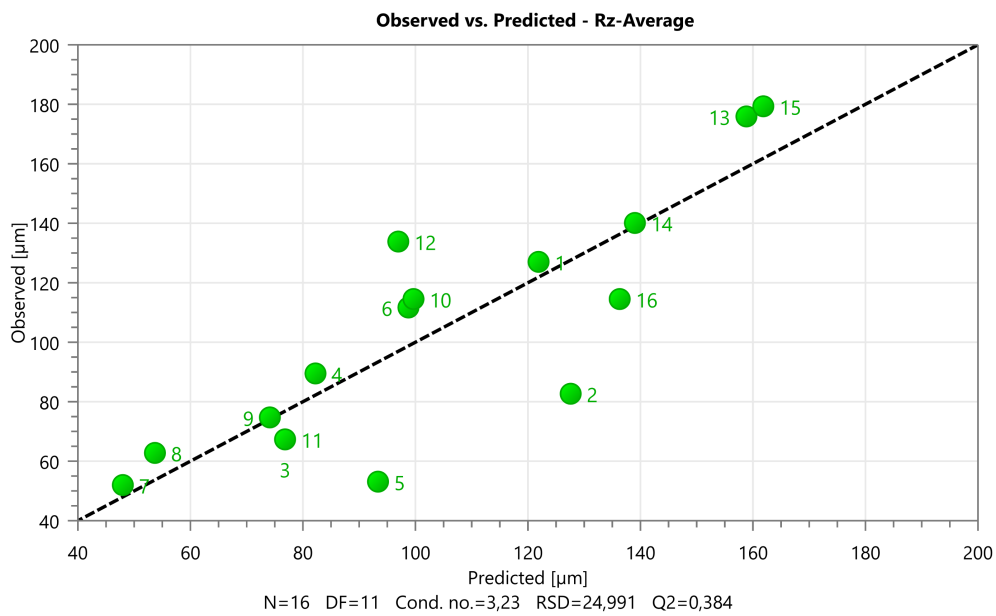


Figure 5.43: Observed versus predicted plot for response variable R_z -Average.

The final step in the basic analysis sequence is the observed versus predicted plot

shown in Figure 5.43 on page 111. Here, a linear regression line is fitted to the data shown in the graph and indicates that there are quite a few deviations around the straight line. This corresponds to the R^2 and Q^2 values that are lower than that of a good model, however still significant. It can therefore be expected that a slightly greater degree of error in the prediction analysis is to be expected. This, however, is still expected to produce good results, regardless.

After the basic analysis is done, more significant insight into the data can be gathered by analysing the response contour and performing an optimisation analysis. The response contour, before optimisation, shows a colour-coded layout that represents the response variable value as the factor values are varied. Figures H.1 to H.3 in Appendix H presents contour plots for laser power versus scan speed, laser power versus hatch spacing, and scan speed versus hatch spacing, respectively. Each plot illustrates what the expected R_z value would be, given a combination of the two relevant factors. From all three plots it becomes apparent that a combination of high laser power, high hatch spacing, and low scan speed minimises the associated R_z value.

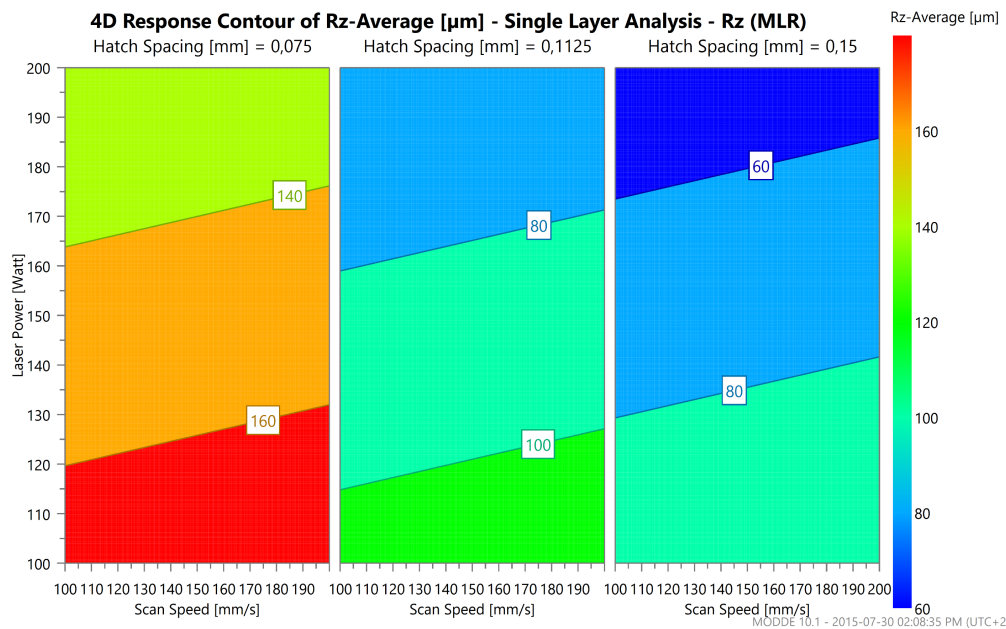


Figure 5.44: 4D contour plot combining laser power, scan speed, hatch spacing and response variable R_z .

Figure 5.44 on page 112 shows a combined, 4D contour plot that illustrates the combined effect of all three factors on the response variable. The plot verifies that high values for laser power and hatch spacing, coupled with low values of scan speed, yields the best results. That is, a combination of these factor values minimises the resultant maximum height of the surface profile.

Using the Optimiser built into the MODDE software the optimal setpoint can be determined, based on the experimental data and the model fitted. The optimiser

setup summary is presented in Tables 4.4 and 4.5 on page 70 for the factors and response variable, respectively.

Table 5.8: Selected setpoint summary - factors.

Factor	Role	Value	Unit	Factor contribution
Scan Speed	Free	100	$mm.s^{-1}$	10,0051
Laser Power	Free	200	<i>Watt</i>	81,2467
Hatch Spacing	Free	0,1425	<i>mm</i>	8,74824
Layer Thickness			<i>mm</i>	

Table 5.9: Selected setpoint summary - response.

Response	Criterion	Value	Unit	log(D)	DPMO	C _{pk}
R_z-Average	Minimize	46,7773	μm	-1,01211	0	2,11401

The selected setpoint is summarised in Tables 5.8 and 5.9 on page 113 for the experiment factors and response variable, respectively. The extended setpoint summary, for both the experiment factors and response variable, is presented in Tables H.1 and H.2 in Appendix H, respectively. The optimal chosen setpoint corresponds to $P = 200W$, $v = 100mm.s^{-1}$, and $h = 0.1425mm$. The optimal response is $R_z = 46.77\mu m$. The alternate setpoints evaluated during the optimisation process are presented in Table H.3 in Appendix H. The results clearly suggest that, based on the model data, the best parameter combination is one of high laser power and hatch spacing, as well as low scan speed.

Figures H.4 to H.6 in Appendix H presents the predictive factor distribution plots used by MODDE Optimiser to determine the optimal setpoint. Also shown, in Figure H.7, is the predictive response distribution associated with these plots. Notice that the majority of the potential factor values for both scan speed and laser power, according to the distribution, are excluded from consideration as these fall outside the minimum and maximum factor levels, respectively. For hatch spacing, however, a wider acceptable range of values are applicable to the analysis.

Based on these distributions, factor effect plots are generated which demonstrate the individual factors' effects on the response variable. These plots are shown in Figures H.8 to H.10 in Appendix H. The predicted response line is presented within a 95% confidence interval. The results shown here reaffirms the results reported previously. Even individually a higher laser power, a lower scan speed, or a higher hatch spacing value tends to decrease the measured R_z value.

Figure 5.45 on page 114 shows the combined factor effect plot for the three factors. The minimum achievable R_z value corresponds to the lowest point on the response line for each factor. From the graph it is clear that hatch spacing has the most significant effect on the achievable R_z value, corroborating the conclusion made from the coefficients plot in Figure 5.38 on page 108.

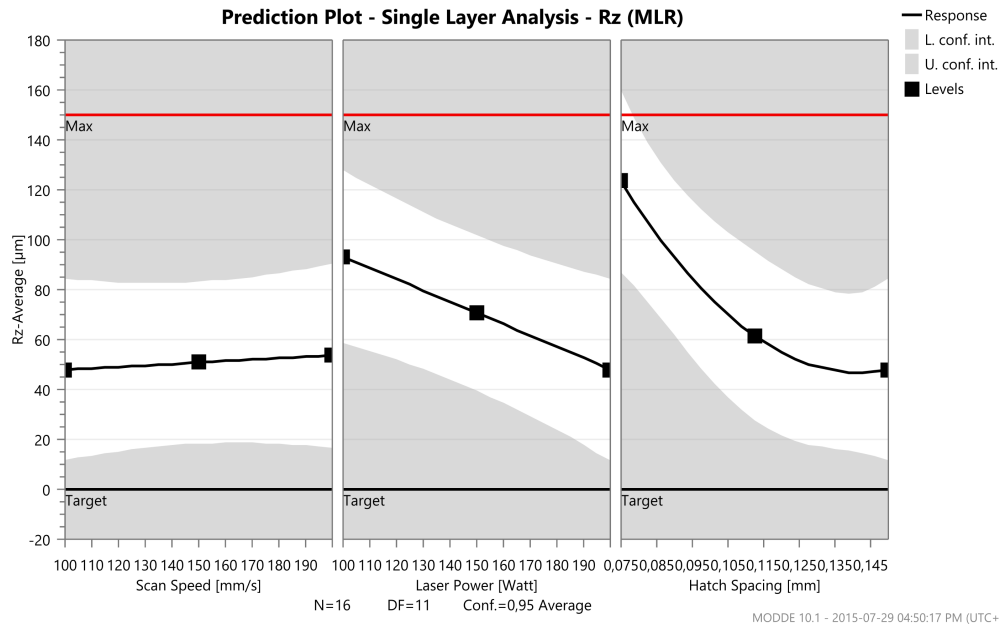


Figure 5.45: Combined factor effect plot for all experiment factors and response variable R_z .

The final part of the MODDE analysis involves plotting the contoured response for each factor pair corresponding to the chosen setpoint. Each graph has a shaded area that indicates the factor setting values that cannot be chosen due to the factor range restrictions established during the optimiser setup process. The unshaded area corresponds to factor value that may be chosen. Furthermore, the chosen setpoint for each factor is indicated by four adjoining arrows in the centre of the graph. Figures H.11 to H.13, shown in Appendix H, presents the resultant graphs.

Figure 5.46 on page 115 shows the so called setpoint windows corresponding to each factor range graphed on the respective axes. This is the acceptable area wherein the alternate setpoints, discussed and presented previously, may be selected.

This section presented the results obtained from the profilometer and statistical analyses carried out for this work. It was found that a combination of high laser power, low scan speed, and high hatch spacing produces the best single layer results. Furthermore, it was found that hatch spacing has the most significant effect on single layer formation in SLM of a cemented tungsten carbide. The following section presents a discussion on the process windows developed from the observable results.

5.3 Process windows

The work presented in the previous section is used to create process windows which describes the expected observable single layer formation phenomena when selectively melting WC-6.6wt.% Co powder. The results are presented in this section.

The work presented here builds on the process windows developed by Kruth *et al.* (2005), Li *et al.* (2010), Zhang *et al.* (2010), and Zhang *et al.* (2012b), among

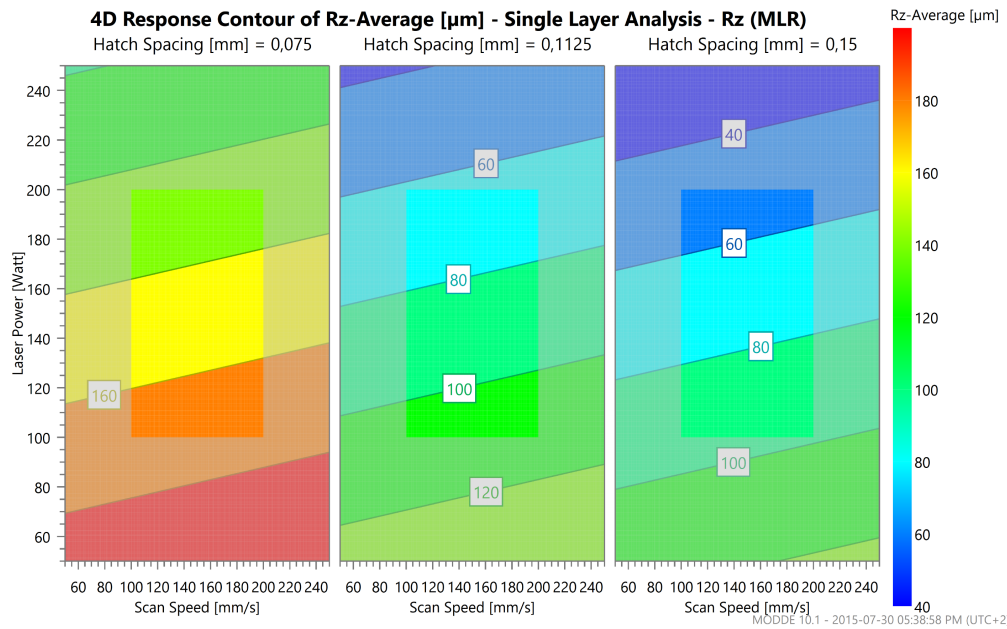


Figure 5.46: 4D response contour plot with selected setpoint for all factors and response variable R_z .

others. In their work they describe the observable sintering behaviour associated with a specific material under investigation when only laser power and scan speed are varied. In this work the process windows incorporate the effect that varying hatch spacing has on the formation of single layers.

From the results reported in the previous sections it is clear that a high laser power, low scan speed, and high hatch spacing combination leads to the best results for the WC-6.6wt.% Co material used in this work. This combination is characterised by low levels of surface protrusion formation, limited to no balling, limited micro-cracking, and almost no significant valley formation (or shrinkage). This processing region is used as the baseline parameter set to describe the observable phenomena in the remaining three regions.

A subset of processing windows are presented, each according to a specific hatch spacing value. These can be seen in Figures 5.8 to 5.11 on page 82, in section 5.2.1. Each subset shows a similar trend for each combination of scan speed and laser power. In comparison to the baseline parameter set (Figure 5.11), low-low ($P - v$) combinations for all three other hatch spacing values are characterised by significant protrusion formation and surface defects. These defects include indistinguishable scan track formation, pitting, localised shrinkage, and a certain degree of balling and/or protrusion formation.

A similar observation can be made for low-high and high-high combinations of laser power and scan speed. When these regions are compared to the baseline process region, again it is clear that scan track formation is not as successful and surface defects are more pronounced.

Figure 5.47 on page 116 presents all 16 experiment samples graphed on the same axes (Y - laser power and X - scan speed) and labelled according to the hatch

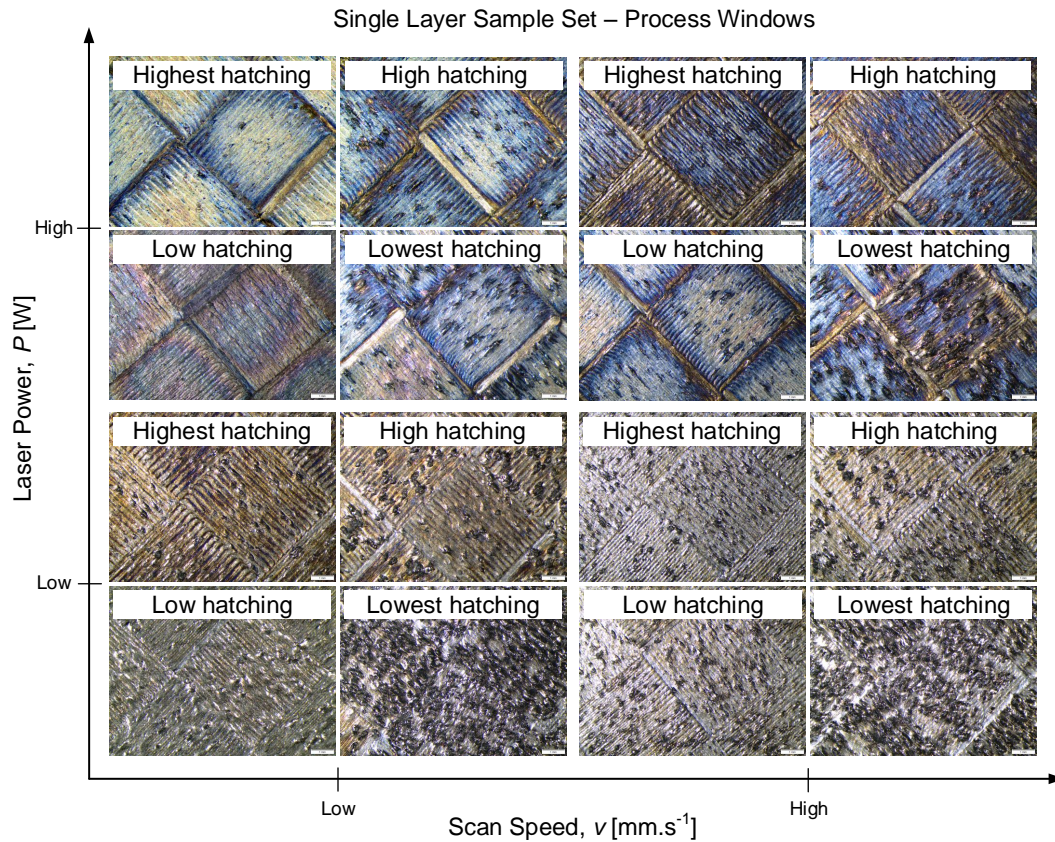


Figure 5.47: Combined microscope images of single layer sample parameter sets, according to hatch spacing.

spacing used. This demonstrates the significant effect that hatch spacing has on the achievable single layers for each laser power-scan speed combination, and confirms the finding that hatch spacing has the most significant effect on single layer formation in SLM of a cemented tungsten carbide.

For each combination (low-low, low-high, high-low, and high-high), as h increases, the presence of surface defects decrease. The same observation is seen in the trend line graphs presented for the surface and roughness profile parameters, according to each parameter set. The individual graphs are shown in section 5.2.2.1 on page 89. The combined graph, presented in Figure 5.48, reveals the same observable trends as that in Figure 5.47.

The surface and roughness profile parameter values show a significant decrease as hatch spacing increases. When the other process regions are compared to the baseline it is apparent that high laser power and high scan speed produces the second best results, low laser power and high scan speed is third, and combinations of low laser power and scan speed produce the worst results. When the microscope images are examined for similar trends, the same results can be concluded.

This chapter presented the results obtained from the experimental work carried out in this study. The material analysis, microscope imaging of the single layer

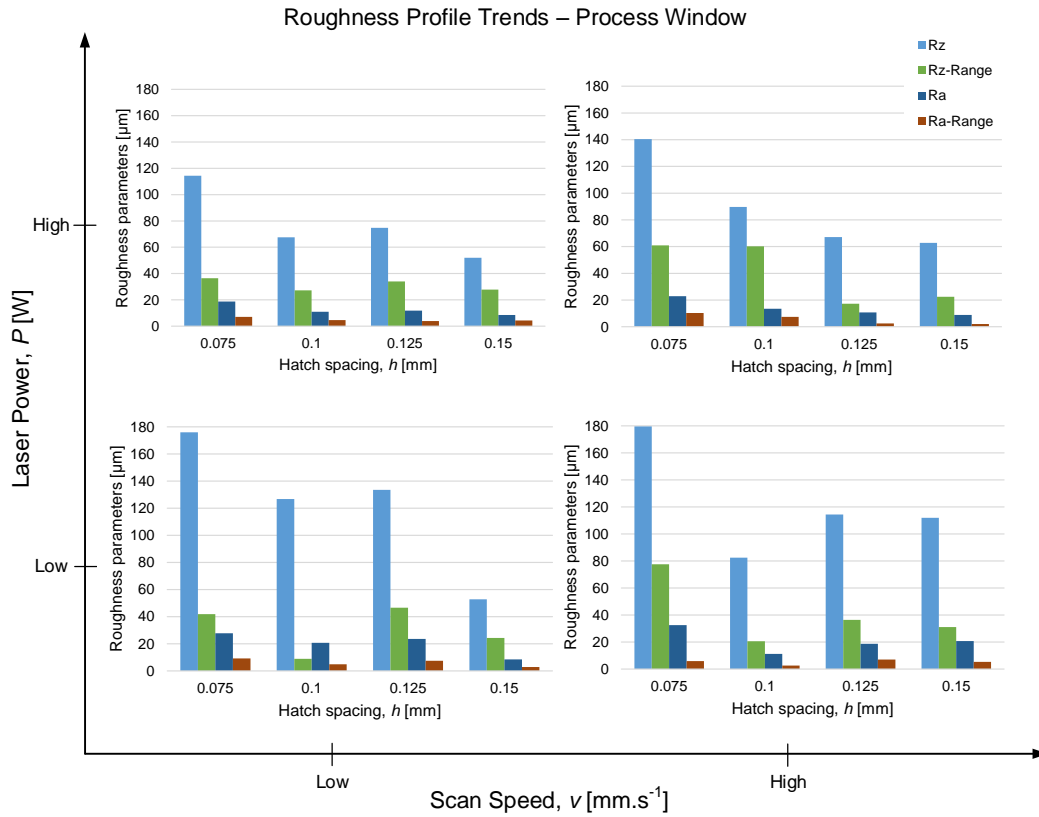


Figure 5.48: Roughness profile trend histograms according to different $P-v$ combinations.

samples, surface and roughness profile results, statistical analysis of the maximum roughness profile height (R_z), and the resultant process windows are discussed. The following chapter presents the conclusions drawn regarding the experimental work carried out in this study.

Chapter 6

Conclusions

This chapter presents the conclusions drawn from the results obtained and presented in chapter 5 on page 74, in this study.

In this study the material analysis showed the tool grade cemented tungsten carbide powder used to have a multi-faceted, inhomogeneous particle shape which lead to insufficient material flow, hindering autonomous powder deposition during processing. Furthermore, in comparison to the benchmark material's particle size distribution (PSD), the PSD of the material used here is significantly smaller. This, coupled with the above mentioned particle shape, reduces the material flow properties of the WC-6.6wt.% Co powder quite significantly. It can be concluded, however, that this material can successfully be additively manufactured using an available selective laser melting (SLM) process. Autonomous deposition of the material is still hindered and poses an obstacle to continuous layer production.

The microscope analysis revealed the presence of evaporated powder particles as a result of significant temperature gradients that develop in the material bed, leading to protrusion formation in the single layer samples. The rapid expansion of the evaporating particles generates an overpressure on the melted zone which results in material ejection from the powder bed. The SLM process is a rapid melting and solidification process that results in the entrapment of the ejecting material in the form a protruding 'spike' on the layer surface. It is observed that an increase in hatch spacing decreases the concentration of thermal energy in the material bed, limiting material ejection, thus reducing the degree of protrusion formation.

Further analysis of the microscope images revealed a certain degree of balling present in every sample, appearing more prominently for some. This is explained by an increase in scan speed which rapidly melts and cools the material, hindering successful wetting of the underlying material layer. This, coupled with the tendency of the molten material to reduce the surface free energy leads to the formation of metal spheres. Two dominant balling mechanisms are identified, namely shrinkage-induced balling, and self-balling. This corresponds to parameter sets with high scan speeds and low laser power. It is concluded that lower scan speed and higher laser power, coupled with high hatch spacing produced the least amount of balling observable on the scan tracks.

Scan track formation, as well as the occurrence of shrinkage, for certain parame-

ter sets are explained by the degree of overlap, and subsequent remelting, of adjacent and perpendicular scan islands (corresponding to an island scan strategy employed during processing). Higher hatch spacing leads to isolation of scan tracks as a result of surface denudation and reduced reheating of previously melted tracks. The remelted area undergoes another cycle of thermal expansion, particle rearrangement, and subsequent shrinkage that forms noticeable valleys at the sample and scan island contours. Shrinkage related surface defects include pitting as a function of particle evaporation at low hatch spacing, balling as a result of low hatch spacing and moderate to high scan speed, and cracking as a result of low hatch spacing and high laser power. It is concluded that higher values of hatch spacing leads to the reduced occurrence of shrinkage (or valley formation). Furthermore, increased shrinkage for a given sample layer will lead to enhanced porosity formation in multi-layer parts, that could lead to delamination and catastrophic failure during processing.

Cracking is also visible as a surface defect, resulting from the temperature gradient mechanism (TGM). The sintered material layer undergoes thermal expansion and subsequent contraction due to rapid cooling that develops high levels of stresses and strains in the surface layer. In brittle material this results in crack formation along grain and contour boundaries. It is concluded that the material exhibits similar behaviour explained by the hot and cold cracking mechanisms.

From the microscope image analysis it is concluded that high values of hatch spacing and laser power, coupled with low scan speed, results in surface layers exhibiting the least amount of protrusion formation and balling, limited shrinkage, sufficient and optimal scan track formation, and little to no micro crack formation. This suggests that it is entirely possible to produce single layer samples from a tool grade cemented tungsten carbide and a SLM technology, however the capability of producing multi-layered samples remains unclear.

The surface and roughness profiles of each single layer sample was measured and the associated parameters were analysed to characterise the sintered layers using quantitative parameters. The results were compared to a benchmark produced from standard parameters and materials associated with the SLM technology used.

The maximum profile height, R_z , of each sample is used to evaluate the capability of each process parameter set to successfully produce a sintered layer from WC-6.6wt.% Co using an available SLM technology. Trend analyses, using several surface and roughness profile parameters (i.e. S_a , S_q , S_p , S_v , S_z , R_a , and R_z among others), was carried out to identify a decreasing pattern showing improved surface formation corresponding to high hatch spacing, low scan speed, and high laser power.

It is concluded that these results quantitatively supports and substantiates the results and conclusions drawn from the microscope image analyses. The surface defects described in the microscope image analysis lends to the explanation of the profilometer results. Furthermore, these results support the conclusion that SLM is capable of successfully producing single layer samples from cemented tungsten carbide powder. These results further support the conclusion that changes in the material, process, and laser parameter values affects the formation of these layers and has been optimised in this work to produce a uniform layer that minimises surface and subsurface defects and has the potential to form the basis of the production of a complete 3D component. As stated, however, multi-layered sample production requires further research.

A SEM analysis of the cross section from the two best samples was carried out to determine what, if any, discernible defects are present as well as what degree of material and heat diffusion is present in the sample substrate. The analysis shows clear signs of heat diffusion into the diffusion area, corresponding to the individual scan track patterns followed during sintering. Also, limited material diffusion is detected during a energy dispersive spectroscopy (EDS) analysis. Low levels of W, C, and the mixed crystal elements Ti, Ta, and Nb are present in the substrate and is found to increase in concentration closer to the SLM layer. Further analysis of anomalies found in the cross sections revealed void formation in the substrate, leading to brittle interlayer bonds which increases the likelihood of catastrophic failure by delamination. This then suggests that, although a SLM process parameter combination has been identified that optimises uniform single layer sample production, the possibility of producing multi-layered samples is still unclear and requires further research.

A statistical analysis was carried out to determine the statistical significance of the data recorded in the surface and roughness profile analyses. The maximum height parameter, R_z , was used in a 2^k Full Factorial design of experiments (DOE) to determine what the optimal parameter value region is to achieve a minimum R_z . The results show that a high laser power, low scan speed, and high hatch spacing results in the best surface formation.

It can thus be concluded that qualitatively, quantitatively, and statistically, the optimal parameter combination for the production of a single uniform material layer, using SLM technology and a tool grade cemented tungsten carbide, is one of high laser power, low scan speed, and high hatch spacing. It is still, however, unclear whether high density ($>95\%$), multi-layered parts can be successfully produced by this optimal parameter value region and whether such a multi-layer part will adhere to industry standards corresponding to hardmetal materials. More research into the material properties, the material behaviour under sintering conditions, and the microstructural changes exhibited by the material during the SLM process is required to conclude whether it is entirely possible to additively manufacture tool grade cemented carbide powder using SLM technology.

Chapter 7

Recommendations and future work

The research in this study formed the fundamental ground work required to successfully build three-dimensional (3D) parts from a cemented tungsten carbide material, using an available selective laser melting (SLM) technology. Since the SLM process is a layer-by-layer process, understanding the forming mechanisms involved in creating a single material layer is required. However, this is only a small part of the requirements to create a functional 3D component in SLM and a significant amount of research into the process and material properties (pertaining to this work) is still required.

There exists other, more challenging, phenomena in SLM of cemented tungsten carbides that requires understanding and optimisation before functionality in the built parts are achieved. This includes, but is not limited to, the following:

1. Material flow issues associated with autonomous powder deposition of a cemented tungsten carbide during SLM processing.
2. Microstructural evolution and grain growth phenomena associated with SLM processing and the resultant mechanical properties of a sintered layer.
3. The development of brittle phases as a result of tempering during SLM, causing catastrophic failure during processing.
4. Residual and thermal stress development in sintered material layers during SLM processing of a cemented tungsten carbide powder material.
5. The thermal expansion and contraction (or shrinkage) of material layers, causing elevated edges and subsequent part deformation during SLM processing of a cemented carbide material.
6. The effect that changing the build substrate has on single and multiple layer formation in SLM of a cemented tungsten carbide powder material.
7. Cemented tungsten carbide multi-layer accretion by SLM and the associated mechanical properties profile of the sintered parts.

The topics listed here are presented in order of intended execution in future work, each building on the accumulated information of the previous studies. In

order to successfully investigate these matters a fundamental understanding of the requirements to successfully sinter a single layer from cemented tungsten carbide is required. The topics of interest listed here all build on the work presented in this study. These topics stem from the research questions and objectives presented in Chapter 2 on page 9, as well as from the identified knowledge gaps in literature pertaining to additive manufacturing (AM) of cemented tungsten carbides. The research questions are all applicable on the topics of interest listed here, with research question 4 (in Chapter 2) having a particular application in solving research topic 7 (above).

List of References

- Agarwala, M., Bourell, D., Beaman, J., Marcus, H. and Barlow, J. (1995). Direct selective laser sintering of metals. *Rapid Prototyping Journal*, vol. 1, no. 1, pp. 26–36. ISSN 1355-2546.
- Allen, C. and Ball, A. (1996 feb). A Review of the Performance of Engineering Materials Under Prevalent Tribological and Wear Situations in South African Industries. *Tribology International*, vol. 29, no. 2, pp. 105–116. ISSN 0301679X.
- Allibert, C.H. (2001). Sintering Features of Cemented Carbides WC-Co Processed From Fine Powders. *International Journal of Refractory Metals and Hard Materials*, vol. 19, pp. 53–61.
- Andren, H.-o. (2001). Microstructures of Cemented Carbides. *Materials and Design*, vol. 22, pp. 491–498.
- Antony, J. (2003a). Full factorial designs. In: *Design of Experiments for Engineers and Scientists*, chap. 6, pp. 54–72. Elsevier Ltd. ISBN 978-981-277-867-3.
- Antony, J. (2003b). Fundamentals of Designing Experiments. In: *Design of Experiments for Engineers and Scientists*, chap. 2, pp. 6–16. Elsevier Ltd. ISBN 978-981-277-867-3.
- Arsecularatne, J., Zhang, L. and Montross, C. (2006 apr). Wear and Tool Life of Tungsten Carbide, PCBN and PCD Cutting Tools. *International Journal of Machine Tools and Manufacture*, vol. 46, no. 5, pp. 482–491. ISSN 08906955.
- Atwood, C., Gribth, M., Harwell, L., Schlienger, E., Ensz, M., Smugeresky, J., Romero, T., Greene, D. and Reckaway, D. (1998). Laser Engineered Net Shaping (LENS): A Tool for Direct Fabrication of Metal Parts. *Proceedings of the International Congress on Applications of Lasers and Electro-Optics '98*, pp. 1–7.
- Badrossamay, M. and Childs, T. (2007). Further studies in selective laser melting of stainless and tool steel powders. *International Journal of Machine Tools and Manufacture*, vol. 47, pp. 779–784. ISSN 08906955.
- Bezuidenhout, M.B. (2015). *Additive Manufacturing Enabled Drug Delivery Features for Titanium-Based Total Hip Replacement Cementless Femoral Stems*. Masters Thesis, Stellenbosch University.
- Blateyron, F. (2013). Characterisation of Areal Surface Texture. In: Leach, R. (ed.), *Characterisation of Areal Surface Texture*, chap. 2, pp. 15–43. Springer-Verlag, Heidelberg. ISBN 978-3-642-36457-0.
- Blott, S.J. and Pye, K. (2006). Particle size distribution analysis of sand-sized particles by laser diffraction: An experimental investigation of instrument sensitivity and the effects of particle shape. *Sedimentology*, vol. 53, no. 3, pp. 671–685. ISSN 00370746.

- Butler, J. (2011 aug). Using Selective Laser Sintering for Manufacturing. *Assembly Automation*, vol. 31, no. 3, pp. 212–219. ISSN 0144-5154.
- Campanelli, S.L., Contuzzi, N., Angelastro, A. and Ludovico, A.D. (2010). Capabilities and Performances of the Selective Laser Melting Process. In: Er, M.J. (ed.), *New Trends in Technologies: Devices, Computer, Communication and Industrial Systems*, chap. 13, pp. 233–252. Sciyo. ISBN 978-953-307-212-8.
- Campbell, R., de Beer, D. and Pei, E. (2011 mar). Additive Manufacturing in South Africa: Building on the Foundations. *Rapid Prototyping Journal*, vol. 17, no. 2, pp. 156–162. ISSN 1355-2546.
- Cavazzuti, M. (2013). Design of Experiments. In: *Optimization Methods: From Theory to Design*, chap. 2, pp. 13–42. Springer-Verlag, Heidelberg. ISBN 9231039989.
- Childs, T., Hauser, C. and Badrossamay, M. (2005). Selective laser sintering (melting) of stainless and tool steel powders: experiments and modelling. *Proceedings of the Institution of Mechanical Engineers, Part B: Journal of Engineering Manufacture*, vol. 219, no. 4, pp. 339–357. ISSN 0954-4054.
- Chua, C., Leong, K. and Lim, C. (2003). *Rapid Prototyping - Principles and Applications*. 2nd edn. World Scientific Publishing Co. Pte. Ltd., Singapore. ISBN 9812381171.
- Ciurana, J., Hernandez, L. and Delgado, J. (2013). Energy density analysis on single tracks formed by selective laser melting with CoCrMo powder material. *International Journal of Advanced Manufacturing Technology*, vol. 68, no. 5-8, pp. 1103–1110. ISSN 02683768.
- Colton, J. (2009). Metal Powder Processing. Tech. Rep., Georgia Institute of Technology.
- Cotteleer, M., Holdowsky, J. and Mahto, M. (2013). The 3D opportunity primer: The basics of additive manufacturing. Tech. Rep., Deloitte University Press.
- Cselle, T. and Barimani, A. (1995). Today's Applications and Future Developments of Coatings for Drills and Rotating Cutting Tools. *Surface and Coatings Technology*, vol. 76-77, pp. 712–718.
- Damm, O. and du Preez, W. (2009). Progress Made by the South African Light Metals Development Network. *Materials Science Forum*, vol. 618-619, pp. 147–154. ISSN 02555476.
- Das, S. (2003). Physical Aspects of Process Control in Selective Laser Sintering of Metals. *Advanced Engineering Materials*, vol. 5, no. 10, pp. 701–711. ISSN 1438-1656.
- De Beer, D. (2011). Establishment of Rapid Prototyping/Additive Manufacturing in South Africa. *The Journal of the South African Institute of Mining and Metallurgy*, vol. 111, pp. 211–215.
- DebRoy, T. and David, S.A. (1995). Physical processes in fusion welding. *Reviews of Modern Physics*, vol. 67, no. 1, pp. 85–112. ISSN 00346861.
- Deprez, K., Vandenberghe, S., Van Audenhaege, K., Van Vaerenbergh, J. and Van Holen, R. (2013 jan). Rapid Additive Manufacturing of MR Compatible Multipinhole Collimators with Selective Laser Melting of Tungsten Powder. *Medical Physics*, vol. 40, no. 1, pp. 012501-1 – 012501-11. ISSN 0094-2405.
- Dimitrov, D. and De Beer, N. (2014). Improvements in the Capability Profile of 3-D Printing: An Update. *South African Journal of Industrial Engineering*, vol. 25, no. August, pp. 1–12.

- Dimitrov, D., Schreve, K., de Beer, N. and Christiane, P. (2008). Three Dimensional Printing in the South African Industrial Environment. *The South African Journal of Industrial Engineering*, vol. 19, no. 1, pp. 195–213.
- Eshel, G., Levy, G.J., Mingelgrin, U. and Singer, M.J. (2004). Critical Evaluation of the Use of Laser Diffraction for Particle-Size Distribution Analysis. *Soil Science Society of America Journal*, vol. 68, no. 3, pp. 736–743. ISSN 1435-0661.
- Eso, O., Fang, Z. and Griffo, A. (2005 jul). Liquid Phase Sintering of Functionally Graded WC-Co Composites. *International Journal of Refractory Metals and Hard Materials*, vol. 23, no. 4-6, pp. 233–241. ISSN 02634368.
- Exner, H., Horn, M., Streek, A., Ullmann, F., Hartwig, L., Regenfuß, P. and Ebert, R. (2008 mar). Laser Micro Sintering: A New Method to Generate Metal and Ceramic Parts of High Resolution with Sub-Micrometer Powder. *Virtual and Physical Prototyping*, vol. 3, no. 1, pp. 3–11. ISSN 1745-2759.
- Glardon, R., Karapatis, N. and Romano, V. (2001). Influence of Nd : YAG Parameters on the Selective Laser Sintering of Metallic Powders. *CIRP Annals - Manufacturing Technology*, vol. 50, no. 1, pp. 133–136. ISSN 00078506 (ISSN).
- Gu, D. and Shen, Y. (2007). Balling phenomena during direct laser sintering of multi-component Cu-based metal powder. *Journal of Alloys and Compounds*, vol. 432, no. 1-2, pp. 163–166. ISSN 09258388.
- Gu, D. and Shen, Y. (2009). Balling phenomena in direct laser sintering of stainless steel powder: Metallurgical mechanisms and control methods. *Materials & Design*, vol. 30, no. 8, pp. 2903–2910. ISSN 02613069.
- Gu, D.D., Meiners, W., Wissenbach, K. and Poprawe, R. (2012 may). Laser additive manufacturing of metallic components: materials, processes and mechanisms. *International Materials Reviews*, vol. 57, no. 3, pp. 133–164. ISSN 0950-6608.
- Gu, D.-d., Shen, Y.-f., Dai, P. and Yang, M.-c. (2006). Microstructure and property of sub-micro WC-10 %Co particulate reinforced Cu matrix composites prepared by selective laser sintering. *Transactions of Nonferrous Metals Society of China*, vol. 16, no. 2, pp. 357–362. ISSN 10036326.
- Hareland, G. (1994). Evaluation of Flour Particle Size Distribution by Laser Diffraction, Sieve Analysis and Near-infrared Reflectance Spectroscopy.
- Hauser, C., Childs, T., Taylor, C. and Badrossamay, M. (2003). Direct Selective Laser Sintering of Tool Steel Powders to High Density. Part A: Effects of Laser Beam Width and Scan Strategy. *14th Proceedings of the Solid Freeform Fabrication Symposium*, pp. 644–655.
- Hopkinson, N. and Dickens, P. (2003). Analysis of rapid manufacturing - using layer manufacturing processes for production. *Mechanical Engineering Science*, vol. 217, no. C1, pp. 31–39. ISSN 0954-4062.
- Human, A. and Exner, H. (1997 jan). The Relationship Between Electrochemical Behaviour and In-Service Corrosion of WC Based Cemented Carbides. *International Journal of Refractory Metals and Hard Materials*, vol. 15, no. 1-3, pp. 65–71. ISSN 02634368.
- Kharanzhevskiy, E., Ipatov, A., Nikolaeva, I. and Zakirova, R. (2015). Short-Pulse Laser Sintering of Multilayer Hard Metal Coatings: Structure and Wear Behavior. *Lasers in Manufacturing and Materials Processing*, vol. 2, no. 2, pp. 91–102. ISSN 2196-7229.

- Kim, H.-C., Shon, I.-J., Garay, J. and Munir, Z. (2004 nov). Consolidation and Properties of Binderless Sub-Micron Tungsten Carbide by Field-Activated Sintering. *International Journal of Refractory Metals and Hard Materials*, vol. 22, no. 6, pp. 257–264. ISSN 02634368.
- Kim, H.-C., Yoon, J.-K., Doh, J.-M., Ko, I.-Y. and Shon, I.-J. (2006 nov). Rapid sintering process and mechanical properties of binderless ultra fine tungsten carbide. *Materials Science and Engineering: A*, vol. 435-436, pp. 717–724. ISSN 09215093.
- Kim, T., Kim, B. and Choi, J. (1997). Prediction of Die Wear in the Wire-Drawing Process. *Journal of Materials Processing Technology*, vol. 65, pp. 11–17.
- Kruth, J. (1991). Material Incess Manufacturing by Rapid Prototyping Techniques. *CIRP Annals - Manufacturing Technology*, vol. 40, no. 2, pp. 603–614.
- Kruth, J., Deckers, J., Yasa, E. and Wauthle, R. (2012). Assessing and comparing influencing factors of residual stresses in selective laser melting using a novel analysis method. *Proceedings of the Institution of Mechanical Engineers, Part B: Journal of Engineering Manufacture*, vol. 226, no. 6, pp. 980–991. ISSN 0954-4054.
- Kruth, J., Leu, M. and Nakagawa, T. (1998). Progress in Additive Manufacturing and Rapid Prototyping. *CIRP Annals - Manufacturing Technology*, vol. 47, no. 2, pp. 525–540.
- Kruth, J., Mercelis, P., Vaerenbergh, J.V., Froyen, L. and Rombouts, M. (2005). Binding Mechanisms in Selective Laser Sintering and Selective Laser Melting. *Rapid Prototyping Journal*, vol. 11, no. 1, pp. 26–36. ISSN 1355-2546.
- Kruth, J., Van der Schueren, B., Bonse, J. and Morren, B. (1996). Basic Powder Metallurgical Aspects in Selective Metal Powder Sintering. *CIRP Annals - Manufacturing Technology*, vol. 45, no. 1, pp. 183–186.
- Kruth, J., Wang, X., Laoui, T. and Froyen, L. (2003). Lasers and materials in selective laser sintering. *Assembly Automation*, vol. 23, no. 4, pp. 357–371. ISSN 0144-5154.
- Kruth, J.P., Froyen, L., Van Vaerenbergh, J., Mercelis, P., Rombouts, M. and Lauwers, B. (2004). Selective laser melting of iron-based powder. *Journal of Materials Processing Technology*, vol. 149, no. 1-3, pp. 616–622. ISSN 09240136.
- Kruth, J.P., Levy, G., Klocke, F. and Childs, T. (2007). Consolidation phenomena in laser and powder-bed based layered manufacturing. *CIRP Annals - Manufacturing Technology*, vol. 56, no. 2, pp. 730–759. ISSN 00078506.
- Kumar, S. (2009 apr). Manufacturing of WC-Co moulds using SLS machine. *Journal of Materials Processing Technology*, vol. 209, no. 8, pp. 3840–3848. ISSN 09240136.
- Kumar, S. and Pelty, L.P. (1994). High-Strength Tungsten Carbide Material for Use in Earth-Boring Bits.
- Lee, K.-H., Lee, S.-K. and Kim, B.-M. (2012 jul). Advanced Simulation of Die Wear Caused by Wire Vibrations During Wire-Drawing Process. *Transactions of Nonferrous Metals Society of China*, vol. 22, no. 7, pp. 1723–1731. ISSN 10036326.
- Levy, G.N., Schindel, R. and Kruth, J. (2003). Rapid Manufacturing and Rapid Tooling with Layer Manufacturing (LM) Technologies, State of the Art and Future Perspectives. *CIRP Annals - Manufacturing Technology*, vol. 52, no. 2, pp. 589–609.

- Li, R., Shi, Y., Liu, J., Xie, Z. and Wang, Z. (2010 sep). Selective Laser Melting W-10 wt.% Cu Composite Powders. *The International Journal of Advanced Manufacturing Technology*, vol. 48, no. 5-8, pp. 597–605. ISSN 0268-3768.
- Marcantonio, G. (2014). *Development of framework for the manufacture of customized titanium cervical cage implants using additive manufacturing*. Masters Thesis, Stellenbosch University.
- Martins, V., Rodrigues, W.C., Ferrandini, P.L., Villarinho, D.J., Knörschild, G.H. and Schaeffer, L. (2011). Comparative studies of WC-Co and WC-Co-Ni composites obtained by conventional powder metallurgy. *Materials Research*, vol. 14, no. 2, pp. 274–279. ISSN 1516-1439.
- Mason, R.L., Gunst, R.F. and Hess, J.L. (2003). Fractional Factorial Experiments. In: *Statistical Design and Analysis of Experiments: With Applications to Engineering and Science*, 2nd edn, chap. 7, pp. 228–270. Wiley-Interscience, Hoboken. ISBN 0471372161.
- Masuda, M., Kuroshima, Y. and Chujo, Y. (1993). Failure of Tungsten Carbide-Cobalt Alloy Tools in Machining of Carbon Materials. *Wear*, vol. 169, pp. 135–140.
- McCandlish, L., Kear, B. and Kim, B. (1992). Processing and properties of nanostructured WC-Co. *Nanostructured Materials*, vol. 1, pp. 119–124.
- Moammer, A. (2011). *Thermal management of moulds and dies: a contribution to improved design and manufacture of tooling for injection moulding*. Masters Thesis, Stellenbosch University.
- Mumtaz, K.A., Erasenthiran, P. and Hopkinson, N. (2008). High density selective laser melting of Waspaloy. *Journal of Materials Processing Technology*, vol. 195, no. 1-3, pp. 77–87. ISSN 09240136.
- Murr, L.E., Gaytan, S.M., Ramirez, D.a., Martinez, E., Hernandez, J., Amato, K.N., Shindo, P.W., Medina, F.R. and Wicker, R.B. (2012 jan). Metal Fabrication by Additive Manufacturing Using Laser and Electron Beam Melting Technologies. *Journal of Materials Science & Technology*, vol. 28, no. 1, pp. 1–14. ISSN 10050302.
- Ott, M. and Zaeh, M.F. (2010). Multi-Material Processing in Additive Manufacturing. In: *SFF Symposium*, pp. 195–203.
- Paul, C. and Khajepour, A. (2008 jul). Automated Laser Fabrication of Cemented Carbide Components. *Optics & Laser Technology*, vol. 40, no. 5, pp. 735–741. ISSN 00303992.
- Pham, D. and Gault, R. (1998 oct). A Comparison of Rapid Prototyping Technologies. *International Journal of Machine Tools and Manufacture*, vol. 38, no. 10-11, pp. 1257–1287. ISSN 08906955.
- Prakash, L.J. (1995 jan). Application of Fine Grained Tungsten Carbide Based Cemented Carbides. *International Journal of Refractory Metals and Hard Materials*, vol. 13, no. 5, pp. 257–264. ISSN 02634368.
- Rawat, S. and Attia, H. (2009 jun). Wear Mechanisms and Tool Life Management of WC-Co Drills During Dry High Speed Drilling of Woven Carbon Fibre Composites. *Wear*, vol. 267, no. 5-8, pp. 1022–1030. ISSN 00431648.
- Santos, E.C., Shiomi, M., Osakada, K. and Laoui, T. (2006). Rapid manufacturing of metal components by laser forming. *International Journal of Machine Tools and Manufacture*, vol. 46, no. 12-13, pp. 1459–1468. ISSN 08906955.

- Schubert, W., Bock, A. and Lux, B. (1995). General aspects and limits of conventional ultrafine WC powder manufacture and hardmetal production. *International Journal of Refractory Metals and Hard Materials*, vol. 13, no. 5, pp. 281–296. ISSN 02634368.
- Schubert, W., Neumeister, H., Kingler, G. and Lux, B. (1998). Hardness to toughness relationship of fine-grained WC-Co hardmetals. *International Journal of Refractory Metals and Hard Materials*, vol. 16, no. 2, pp. 133–142. ISSN 02634368.
- Senthilkumaran, K., Pandey, P.M. and Rao, P.V.M. (2009). Influence of building strategies on the accuracy of parts in selective laser sintering. *Materials and Design*, vol. 30, no. 8, pp. 2946–2954. ISSN 02641275.
- Shaw, M., Stableford, W. and Sansome, D. (1970 jun). Critical Review of Drawing with Particular Reference to Lubrication. *International Journal of Machine Tool Design and Research*, vol. 10, no. 2, pp. 203–212. ISSN 00207357.
- Shiomi, M., Osakada, K., Nakamura, K., Yamashita, T. and Abe, F. (2004). Residual Stress within Metallic Model Made by Selective Laser Melting Process. *Annals of the CIRP*, vol. 53, no. 1, pp. 195–198. ISSN 00078506.
- Shiomi, M., Yoshidome, A., Abe, F. and Osakada, K. (1999). Finite element analysis of melting and solidifying processes in laser rapid prototyping of metallic powders. *International Journal of Machine Tools and Manufacture*, vol. 39, no. 2, pp. 237–252. ISSN 08906955.
- Simchi, A. (2006). Direct laser sintering of metal powders: Mechanism, kinetics and microstructural features. *Materials Science and Engineering A*, vol. 428, no. 1-2, pp. 148–158. ISSN 09215093.
- Sinirlioglu, M.C. (2009). Rapid Manufacturing of Dental and Medical Parts via LASERCUSING Technology using Titanium and CoCr Powder Materials. In: *US-Turkey Workshop on Rapid Technologies*, pp. 89–92.
- Tolochko, N., Mozzharov, S., Laoui, T. and Froyen, L. (2003). Selective laser sintering of single and two component metal powders. *Rapid Prototyping Journal*, vol. 9, no. 2, pp. 68–78. ISSN 1355-2546.
- Tolochko, N.K., Mozzharov, S.E., Yadroitsev, I.a., Laoui, T., Froyen, L., Titov, V.I. and Ignatiev, M.B. (2004). Balling processes during selective laser treatment of powders. *Rapid Prototyping Journal*, vol. 10, no. 2, pp. 78–87. ISSN 1355-2546.
- Upadhyaya, G.S. (1998). Sintering Behaviour of Cemented Carbides. In: *Cemented Tungsten Carbides*, chap. 5, pp. 138–165. Noyes Publications.
- Upadhyaya, G.S. (2001). Materials Science of Cemented Carbides - An Overview. *Materials and Design*, vol. 22, pp. 483–489.
- van Staden, A.C. (2013). *Conformal Cooling and Metal Additive Manufacturing for Enhanced Performance in Wire-Drawing Dies*. Undergraduate, Stellenbosch University.
- Wang, X., Hwang, K.S., Koopman, M., Fang, Z.Z. and Zhang, L. (2013 jan). Mechanical Properties and Wear Resistance of Functionally Graded WC-Co. *International Journal of Refractory Metals and Hard Materials*, vol. 36, pp. 46–51. ISSN 02634368.
- Wang, X.C., Laoui, T., Bonse, J., Kruth, J., Lauwers, B. and Froyen, L. (2002 mar). Direct Selective Laser Sintering of Hard Metal Powders: Experimental Study and Simulation. *The International Journal of Advanced Manufacturing Technology*, vol. 19, no. 5, pp. 351–357. ISSN 0268-3768.

- Webb, P.A. (2000). A Primer on Particle Sizing by Static Light Scattering.
- Wentzel, E. and Allen, C. (1997). The Erosion-Corrosion Resistance of Tungsten-Carbide Hard Metals. *International Journal of Refractory Metals and Hard Materials*, vol. 15, pp. 81–87.
- Wohlers, T. and Gornet, T. (2012). Wohlers Report 2012 - Additive Manufacturing and 3D Printing State of the Industry. Tech. Rep., Wohlers Associates, Inc., Fort Collins.
- Yadroitsev, I., Bertrand, P. and Smurov, I. (2007a). Parametric analysis of the selective laser melting process. *Applied Surface Science*, vol. 253, no. 19, pp. 8064–8069. ISSN 01694332.
- Yadroitsev, I., Gusarov, a., Yadroitsava, I. and Smurov, I. (2010). Single track formation in selective laser melting of metal powders. *Journal of Materials Processing Technology*, vol. 210, no. 12, pp. 1624–1631. ISSN 09240136.
- Yadroitsev, I. and Smurov, I. (2010). Selective laser melting technology: From the single laser melted track stability to 3D parts of complex shape. *Physics Procedia*, vol. 5, pp. 551–560. ISSN 18753884.
- Yadroitsev, I. and Smurov, I. (2011). Surface morphology in selective laser melting of metal powders. *Physics Procedia*, vol. 12, pp. 264–270. ISSN 18753884.
- Yadroitsev, I., Thivillon, L., Bertrand, P. and Smurov, I. (2007b). Strategy of manufacturing components with designed internal structure by selective laser melting of metallic powder. *Applied Surface Science*, vol. 254, no. 4, pp. 980–983. ISSN 01694332.
- Yasa, E., Deckers, J., Craeghs, T., Badrossamay, M. and Kruth, J. (2009). Investigation on occurrence of elevated edges in selective laser melting. In: *Twentieth Annual International Solid Freeform Fabrication Symposium*, pp. 180–192.
- Yasa, E. and Kruth, J. (2011). Application of Laser Re-Melting on Selective Laser Melting Parts. *Advances in Production Engineering and Management*, vol. 6, no. 4, pp. 259–270.
- Zaeh, M.F. and Ott, M. (2011 jan). Investigations on Heat Regulation of Additive Manufacturing Processes for Metal Structures. *CIRP Annals - Manufacturing Technology*, vol. 60, no. 1, pp. 259–262. ISSN 00078506.
- ZCorporation (2004). 3D Printing in Manufacturing, Architecture, and Education. Tech. Rep., ZCorporation, Massachusetts.
- Zhang, D., Cai, Q. and Liu, J. (2012 deca). Formation of Nanocrystalline Tungsten by Selective Laser Melting of Tungsten Powder. *Materials and Manufacturing Processes*, vol. 27, no. 12, pp. 1267–1270. ISSN 1042-6914.
- Zhang, D., Cai, Q., Liu, J., He, J. and Li, R. (2012 novb). Microstructural Evolvement and Formation of Selective Laser Melting W-Ni-Cu Composite Powder. *The International Journal of Advanced Manufacturing Technology*, vol. 67, no. 9-12, pp. 2233–2242. ISSN 0268-3768.
- Zhang, D., Cai, Q., Liu, J. and Li, R. (2010 aug). Research on Process and Microstructure Formation of W-Ni-Fe Alloy Fabricated by Selective Laser Melting. *Journal of Materials Engineering and Performance*, vol. 20, no. 6, pp. 1049–1054. ISSN 1059-9495.

Appendices

Appendix A

Laser Diffraction Analysis report

The Laser Diffraction Analysis report is presented here. It contains the complete report set for the material analysis carried out using a Saturn Digisizer II from Micromeritics. The results from three separate tests are shown, including the averaged results, and finally the Goodness of Fit test results are shown which validate, statistically, the fitted model. For all three tests the Volume Frequency versus Particle Diameter is graphed, as well as the Cumulative Finer Volume Percent versus Particle Diameter.



Micromeritics Instrument Corporation

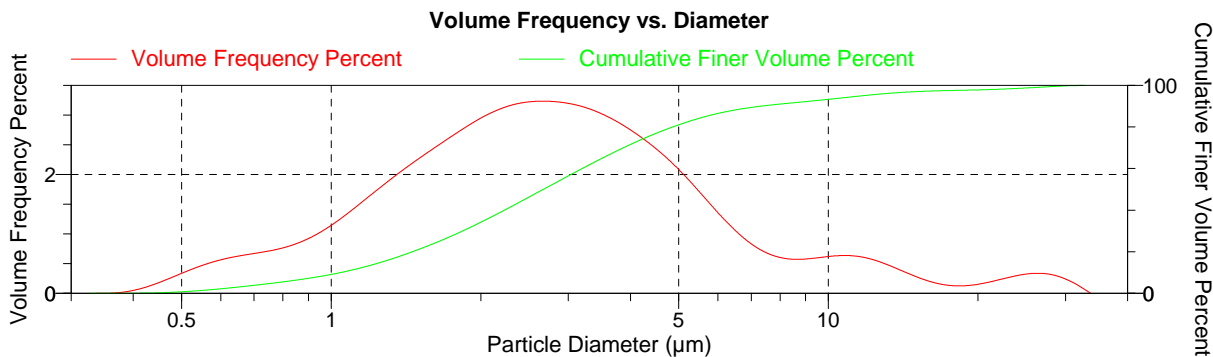
Saturn DigiSizer 5200 V1.10 Saturn DigiSizer 5200 V1.10 5200 LSHU V2.01 S/N 216 Page 1

Sample: WC 6.6 wt% Co
 Operator: H Botha, Prosesing
 Submitter: Coetzee van Staden, Meg Ing
 File: C:\5200\DATA\STD\002-890.SMP

Test Number: 3 Model: (1.768, 1.000000), 1.331
 Analyzed: 2015/03/25 12:59:54PM Material: Tungsten / Water
 Reported: 2015/03/26 15:43:22PM Background: Water RI 1.331
 Background: 2015/03/25 9:04:37PM Smoothing: Medium

Comments: 0.0005% TSP

Combined Report



Summary Report

Analysis Conditions

FlowRate: 12.0 l/m Ultrasonic intensity: Not Used
 Circulation time: 60 sec Ultrasonic time: Not Used

Sample

Sample Concentration: 0.00178 %
 Obscuration: 14.1 %

Volume Distribution Arithmetic Statistics

Mean	3.900	Std Dev of 3	0.134	Mode	2.677	Std Dev of 3	0.000
Median	2.671		0.036				

Selected Sizes

Diameter (µm)	Percent Finer
100.0	100.0
50.00	100.0
20.00	97.8
10.00	93.3
1.000	9.1

Peaks

Peak Number	% of Dist. of Dist.*	% of Dist. Std Dev of 3	Mean	Mean Std Dev of 3	Median	Median Std Dev of 3	Mode
1	91.9	N/A	2.851	N/A	2.484	N/A	2.677
2	5.8	N/A	11.86	N/A	11.43	N/A	10.66

* Peaks must comprise at least 5.00 % of the distribution.



Micromeritics Instrument Corporation

Saturn DigiSizer 5200 V1.10

Saturn DigiSizer 5200 V1.10

5200 LSHU V2.01 S/N 216

Page 2

Sample: WC 6.6 wt% Co
 Operator: H Botha, Prosesing
 Submitter: Coetzee van Staden, Meg Ing
 File: C:\5200\DATA\STD\002-890.SMP

Test Number: 3

Analyzed: 2015/03/25 12:59:54PM

Reported: 2015/03/26 15:43:22PM

Background: 2015/03/25 9:04:37PM

Model: (1.768, 1.000000), 1.331

Material: Tungsten / Water

Background: Water RI 1.331

Smoothing: Medium

Comments: 0.0005% TSP

Report by Size Table

Low Diameter (µm)	Cumulative Volume Finer (Percent)	Low Diameter (µm)	Cumulative Volume Finer (Percent)	Low Diameter (µm)	Cumulative Volume Finer (Percent)	Low Diameter (µm)	Cumulative Volume Finer (Percent)
30.000	99.8	7.000	89.4	2.000	34.2	0.600	2.2
20.000	97.8	6.000	86.5	1.000	9.1	0.500	0.7
10.000	93.3	5.000	81.0	0.900	7.2	0.400	0.0
9.000	92.2	4.000	71.6	0.800	5.5		
8.000	91.0	3.000	56.5	0.700	3.8		



Micromeritics Instrument Corporation

Saturn DigiSizer 5200 V1.10 Saturn DigiSizer 5200 V1.10 5200 LSHU V2.01 S/N 216 Page 3

Sample: WC 6.6 wt% Co
 Operator: H Botha, Prosesing
 Submitter: Coetzee van Staden, Meg Ing
 File: C:\5200\DATA\STD\002-890.SMP

Test Number: 3 Model: (1.768, 1.000000), 1.331
 Analyzed: 2015/03/25 12:59:54PM Material: Tungsten / Water
 Reported: 2015/03/26 15:43:22PM Background: Water RI 1.331
 Background: 2015/03/25 9:04:37PM Smoothing: Medium

Comments: 0.0005% TSP

Report by Volume Percent

Low Diameter (µm)	Cumulative Volume Finer (Percent)	Low Diameter (µm)	Cumulative Volume Finer (Percent)	Low Diameter (µm)	Cumulative Volume Finer (Percent)
7.319	90.0	2.671	50.0	1.045	10.0



Micromeritics Instrument Corporation

Saturn DigiSizer 5200 V1.10

Saturn DigiSizer 5200 V1.10

5200 LSHU V2.01 S/N 216

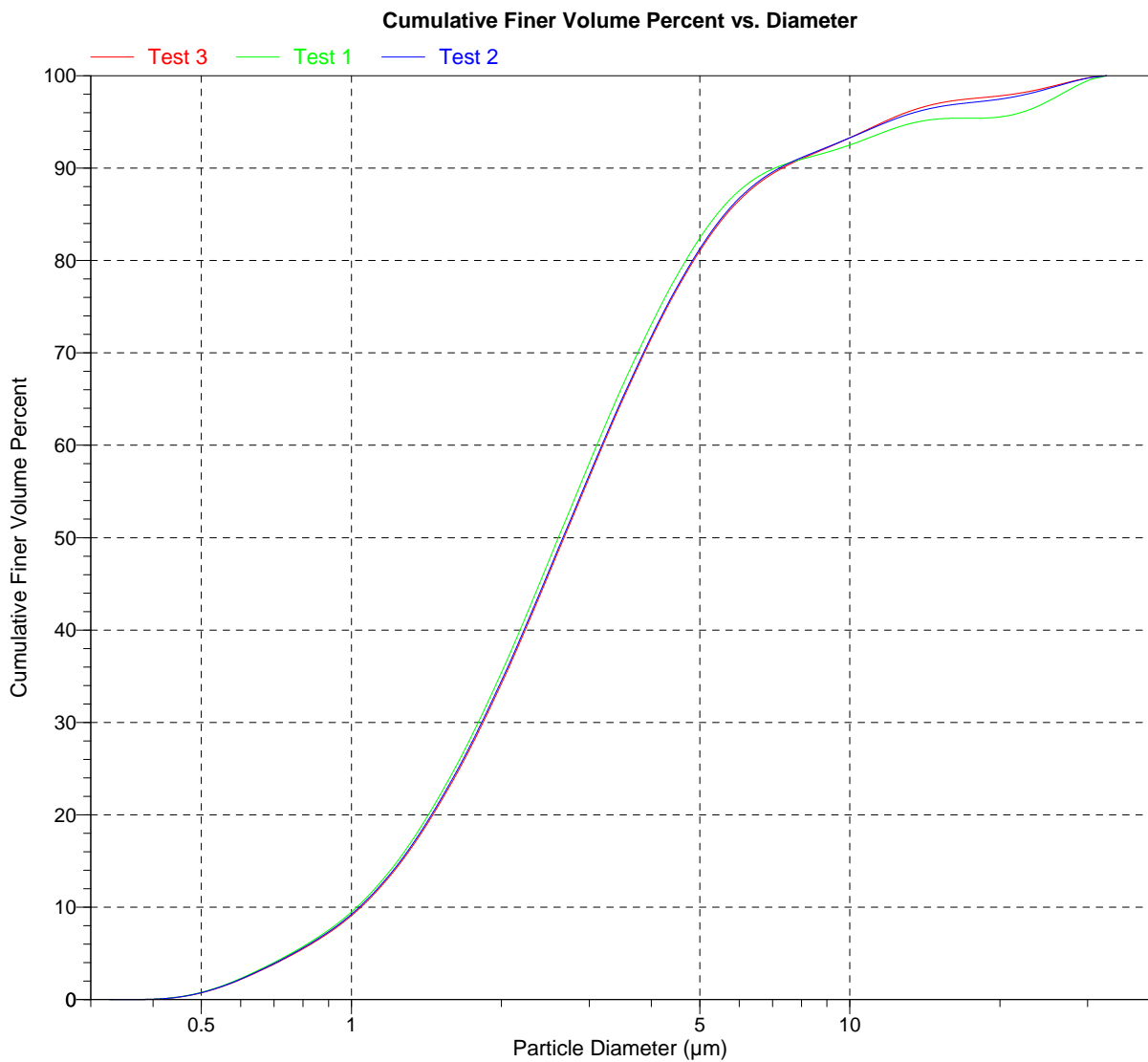
Page 4

Sample: WC 6.6 wt% Co
Operator: H Botha, Prosesing
Submitter: Coetzee van Staden, Meg Ing
File: C:\5200\DATA\STD\002-890.SMP

Test Number: 3
Analyzed: 2015/03/25 12:59:54PM
Reported: 2015/03/26 15:43:22PM
Background: 2015/03/25 9:04:37PM

Model: (1.768, 1.000000), 1.331
Material: Tungsten / Water
Background: Water RI 1.331
Smoothing: Medium

Comments: 0.0005% TSP





Micromeritics Instrument Corporation

Saturn DigiSizer 5200 V1.10

Saturn DigiSizer 5200 V1.10

5200 LSHU V2.01 S/N 216

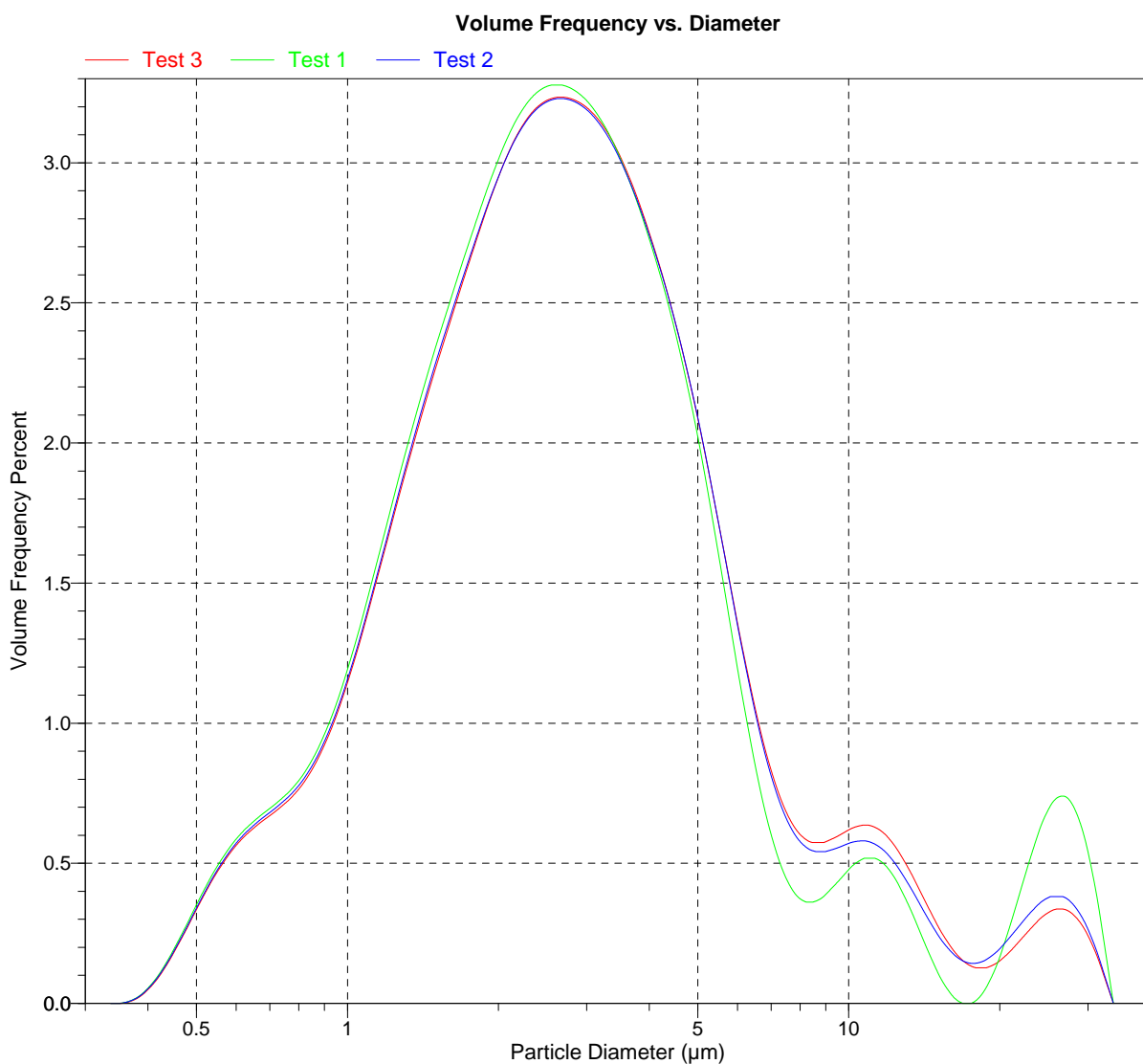
Page 5

Sample: WC 6.6 wt% Co
Operator: H Botha, Prosesing
Submitter: Coetzee van Staden, Meg Ing
File: C:\5200\DATA\STD\002-890.SMP

Test Number: 3
Analyzed: 2015/03/25 12:59:54PM
Reported: 2015/03/26 15:43:22PM
Background: 2015/03/25 9:04:37PM

Model: (1.768, 1.000000), 1.331
Material: Tungsten / Water
Background: Water RI 1.331
Smoothing: Medium

Comments: 0.0005% TSP





Micromeritics Instrument Corporation

Saturn DigiSizer 5200 V1.10

Saturn DigiSizer 5200 V1.10

5200 LSHU V2.01 S/N 216

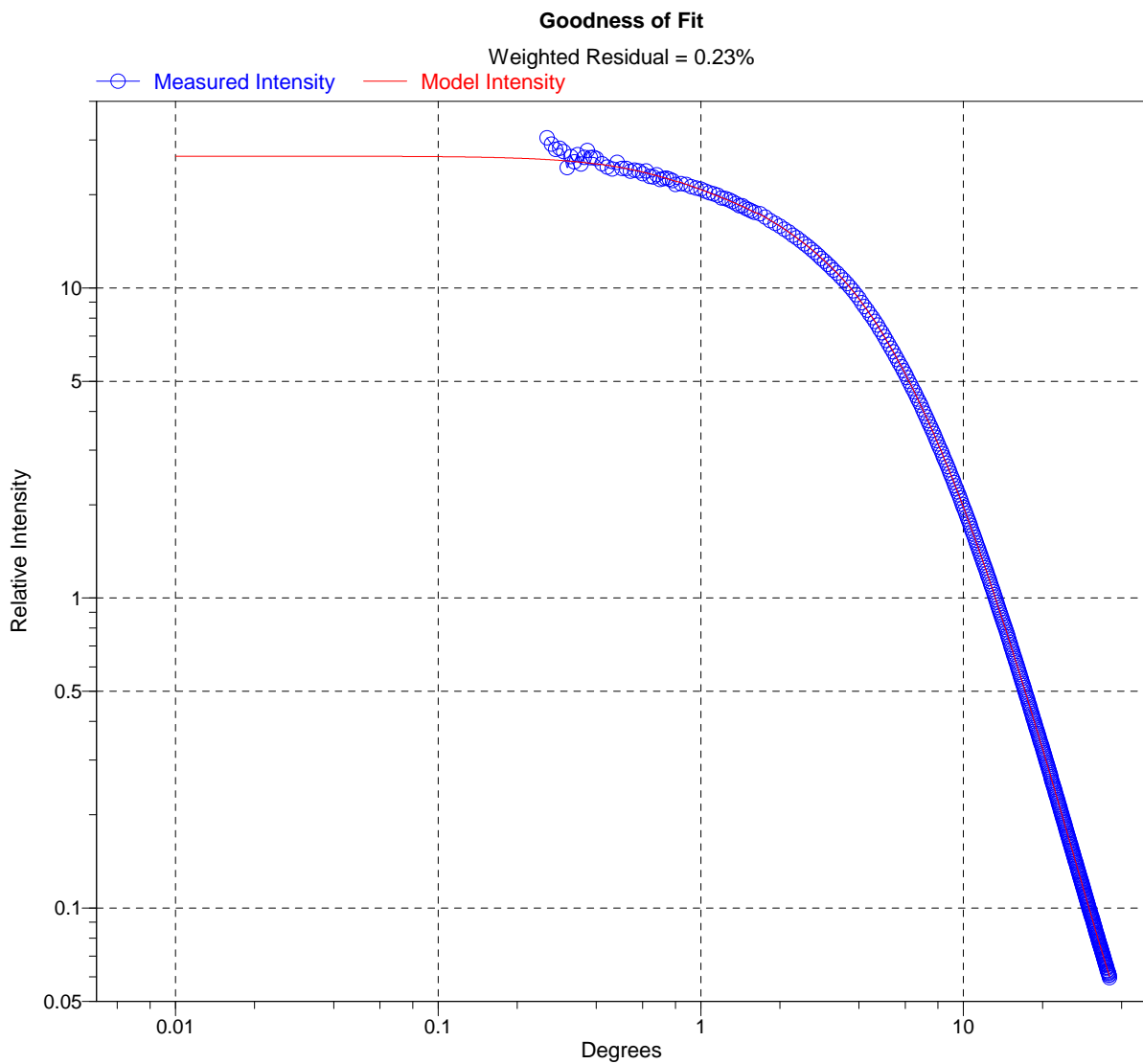
Page 6

Sample: WC 6.6 wt% Co
Operator: H Botha, Prosesing
Submitter: Coetzee van Staden, Meg Ing
File: C:\5200\DATA\STD\002-890.SMP

Test Number: 3
Analyzed: 2015/03/25 12:59:54PM
Reported: 2015/03/26 15:43:22PM
Background: 2015/03/25 9:04:37PM

Model: (1.768, 1.000000), 1.331
Material: Tungsten / Water
Background: Water RI 1.331
Smoothing: Medium

Comments: 0.0005% TSP



Appendix B

Concept Laser CL20ES data sheet

The material data sheet for the standard Stainless Steel (CL20ES) powder, produced and supplied by Concept Laser GmbH for the M2 LaserCusing[®], is presented here. This demonstrates the technical specifications associated with a standard, optimised material used to produce functional components.

CL 20ES Stainless steel

Stainless steel (powder), chemical composition according to 1.4404, X 2 CrNiMo 17 13 2, 316L

CL 20ES is an austenitic stainless steel for the production of functional parts or components for pre-production moulds.

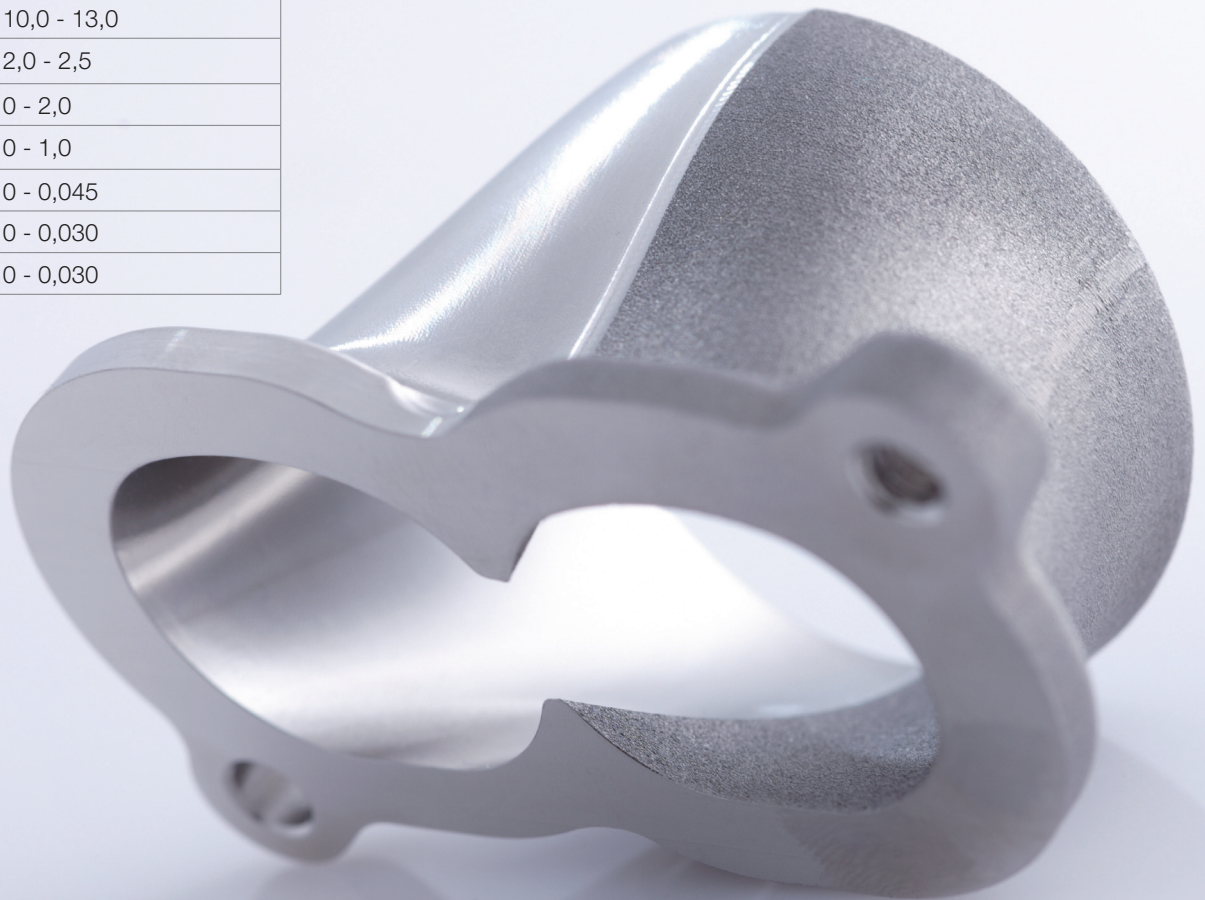
26

Fe

55,847

CHEMICAL COMPOSITION

Component	Indicative value (%)
Fe	Balance
Cr	16,5 - 18,5
Ni	10,0 - 13,0
Mo	2,0 - 2,5
Mn	0 - 2,0
Si	0 - 1,0
P	0 - 0,045
C	0 - 0,030
S	0 - 0,030



RANGE OF APPLICATION

The material is used for manufacturing acid- and corrosion resistant prototypes, unique or series production parts in the following fields: Plant engineering, automotive industry, medical technology, jewellery and components for moulds.

TECHNICAL DATA

Yield Point R_{e}^1	470 N/mm ²
Tensile Strength R_m^1	570 N/mm ²
Elongation A ^{1,2}	> 15 %
Young's modulus ³	approx. $200 \cdot 10^3$ N/mm ²
Thermal conductivity λ^3	approx. 15 W/mK
Hardness ⁴	20 HRC

¹ Tensile test at 20°C according to DIN EN 50125

² By using a special heat treatment a higher elongation can be achieved.

³ Specification according to the material manufacturer's data sheet.

⁴ Hardness test according to DIN EN ISO 6508

CL 20ES

Stainless steel

MICROSECTION

Test piece (x 20 magnification)



Test piece (x 100 magnification)



HEAT TREATMENT

Optional for parts that are sensitive to warpage:
Heat up in 3 hours to 550°C. Maintain temperature for 6 hours. Subsequently allow the component cooling down in the oven or at ambient atmosphere.

MICROSTRUCTURE

Components made from stainless steel CL 20ES display a homogeneous, dense structure after they are manufactured by means of the metal laser melting process LaserCUSING®.

Concept Laser GmbH
An der Zeil 8
D 96215 Lichtenfels

Sales Department
info@concept-laser.de
T: +49 (0)95 71.949 238
F: +49 (0)95 71.949 249

A company of

HOFMANN
innovation group

Appendix C

Profilometer analysis - equipment and software setup

The software and hardware setup for the profilometer analysis is illustrated here. Images taken from the software dashboard, as well as the physical sample setup and probe specification plaque is shown to demonstrate the procedure followed during the analysis.

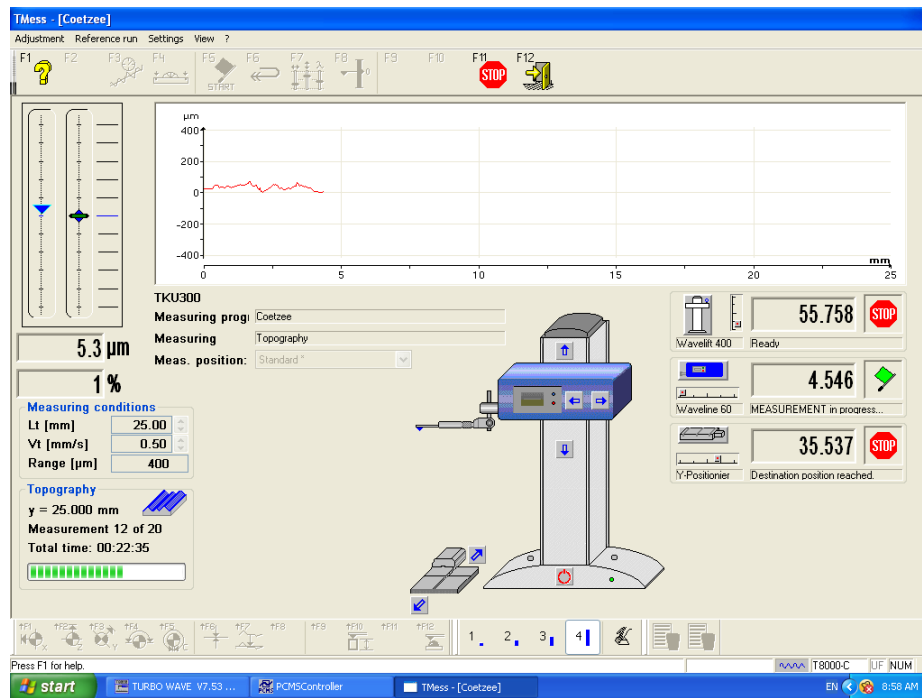


Figure C.1: Process monitoring interface for the measurement software.

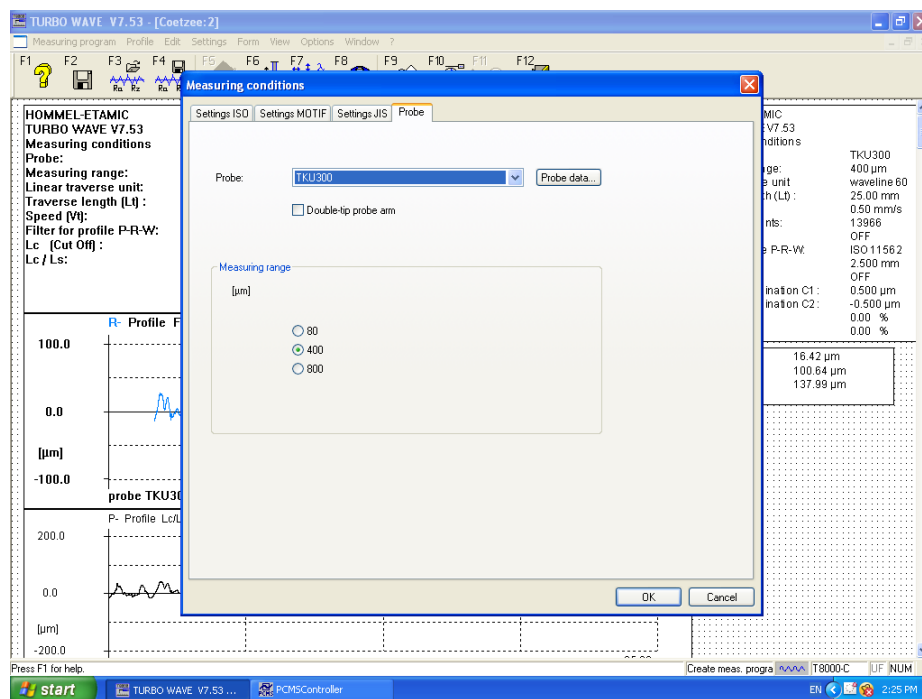


Figure C.2: Probe selection and measurement range setup.

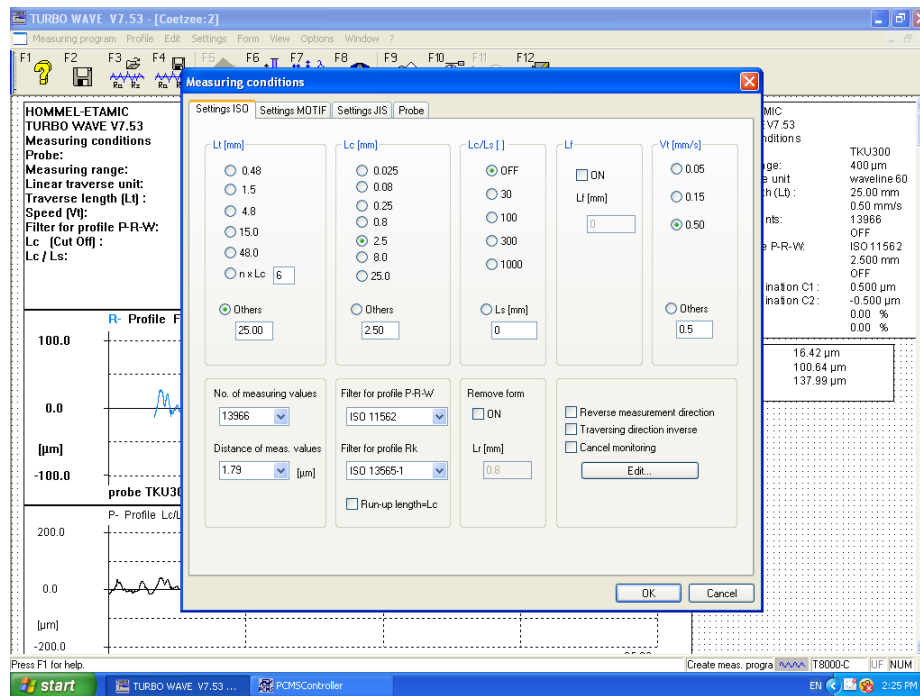


Figure C.3: Measuring conditions selection interface for the measurement software.

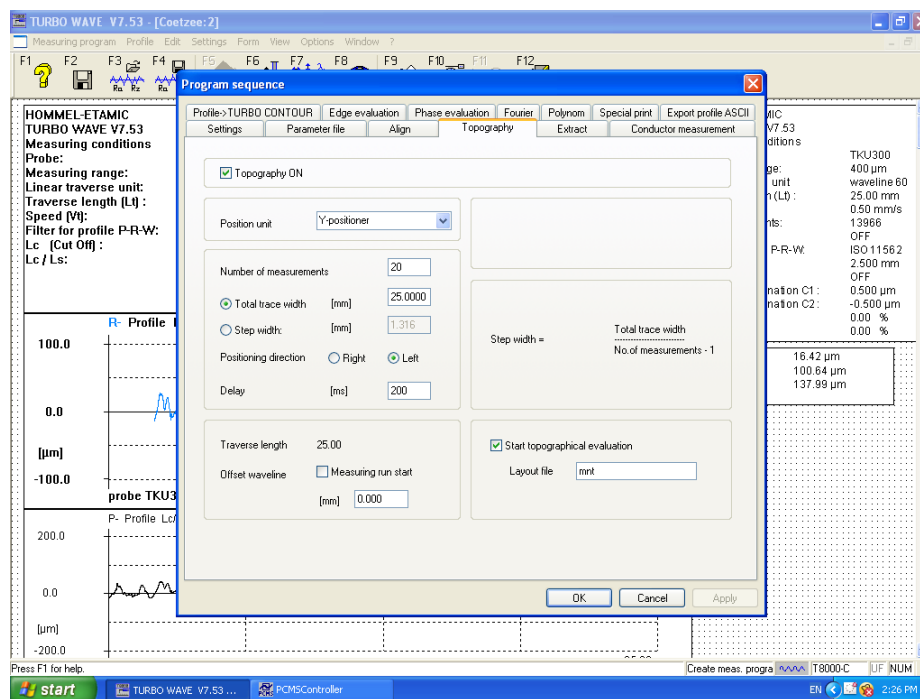


Figure C.4: Topography settings in the program sequence for the measurement software.

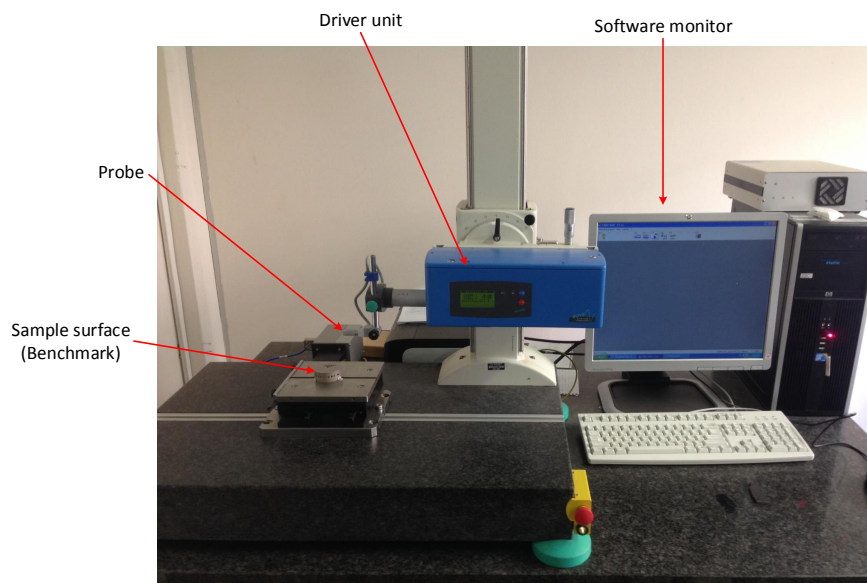


Figure C.5: Profilometer equipment setup.



Figure C.6: Probe set specifications plaque.

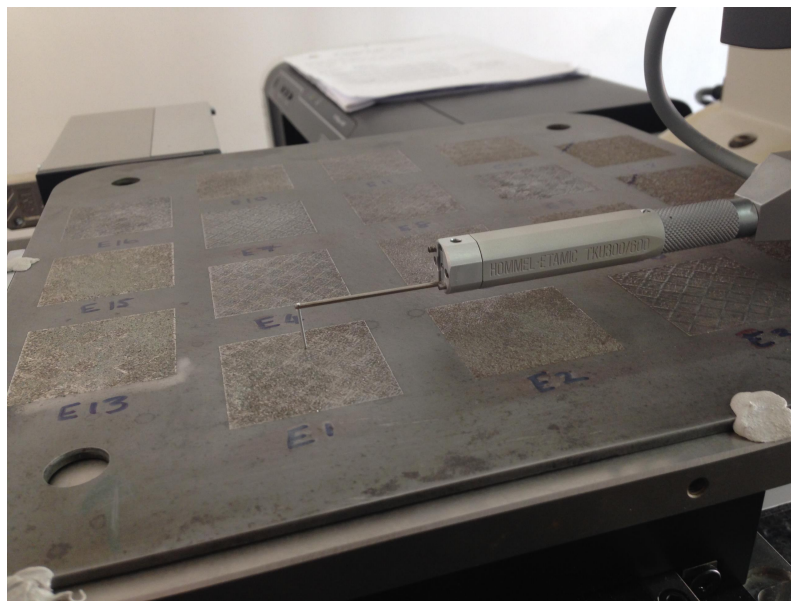


Figure C.7: Sample profile measurement example.

Appendix D

Screening experiment results - MODDE example

The following images are presented as demonstrative aids, illustrating and describing the analysis tools (and associated outputs) embedded in the MODDE DOE software. The example work is based on the Willgerodt Kindler reaction studied by Torbjörn Lundstadt in 1986. The study was completed towards obtaining his PhD. This is presented as a tutorial by Umetrics intended as training material to familiarise the analyst with the DOE environment.

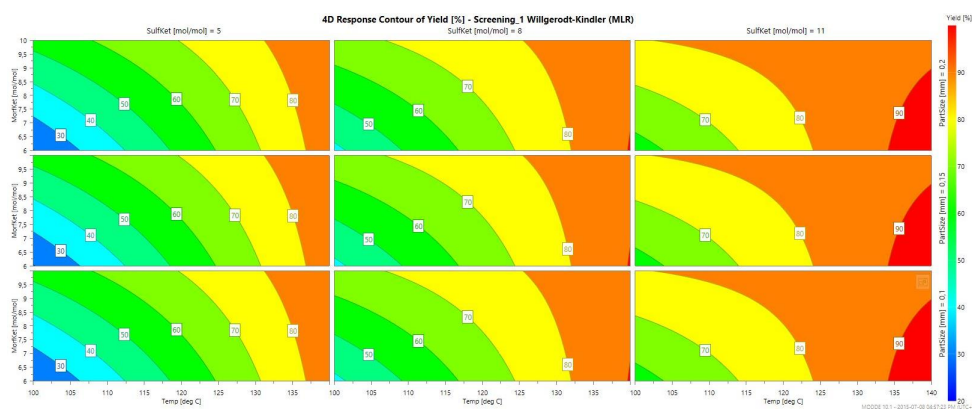


Figure D.1: 4D contour plot.

Figure D.1 illustrates the 4-dimensional (4D) contour plot analysis tool embedded in MODDE. The contour plot illustrates the effect that varying three factors has on the response variable. From this image it is possible to determine what the factor values should be to obtain a theoretically optimal response (in this case a 100% reaction yield). As stated, however, this is merely theoretical and system and factor constraints preclude the use of certain factor values and combinations. It should be noted that the use of a 4D contour plot is only useful when there are four factors being varied in the analysis. In this work, only three factors are varied, therefore a

3D contour plot is presented. The analysis and interpretation of the plot remains the same.

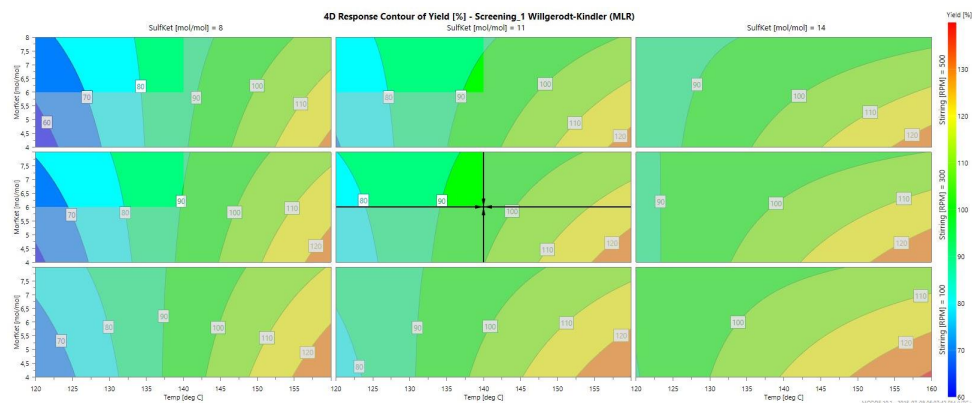


Figure D.2: 4D contour plot indicating the optimal setpoint.

Figure D.2 shows another 4D contour plot, this one showing the best result (i.e. the factor values resulting in the best response values). The four arrows in the centre of the graph indicate the optimal factor settings (also known as the setpoint) and the expected optimal yield percentage.

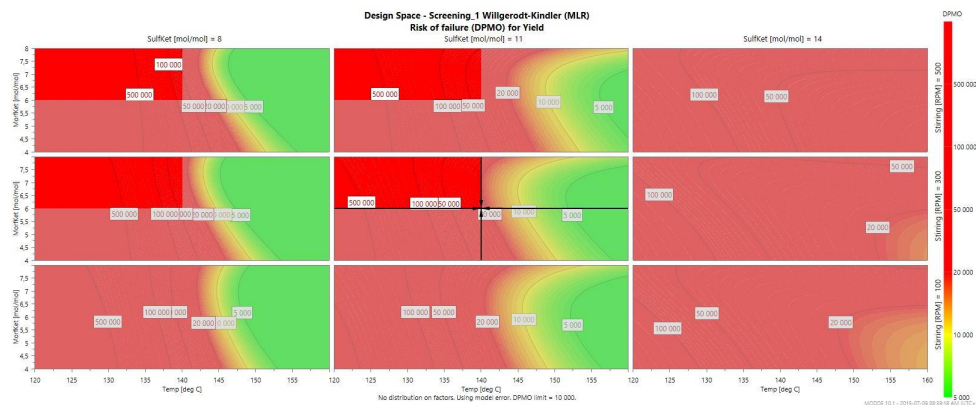


Figure D.3: 4D contour plot of defect per million opportunities (DPMO) for the given setpoint.

Figure D.3 demonstrates a 4D contour plot used to analyse the defects per million opportunities (DPMO), corresponding to the optimal setpoint. In this case approximately 20,000/1,000,000 (or 2%) defects would be expected for this reaction. It should be noted that, without the use or addition of centre points the model is

unable to form adequate predictions regarding process failures and can therefore not be reported in this work.

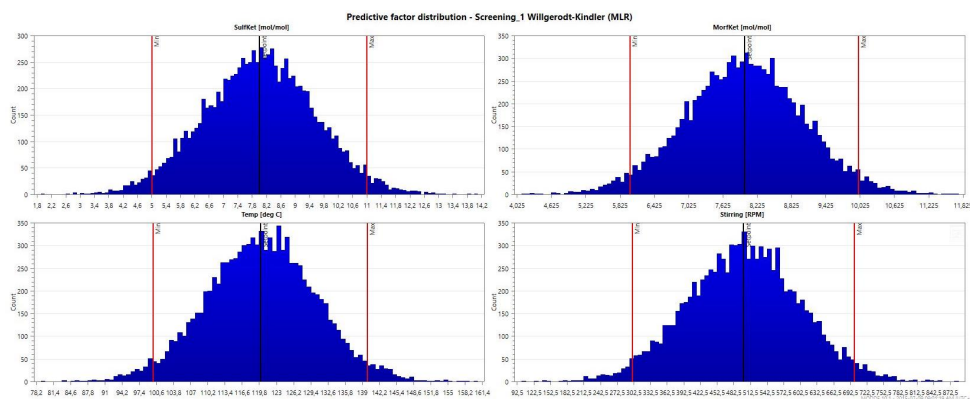


Figure D.4: Factor distribution plot.

Figure D.4 shows the predictive factor distribution, indicating the 95% confidence bands, which is used to generate the predictive response distribution shown in Figure D.5. The factor distribution is used by MODDE as the acceptable range for factor variation during response optimisation and setpoint analysis.

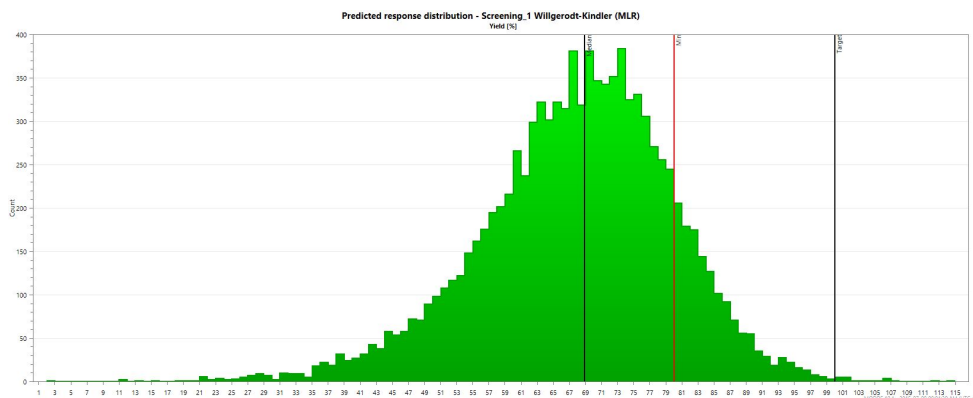


Figure D.5: Response distribution plot.

Figure D.5 demonstrates the response distribution plot generated during setpoint analysis. The graph shows how the response value varies according to variations in the factor settings, based on the factor distributions shown in Figure D.4. Again, the responses are shown within 95% confidence bands and the target value as well as minimum/maximum values are indicated. This plot, for example, shows that the reaction is unlikely to reach the target yield percentage. However, a correct

parameter combination suggests that at least a 95% yield can be achieved (based on the optimiser results).

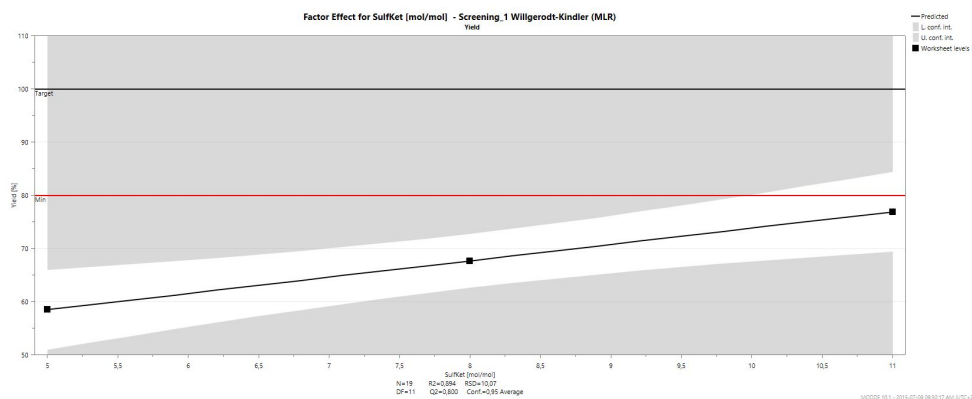


Figure D.6: Factor effect plot for the SulfKet [mol/mol] factor, provided in a 95% confidence band.

Figure D.6 shows the factor effect plot for a specific factor associated with the reaction in this example analysis. This plot shows, within 95% confidence bands, what the individual factor effect is on the yield percentage. This plot can be generated for any and all factors involved in the analysis.

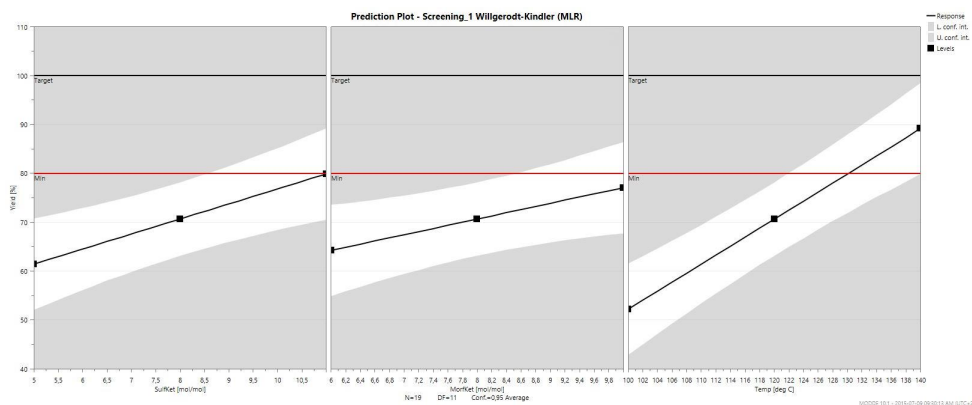


Figure D.7: Yield percentage prediction plot for three factors, provided in a 95% confidence band.

Figure D.7 shows the combined factor effects for three factors, within 95% confidence bands. Here, the maximum yield percentage corresponds to the limiting factor. That is, the factor that indicates the lowest maximum yield is the limiting factor.

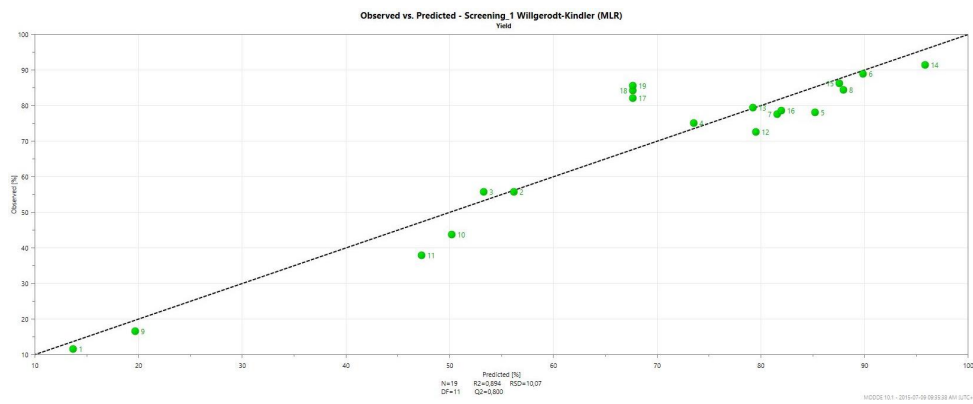


Figure D.8: Observed versus predicted yield percentage plot used in regression analysis.

Figure D.8 shows the Observed versus Predicted plot for the example analysis. It is used to fit a regression line to the data which forms the basis of the prediction model. As in this case, plots where the graphed points are close to the regression line indicates a good model. Here it is important to note that models having $Df < 3$ will implicitly give a perfect fit.

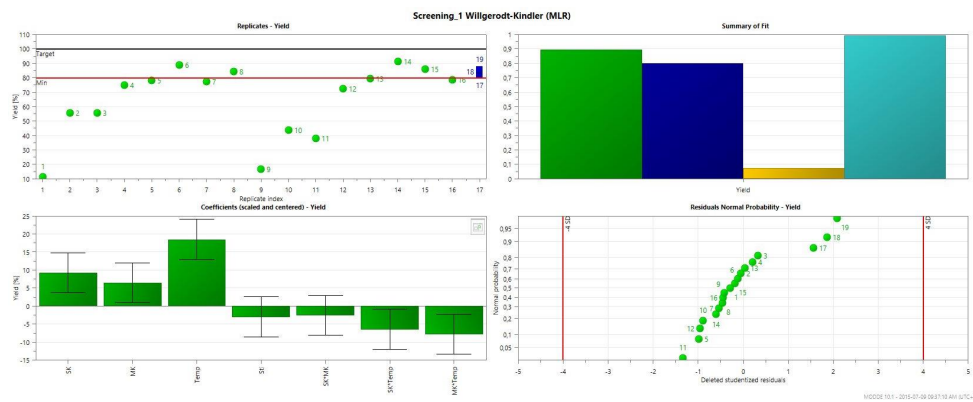


Figure D.9: Summary plot showing the Replicates, Summary of fit, Coefficients, and Residuals normal probability plots.

Figure D.9 is a summary plot that shows the Replicates, Summary of fit, Coefficients, and Residuals normal probability plots for the example analysis. Generally this will be used for a quick analysis to determine key aspects of the model (e.g. validity). The plots contained herein are described and explained in section 4.2.4.4 on page 68.

Figure D.10 shows the tabulated alternate setpoints that are evaluated during the optimisation process. Two important statistics are used to determine which

	1	2	3	4	5	6	7	8	9	10
	SulfKet	MorfKet	Temp	PartSize	Stirring	Yield	Iterations	log(D)	DPMO	Cpk (Yield)
1	10,9638	6,00152	139,997		301,569	95,7384	11	-1,34292	20900	0,685368
2	10,7994	6,11717	139,967		308,37	95,0988	13	-1,22146	20800	0,685168
3	10,9972	6,00025	139,685		300,161	95,5116	11	-1,29788	24800	0,664821
4	11	6,1874	140		320,204	95,1611	13	-1,23257	22200	0,681284
5	10,9958	6,00075	139,998		300,02	95,8207	11	-1,35986	22600	0,682727
6	10,6951	6,08729	139,837		307,918	94,8502	92	-1,17848	21900	0,67484
7	10,6227	6,17888	139,668		302,535	94,4724	91	-1,11699	24300	0,663881
8	11	6,36366	140		335,442	94,5866	15	-1,13511	23500	0,674961
9	10,7824	6,00035	139,999		300,043	95,4447	11	-1,28503	21300	0,683599
10	10,9621	7,28603	139,998		302,379	93,2207	24	-0,939688	22700	0,685778
11	11	6,00061	139,619		300,171	95,4504	11	-1,28611	23800	0,6645
12	10,9953	6,26984	140		300,637	95,2842	11	-1,25495	20500	0,689147
13	10,9924	6,18578	139,454		303,888	94,8736	93	-1,18244	25200	0,664598
14	10,9843	6,22452	139,692		314,794	94,8502	98	-1,17848	24100	0,666681
15	11	6,00126	139,736		300,078	95,5665	11	-1,30857	27300	0,656349
16	11	6,02112	140		314,038	95,5803	11	-1,31127	21300	0,685126
17	10,9849	6,05385	139,781		302,638	95,445	11	-1,28508	25000	0,658337
18	10,7357	6,4544	139,847		310,715	94,2195	17	-1,07813	22300	0,691882
19	10,9233	6,19156	139,986		324,222	94,9499	13	-1,19546	23700	0,663907
20	11	6	140		300	95,8319	11	-1,36218	24200	0,68171

Figure D.10: Optimisation output summarising evaluated setpoints.

setpoint yields the best result: 1) a $\log(D)$ value, and 2) number of defects per million opportunities (DPMO). In this example, the highest yeild is determine by the lowest $\log(D)$ value.

Appendix E

Single layer microscope images

The complete set of microscope images, taken from the experiment samples, are presented here. The images are captured using an Olympus SZX7 Stereo-microscope System. Each image shows the corresponding sample under both 1.25 and 3.20 times magnification.

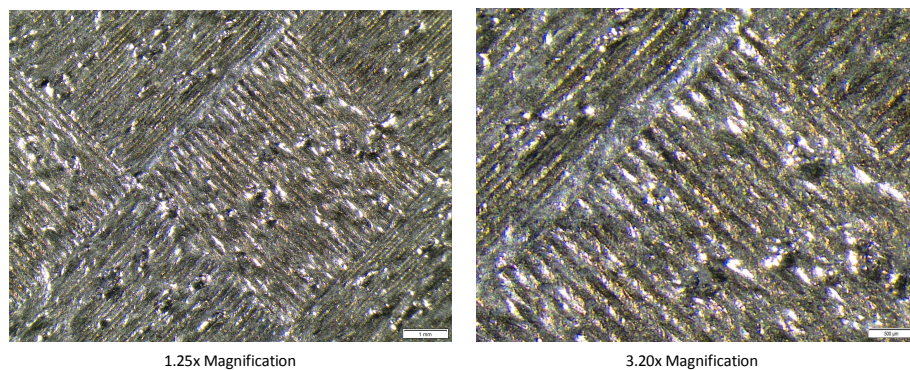


Figure E.1: Single layer sample E1 at 1.25 and 3.20 times magnification.

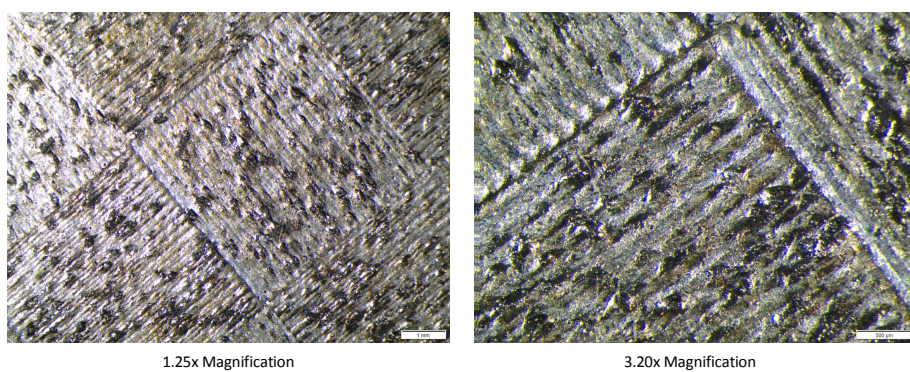


Figure E.2: Single layer sample E2 at 1.25 and 3.20 times magnification.

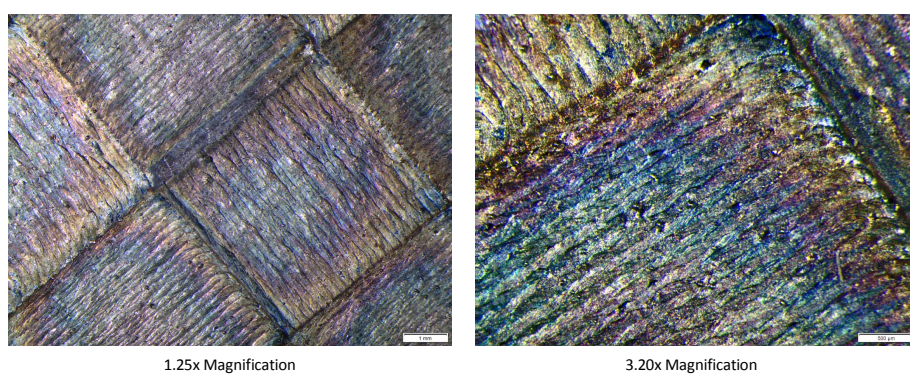


Figure E.3: Single layer sample E3 at 1.25 and 3.20 times magnification.

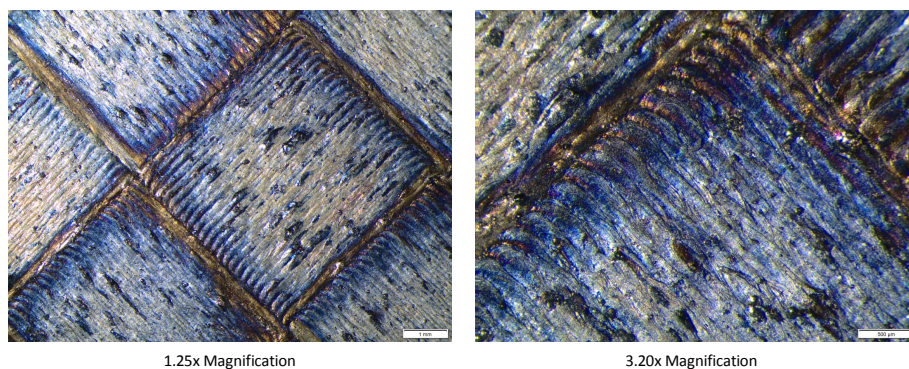


Figure E.4: Single layer sample E4 at 1.25 and 3.20 times magnification.

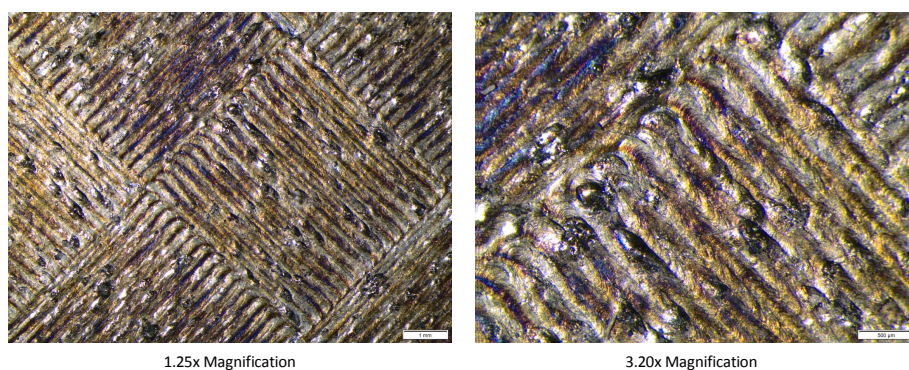


Figure E.5: Single layer sample E5 at 1.25 and 3.20 times magnification.

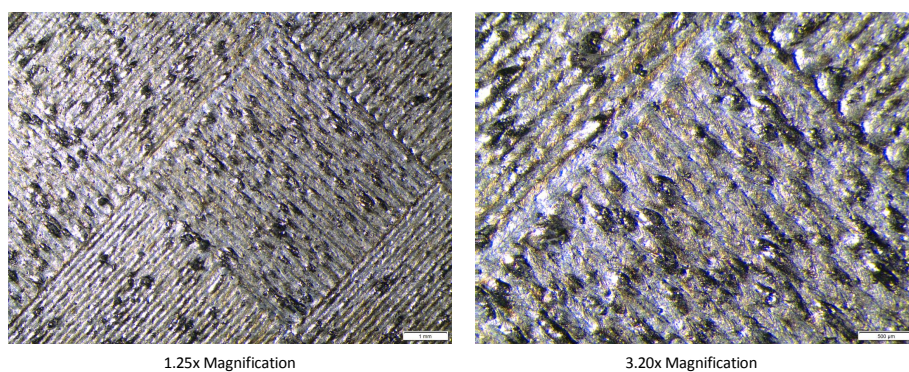


Figure E.6: Single layer sample E6 at 1.25 and 3.20 times magnification.

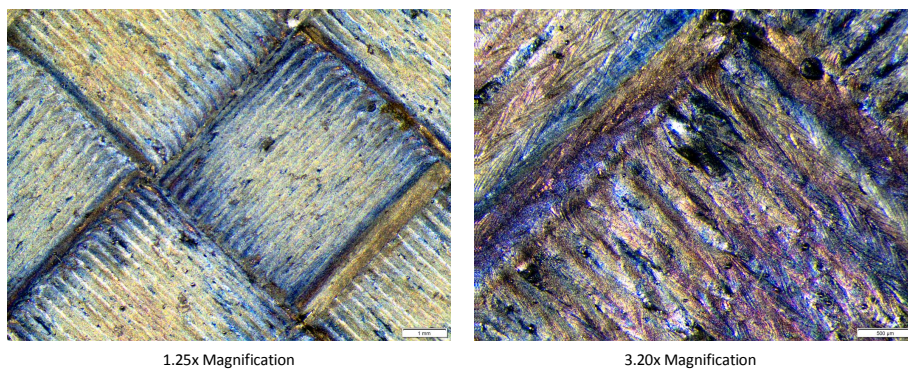


Figure E.7: Single layer sample E7 at 1.25 and 3.20 times magnification.

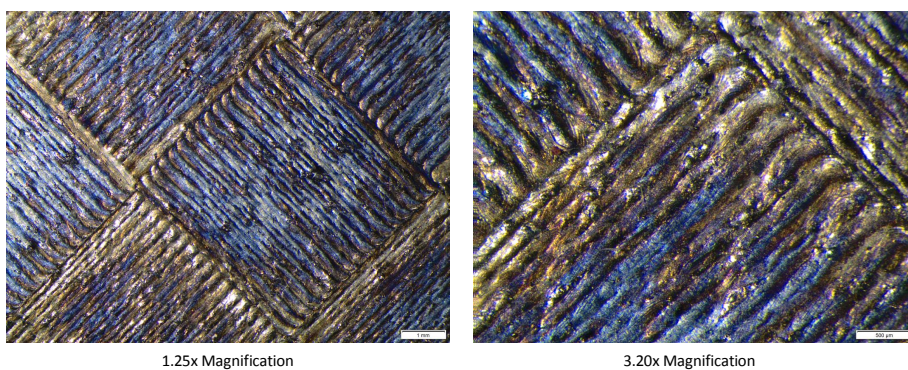


Figure E.8: Single layer sample E8 at 1.25 and 3.20 times magnification.

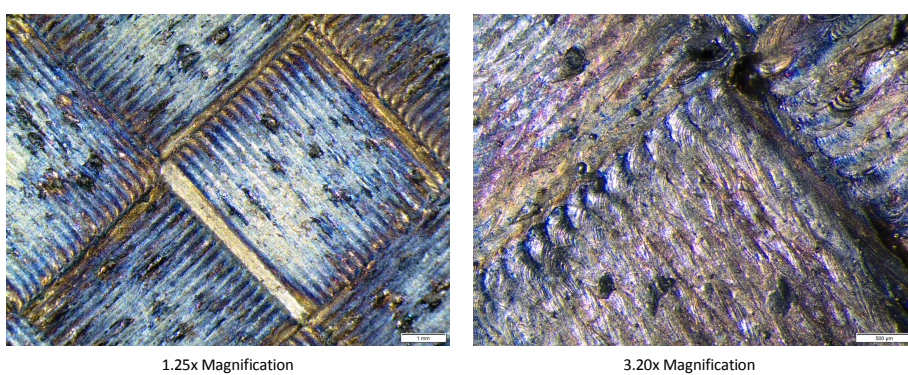


Figure E.9: Single layer sample E9 at 1.25 and 3.20 times magnification.

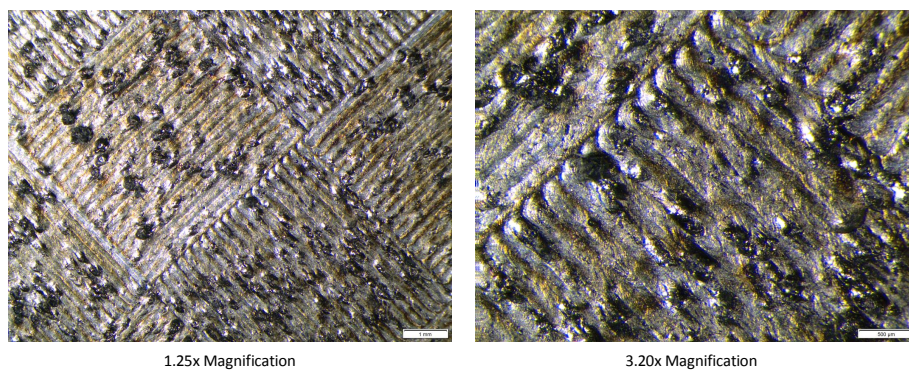


Figure E.10: Single layer sample E10 at 1.25 and 3.20 times magnification.

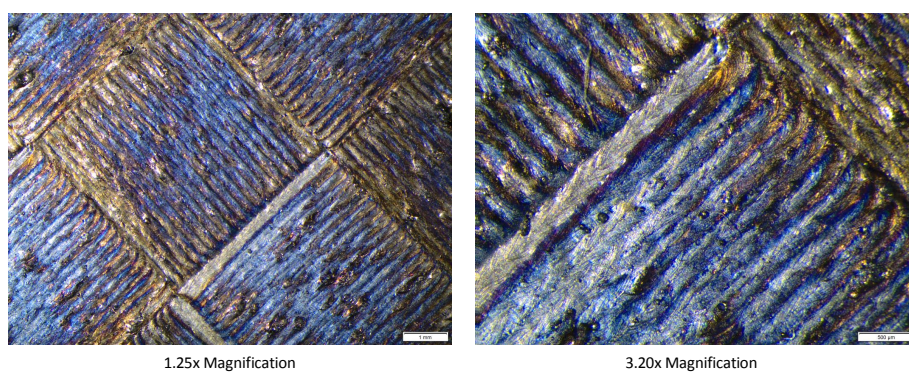


Figure E.11: Single layer sample E11 at 1.25 and 3.20 times magnification.

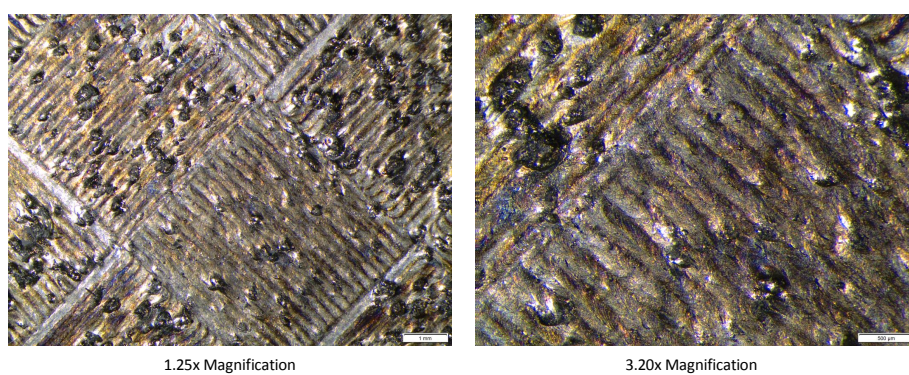


Figure E.12: Single layer sample E12 at 1.25 and 3.20 times magnification.

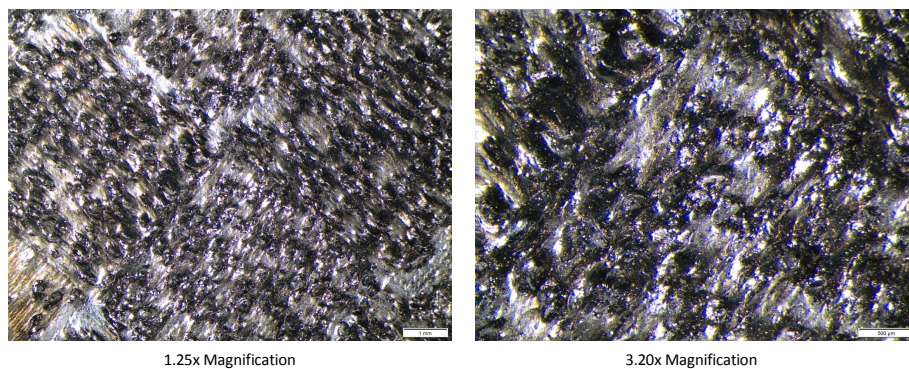


Figure E.13: Single layer sample E13 at 1.25 and 3.20 times magnification.

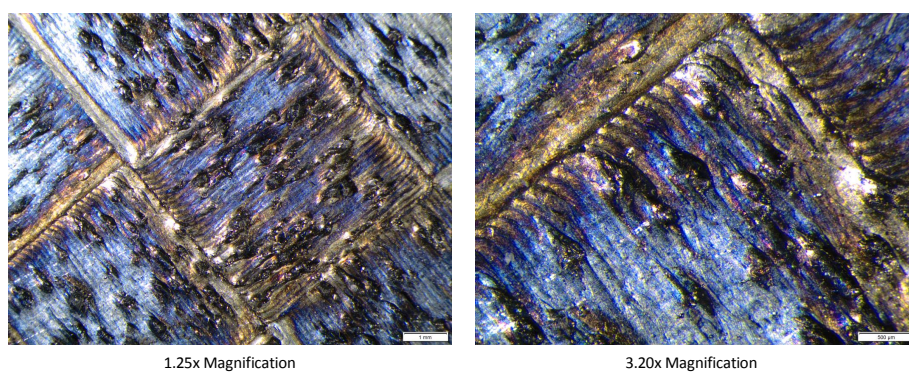


Figure E.14: Single layer sample E14 at 1.25 and 3.20 times magnification.

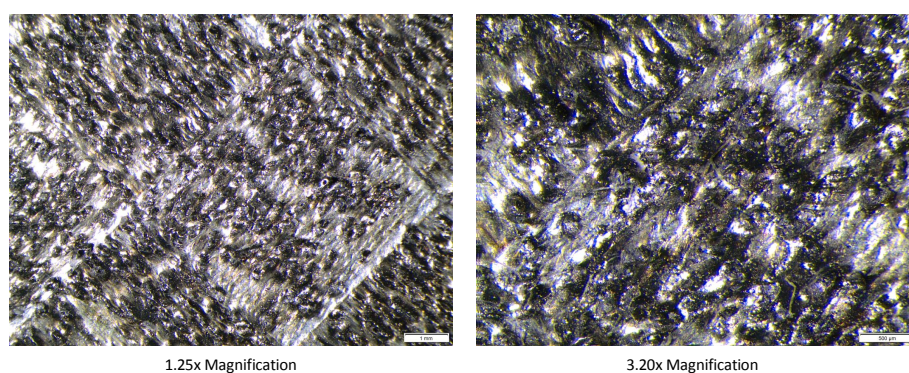


Figure E.15: Single layer sample E15 at 1.25 and 3.20 times magnification.

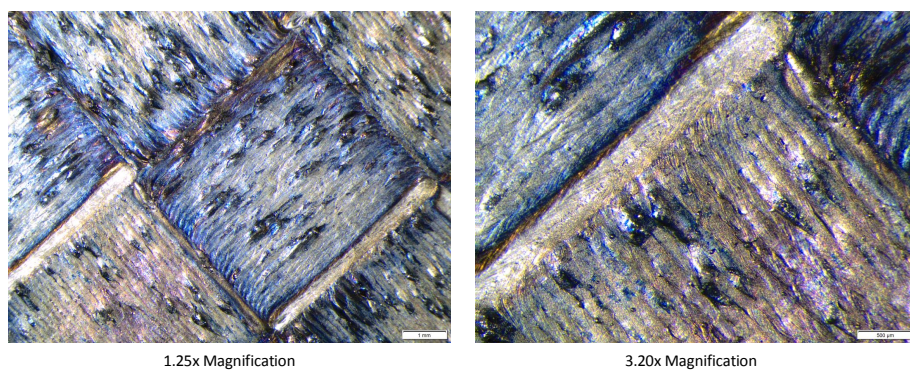


Figure E.16: Single layer sample E16 at 1.25 and 3.20 times magnification.

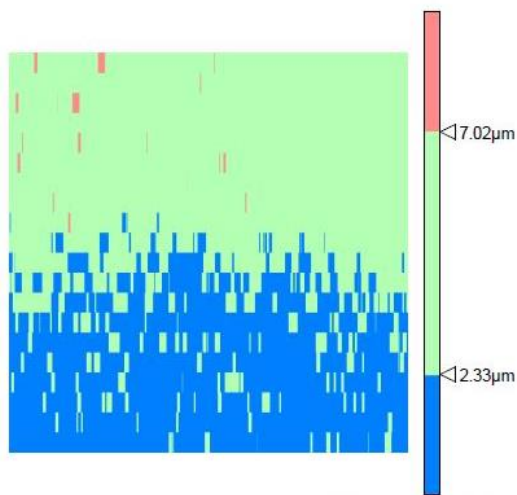
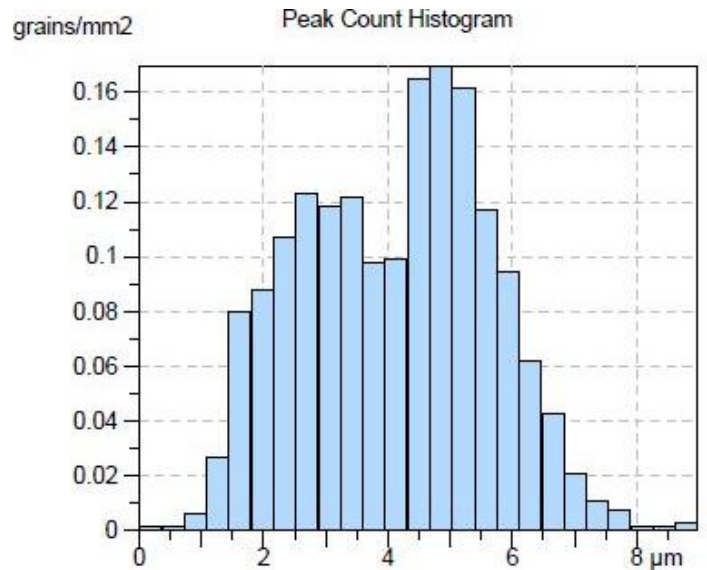
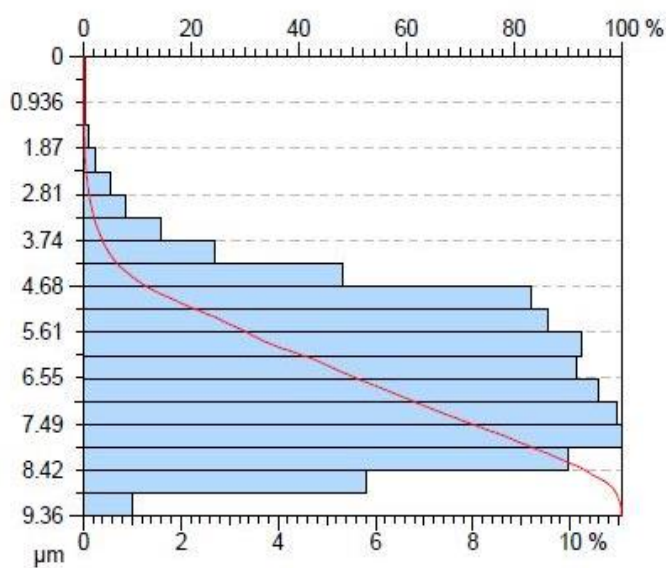
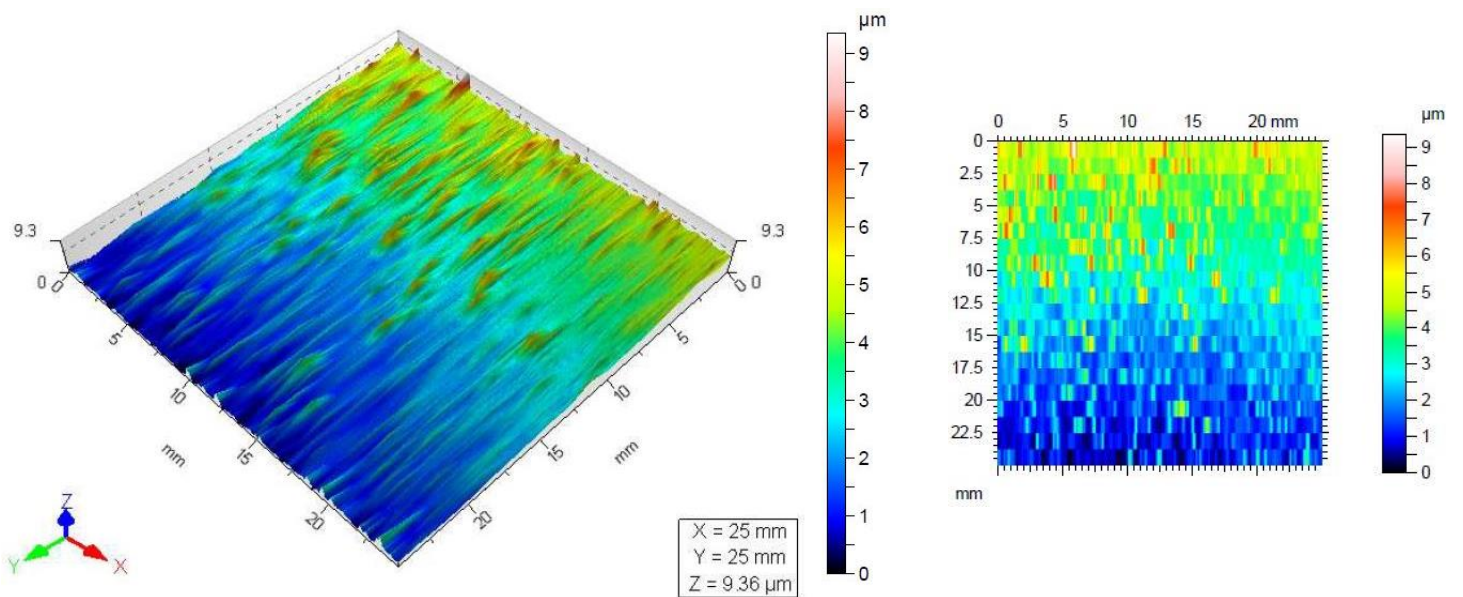
Appendix F

HommelMap Basic Reports

The surface profile analysis results are shown here. The analysis software used is HommelMap Basic 6.2.6190. For each sample the 3D surface profile, the peak count histogram, and summary statistics are presented, among others.

HommelMap Basic 6.2.6190 Report – Sample E1

Parameters: P = 100W, v = 100mm.s⁻¹, h = 0.100mm, d = 0.150mm



	Blue	Green	Red
Projected Area (%)	38.6	61.0	0.448
Volume of void (%)	14.0	80.3	99.9
Volume of material (%)	86.0	19.7	0.124
Volume of void (μm.mm2/mm2)	0.328	3.77	2.33
Volume of material (μm.mm2/mm2)	2.01	0.923	0.0029
Mean thickness of void (μm)	0.328	3.77	2.33
Mean thickness of material (μm)	2.01	0.923	0.0029

Identity card

Name: Topography
Filename: C:\T8000\DA TENyero\Topography.top

Axis: X
Length: 25.0 mm
Size: 14706 points
Spacing: 1.70 μm
Offset: 0.00 mm

Axis: Y
Length: 25.0 mm
Size: 20 lines
Spacing: 1316 μm
Offset: 0.00 mm

Axis: Z
Length: 9.36 μm
Z min: -5.06 μm
Z max: 4.30 μm
Size: 9357 digits
Spacing: 1.00 nm

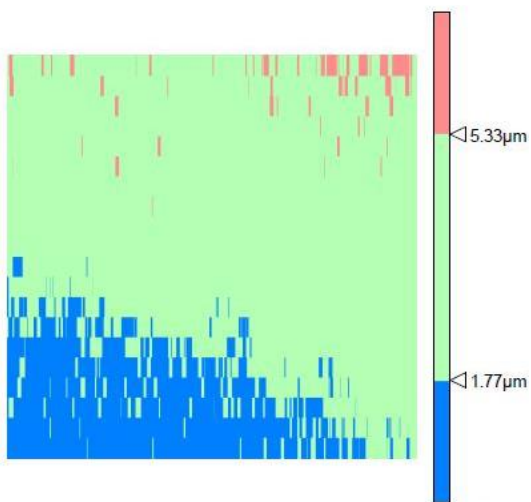
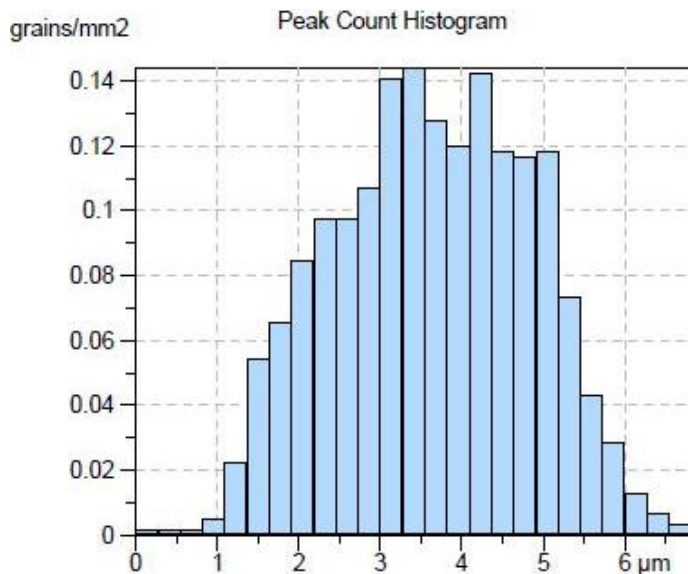
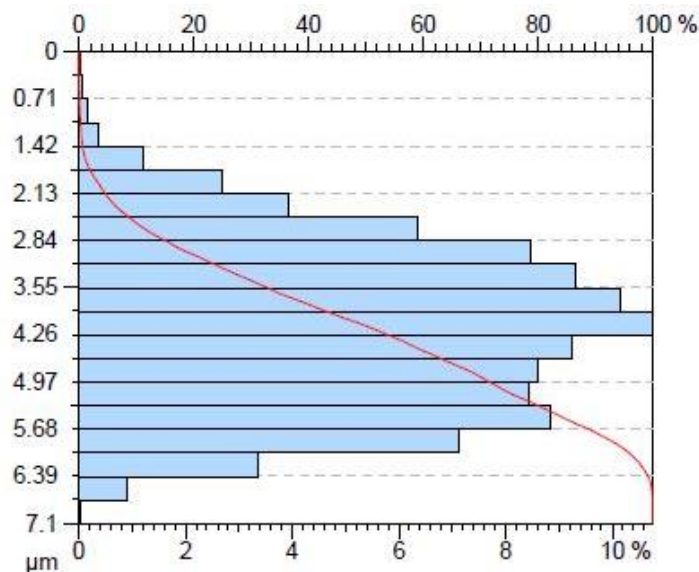
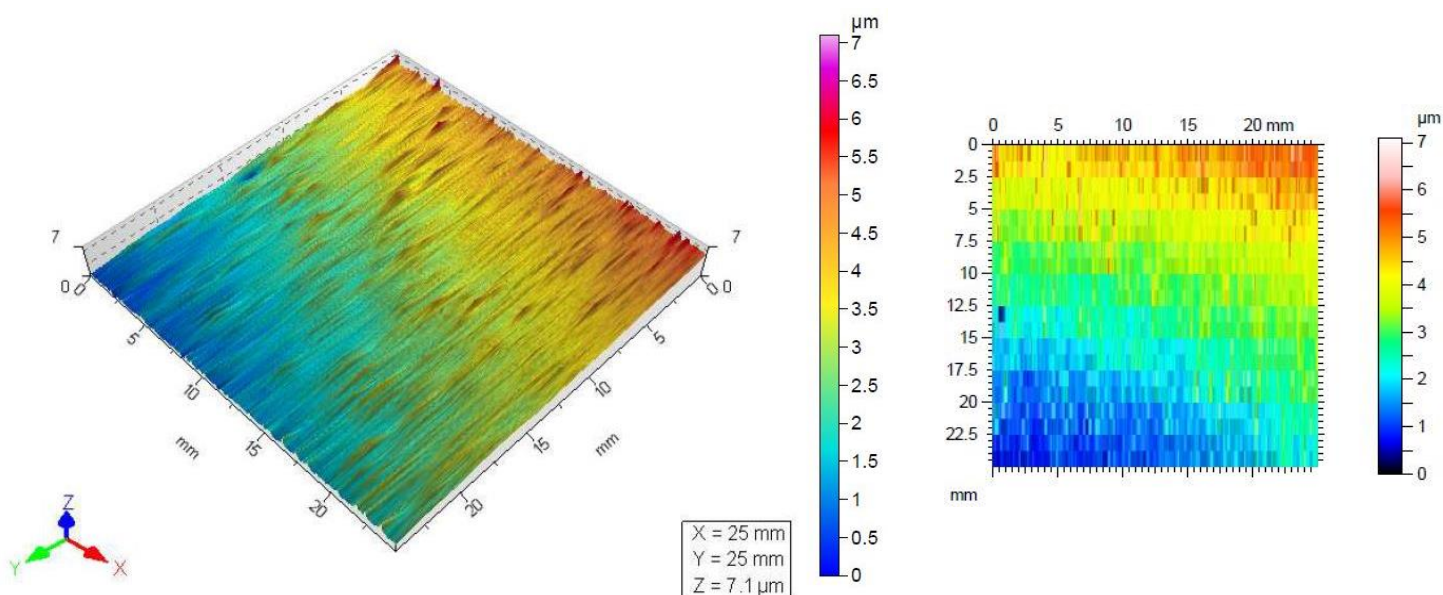
DIN ISO 25178

Height Parameters

Sq	1.44	μm
Ssk	0.390	
Sku	2.71	
Sp	6.42	μm
Sv	2.93	μm
Sz	9.36	μm
Sa	1.20	μm

HommelMap Basic 6.2.6190 Report – Sample E2

Parameters: P = 100W, v = 200mm.s⁻¹, h = 0.100mm, d = 0.150mm



	Blue	Green	Red
Projected Area (%)	20.0	78.1	1.82
Volume of void (%)	5.17	64.5	99.7
Volume of material (%)	94.8	35.5	0.339
Volume of void (μm.mm ² /mm ²)	0.0915	2.30	1.76
Volume of material (μm.mm ² /mm ²)	1.68	1.26	0.00601
Mean thickness of void (μm)	0.0915	2.30	1.76
Mean thickness of material (μm)	1.68	1.26	0.00601

Identity card

Name: Topography
Filename: C:\T8000\DA TENyero\Topography.top

Axis: X
Length: 25.0 mm
Size: 14706 points
Spacing: 1.70 μm
Offset: 0.00 mm

Axis: Y
Length: 25.0 mm
Size: 20 lines
Spacing: 1316 μm
Offset: 0.00 mm

Axis: Z
Length: 7.10 μm
Z min: -4.82 μm
Z max: 2.28 μm
Size: 7098 digits
Spacing: 1.00 nm

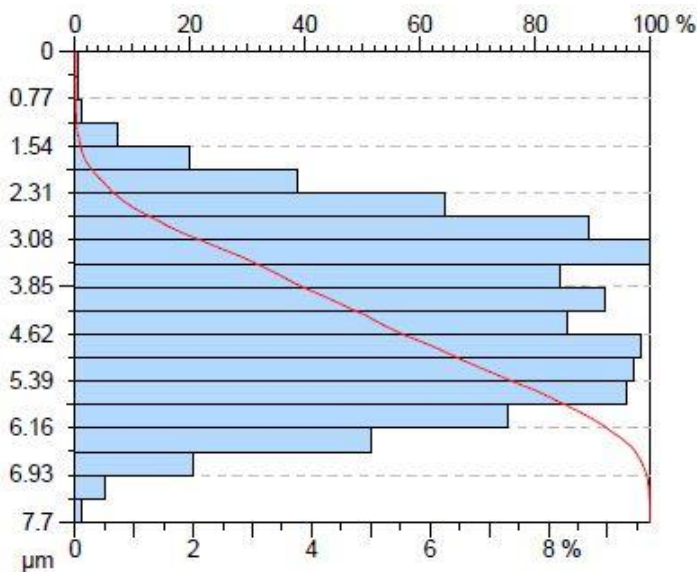
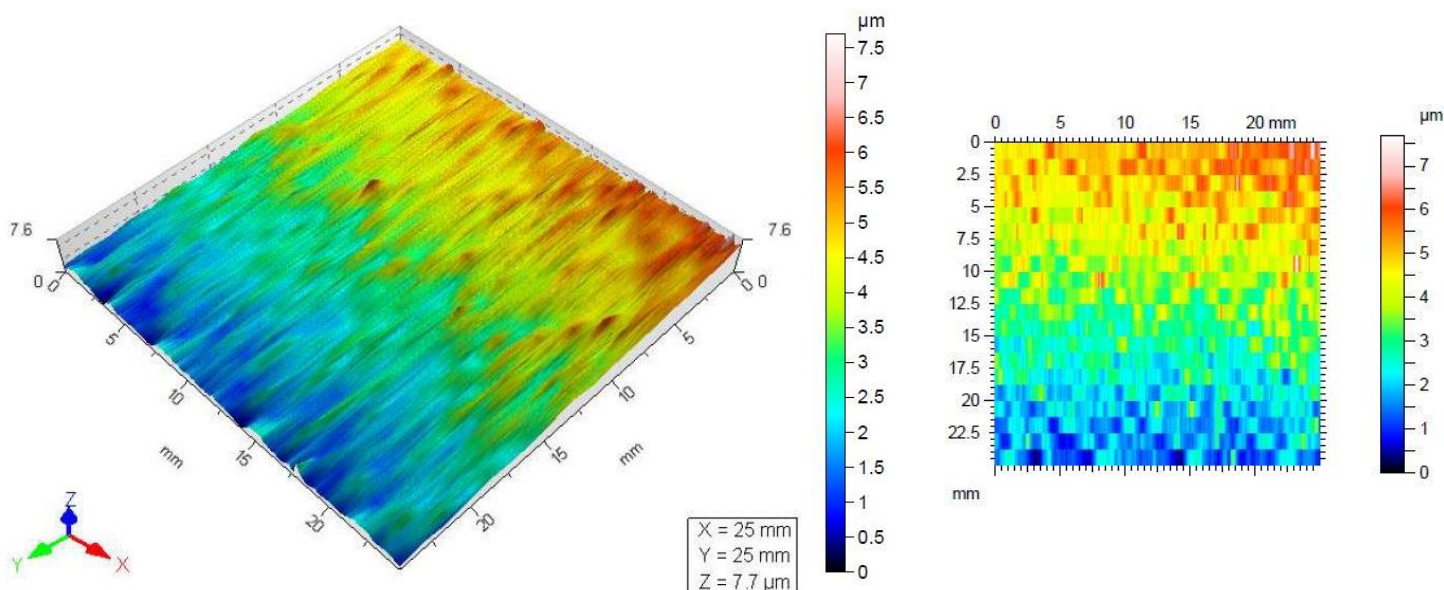
DIN ISO 25178

Height Parameters

Sq	1.19	μm
Ssk	0.128	
Sku	2.28	
Sp	4.15	μm
Sv	2.95	μm
Sz	7.10	μm
Sa	0.990	μm

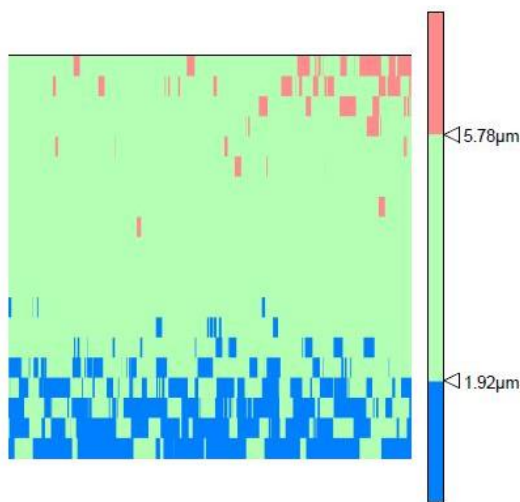
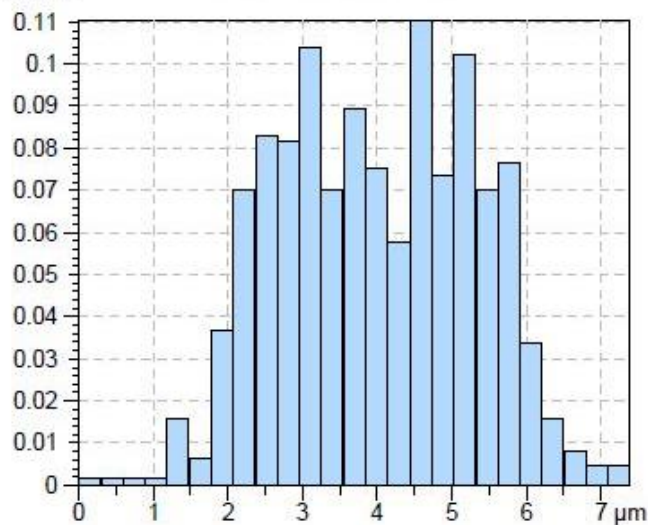
HommelMap Basic 6.2.6190 Report – Sample E3

Parameters: P = 200W, v = 100mm.s⁻¹, h = 0.100mm, d = 0.150mm



grains/mm²

Peak Count Histogram



Identity card

Name: Topography
Filename: C:\T8000\DATA\Temyer\Topography.top

Axis: X
Length: 25.0 mm
Size: 14706 points
Spacing: 1.70 μm
Offset: 0.00 mm

Axis: Y
Length: 25.0 mm
Size: 20 lines
Spacing: 1316 μm
Offset: 0.00 mm

Axis: Z
Length: 7.70 μm
Z min: -5.0 μm
Z max: 2.70 μm
Size: 7697 digits
Spacing: 1.00 nm

DIN ISO 25178

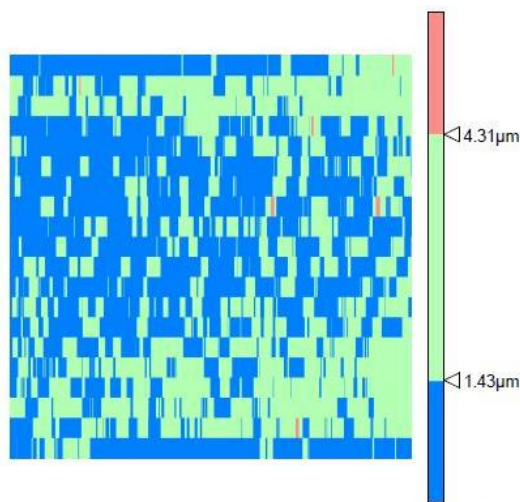
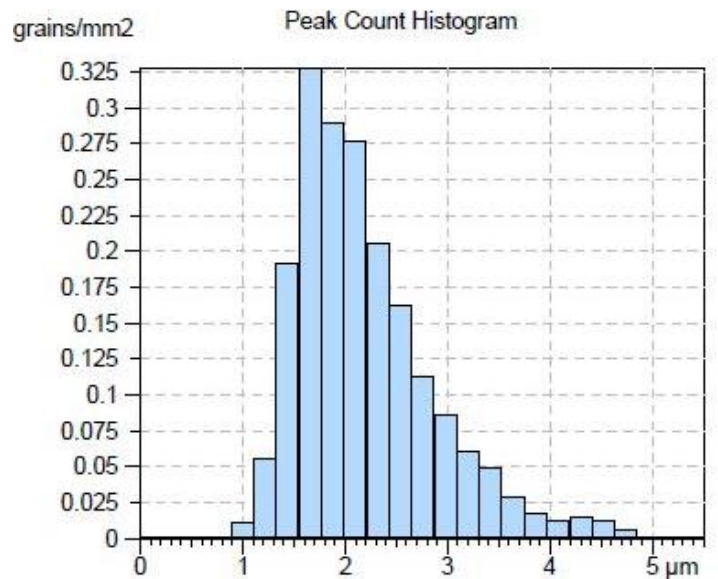
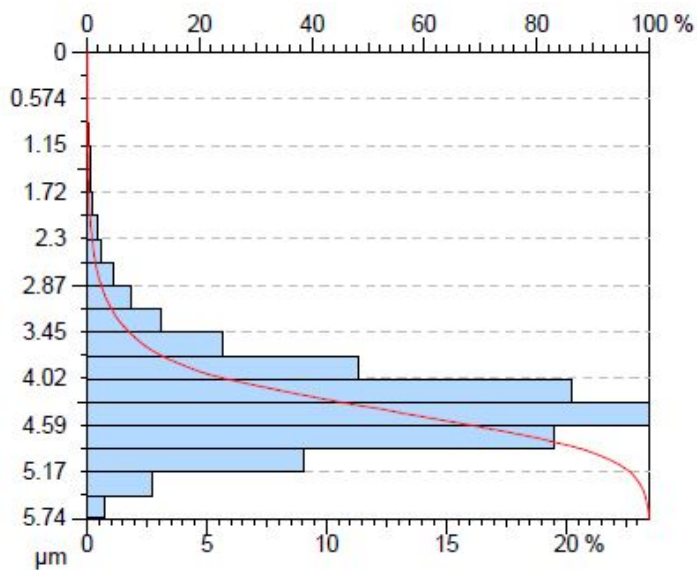
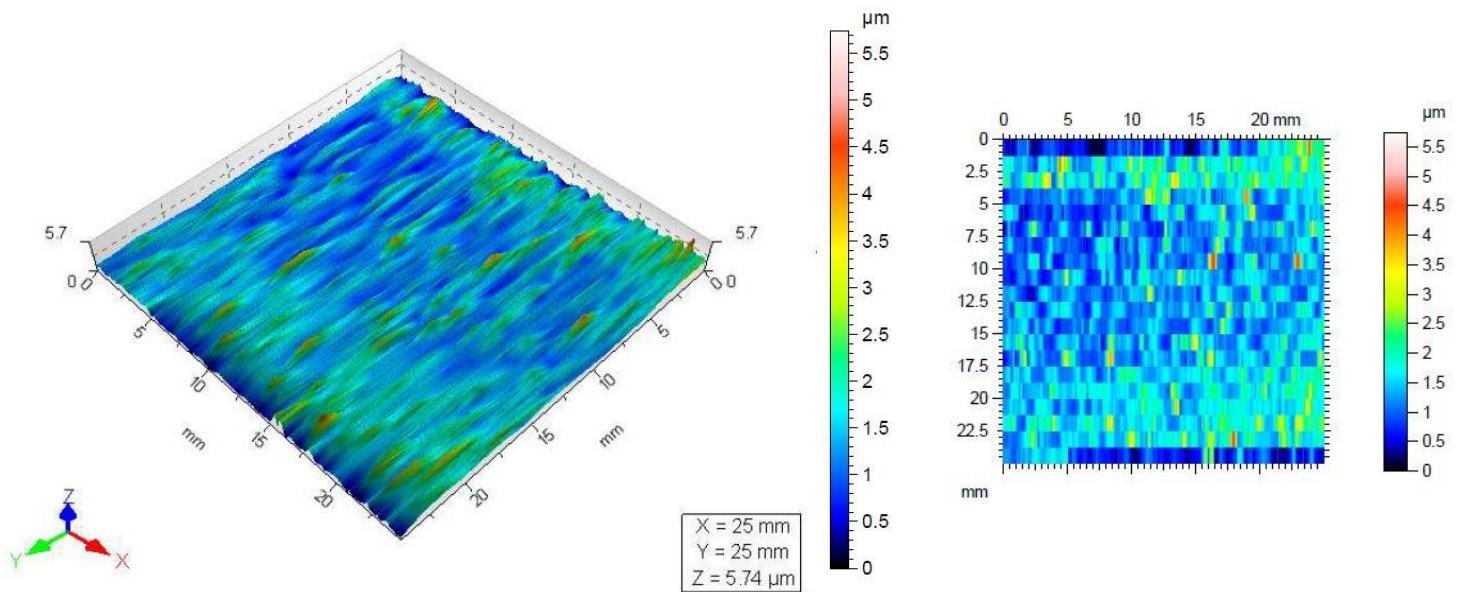
Height Parameters

Sq	1.32	μm
Ssk	0.0702	
Sku	2.15	
Sp	4.28	μm
Sv	3.42	μm
Sz	7.70	μm
Sa	1.12	μm

Projected Area (%)	14.7	82.4	2.85
Volume of void (%)	3.50	59.6	99.5
Volume of material (%)	96.5	40.4	0.492
Volume of void (μm.mm ² /mm ²)	0.0672	2.30	1.91
Volume of material (μm.mm ² /mm ²)	1.85	1.56	0.00944
Mean thickness of void (μm)	0.0672	2.30	1.91
Mean thickness of material (μm)	1.85	1.56	0.00944

HommelMap Basic 6.2.6190 Report – Sample E4

Parameters: P = 200W, v = 200mm.s⁻¹, h = 0.100mm, d = 0.150mm



	■	■	■
Projected Area (%)	55.0	44.8	0.197
Volume of void (%)	14.7	92.4	100
Volume of material (%)	85.3	7.57	0.0333
Volume of void (μm.mm2/mm2)	0.211	2.66	1.43
Volume of material (μm.mm2/mm2)	1.22	0.218	0.000477
Mean thickness of void (μm)	0.211	2.66	1.43
Mean thickness of material (μm)	1.22	0.218	0.000477

Identity card

Name: Topography
Filename: C:\T8000\DATEN\lyero\Topography.top

Axis: X
Length: 25.0 mm
Size: 14706 points
Spacing: 1.70 μm
Offset: 0.00 mm

Axis: Y
Length: 25.0 mm
Size: 20 lines
Spacing: 1316 μm
Offset: 0.00 mm

Axis: Z
Length: 5.74 μm
Z min: -0.527 μm
Z max: 5.22 μm
Size: 5743 digits
Spacing: 1.00 nm

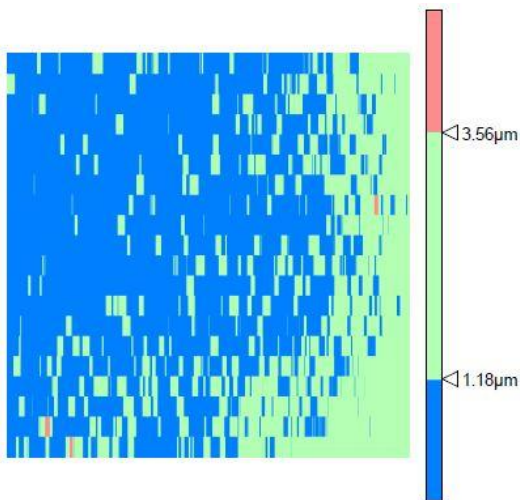
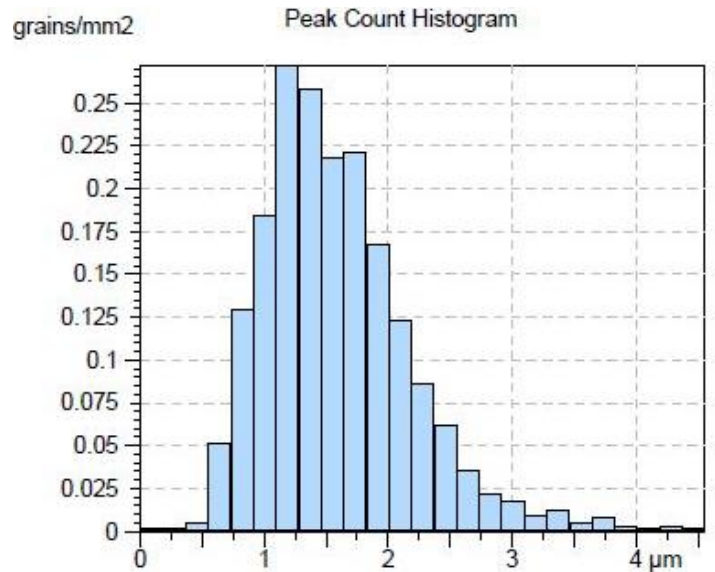
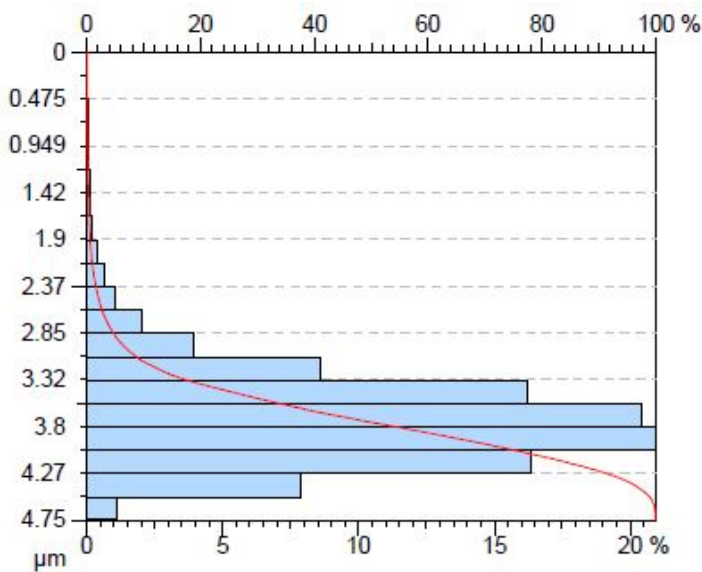
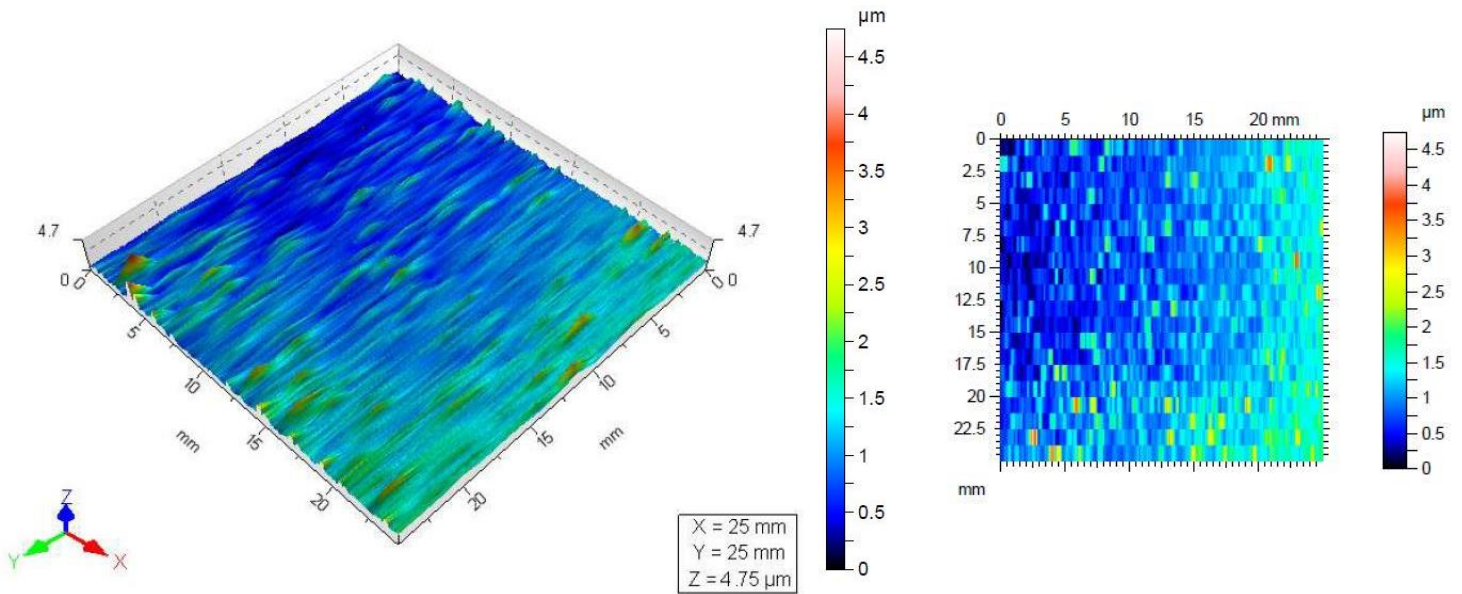
DIN ISO 25178

Height Parameters

Parameter	Value	Unit
Sq	0.580	μm
Ssk	1.15	
Sku	6.02	
Sp	4.30	μm
Sv	1.44	μm
Sz	5.74	μm
Sa	0.430	μm

HommelMap Basic 6.2.6190 Report – Sample E5

Parameters: P = 100W, v = 100mm.s⁻¹, h = 0.150mm, d = 0.150mm



	Blue	Green	Red
Projected Area (%)	66.2	33.7	0.142
Volume of void (%)	22.4	94.7	100
Volume of material (%)	77.6	5.27	0.0455
Volume of void (μm.mm2/mm2)	0.266	2.25	1.18
Volume of material (μm.mm2/mm2)	0.918	0.125	0.000539
Mean thickness of void (μm)	0.266	2.25	1.18
Mean thickness of material (μm)	0.918	0.125	0.000539

Identity card

Name: Topography
Filename: C:\T8000\DATEN\yero\Topography.top

Axis: X
Length: 25.0 mm
Size: 14706 points
Spacing: 1.70 μm
Offset: 0.00 mm

Axis: Y
Length: 25.0 mm
Size: 20 lines
Spacing: 1316 μm
Offset: 0.00 mm

Axis: Z
Length: 4.75 μm
Z min: -0.382 μm
Z max: 4.37 μm
Size: 4747 digits
Spacing: 1.00 nm

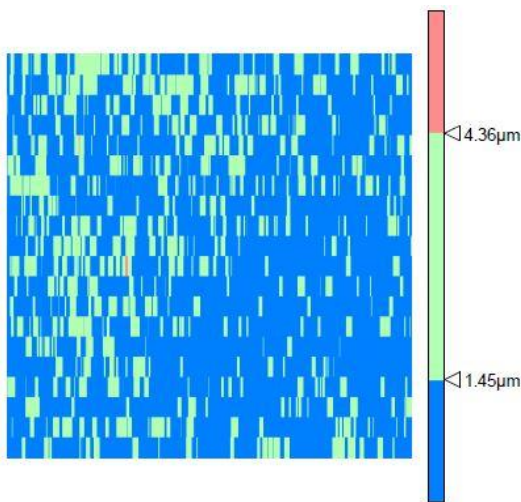
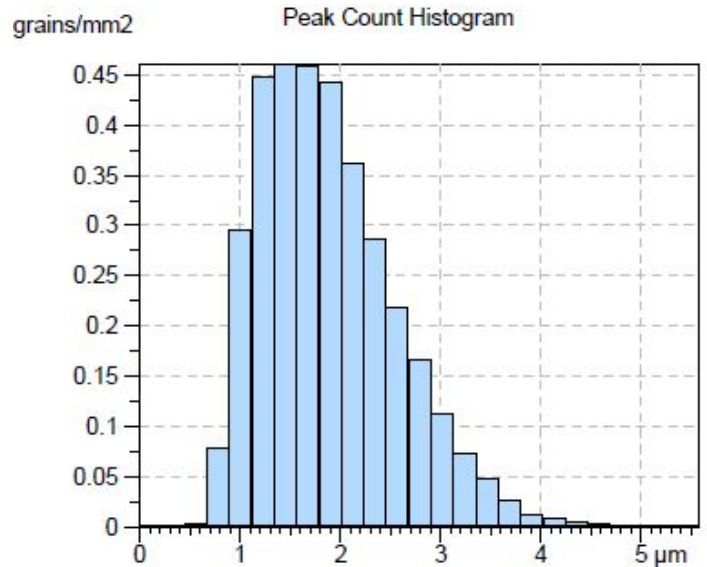
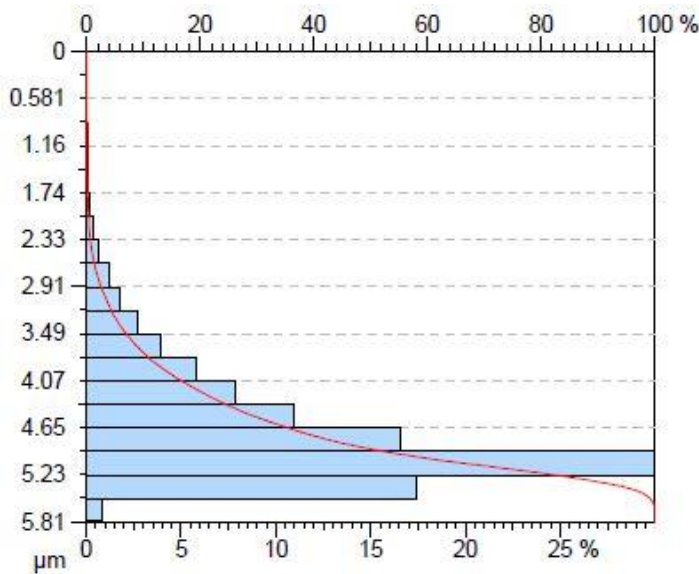
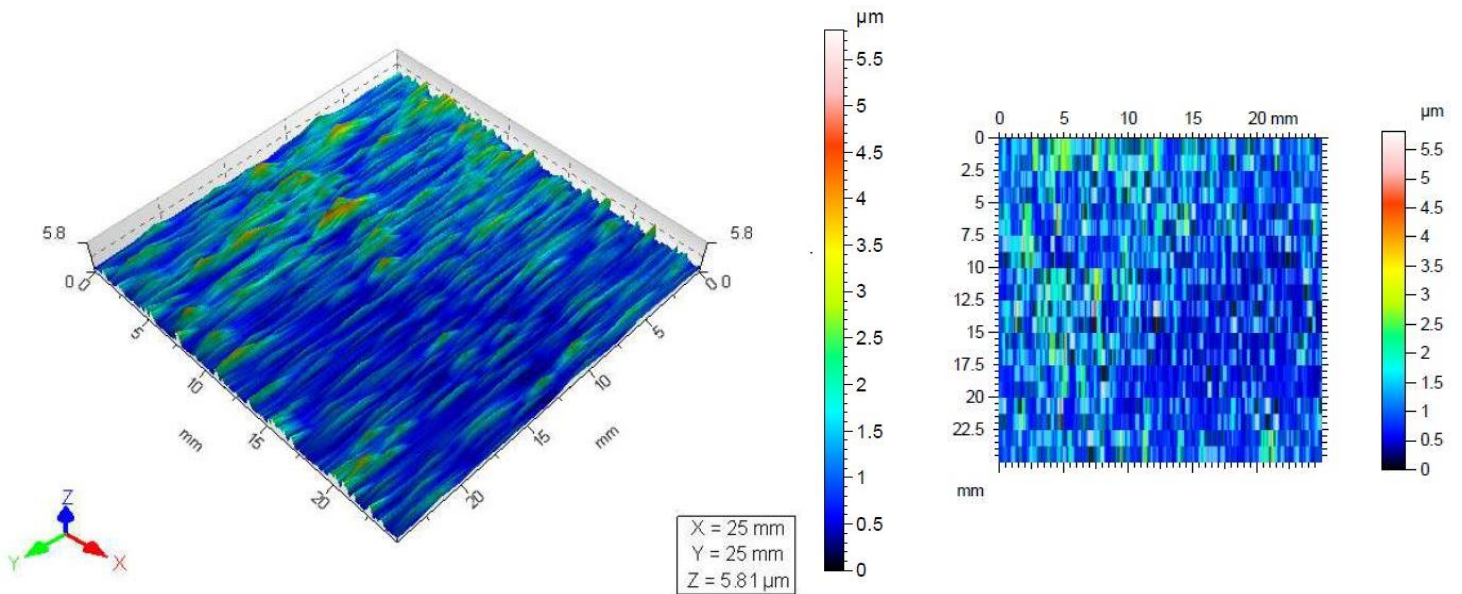
DIN ISO 25178

Height Parameters

Sq	0.478	μm
Ssk	1.21	
Sku	6.56	
Sp	3.70	μm
Sv	1.04	μm
Sz	4.75	μm
Sa	0.362	μm

HommelMap Basic 6.2.6190 Report – Sample E6

Parameters: P = 100W, v = 200mm.s⁻¹, h = 0.150mm, d = 0.150mm



Projected Area (%)	75.4	24.5	0.0391
Volume of void (%)	33.6	94.5	100
Volume of material (%)	66.4	5.54	0.00588
Volume of void (μm.mm2/mm2)	0.487	2.75	1.45
Volume of material (μm.mm2/mm2)	0.963	0.162	8.53e-005
Mean thickness of void (μm)	0.487	2.75	1.45
Mean thickness of material (μm)	0.963	0.162	8.53e-005

Identity card

Name: Topography
Filename: C:\T8000\DATEN\yero\Topography.top

Axis: X
Length: 25.0 mm
Size: 14706 points
Spacing: 1.70 μm
Offset: 0.00 mm

Axis: Y
Length: 25.0 mm
Size: 20 lines
Spacing: 1316 μm
Offset: 0.00 mm

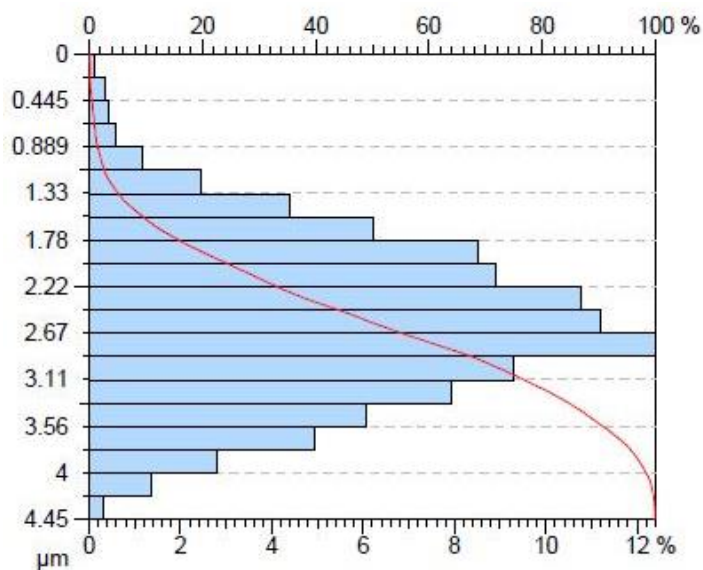
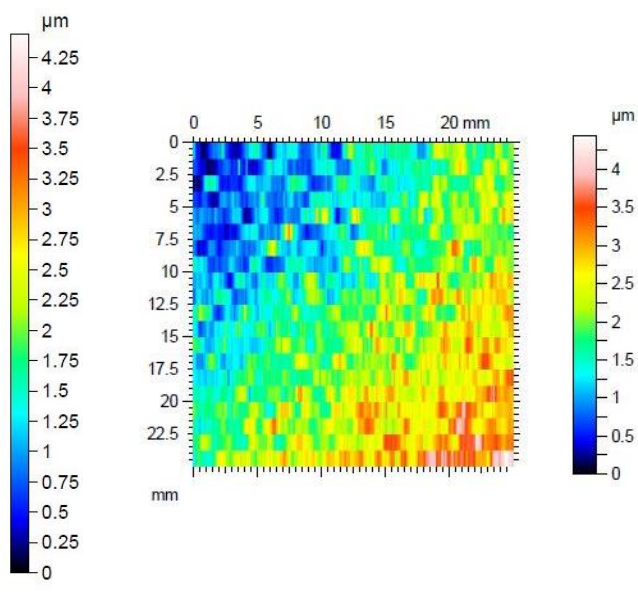
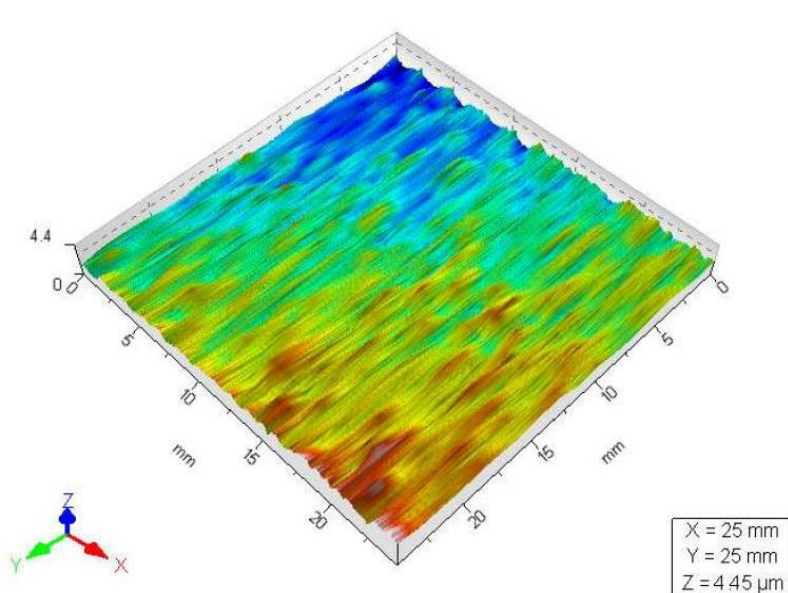
Axis: Z
Length: 5.81 μm
Z min: -0.681 μm
Z max: 5.13 μm
Size: 5814 digits
Spacing: 1.00 nm

DIN ISO 25178

Height Parameters		
Sq	0.673	μm
Ssk	1.44	
Sku	5.11	
Sp	4.69	μm
Sv	1.12	μm
Sz	5.81	μm
Sa	0.521	μm

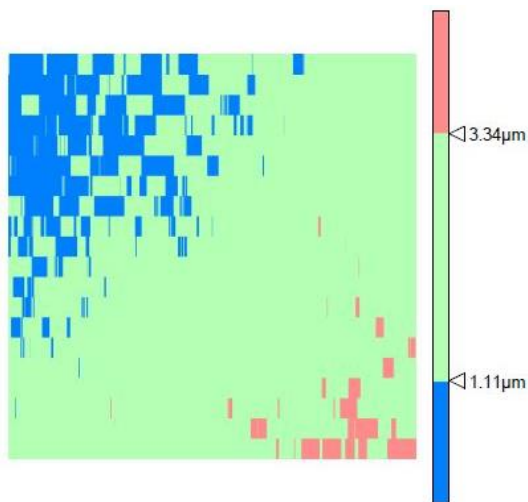
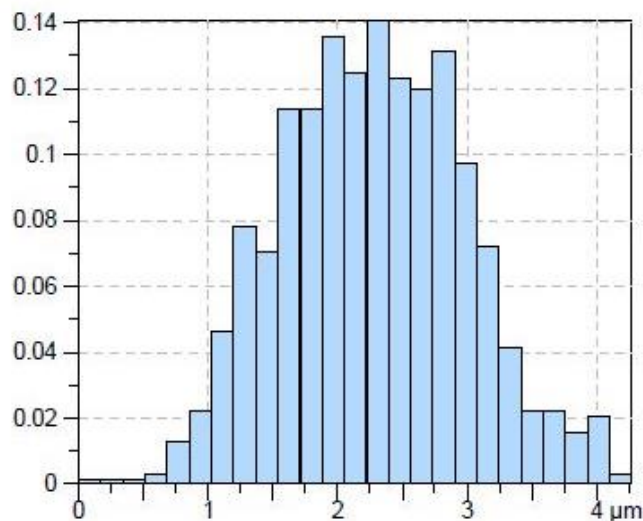
HommelMap Basic 6.2.6190 Report – Sample E7

Parameters: P = 200W, v = 100mm.s⁻¹, h = 0.150mm, d = 0.150mm



grains/mm²

Peak Count Histogram



	Blue	Green	Red
Projected Area (%)	15.2	82.2	2.60
Volume of void (%)	4.51	62.6	99.2
Volume of material (%)	95.5	37.4	0.807
Volume of void (μm.mm ² /mm ²)	0.050	1.40	1.10
Volume of material (μm.mm ² /mm ²)	1.06	0.834	0.00894
Mean thickness of void (μm)	0.050	1.40	1.10
Mean thickness of material (μm)	1.06	0.834	0.00894

Identity card

Name: Topography
Filename: C:\T8000\DATEN\yerol\Topography.top

Axis: X
Length: 25.0 mm
Size: 14706 points
Spacing: 1.70 μm
Offset: 0.00 mm

Axis: Y
Length: 25.0 mm
Size: 20 lines
Spacing: 1316 μm
Offset: 0.00 mm

Axis: Z
Length: 4.45 μm
Z min: -1.03 μm
Z max: 3.42 μm
Size: 4447 digits
Spacing: 1.00 nm

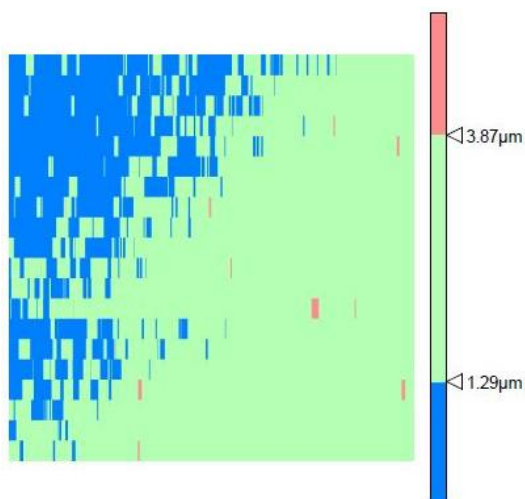
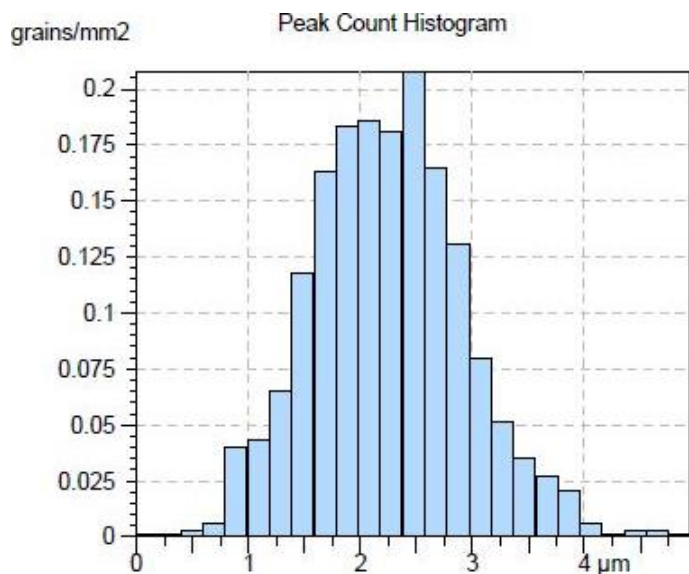
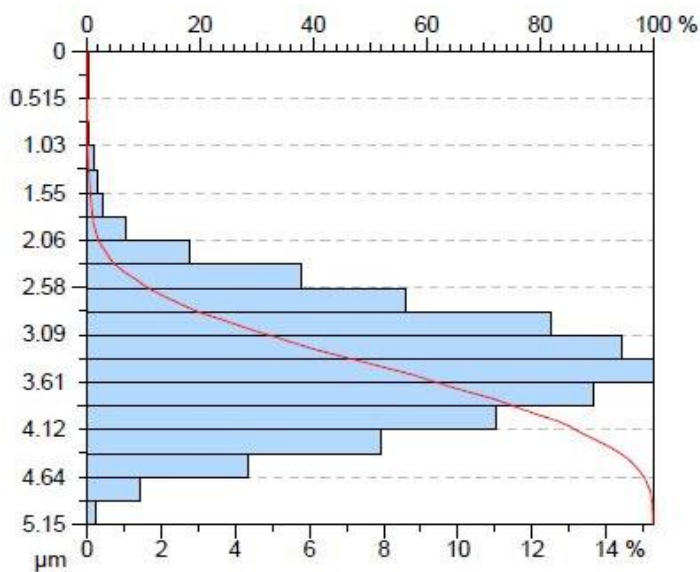
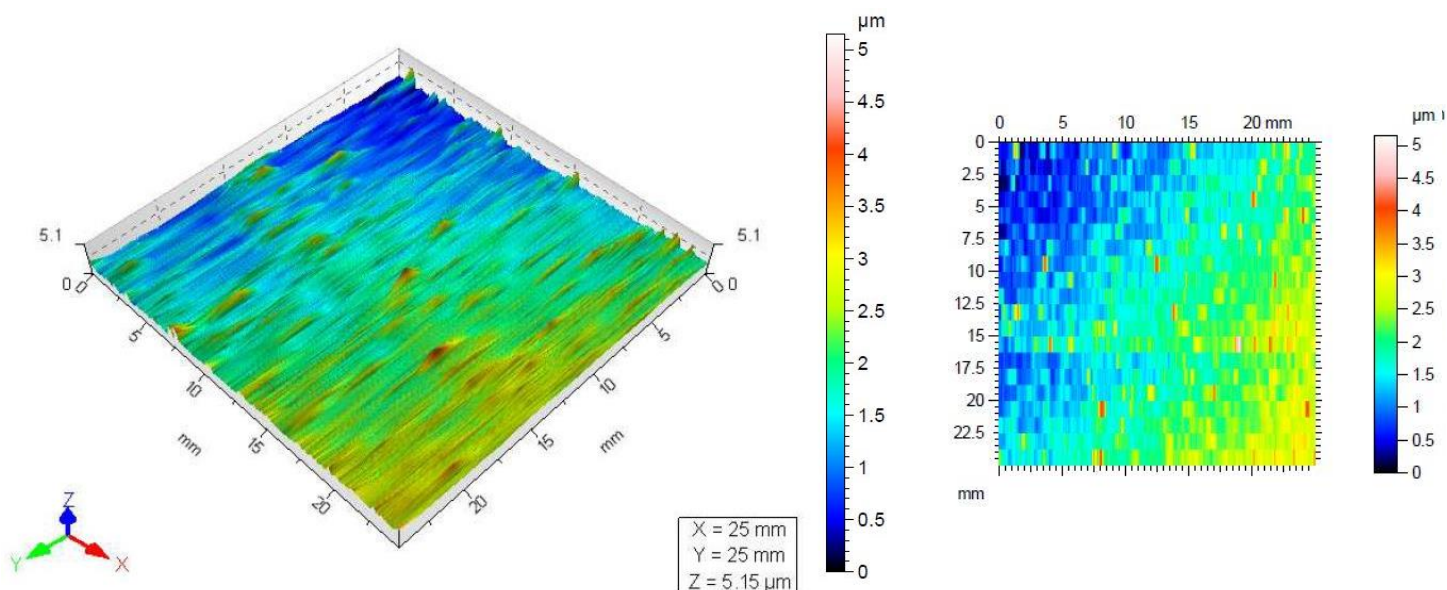
DIN ISO 25178

Height Parameters

Sq	0.741	μm
Ssk	0.158	
Sku	2.75	
Sp	2.54	μm
Sv	1.90	μm
Sz	4.45	μm
Sa	0.599	μm

HommelMap Basic 6.2.6190 Report – Sample E8

Parameters: P = 200W, v = 200mm.s⁻¹, h = 0.150mm, d = 0.150mm



	Blue	Green	Red
Projected Area (%)	24.8	74.9	0.299
Volume of void (%)	6.60	78.4	99.9
Volume of material (%)	93.4	21.6	0.0758
Volume of void (μm.mm ² /mm ²)	0.0848	2.02	1.29
Volume of material (μm.mm ² /mm ²)	1.20	0.556	0.000975
Mean thickness of void (μm)	0.0848	2.02	1.29
Mean thickness of material (μm)	1.20	0.556	0.000975

Identity card

Name: Topography
Filename: C:\T8000\DATA\T8000\Topography.top

Axis: X
Length: 25.0 mm
Size: 14706 points
Spacing: 1.70 μm
Offset: 0.00 mm

Axis: Y
Length: 25.0 mm
Size: 20 lines
Spacing: 1316 μm
Offset: 0.00 mm

Axis: Z
Length: 5.15 μm
Z min: -0.876 μm
Z max: 4.28 μm
Size: 5153 digits
Spacing: 1.00 nm

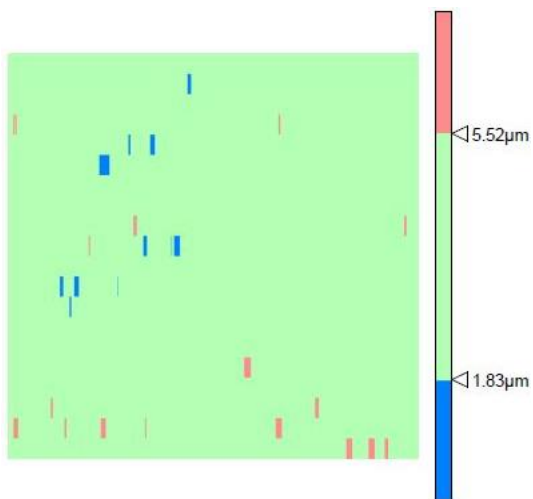
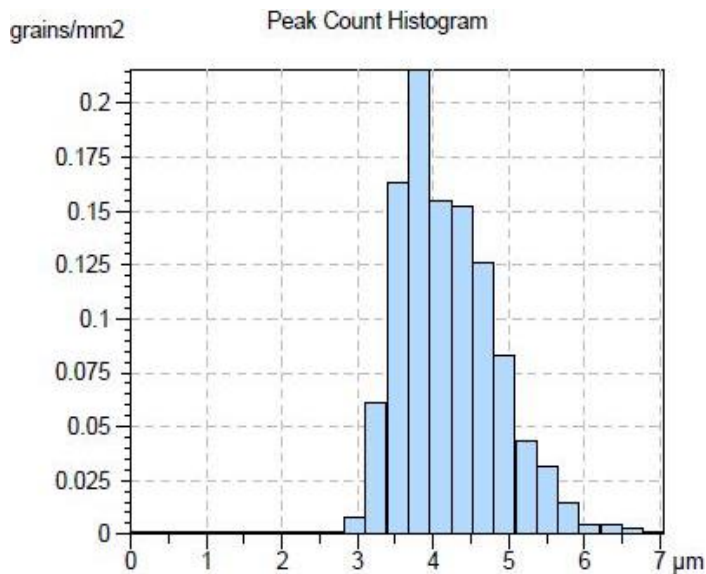
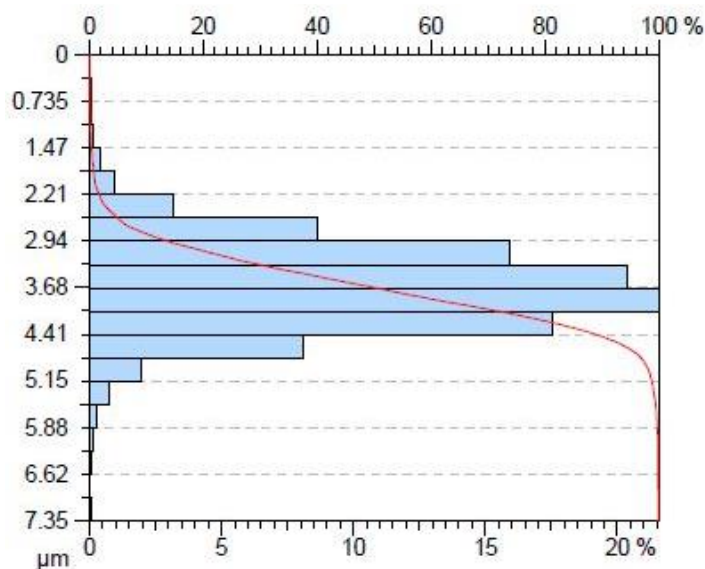
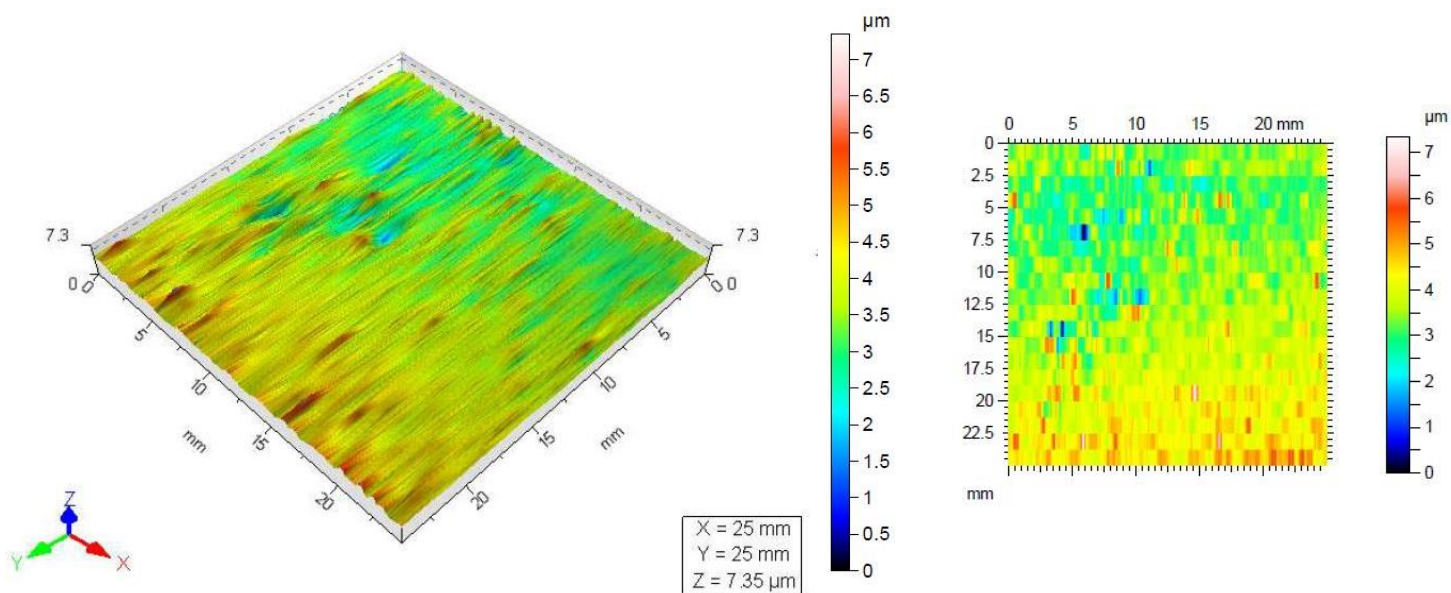
DIN ISO 25178

Height Parameters

Sq	0.650	μm
Ssk	0.280	
Sku	3.15	
Sp	3.39	μm
Sv	1.76	μm
Sz	5.15	μm
Sa	0.522	μm

HommelMap Basic 6.2.6190 Report – Sample E9

Parameters: P = 150W, v = 100mm.s⁻¹, h = 0.125mm, d = 0.150mm



	Blue	Green	Red
Projected Area (%)	0.489	98.8	0.697
Volume of void (%)	0.137	49.5	99.8
Volume of material (%)	99.9	50.5	0.175
Volume of void (μm.mm ² /mm ²)	0.00251	1.82	1.83
Volume of material (μm.mm ² /mm ²)	1.83	1.86	0.00322
Mean thickness of void (μm)	0.00251	1.82	1.83
Mean thickness of material (μm)	1.83	1.86	0.00322

Identity card

Name: Topography
Filename: C:\T8000\DATA\Temyerol\Topography.top

Axis: X
Length: 25.0 mm
Size: 14706 points
Spacing: 1.70 μm
Offset: 0.00 mm

Axis: Y
Length: 25.0 mm
Size: 20 lines
Spacing: 1316 μm
Offset: 0.00 mm

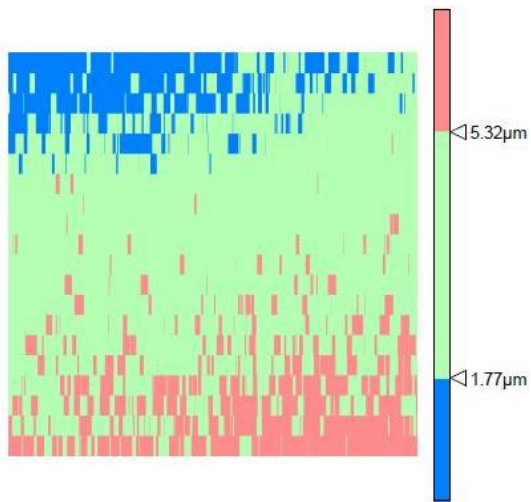
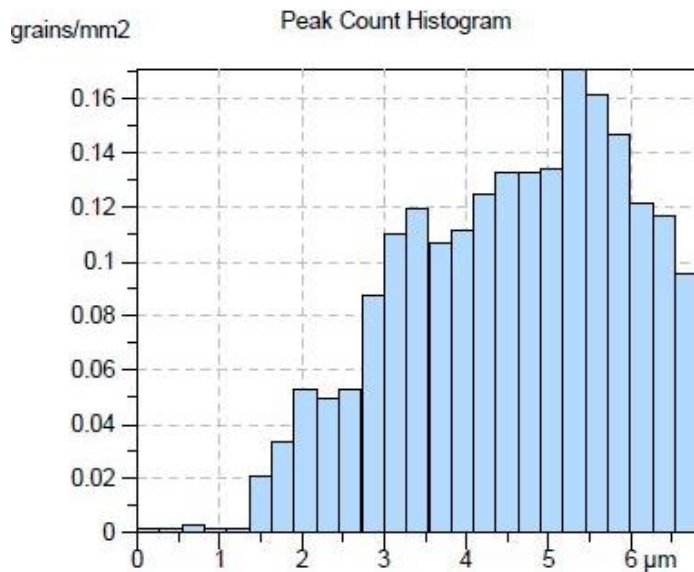
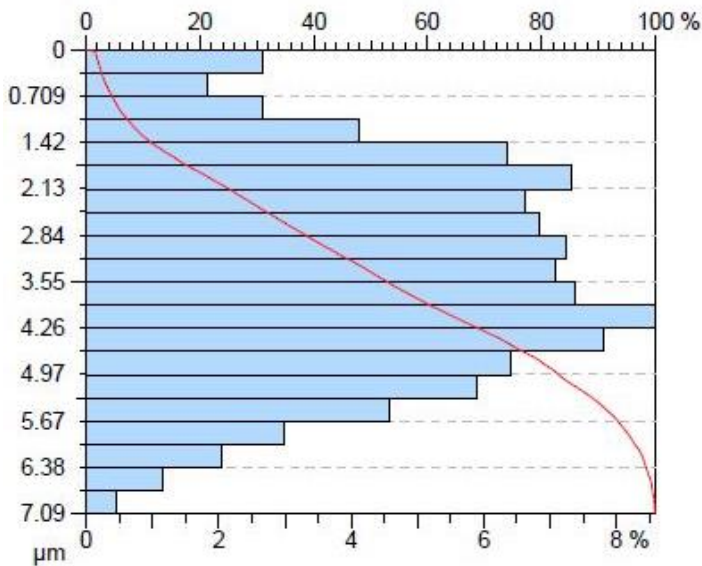
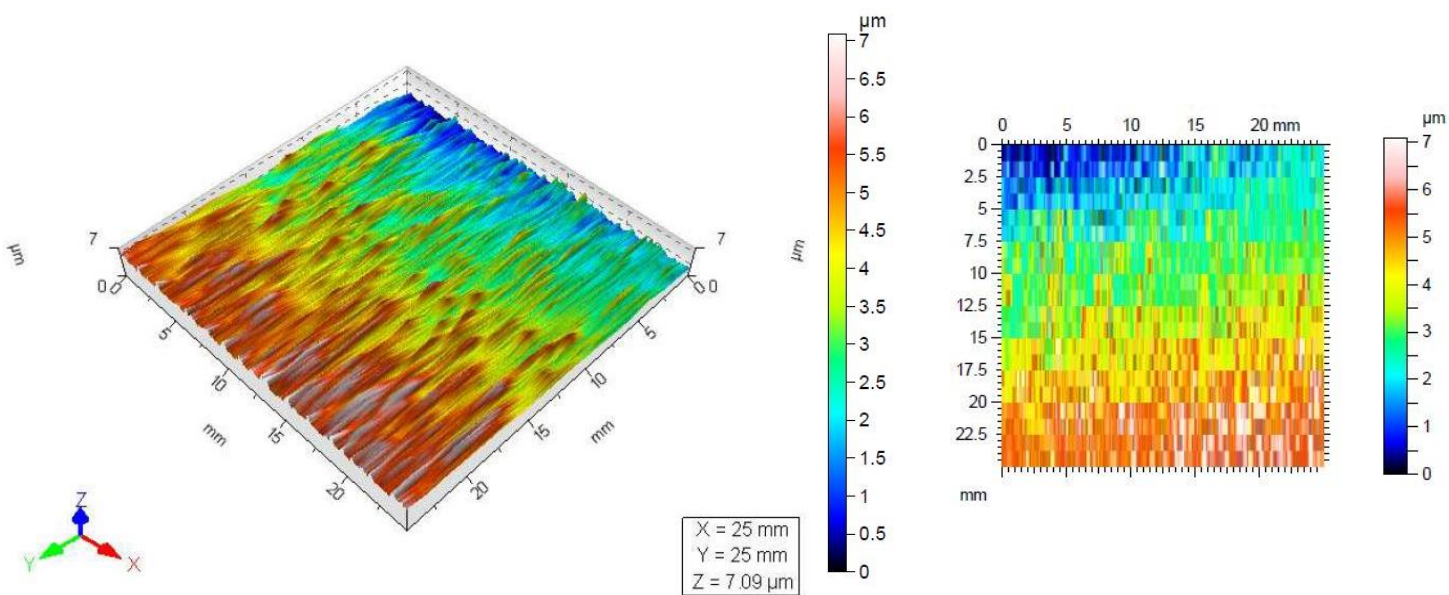
Axis: Z
Length: 7.35 μm
Z min: -3.31 μm
Z max: 4.04 μm
Size: 7351 digits
Spacing: 1.00 nm

DIN ISO 25178

Height Parameters		
Sq	0.665	μm
Ssk	0.108	
Sku	4.29	
Sp	3.66	μm
Sv	3.69	μm
Sz	7.35	μm
Sa	0.524	μm

HommelMap Basic 6.2.6190 Report – Sample E10

Parameters: P = 100W, v = 150mm.s⁻¹, h = 0.125mm, d = 0.150mm



	Blue	Green	Red
Projected Area (%)	11.1	71.3	17.6
Volume of void (%)	3.44	46.4	93.1
Volume of material (%)	96.6	53.6	6.91
Volume of void (μm.mm ² /mm ²)	0.0609	1.65	1.65
Volume of material (μm.mm ² /mm ²)	1.71	1.90	0.122
Mean thickness of void (μm)	0.0609	1.65	1.65
Mean thickness of material (μm)	1.71	1.90	0.122

Identity card

Name: Topography
Filename: C:\Documents and Settings\OPERATOR\M\Documents\Coetzee\Topography.top

Axis: X
Length: 25.0 mm
Size: 14706 points
Spacing: 1.70 μm
Offset: 0.00 mm

Axis: Y
Length: 25.0 mm
Size: 20 lines
Spacing: 1316 μm
Offset: 0.00 mm

Axis: Z
Length: 7.09 μm
Z min: -0.386 μm
Z max: 6.71 μm
Size: 7093 digits
Spacing: 1.00 mm

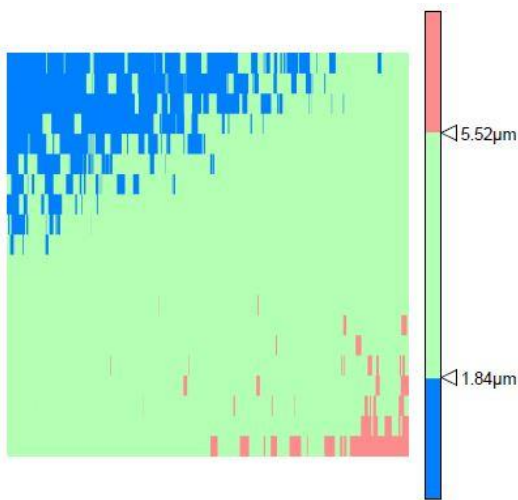
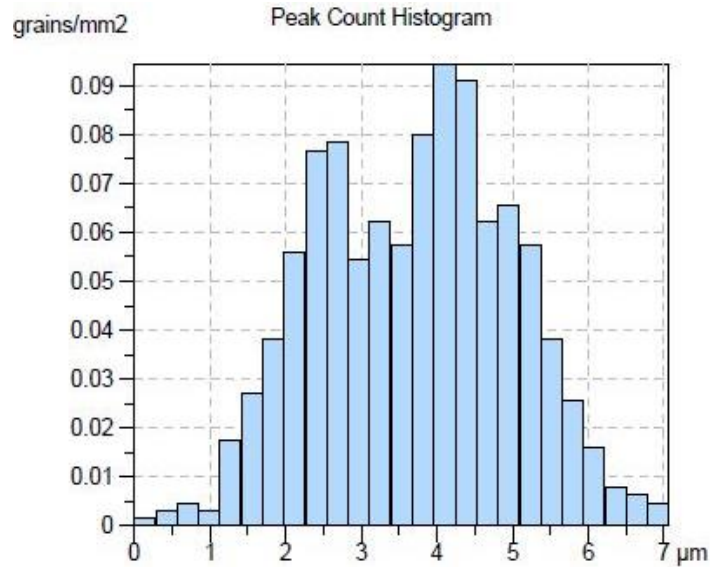
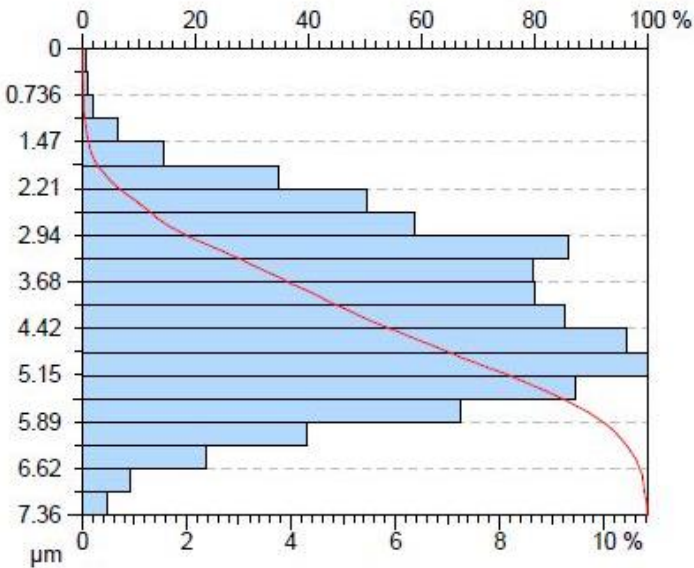
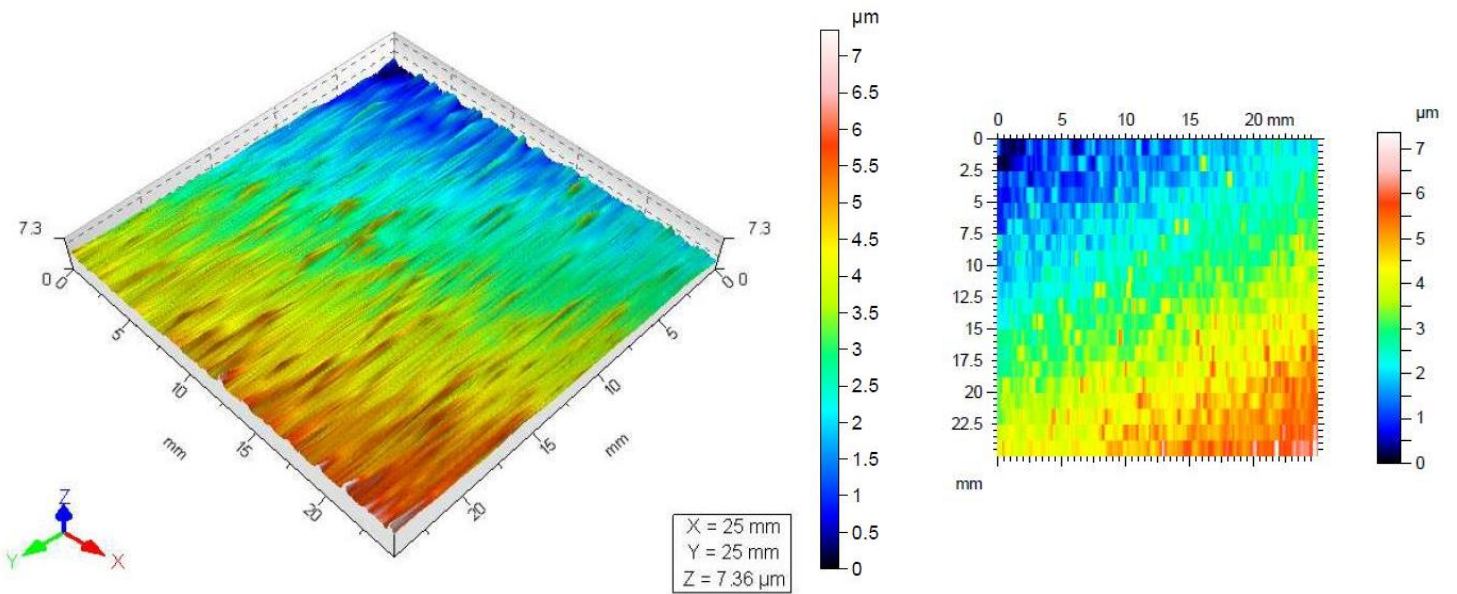
DIN ISO 25178

Height Parameters

Sq	1.56	μm
Ssk	0.0568	
Sku	2.26	
Sp	3.36	μm
Sv	3.73	μm
Sz	7.09	μm
Sa	1.30	μm

HommelMap Basic 6.2.6190 Report – Sample E11

Parameters: P = 150W, v = 150mm.s⁻¹, h = 0.125mm, d = 0.150mm



	15.0	82.4	2.58
Projected Area (%)	15.0	82.4	2.58
Volume of void (%)	4.03	61.7	99.5
Volume of material (%)	96.0	38.3	0.547
Volume of void (μm.mm2/mm2)	0.074	2.28	1.83
Volume of material (μm.mm2/mm2)	1.76	1.41	0.010
Mean thickness of void (μm)	0.074	2.28	1.83
Mean thickness of material (μm)	1.76	1.41	0.010

Identity card

Name: Topography
Filename: C:\Documents and Settings\OPERATOR\M Documents\Coetzee\Topography.top

Axis: X
Length: 25.0 mm
Size: 14706 points
Spacing: 1.70 μm
Offset: 0.00 mm

Axis: Y
Length: 25.0 mm
Size: 20 lines
Spacing: 1316 μm
Offset: 0.00 mm

Axis: Z
Length: 7.36 μm
Z min: -0.668 μm
Z max: 6.69 μm
Size: 7361 digits
Spacing: 1.00 nm

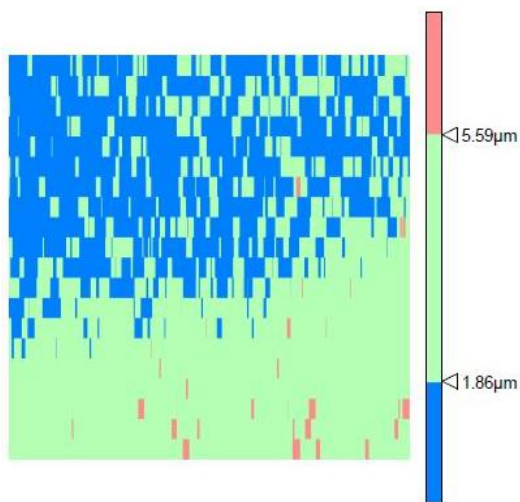
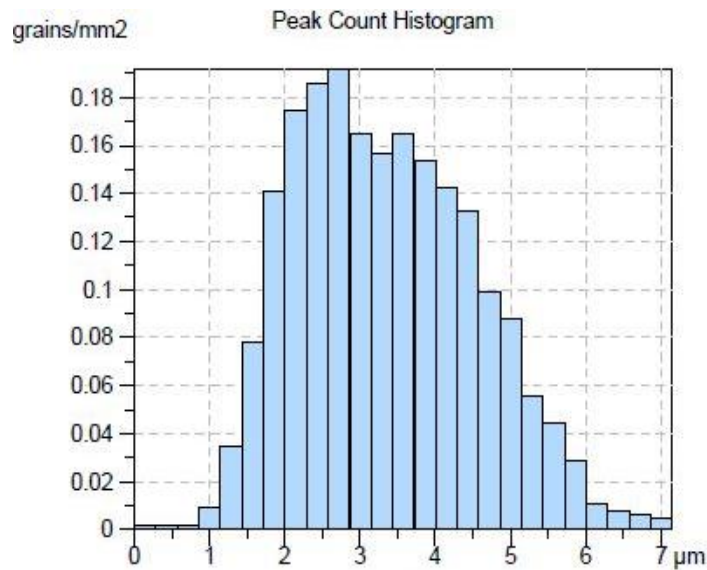
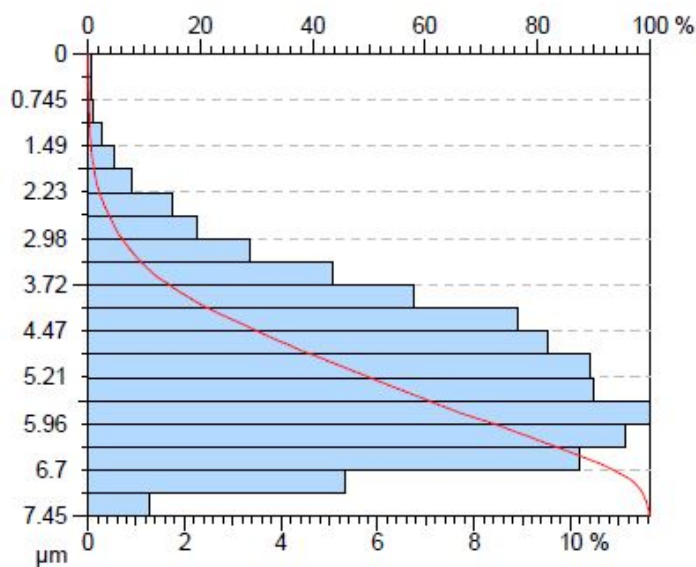
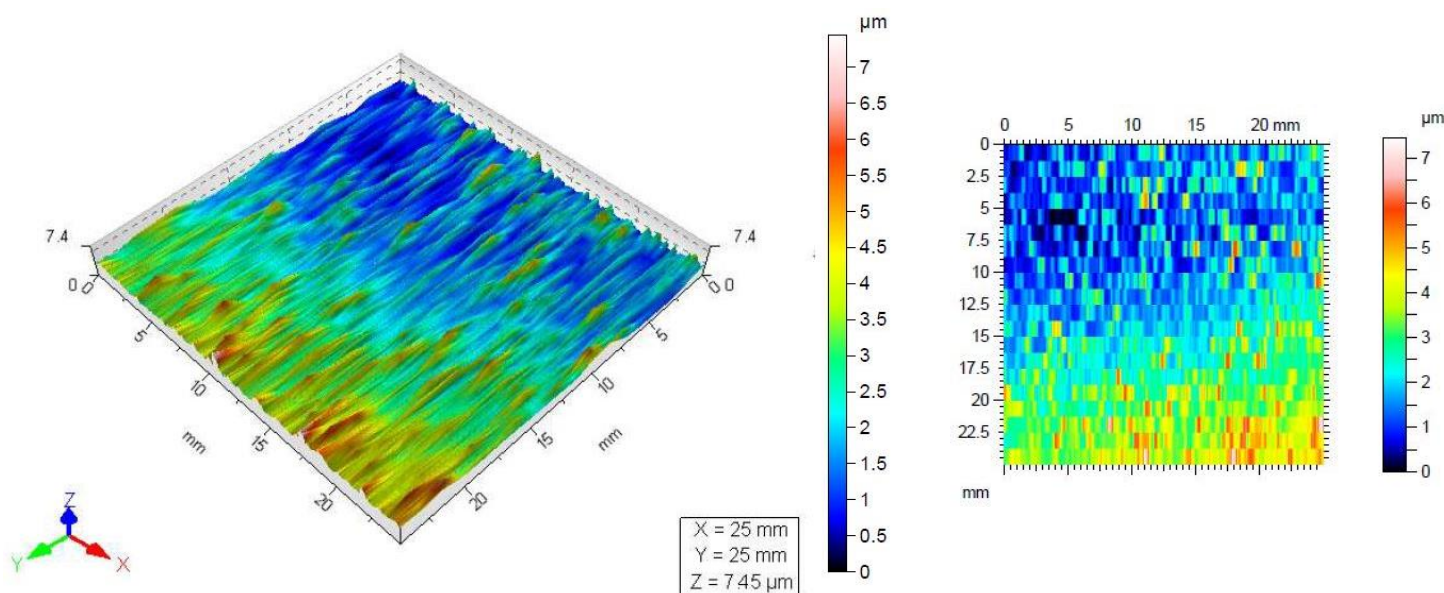
DIN ISO 25178

Height Parameters

Sq	1.26	μm
Ssk	0.140	
Sku	2.38	
Sp	4.18	μm
Sv	3.18	μm
Sz	7.36	μm
Sa	1.05	μm

HommelMap Basic 6.2.6190 Report – Sample E12

Parameters: P = 100W, v = 100mm.s⁻¹, h = 0.125mm, d = 0.150mm



	Blue	Green	Red
Projected Area (%)	39.3	59.6	1.07
Volume of void (%)	14.2	79.3	99.7
Volume of material (%)	85.8	20.7	0.298
Volume of void (μm.mm ² /mm ²)	0.264	2.96	1.85
Volume of material (μm.mm ² /mm ²)	1.59	0.772	0.00553
Mean thickness of void (μm)	0.264	2.96	1.85
Mean thickness of material (μm)	1.59	0.772	0.00553

Identity card

Name: Topography
Filename: C:\Documents and Settings\OPERATORM\Documents
\Coetzel\Topography.top

Axis: X
Length: 25.0 mm
Size: 14706 points
Spacing: 1.70 μm
Offset: 0.00 mm

Axis: Y
Length: 25.0 mm
Size: 20 lines
Spacing: 1316 μm
Offset: 0.00 mm

Axis: Z
Length: 7.45 μm
Z min: -0.886 μm
Z max: 6.56 μm
Size: 7448 digits
Spacing: 1.00 nm

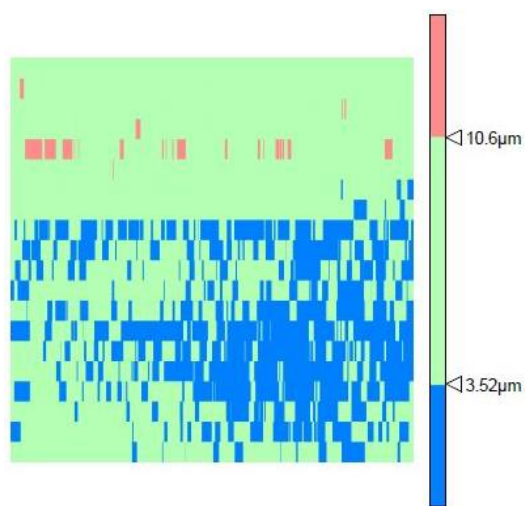
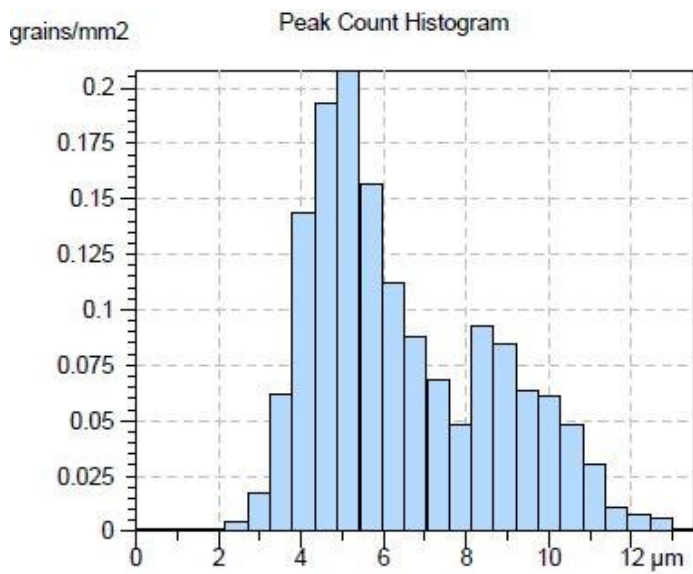
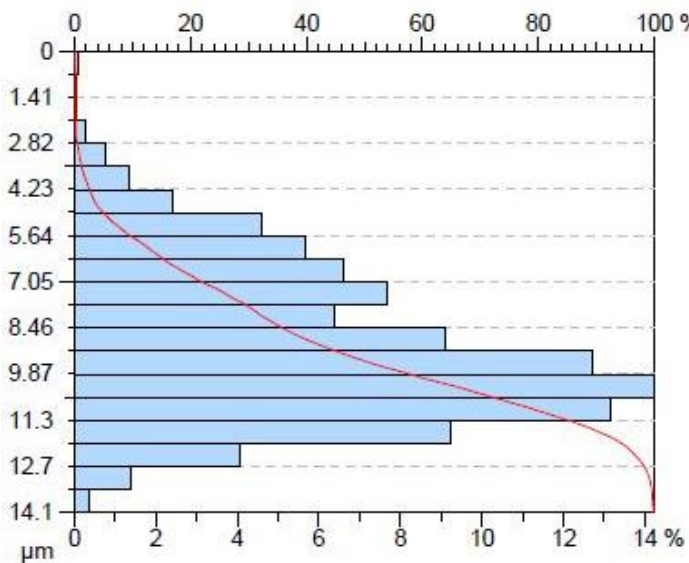
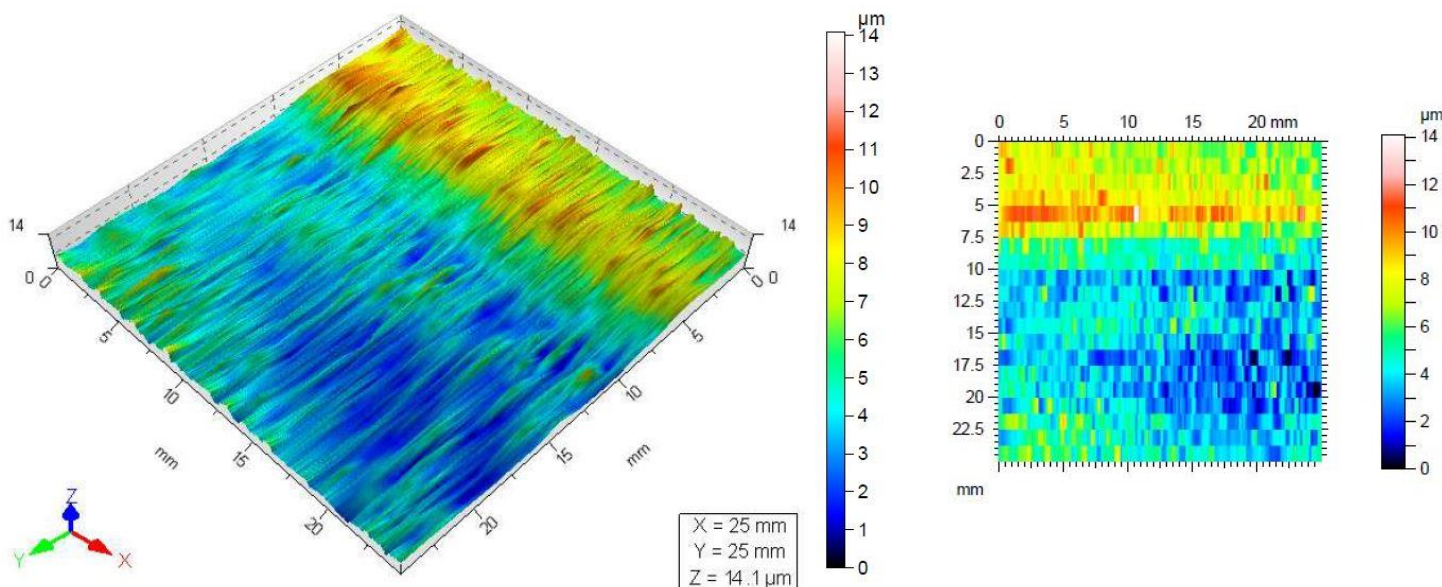
DIN ISO 25178

Height Parameters

Sq	1.23	μm
Ssk	0.586	
Sku	2.99	
Sp	5.08	μm
Sv	2.37	μm
Sz	7.45	μm
Sa	1.01	μm

HommelMap Basic 6.2.6190 Report – Sample E13

Parameters: P = 125W, v = 125mm.s⁻¹, h = 0.075mm, d = 0.150mm



	Blue	Green	Red
Projected Area (%)	27.9	71.0	1.14
Volume of void (%)	7.06	74.2	99.8
Volume of material (%)	92.9	25.8	0.227
Volume of void (μm.mm ² /mm ²)	0.248	5.24	3.51
Volume of material (μm.mm ² /mm ²)	3.27	1.82	0.00799
Mean thickness of void (μm)	0.248	5.24	3.51
Mean thickness of material (μm)	3.27	1.82	0.00799

Identity card

Name: Topography
 Filename: C:\T8000\DATEN\yero\Topography.top

Axis: X
 Length: 25.0 mm
 Size: 14706 points
 Spacing: 1.70 μm
 Offset: 0.00 mm

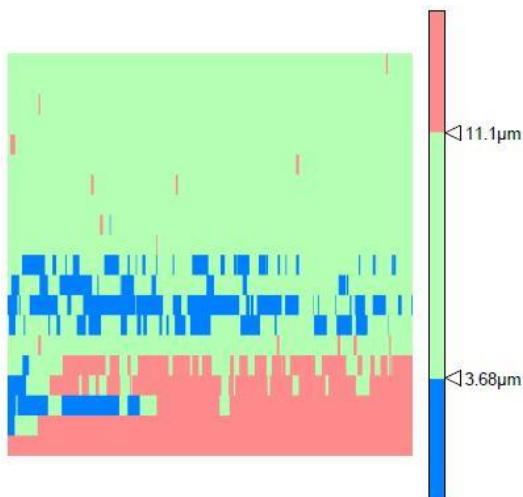
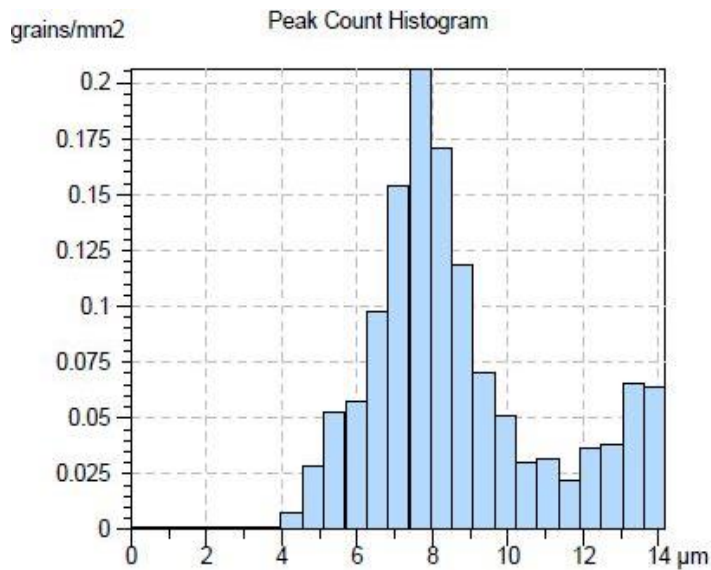
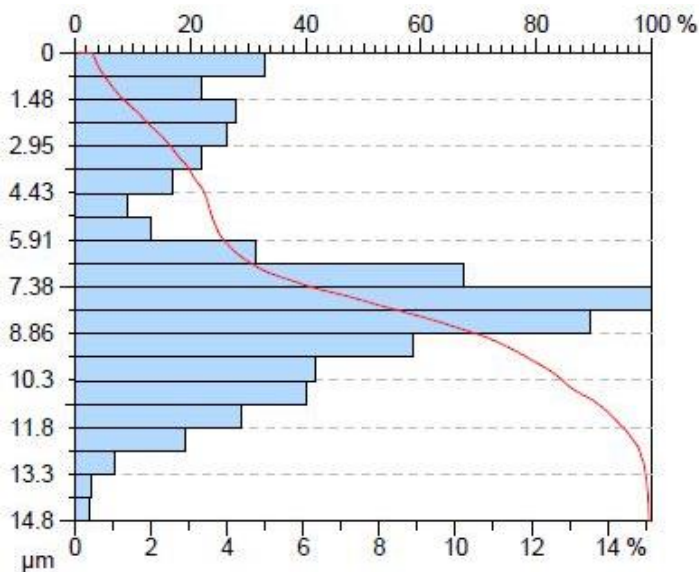
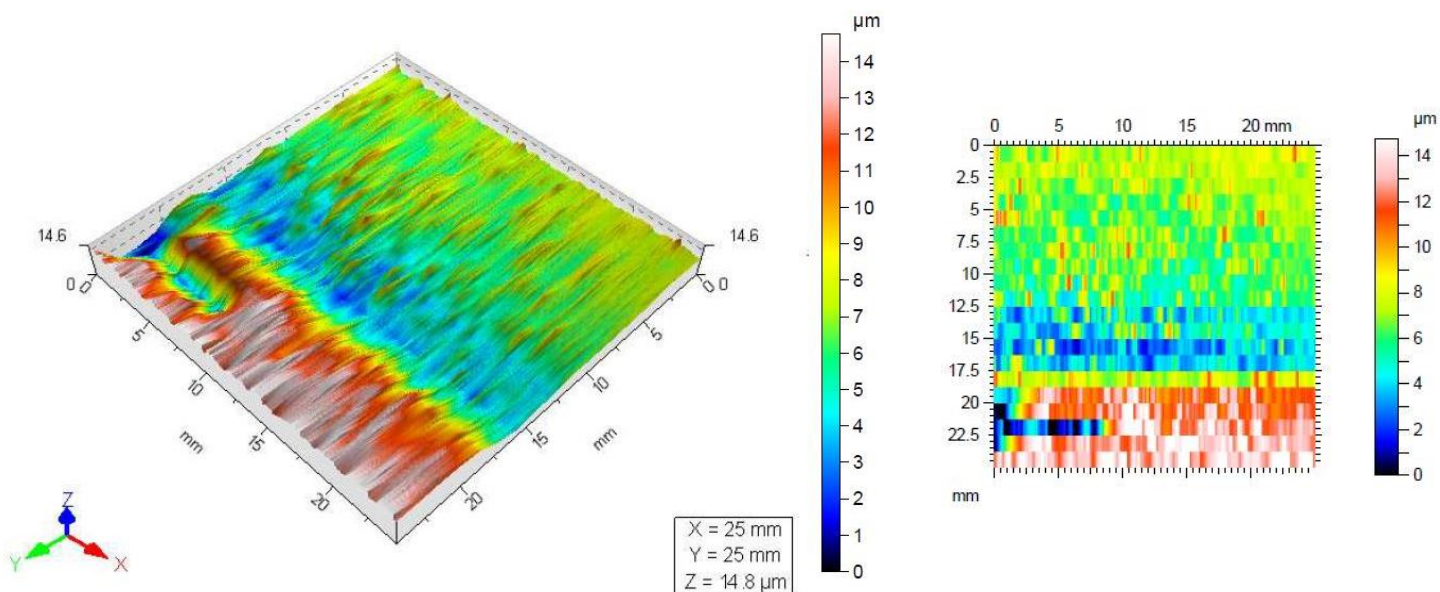
Axis: Y
 Length: 25.0 mm
 Size: 20 lines
 Spacing: 1316 μm
 Offset: 0.00 mm

Axis: Z
 Length: 14.1 μm
 Z min: -7.48 μm
 Z max: 6.61 μm
 Size: 14093 digits
 Spacing: 1.00 nm

DIN ISO 25178		
Height Parameters		
Sq	2.26	μm
Ssk	0.540	
Sku	2.65	
Sp	9.00	μm
Sv	5.09	μm
Sz	14.1	μm
Sa	1.87	μm

HommelMap Basic 6.2.6190 Report – Sample E14

Parameters: P = 175W, v = 175mm.s⁻¹, h = 0.075mm, d = 0.150mm



	Blue	Green	Red
Projected Area (%)	9.24	71.0	19.8
Volume of void (%)	2.58	51.3	89.3
Volume of material (%)	97.4	48.7	10.7
Volume of void (μm.mm²/mm²)	0.095	3.80	3.29
Volume of material (μm.mm²/mm²)	3.59	3.60	0.394
Mean thickness of void (μm)	0.095	3.80	3.29
Mean thickness of material (μm)	3.59	3.60	0.394

Identity card

Name: Topography
Filename: C:\T8000\DA\TENyero\Topography.top

Axis: X
Length: 25.0 mm
Size: 14706 points
Spacing: 1.70 μm
Offset: 0.00 mm

Axis: Y
Length: 25.0 mm
Size: 20 lines
Spacing: 1316 μm
Offset: 0.00 mm

Axis: Z
Length: 14.8 μm
Z min: -8.05 μm
Z max: 6.72 μm
Size: 14769 digits
Spacing: 1.00 nm

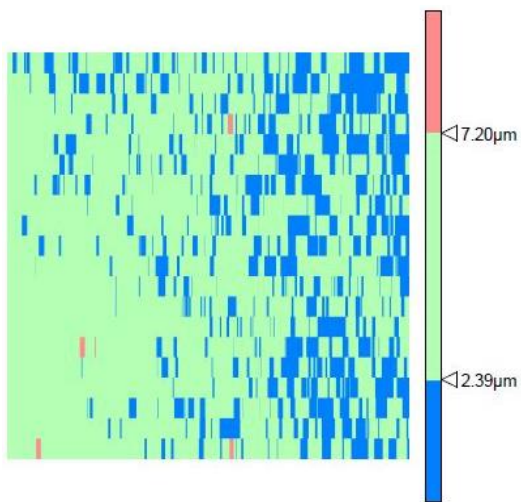
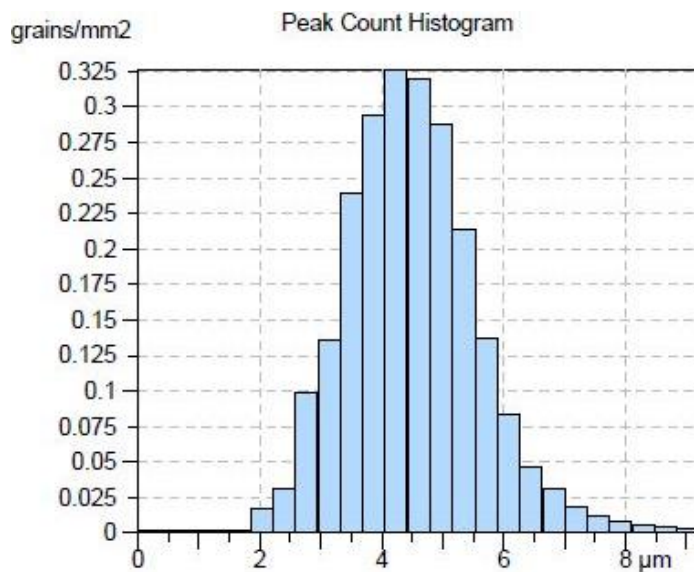
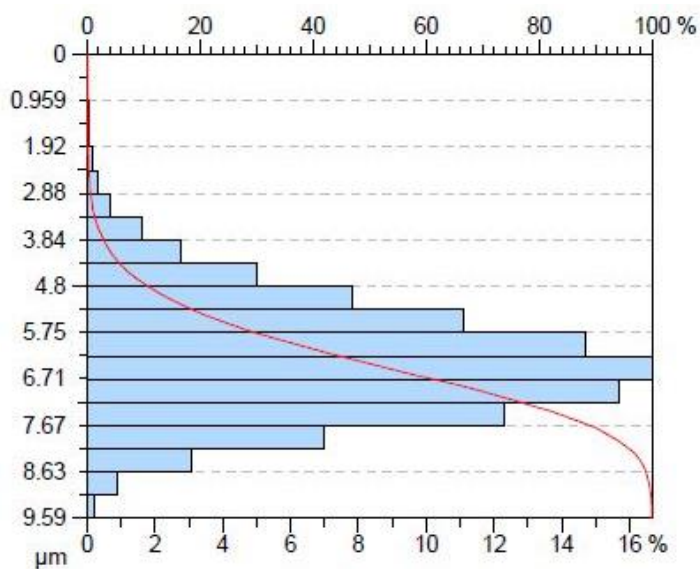
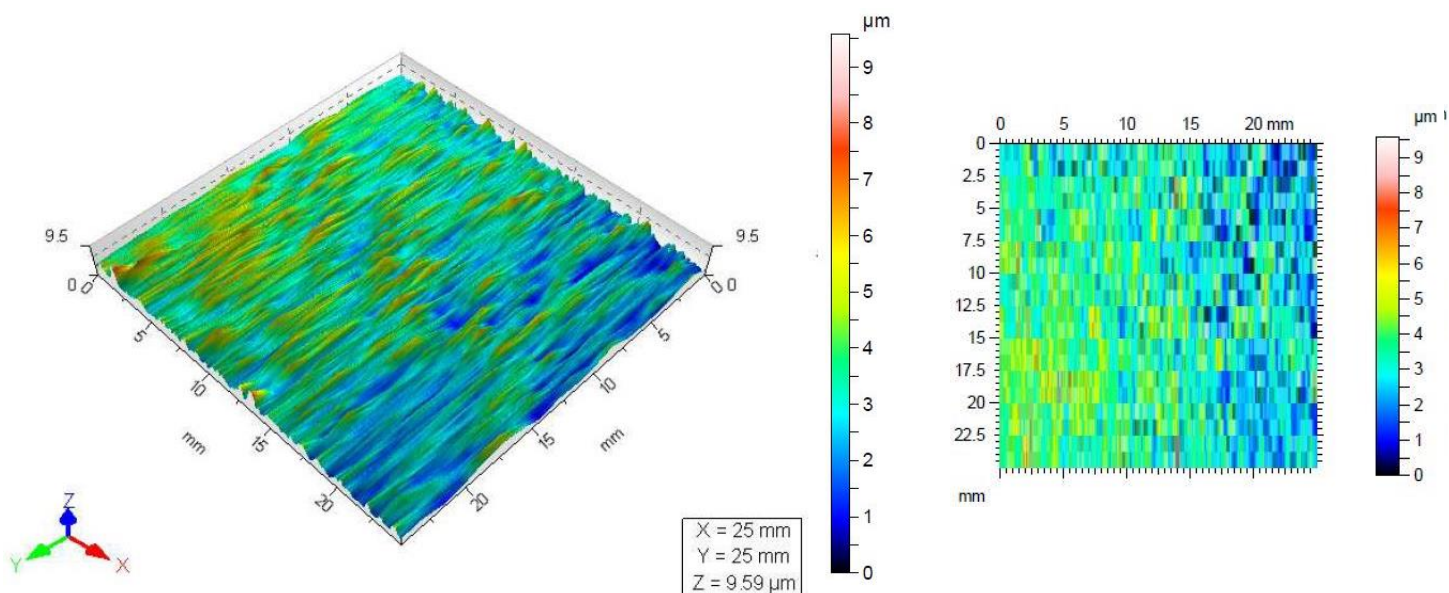
DIN ISO 25178

Height Parameters

Sq	3.30	μm
Ssk	0.573	
Sku	2.65	
Sp	7.18	μm
Sv	7.59	μm
Sz	14.8	μm
Sa	2.58	μm

HommelMap Basic 6.2.6190 Report – Sample E15

Parameters: P = 125W, v = 175mm.s⁻¹, h = 0.075mm, d = 0.150mm



	Blue	Green	Red
Projected Area (%)	23.2	76.6	0.254
Volume of void (%)	5.35	78.8	99.9
Volume of material (%)	94.6	21.2	0.0586
Volume of void (μm.mm ² /mm ²)	0.128	3.78	2.39
Volume of material (μm.mm ² /mm ²)	2.26	1.02	0.0014
Mean thickness of void (μm)	0.128	3.78	2.39
Mean thickness of material (μm)	2.26	1.02	0.0014

Identity card

Name: Topography
Filename: C:\T8000\DATA\Myer\Topography.top

Axis: X
Length: 25.0 mm
Size: 14706 points
Spacing: 1.70 μm
Offset: 0.00 mm

Axis: Y
Length: 25.0 mm
Size: 20 lines
Spacing: 1316 μm
Offset: 0.00 mm

Axis: Z
Length: 9.59 μm
Z min: -3.79 μm
Z max: 5.81 μm
Size: 9591 digits
Spacing: 1.00 nm

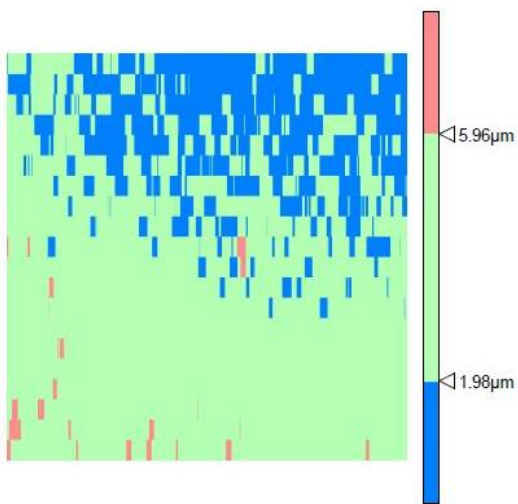
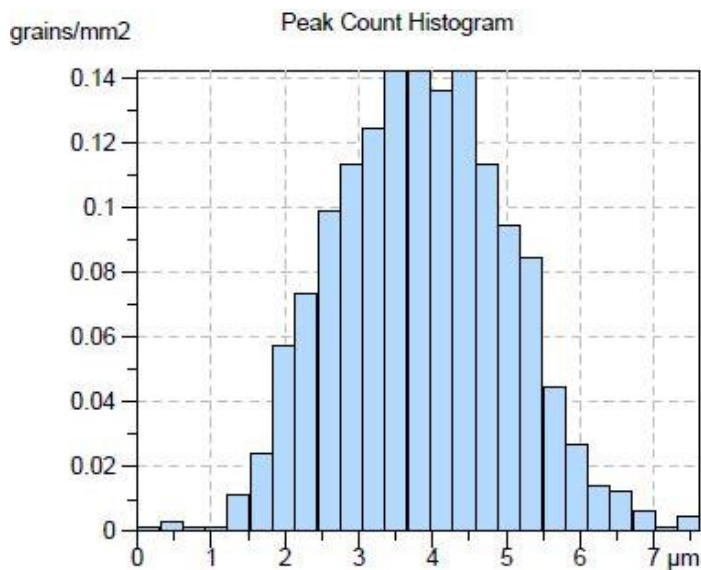
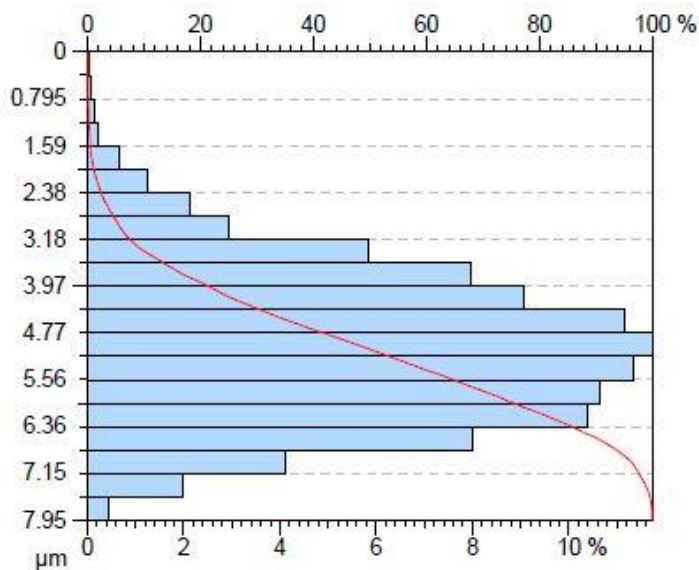
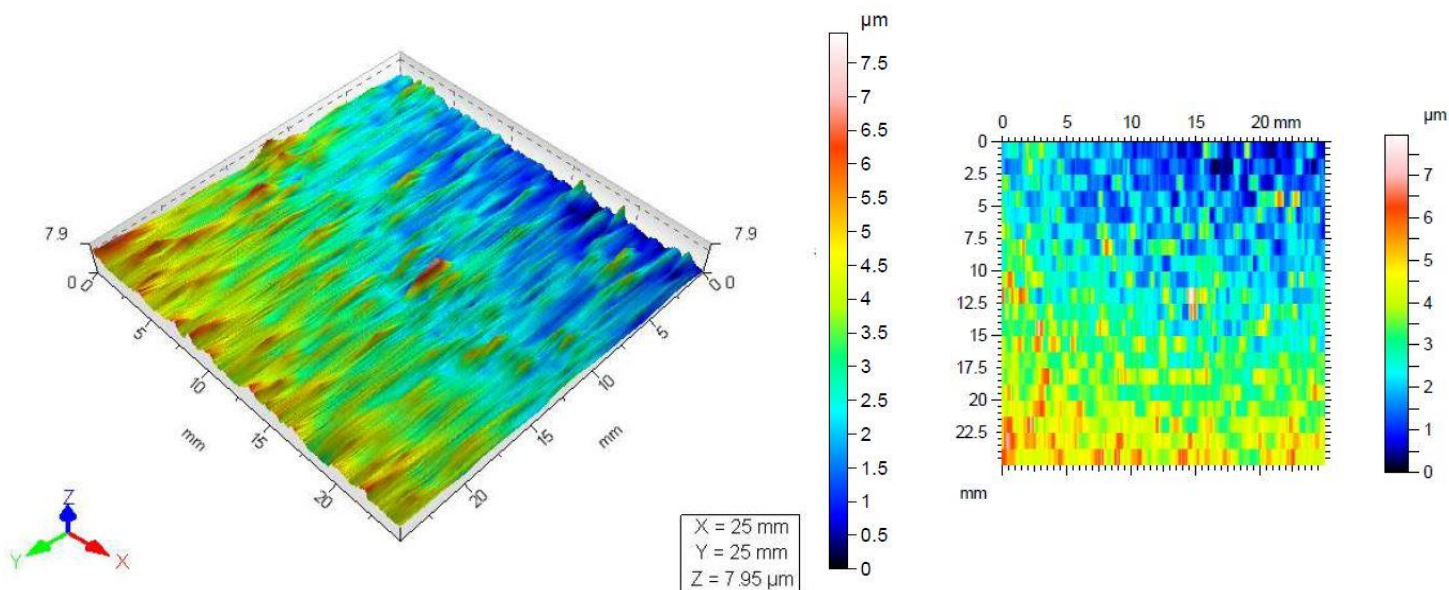
DIN ISO 25178

Height Parameters

Sq	1.17	μm
Ssk	0.459	
Sku	3.32	
Sp	6.30	μm
Sv	3.29	μm
Sz	9.59	μm
Sa	0.932	μm

HommelMap Basic 6.2.6190 Report – Sample E16

Parameters: P = 175W, v = 125mm.s⁻¹, h = 0.075mm, d = 0.150mm



	Blue	Green	Red
Projected Area (%)	24.6	74.2	1.12
Volume of void (%)	7.00	72.4	99.7
Volume of material (%)	93.0	27.6	0.276
Volume of void (μm.mm2/mm2)	0.139	2.88	1.98
Volume of material (μm.mm2/mm2)	1.84	1.10	0.00548
Mean thickness of void (μm)	0.139	2.88	1.98
Mean thickness of material (μm)	1.84	1.10	0.00548

Identity card

Name: Topography
Filename: C:\Documents and Settings\OPERATOR\M Documents
\Coetzeel\Topography.top

Axis: X
Length: 25.0 mm
Size: 14706 points
Spacing: 1.70 μm
Offset: 0.00 mm

Axis: Y
Length: 25.0 mm
Size: 20 lines
Spacing: 1316 μm
Offset: 0.00 mm

Axis: Z
Length: 7.95 μm
Z min: -1.71 μm
Z max: 6.24 μm
Size: 7946 digits
Spacing: 1.00 nm

DIN ISO 25178

Height Parameters

Parameter	Value	Unit
Sq	1.24	μm
Ssk	0.336	
Sku	2.81	
Sp	5.00	μm
Sv	2.95	μm
Sz	7.95	μm
Sa	1.01	μm

Appendix G

Hommel-etamic Turbo Wave V7.53 reports

The Hommel-etamic Turbo Wave V7.53 reports, for each single layer sample, are presented here. The first page of each report is the standardised calibration certificate which is included for the first sample (E1) report. Since each report differs only in the content on the second page, the first page of the report is shown once for sample E1 and thereafter only page two is shown. The reports are organised from E1-E16, sequentially. The final report page pertains to the benchmark sample used in this work.



Calibration Certificate

for tracing units

Hommelwerke GmbH's Calibration Certificates document the function of components combined in one tracing system using the calibrated values of a standard as reference. Any new or repaired components were set and checked at our works prior to the issue of this certificate.

Measurement conditions under which the certificate was issued conform to the DIN ISO regulations for roughness measurement. The standards are subject to gauge management (see page 2).

The user is responsible for keeping to an appropriate recalibration schedule.

We recommend annual checks or semi-annual checks for multiple shift operation within the frame of our service contract.

Customer:

Order #:

Equipment tested: Manufacturer's #

HOMMEL TESTER T8000:

Softwareversion: 7.53

Traverse unit: WL120/

Pick-up: TKU300/

The tracing system meets the calibrated values of the standard within a tolerance band of $\pm 3\%$

Date: 16.07.15

Inspected by: xx

Signature:

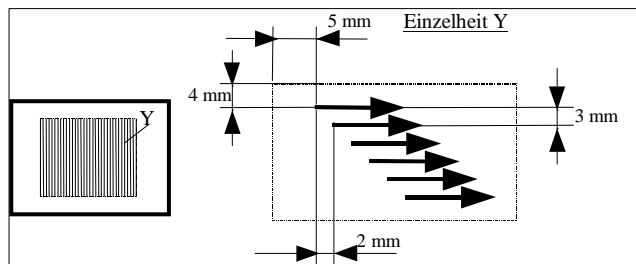
Standard

Standard: Geometrienormal (RND)
 Manufacturer's #: 3048
 Calibration mark: 4816|DKD-K-02401|2010-10

Calibrated values
Ra 3_25 μm
Rz DIN 10_35 μm
Rmax 10_37 μm

Traceability
 the standard has been calibrated to a measurement uncertainty of 5%. It is traceable to national standards relating to physical units in conformance with the international units system (SI)

Data-point plan

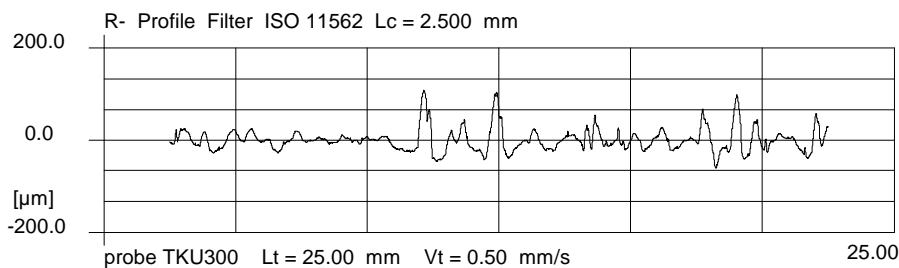


Measuring report HOMMEL TESTER T8000

HOMMEL-ETAMIC
 TURBO WAVE V7.53
 Measuring conditions
 Traverse length (Lt) : 25.00 mm
 Speed (Vt): 0.50 mm/s
 Probe factor: OFF
 Filter for profile P-R-W: ISO 11562
 Lc (Cut Off) : 2.500 mm
 Lc / Ls: OFF

Statistics n = 6

No.	Parameters	Xq	Range	S	Xmax	Xmin
1	Ra	20.78	4.91	1.81	23.26	18.35
2	Rz	126.75	8.87	3.02	130.23	121.36
3	Rmax	189.34	74.15	27.80	224.55	150.40



Standard

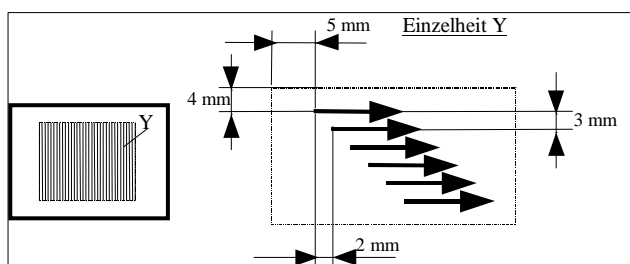
Standard: Geometrienormal (RND)
 Manufacturer's #: 3048
 Calibration mark: 4816|DKD-K-02401|2010-10

Calibrated values

Ra	3_25 μm
Rz DIN	10_35 μm
Rmax	10_37 μm

Traceability the standard has been calibrated to a measurement uncertainty of 5%. It is traceable to national standards relating to physical units in conformance with the international units system (SI)

Data-point plan

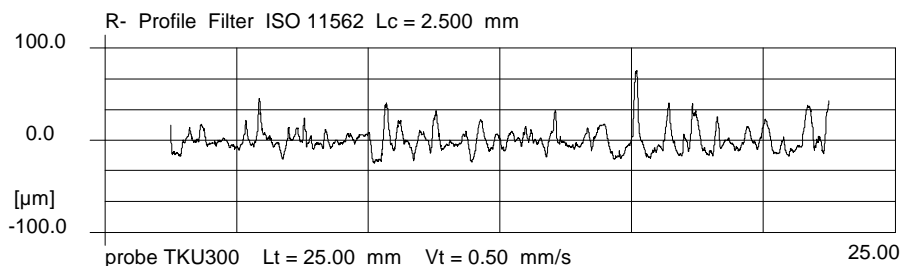


Measuring report HOMMEL TESTER T8000

HOMMEL-ETAMIC
 TURBO WAVE V7.53
 Measuring conditions
 Traverse length (Lt) : 25.00 mm
 Speed (Vt): 0.50 mm/s
 Probe factor: OFF
 Filter for profile P-R-W: ISO 11562
 Lc (Cut Off) : 2.500 mm
 Lc / Ls: OFF

Statistics n = 6

No.	Parameters	Xq	Range	S	Xmax	Xmin
1	Ra	11.24	2.65	1.04	12.16	9.51
2	Rz	82.41	20.65	7.01	91.51	70.86
3	Rmax	126.36	76.83	27.45	162.48	85.65



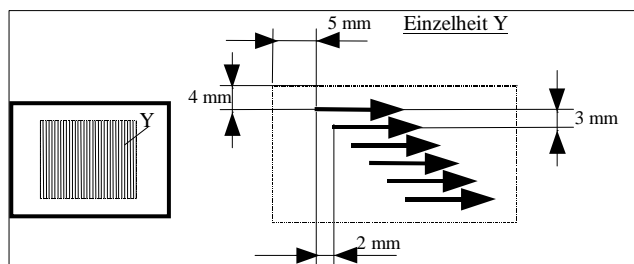
Standard

Standard: Geometrienormal (RND)
 Manufacturer's #: 3048
 Calibration mark: 4816|DKD-K-02401|2010-10

Calibrated values
Ra 3_25 μm
Rz DIN 10_35 μm
Rmax 10_37 μm

Traceability the standard has been calibrated to a measurement uncertainty of 5%. It is traceable to national standards relating to physical units in conformance with the international units system (SI)

Data-point plan

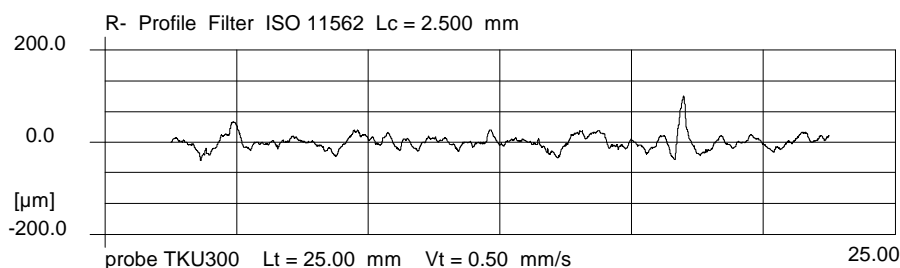


Measuring report HOMMEL TESTER T8000

HOMMEL-ETAMIC
 TURBO WAVE V7.53
 Measuring conditions
 Traverse length (Lt) : 25.00 mm
 Speed (Vt): 0.50 mm/s
 Probe factor: OFF
 Filter for profile P-R-W: ISO 11562
 Lc (Cut Off) : 2.500 mm
 Lc / Ls: OFF

Statistics n = 6

No.	Parameters	Xq	Range	S	Xmax	Xmin
1	Ra	11.00	4.61	1.54	13.42	8.81
2	Rz	67.53	27.26	9.20	83.18	55.92
3	Rmax	89.06	42.07	17.06	111.97	69.90



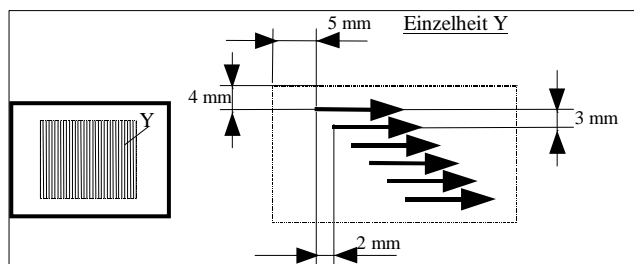
Standard

Standard: Geometrienormal (RND)
 Manufacturer's #: 3048
 Calibration mark: 4816|DKD-K-02401|2010-10

Calibrated values
Ra 3_25 μm
Rz DIN 10_35 μm
Rmax 10_37 μm

Traceability the standard has been calibrated to a measurement uncertainty of 5%. It is traceable to national standards relating to physical units in conformance with the international units system (SI)

Data-point plan

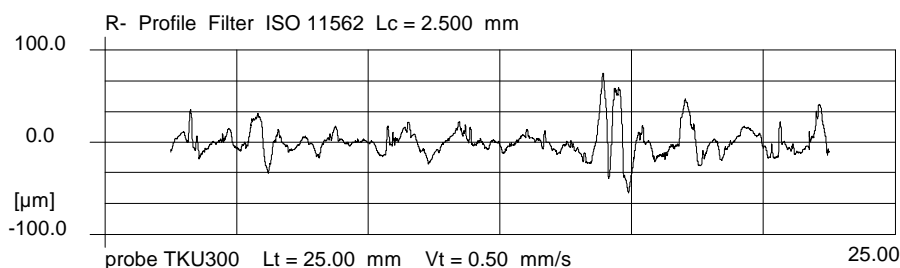


Measuring report HOMMEL TESTER T8000

HOMMEL-ETAMIC
 TURBO WAVE V7.53
 Measuring conditions
 Traverse length (Lt) : 25.00 mm
 Speed (Vt): 0.50 mm/s
 Probe factor: OFF
 Filter for profile P-R-W: ISO 11562
 Lc (Cut Off) : 2.500 mm
 Lc / Ls: OFF

Statistics n = 6

No.	Parameters	Xq	Range	S	Xmax	Xmin
1	Ra	13.45	7.36	2.43	17.65	10.29
2	Rz	89.71	60.12	19.04	119.30	59.18
3	Rmax	130.74	103.08	32.53	185.83	82.75



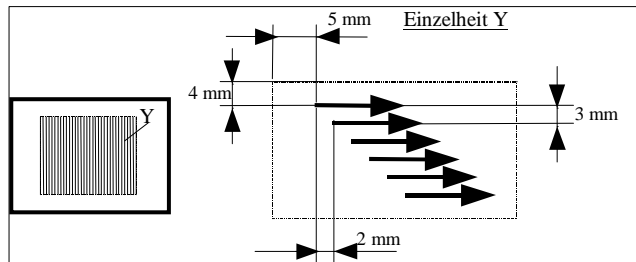
Standard

Standard: Geometrienormal (RND)
 Manufacturer's #: 3048
 Calibration mark: 4816|DKD-K-02401|2010-10

Calibrated values
Ra 3_25 μm
Rz DIN 10_35 μm
Rmax 10_37 μm

Traceability the standard has been calibrated to a measurement uncertainty of 5%. It is traceable to national standards relating to physical units in conformance with the international units system (SI)

Data-point plan

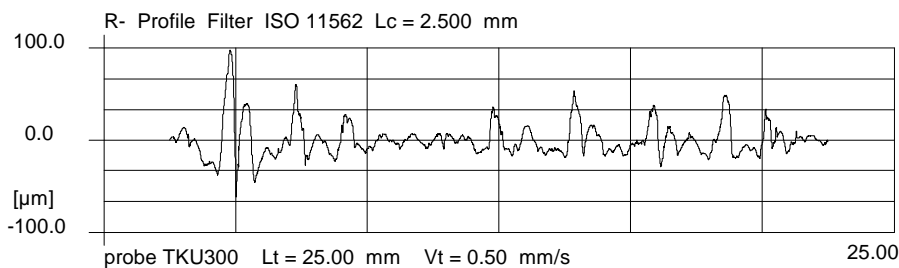


Measuring report HOMMEL TESTER T8000

HOMMEL-ETAMIC
 TURBO WAVE V7.53
 Measuring conditions
 Traverse length (Lt) : 25.00 mm
 Speed (Vt): 0.50 mm/s
 Probe factor: OFF
 Filter for profile P-R-W: ISO 11562
 Lc (Cut Off) : 2.500 mm
 Lc / Ls: OFF

Statistics n = 6

No.	Parameters	Xq	Range	S	Xmax	Xmin
1	Ra	8.54	2.82	0.98	10.18	7.36
2	Rz	52.85	24.26	8.65	63.08	38.82
3	Rmax	82.77	39.54	12.17	102.15	62.61



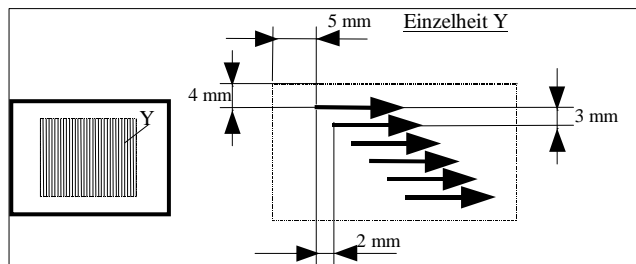
Standard

Standard: Geometrienormal (RND)
 Manufacturer's #: 3048
 Calibration mark: 4816|DKD-K-02401|2010-10

Calibrated values
Ra 3_25 μm
Rz DIN 10_35 μm
Rmax 10_37 μm

Traceability
 the standard has been calibrated to a measurement uncertainty of 5%. It is traceable to national standards relating to physical units in conformance with the international units system (SI)

Data-point plan

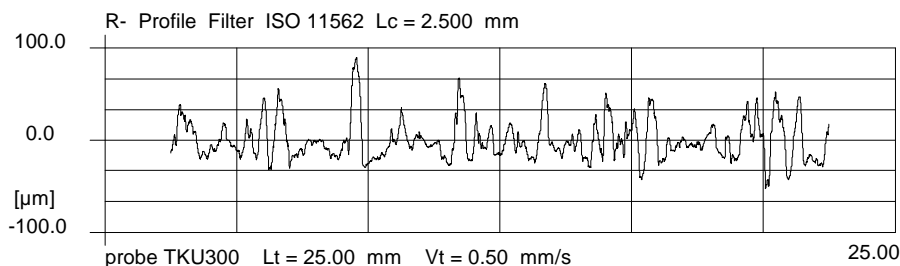


Measuring report HOMMEL TESTER T8000

HOMMEL-ETAMIC
 TURBO WAVE V7.53
 Measuring conditions
 Traverse length (Lt) : 25.00 mm
 Speed (Vt): 0.50 mm/s
 Probe factor: OFF
 Filter for profile P-R-W: ISO 11562
 Lc (Cut Off) : 2.500 mm
 Lc / Ls: OFF

Statistics n = 6

No.	Parameters	Xq	Range	S	Xmax	Xmin
1	Ra	20.71	5.34	1.70	23.85	18.51
2	Rz	111.94	31.06	11.08	125.78	94.72
3	Rmax	139.39	55.19	18.17	169.39	114.20



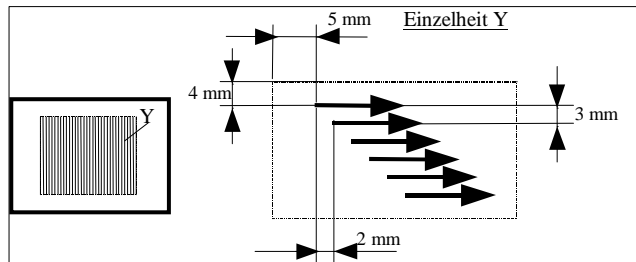
Standard

Standard: Geometrienormal (RND)
 Manufacturer's #: 3048
 Calibration mark: 4816|DKD-K-02401|2010-10

Calibrated values
Ra 3_25 μm
Rz DIN 10_35 μm
Rmax 10_37 μm

Traceability the standard has been calibrated to a measurement uncertainty of 5%. It is traceable to national standards relating to physical units in conformance with the international units system (SI)

Data-point plan

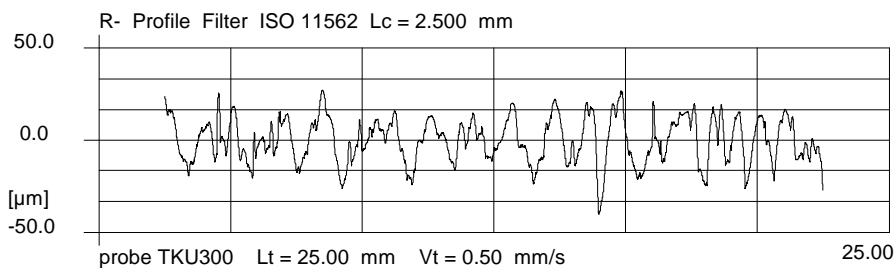


Measuring report HOMMEL TESTER T8000

HOMMEL-ETAMIC
 TURBO WAVE V7.53
 Measuring conditions
 Traverse length (Lt) : 25.00 mm
 Speed (Vt): 0.50 mm/s
 Probe factor: OFF
 Filter for profile P-R-W: ISO 11562
 Lc (Cut Off) : 2.500 mm
 Lc / Ls: OFF

Statistics n = 6

No.	Parameters	Xq	Range	S	Xmax	Xmin
1	Ra	8.44	4.38	1.45	11.05	6.67
2	Rz	52.02	27.74	9.38	66.75	39.01
3	Rmax	72.24	49.23	16.79	92.52	43.29



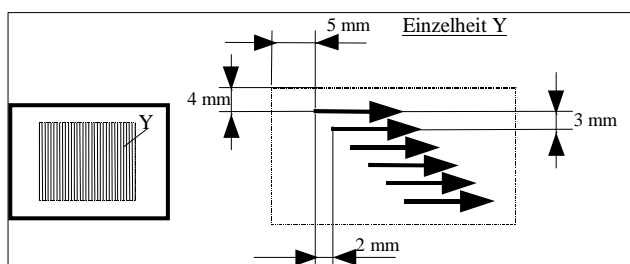
Standard

Standard: Geometrienormal (RND)
 Manufacturer's #: 3048
 Calibration mark: 4816|DKD-K-02401|2010-10

Calibrated values
Ra 3_25 μm
Rz DIN 10_35 μm
Rmax 10_37 μm

Traceability
 the standard has been calibrated to a measurement uncertainty of 5%. It is traceable to national standards relating to physical units in conformance with the international units system (SI)

Data-point plan

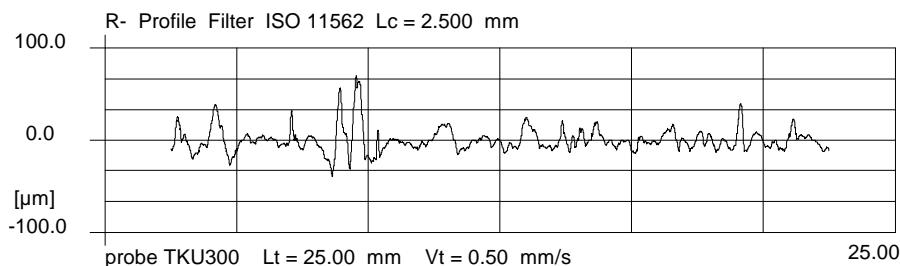


Measuring report HOMMEL TESTER T8000

HOMMEL-ETAMIC
 TURBO WAVE V7.53
 Measuring conditions
 Traverse length (Lt) : 25.00 mm
 Speed (Vt): 0.50 mm/s
 Probe factor: OFF
 Filter for profile P-R-W: ISO 11562
 Lc (Cut Off) : 2.500 mm
 Lc / Ls: OFF

Statistics n = 6

No.	Parameters	Xq	Range	S	Xmax	Xmin
1	Ra	8.86	2.00	0.65	10.19	8.19
2	Rz	62.81	22.47	7.65	79.56	57.09
3	Rmax	92.97	39.92	13.92	121.15	81.23



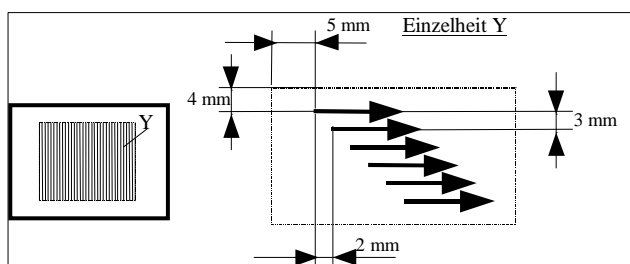
Standard

Standard: Geometrienormal (RND)
 Manufacturer's #: 3048
 Calibration mark: 4816|DKD-K-02401|2010-10

Calibrated values
Ra 3_25 μm
Rz DIN 10_35 μm
Rmax 10_37 μm

Traceability
 the standard has been calibrated to a measurement uncertainty of 5%. It is traceable to national standards relating to physical units in conformance with the international units system (SI)

Data-point plan

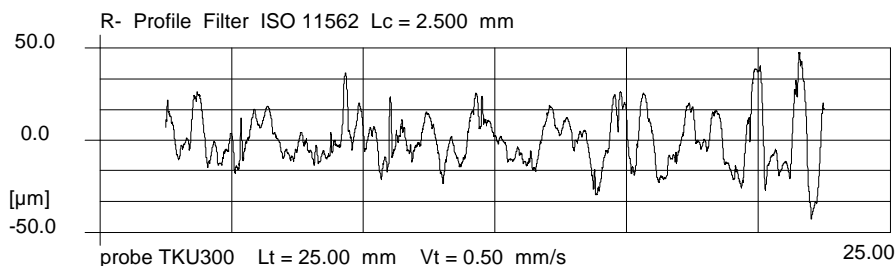


Measuring report HOMMEL TESTER T8000

HOMMEL-ETAMIC
 TURBO WAVE V7.53
 Measuring conditions
 Traverse length (Lt) : 25.00 mm
 Speed (Vt): 0.50 mm/s
 Probe factor: OFF
 Filter for profile P-R-W: ISO 11562
 Lc (Cut Off) : 2.500 mm
 Lc / Ls: OFF

Statistics n = 6

No.	Parameters	Xq	Range	S	Xmax	Xmin
1	Ra	11.89	3.94	1.33	13.68	9.74
2	Rz	74.81	33.99	10.39	91.96	57.97
3	Rmax	122.18	77.04	25.97	157.13	80.09



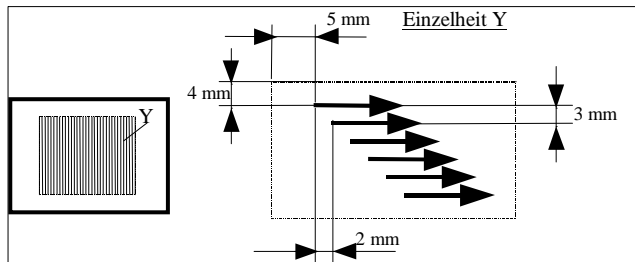
Standard

Standard: Geometrienormal (RND)
 Manufacturer's #: 3048
 Calibration mark: 4816|DKD-K-02401|2010-10

Calibrated values
Ra 3_25 μm
Rz DIN 10_35 μm
Rmax 10_37 μm

Traceability the standard has been calibrated to a measurement uncertainty of 5%. It is traceable to national standards relating to physical units in conformance with the international units system (SI)

Data-point plan

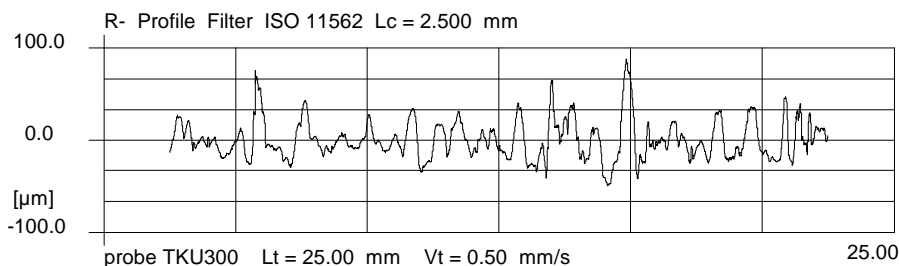


Measuring report HOMMEL TESTER T8000

HOMMEL-ETAMIC
 TURBO WAVE V7.53
 Measuring conditions
 Traverse length (Lt) : 25.00 mm
 Speed (Vt): 0.50 mm/s
 Probe factor: OFF
 Filter for profile P-R-W: ISO 11562
 Lc (Cut Off) : 2.500 mm
 Lc / Ls: OFF

Statistics n = 6

No.	Parameters	Xq	Range	S	Xmax	Xmin
1	Ra	18.73	7.07	2.36	22.67	15.60
2	Rz	114.36	36.41	15.08	136.48	100.07
3	Rmax	183.50	114.68	42.84	252.65	137.97



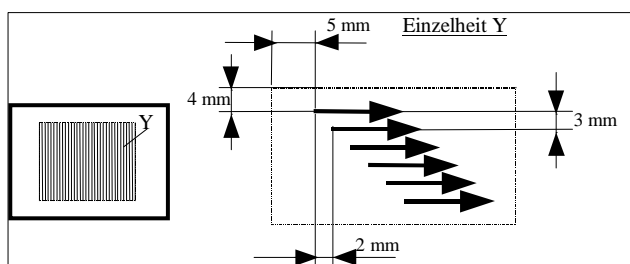
Standard

Standard: Geometrienormal (RND)
 Manufacturer's #: 3048
 Calibration mark: 4816|DKD-K-02401|2010-10

Calibrated values
Ra 3_25 μm
Rz DIN 10_35 μm
Rmax 10_37 μm

Traceability
 the standard has been calibrated to a measurement uncertainty of 5%. It is traceable to national standards relating to physical units in conformance with the international units system (SI)

Data-point plan

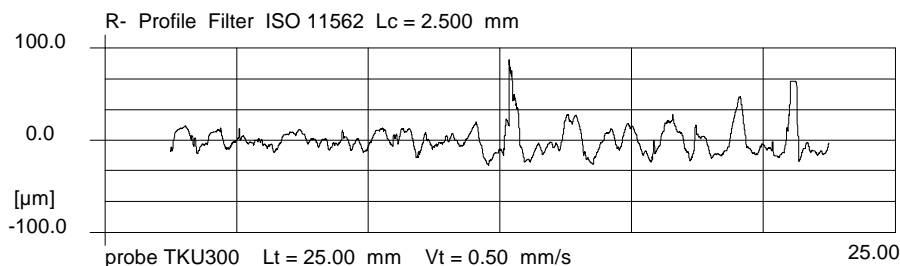


Measuring report HOMMEL TESTER T8000

HOMMEL-ETAMIC
 TURBO WAVE V7.53
 Measuring conditions
 Traverse length (Lt) : 25.00 mm
 Speed (Vt): 0.50 mm/s
 Probe factor: OFF
 Filter for profile P-R-W: ISO 11562
 Lc (Cut Off) : 2.500 mm
 Lc / Ls: OFF

Statistics n = 6

No.	Parameters	Xq	Range	S	Xmax	Xmin
1	Ra	10.71	2.43	0.79	12.05	9.62
2	Rz	67.06	17.22	6.20	74.03	56.81
3	Rmax	104.87	34.70	15.02	124.14	89.44



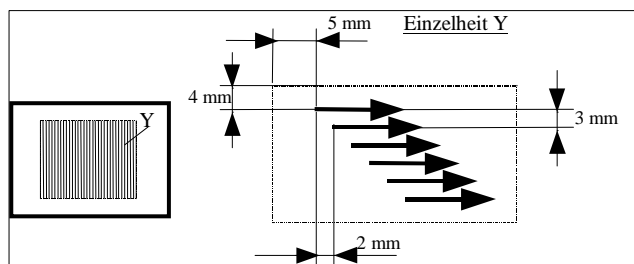
Standard

Standard: Geometrienormal (RND)
 Manufacturer's #: 3048
 Calibration mark: 4816|DKD-K-02401|2010-10

Calibrated values
Ra 3_25 μm
Rz DIN 10_35 μm
Rmax 10_37 μm

Traceability
 the standard has been calibrated to a measurement uncertainty of 5%. It is traceable to national standards relating to physical units in conformance with the international units system (SI)

Data-point plan

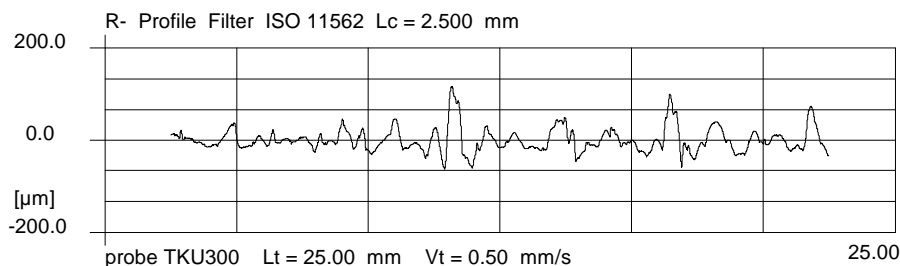


Measuring report HOMMEL TESTER T8000

HOMMEL-ETAMIC
 TURBO WAVE V7.53
 Measuring conditions
 Traverse length (Lt) : 25.00 mm
 Speed (Vt): 0.50 mm/s
 Probe factor: OFF
 Filter for profile P-R-W: ISO 11562
 Lc (Cut Off) : 2.500 mm
 Lc / Ls: OFF

Statistics n = 6

No.	Parameters	Xq	Range	S	Xmax	Xmin
1	Ra	23.60	7.55	2.74	26.11	18.56
2	Rz	133.59	46.69	14.95	159.61	112.92
3	Rmax	202.79	142.20	49.58	290.06	147.86



Standard

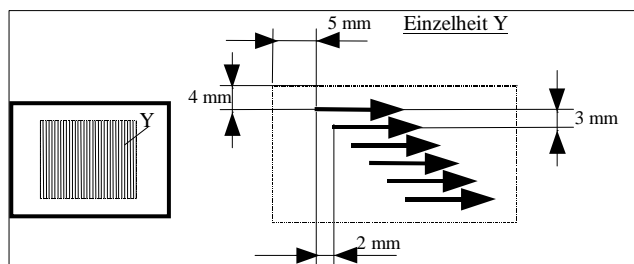
Standard: Geometrienormal (RND)
 Manufacturer's #: 3048
 Calibration mark: 4816|DKD-K-02401|2010-10

Calibrated values

Ra	3_25 μm
Rz DIN	10_35 μm
Rmax	10_37 μm

Traceability the standard has been calibrated to a measurement uncertainty of 5%. It is traceable to national standards relating to physical units in conformance with the international units system (SI)

Data-point plan

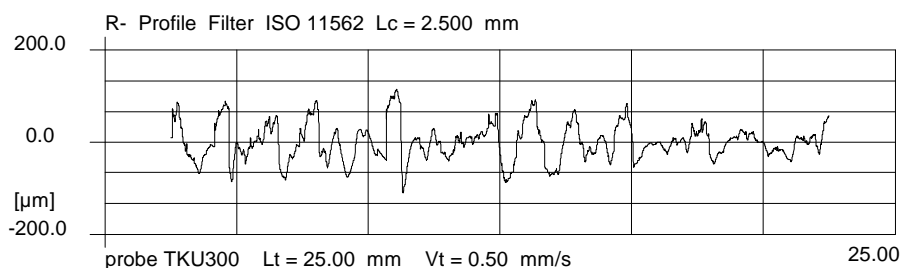


Measuring report HOMMEL TESTER T8000

HOMMEL-ETAMIC
 TURBO WAVE V7.53
 Measuring conditions
 Traverse length (Lt) : 25.00 mm
 Speed (Vt): 0.50 mm/s
 Probe factor: OFF
 Filter for profile P-R-W: ISO 11562
 Lc (Cut Off) : 2.500 mm
 Lc / Ls: OFF

Statistics n = 6

No.	Parameters	Xq	Range	S	Xmax	Xmin
1	Ra	27.79	9.17	3.50	33.60	24.43
2	Rz	175.99	41.88	17.16	196.17	154.29
3	Rmax	235.07	75.98	29.18	278.90	202.92



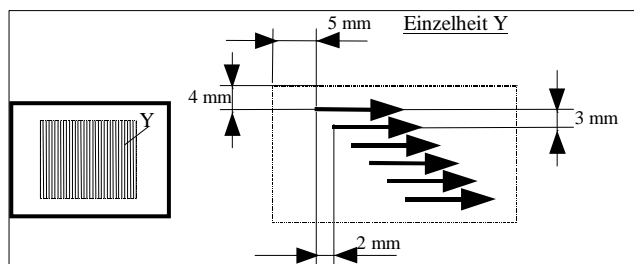
Standard

Standard: Geometrienormal (RND)
 Manufacturer's #: 3048
 Calibration mark: 4816|DKD-K-02401|2010-10

Calibrated values
Ra 3_25 μm
Rz DIN 10_35 μm
Rmax 10_37 μm

Traceability the standard has been calibrated to a measurement uncertainty of 5%. It is traceable to national standards relating to physical units in conformance with the international units system (SI)

Data-point plan

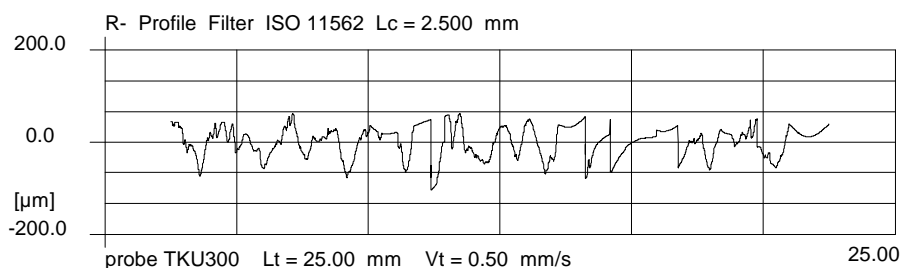


Measuring report HOMMEL TESTER T8000

HOMMEL-ETAMIC
 TURBO WAVE V7.53
 Measuring conditions
 Traverse length (Lt) : 25.00 mm
 Speed (Vt): 0.50 mm/s
 Probe factor: OFF
 Filter for profile P-R-W: ISO 11562
 Lc (Cut Off) : 2.500 mm
 Lc / Ls: OFF

Statistics n = 6

No.	Parameters	Xq	Range	S	Xmax	Xmin
1	Ra	22.85	10.33	3.58	29.65	19.32
2	Rz	140.38	60.93	20.51	181.44	120.51
3	Rmax	206.80	98.00	31.87	275.95	177.95



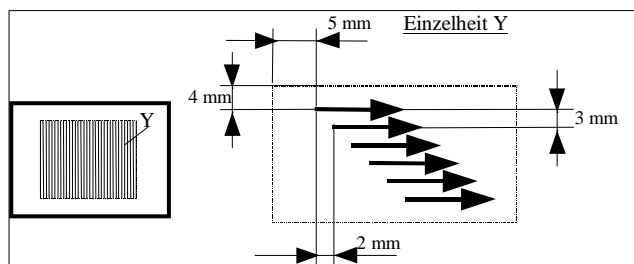
Standard

Standard: Geometrienormal (RND)
 Manufacturer's #: 3048
 Calibration mark: 4816|DKD-K-02401|2010-10

Calibrated values
Ra 3_25 μm
Rz DIN 10_35 μm
Rmax 10_37 μm

Traceability
 the standard has been calibrated to a measurement uncertainty of 5%. It is traceable to national standards relating to physical units in conformance with the international units system (SI)

Data-point plan

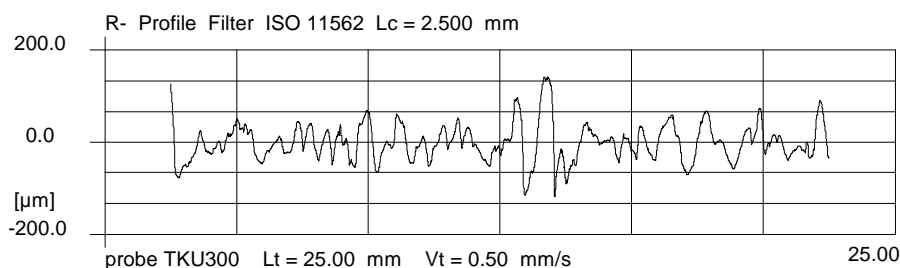


Measuring report HOMMEL TESTER T8000

HOMMEL-ETAMIC
 TURBO WAVE V7.53
 Measuring conditions
 Traverse length (Lt) : 25.00 mm
 Speed (Vt): 0.50 mm/s
 Probe factor: OFF
 Filter for profile P-R-W: ISO 11562
 Lc (Cut Off) : 2.500 mm
 Lc / Ls: OFF

Statistics n = 6

No.	Parameters	Xq	Range	S	Xmax	Xmin
1	Ra	32.55	5.94	2.29	35.03	29.09
2	Rz	179.55	77.61	25.22	222.94	145.33
3	Rmax	244.17	147.99	53.07	345.87	197.88



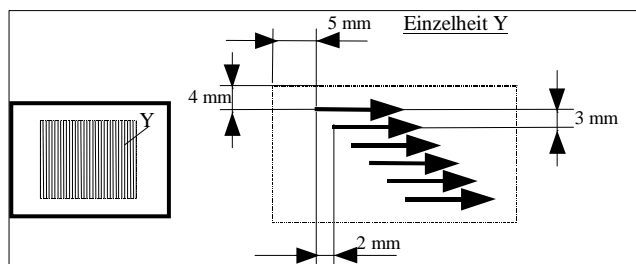
Standard

Standard: Geometrienormal (RND)
 Manufacturer's #: 3048
 Calibration mark: 4816|DKD-K-02401|2010-10

Calibrated values
Ra 3_25 μm
Rz DIN 10_35 μm
Rmax 10_37 μm

Traceability
 the standard has been calibrated to a measurement uncertainty of 5%. It is traceable to national standards relating to physical units in conformance with the international units system (SI)

Data-point plan

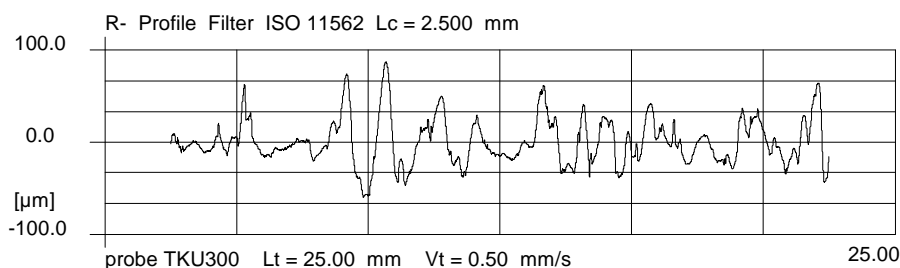


Measuring report HOMMEL TESTER T8000

HOMMEL-ETAMIC
 TURBO WAVE V7.53
 Measuring conditions
 Traverse length (Lt) : 25.00 mm
 Speed (Vt): 0.50 mm/s
 Probe factor: OFF
 Filter for profile P-R-W: ISO 11562
 Lc (Cut Off) : 2.500 mm
 Lc / Ls: OFF

Statistics n = 6

No.	Parameters	Xq	Range	S	Xmax	Xmin
1	Ra	18.73	7.07	2.36	22.67	15.60
2	Rz	114.36	36.41	15.08	136.48	100.07
3	Rmax	183.50	114.68	42.84	252.65	137.97



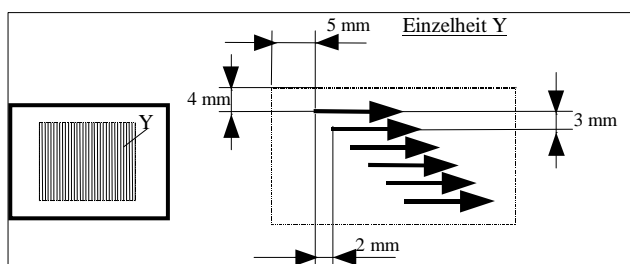
Standard

Standard: Geometrienormal (RND)
 Manufacturer's #: 3048
 Calibration mark: 4816|DKD-K-02401|2010-10

Calibrated values
Ra 3.25 μm
Rz DIN 10.35 μm
Rmax 10.37 μm

Traceability the standard has been calibrated to a measurement uncertainty of 5%. It is traceable to national standards relating to physical units in conformance with the international units system (SI)

Data-point plan

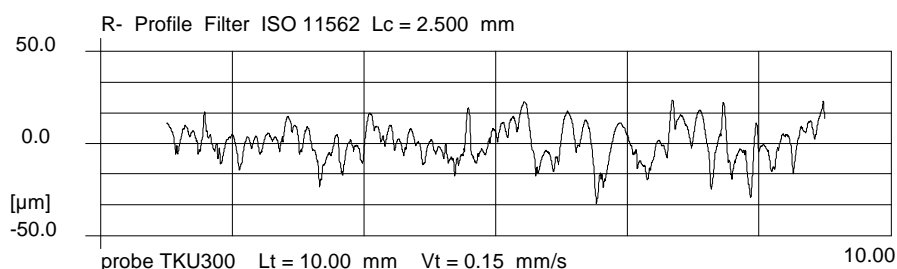


Measuring report HOMMEL TESTER T8000

HOMMEL-ETAMIC
 TURBO WAVE V7.53
 Measuring conditions
 Traverse length (Lt) : 10.00 mm
 Speed (Vt): 0.15 mm/s
 Probe factor: OFF
 Filter for profile P-R-W: ISO 11562
 Lc (Cut Off) : 2.500 mm
 Lc / Ls: OFF

Statistics n = 6

No.	Parameters	Xq	Range	S	Xmax	Xmin
1	Ra	11.04	3.90	1.27	12.96	9.06
2	Rz	59.53	21.14	6.80	69.69	48.55
3	Rmax	77.86	16.62	6.17	85.52	68.00



Appendix H

MODDE analysis results

The results from the statistical analysis, using the roughness profile parameter R_z as response variable, is presented here. The statistical analysis is carried out using MODDE by Umetrics, a Design of Experiments (DOE) software which enables complex analysis and optimisation of experiments.

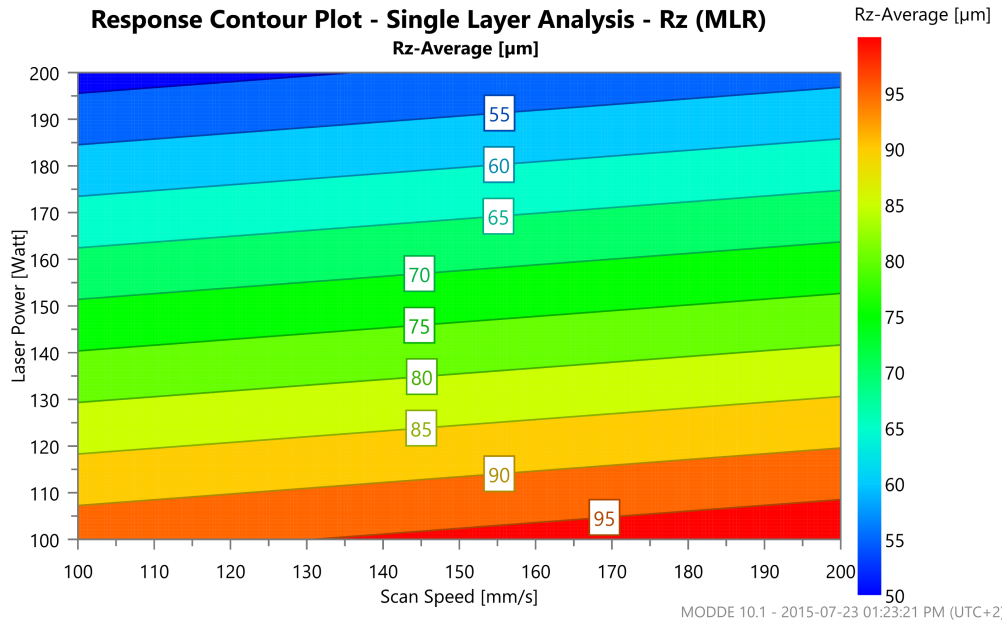


Figure H.1: Contour plot combining laser power, scan speed, and response variable R_z .

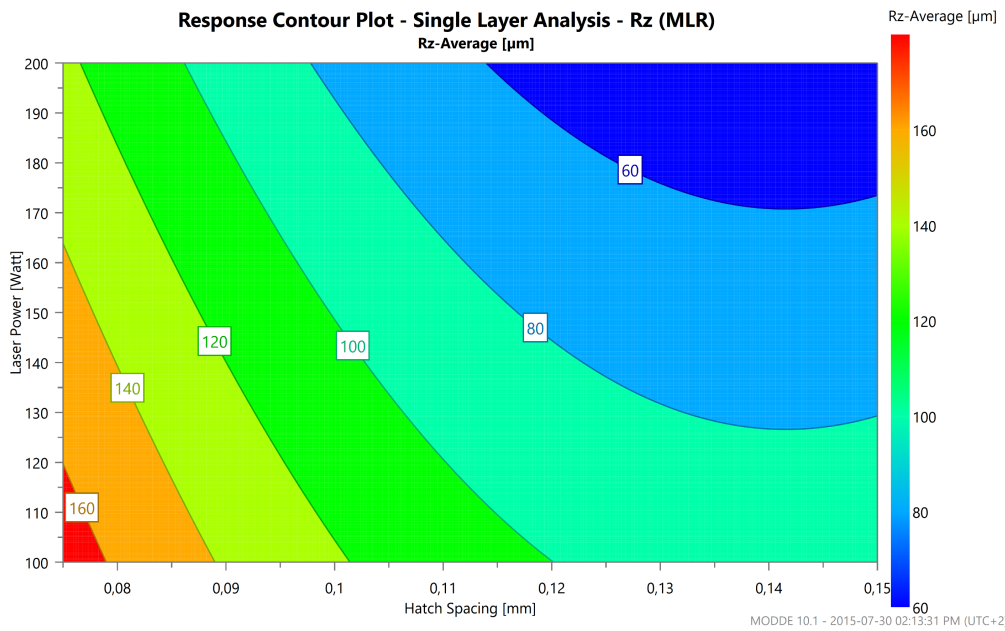


Figure H.2: Contour plot combining laser power, hatch spacing, and response variable R_z .

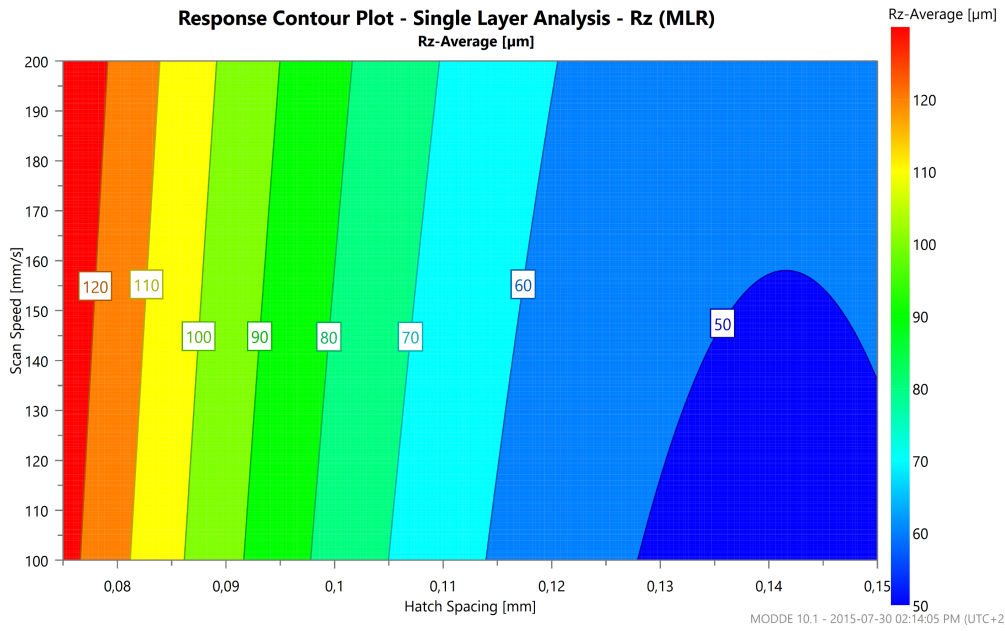


Figure H.3: Contour plot combining scan speed, hatch spacing, and response variable R_z .

Table H.1: Extended setpoint summary for experiment factors.

Factor	Scan Speed	Laser Power	Hatch Spacing
Low	36,38	127,31	0,0984
Setpoint	100,00	200,00	0,1425
High	163,63	272,69	0,1866
Distribution	Normal	Normal	Normal
Possible Minimum	77,50	77,50	0,0656
Possible Maximum	222,50	222,50	0,1669
Experimental Minimum	100,00	100,00	0,0750
Experimental Maximum	200,00	200,00	0,1500

Table H.2: Extended setpoint summary for response variable R_z .

Response	Rz-Average	Model Error Included in Predictions	Number of Samples
DPMO	10499	Yes	10000
C_{pk} Estimate	0,942051		
% out of Range	1,05		
Average	55,0843		
Median	54,6375		
1 st Quartile	35,4964		
3 rd Quartile	73,6591		
Std. Dev.	33,5847		
Skewness	0,513885		
DF	11		

Table H.3: Alternate setpoints as determined by the MODDE Optimiser.

No.	Scan Speed	Laser Power	Hatch Spacing	R _z -Average	Iterations	log(D)	C _{pk}
1	101,55	190,58	0,1482	51,88	64,00	-0,92	1,97
2	120,03	199,70	0,1479	48,71	40,00	-0,98	2,09
3	134,63	197,55	0,1398	49,86	28,00	-0,96	2,40
4	110,00	200,00	0,1425	47,34	8,00	-1,00	2,19
5	178,03	198,57	0,1378	52,01	55,00	-0,92	2,16
6	189,67	199,92	0,1406	51,82	46,00	-0,92	2,04
7	197,45	198,44	0,1398	52,96	49,00	-0,90	1,95
8	170,00	200,00	0,1425	50,68	10,00	-0,94	2,21
9	130,57	199,90	0,1464	48,93	38,00	-0,97	2,18
10	100,00	200,00	0,1425	46,78	7,00	-1,01	2,11
11	180,00	200,00	0,1425	51,24	7,00	-0,93	2,13
12	110,54	199,53	0,1420	47,57	28,00	-1,00	2,18

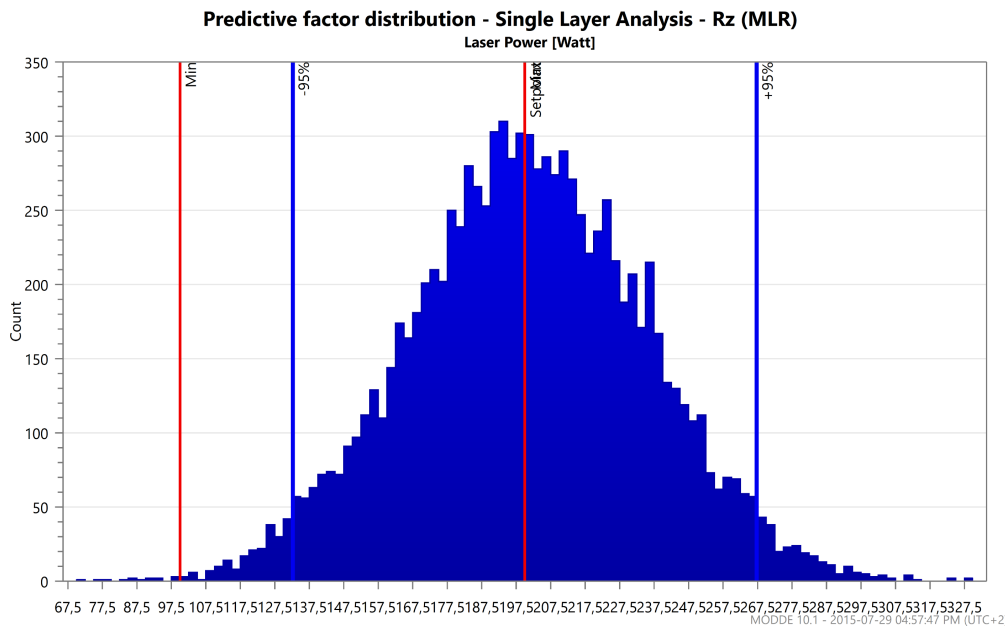


Figure H.4: Predictive factor distribution plot for laser power.

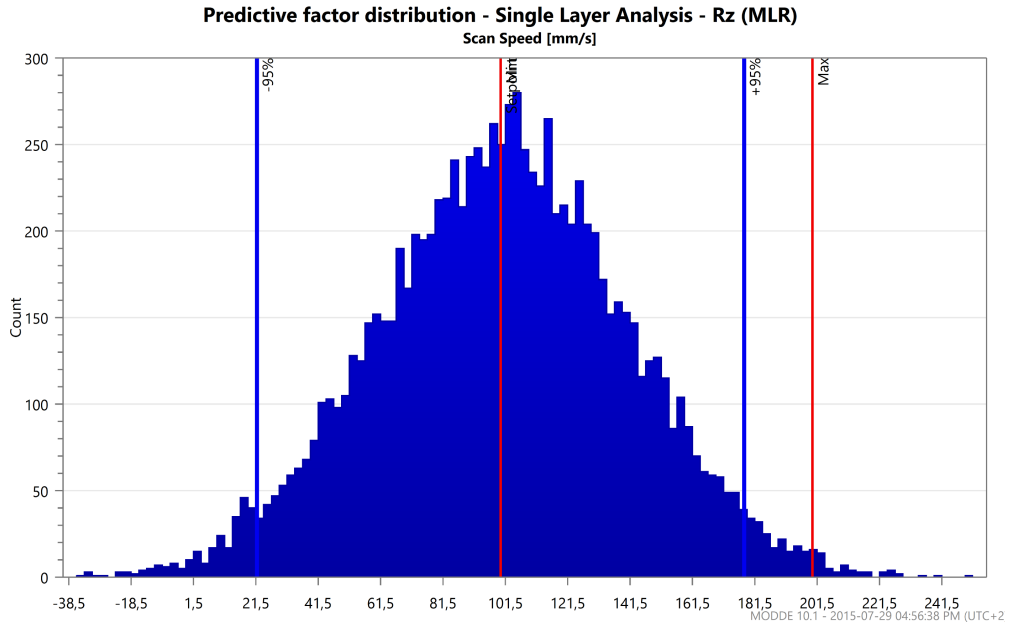


Figure H.5: Predictive factor distribution plot for scan speed.

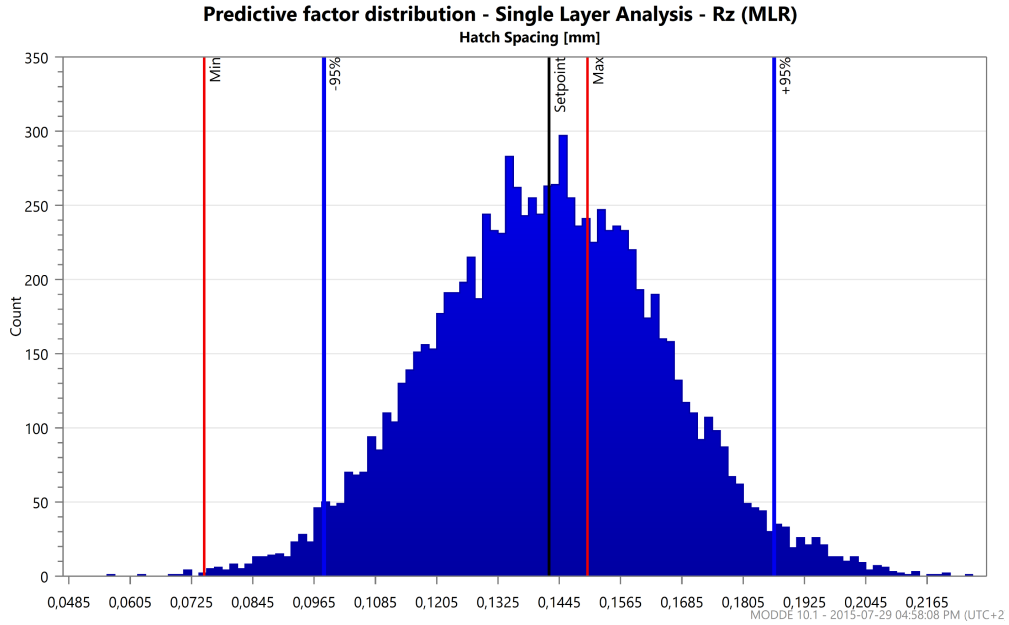


Figure H.6: Predictive factor distribution plot for hatch spacing.

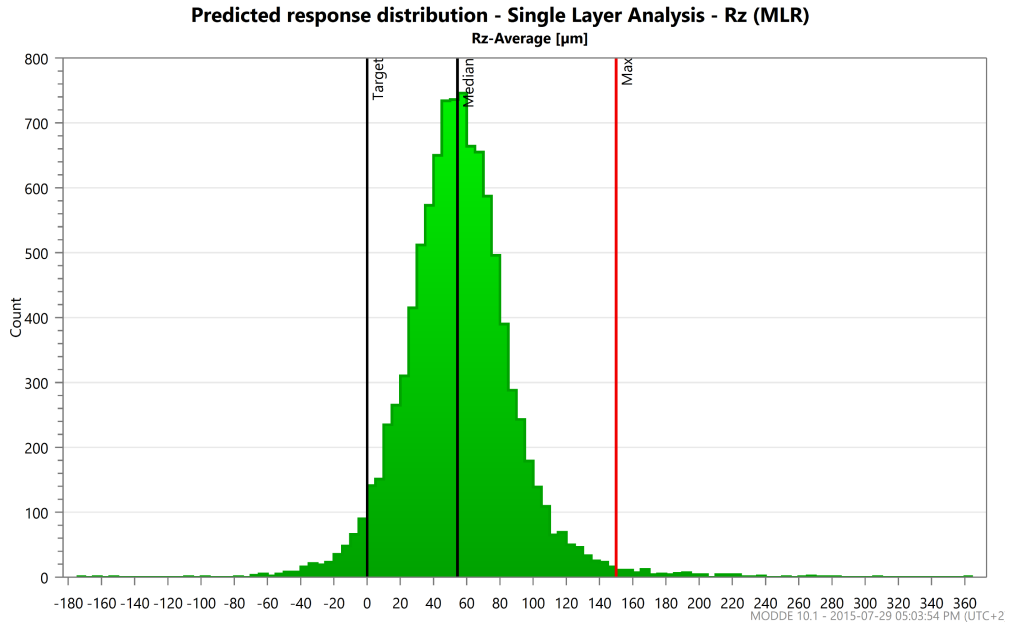


Figure H.7: Predictive response distribution plot for response variable R_z .

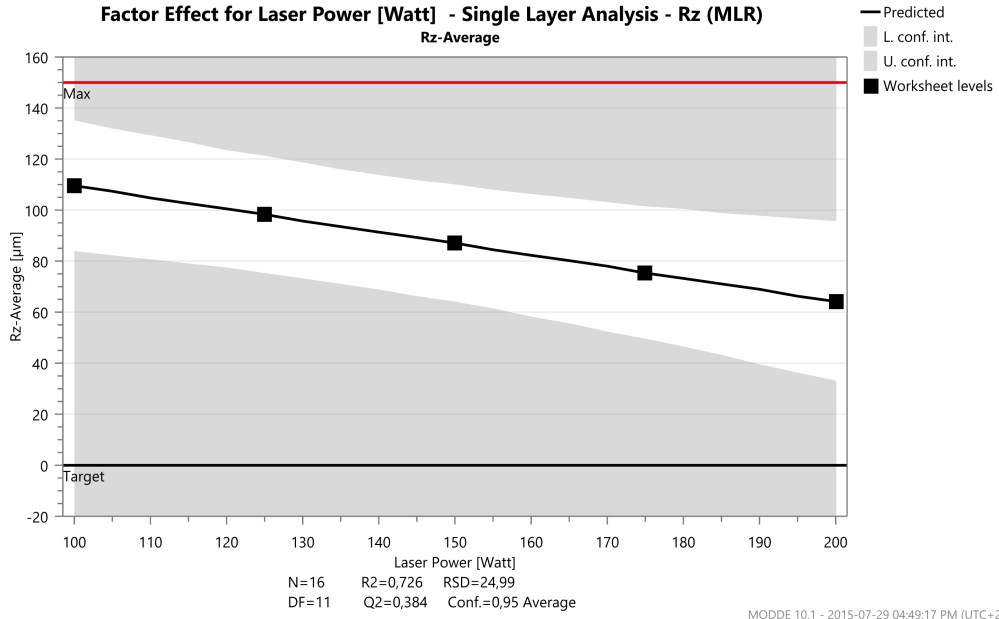


Figure H.8: Factor effect plot for laser power.

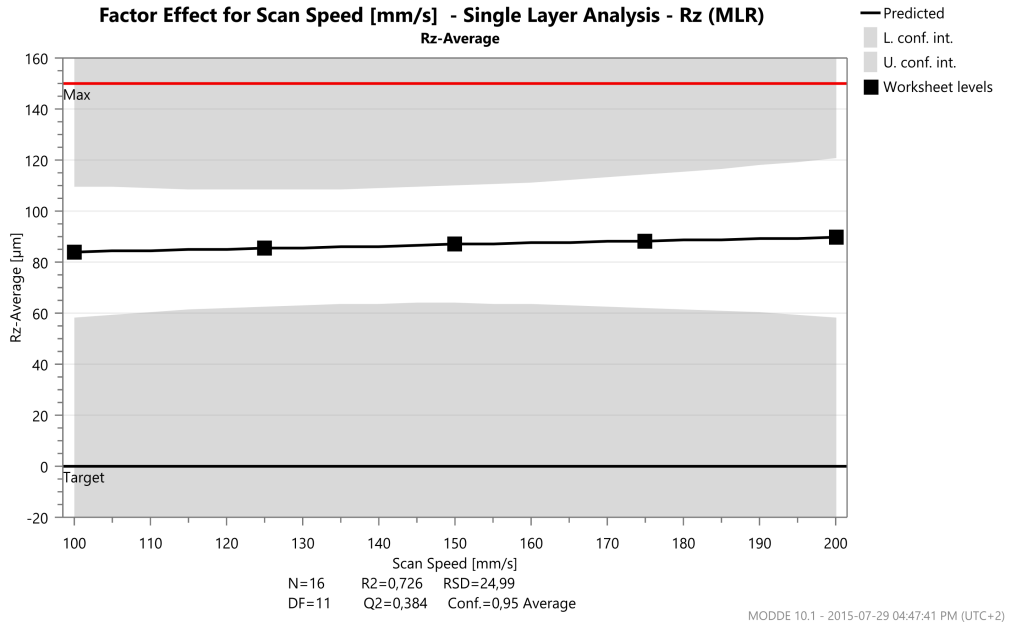


Figure H.9: Factor effect plot for scan speed.

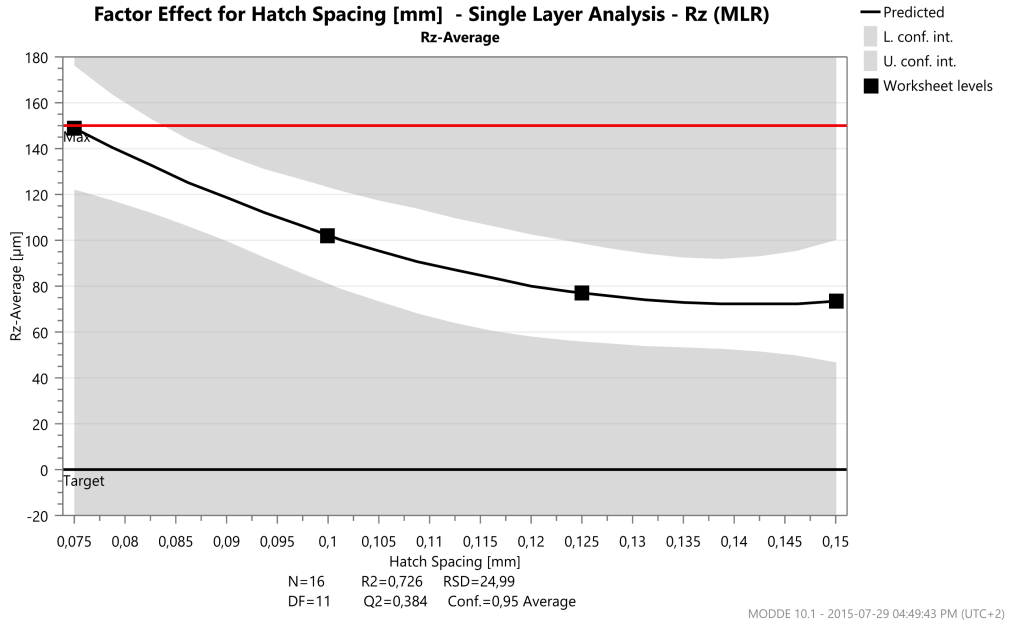


Figure H.10: Factor effect plot for hatch spacing.

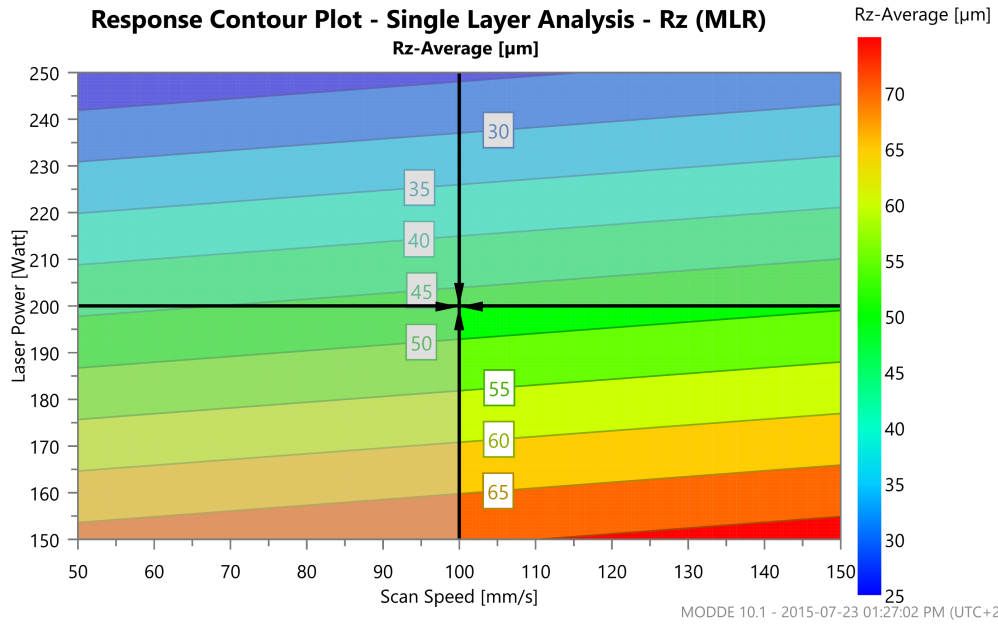


Figure H.11: Response contour plot with selected setpoint for laser power and scan speed.

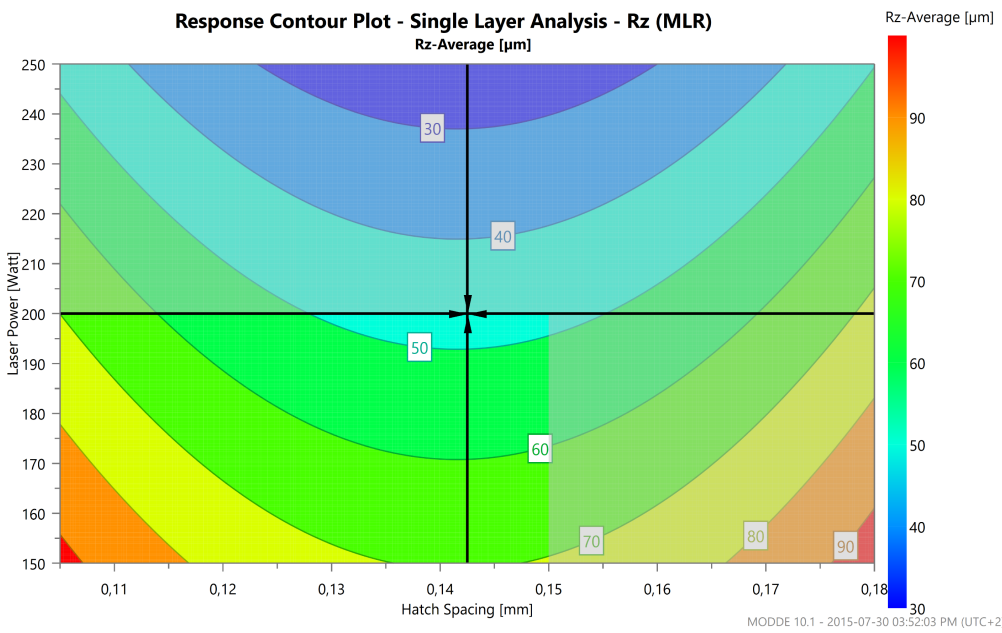


Figure H.12: Response contour plot with selected setpoint for laser power and hatch spacing.

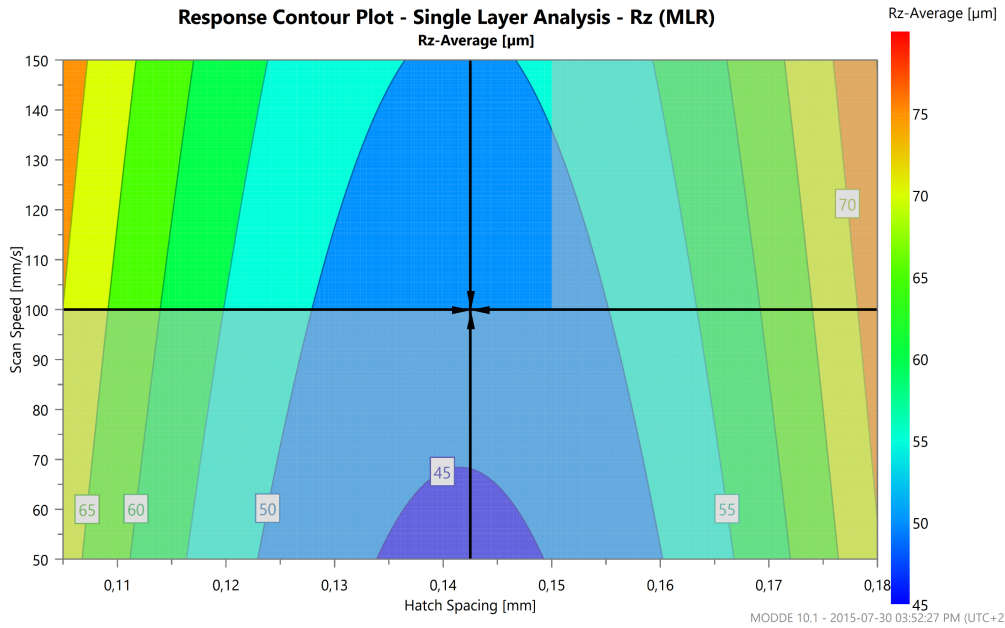


Figure H.13: Response contour plot with selected setpoint for scan speed and hatch spacing.

Table H.4: MODDE model predictions based on experimental parameter values.

Scan Speed	Laser Power	Hatch Spacing	Layer Thickness	R _z -Average	Lower	Upper
100	100	0,1	0,15	122,023	94,6479	149,399
200	100	0,1	0,15	127,601	95,2096	159,992
100	200	0,1	0,15	76,7328	44,3416	109,124
200	200	0,1	0,15	82,3101	46,9684	117,652
100	100	0,15	0,15	93,284	58,7366	127,831
200	100	0,15	0,15	98,8613	62,4366	135,286
100	200	0,15	0,15	47,9933	11,5686	84,4179
200	200	0,15	0,15	53,5706	16,6916	90,4496
100	150	0,125	0,15	74,1713	49,771	98,5716
150	100	0,125	0,15	99,6053	75,205	124,006
150	150	0,125	0,15	76,96	55,5595	98,3604
100	100	0,125	0,15	96,8167	70,2124	123,421
125	125	0,075	0,15	158,976	128,941	189,011
175	175	0,075	0,15	139,119	110,505	167,734
175	125	0,075	0,15	161,765	132,219	191,31
125	175	0,075	0,15	136,331	106,785	165,876

Table H.5: Descriptive worksheet statistics.

Worksheet statistics	Rz-Average
Worksheet runs	16,000
N	16,000
Min	52,020
Max	179,550
Mean	102,882
Q(25%)	67,295
Q(75%)	130,170
Median	100,825
Std. dev.	40,904
Min/Max	0,290
Std. dev./Mean	0,398
Skewness	0,552
Skewness test	0,979
Kurtosis	-0,651

Table H.6: Descriptive model statistics.

Model statistics	Rz-Average
Model type	Evaluation of MLR model
Scaling type	All factors are orthogonally scaled
DF	11
R ²	0,726
R ² adj	0,627
Q ²	0,384
Condition number	3,22959
Model terms	5
DF residual	11
RSD	24,991
P _{model}	0,004
DF _{lack of fit}	-
Plack of fit	-
DF _{pure error (repl. runs)}	-
SD _{pure error}	-

Appendix I

COMA'16 conference article

The COMA'16 conference article, which has been submitted, accepted, and reviewed for this work, is presented here. This is the final revision format that will be published in the conference proceedings for COMA 2016.

Characteristics of single layer Selective Laser Melted tool grade cemented tungsten carbide

A.C. van Staden^{1,3}, D. Hagedorn-Hansen¹, G.A Oosthuizen¹, N. Sacks^{2,3}

¹RPD Labs, Department of Industrial Engineering, University of Stellenbosch

²School of Chemical & Metallurgical Engineering, University of the Witwatersrand, Johannesburg, South Africa

³DST-NRF Centre of Excellence in Strong Materials, South Africa

Abstract

Cemented carbide tools, specifically tungsten carbide based alloys, have found a wide range of application fields including manufacturing, agriculture, and mining, among others. A need for customised tooling solutions using cemented carbide alloys have been identified. Additive manufacturing is chosen as a novel manufacturing process due to its superior material and process flexibility. The study investigates the melting behaviour observable during the SLM process using a tool grade cemented tungsten carbide powder. The laser power, scan velocity, and hatch spacing of the SLM process are varied and single powder layers are sintered accordingly. This is done to determine the varying influence these parameter combinations have on the melting behaviour of the material during sintering. For each set of parameter combinations the test samples were analysed using microscopic imaging. It is found that a combination of high laser power, high hatch spacing, and low scan speed yields the best results.

Keywords

Additive manufacturing, carbides, process windows

1 INTRODUCTION

The South African (SA) manufacturing industry faces specific challenges such as a relatively limited market - as compared to the European and US industries - as well as competition from Eastern sources (e.g. China's tooling industry) using low manufacturing input costs. In the SA context a rising need for customised industrial application solutions exists. Using customised tools could provide a competitive advantage allowing SA to compete on a global scale. Areas of customisation include tool geometry and material composition. Materials include carbon and alloy steels, stainless steels, cast iron, aluminium and titanium alloys, polymers, ceramics, tungsten carbide alloys, cermets, and other composites. Tools used in a wide range of industrial applications rely on the superior wear resistance and hardness of hardmetals, such as cemented carbides [1]. Cemented carbides consist of a carbide phase that provides excellent wear resistance and a binder phase that provides toughness and ductility. For specialist applications of cemented carbides, SA players need to exploit market niches where local conditions define a unique product. For example, Allen and Ball [2] determined that wear rates can vary by up to 20 orders of magnitude in agricultural applications. In power generation, ceramics and cemented carbides offer the ideal abrasive wear resistance required. These applications all require specific tooling solutions. SA players must be provided with rapid prototyping (RP) capability, using cemented carbide materials, to open up new possibilities. Specifically purposed tool design, as well as the ability to iteratively adapt the tool, is required. In additive manufacturing (AM) processes several variables influence the final part properties. In powder-based AM, these include the material, the

process, and the energy source used to sinter the material [3]. Process related parameters include single layer thickness, scan velocity, hatch spacing, and scan strategy. An example scan strategy is the island scan strategy patented by Concept Laser GmbH that divides the scanned area into square sections (or islands) [4]. The scan sequence is randomised to determine in what order each island is scanned. Laser specific parameters include laser power, spot diameter, wavelength, and energy per laser pulse. Material specific parameters include type, particle size, particle distribution, particle shape, and percentage composition. To improve upon the resultant part properties using selective laser melting (SLM) and hardmetal powders, the laser power, scan speed, scan interval, powder mixture ratio, and particle shape and size influences must to be investigated [5]. To achieve favourable microstructural and mechanical properties, significant emphasis is required on the design strategy of powder materials as well as the laser control processes [6]. Thus a specifically tailored production strategy must be designed for a novel material. Investigation of single layer formation in a SLM process could establish a foundation for defining processing parameters for the powder material under investigation [7]. Kruth et al. [8] identified two crucial parameters influencing the dimensional control of the scan tracks: 1) scan speed and 2) laser power. Scan speed relates to track width, whereas laser power affects track thickness. Other parameters, found to also influence the formation of single layers, include layer thickness and hatch spacing, among others. Varying combinations of these parameters enables the formation of process windows, based on the observable melting activity. Process windows must be established

experimentally for any novel material to avoid scan track instabilities (such as spheroidisation) and excessive part porosity [9]. Spheroidisation is the formation of isolated metal spheres having a diameter equal to the incident laser beam [3], [6], [10], [11]. The material is rapidly melted, and subsequently cooled, due to the rapid scan speed. Successful wetting of the underlying layer is hindered and the tendency to reduce the surface free energy dominates the molten material behaviour, thus forming these spheres. Gu and Shen [11] termed this 'shrinkage-induced balling' which they attributed to a significant capillary instability effect. The formation of these spheres hinders subsequent powder deposition and results in a decrease of the layer and final part density, as well as a reduction in the mechanical properties [3], [10], [11]. Several single layer experiments using an unconventional powder produced process windows identifying four melting states: 1) over melting, 2) moderate melting, 3) spheroidisation, and 4) insufficient melting [7], [12], [13]. The process windows are established through varying combinations of scan speed and laser power. Careful selection of both laser processing and powder deposition parameters are necessary to establish a suitable processing window and avoid spheroidisation [6]. This is required to maintain a moderate temperature field and avoid overheating of the powder material. A parameter relating laser power (P), scan speed (v), hatch spacing (h), and layer thickness (d) is the volumetric energy density (VED):

$$VED = \frac{P}{vhd} \quad (1)$$

High VED [$\text{J}\cdot\text{mm}^{-3}$] values are required to initialise melting activity in the powder bed. This should be limited to slightly higher than the material's melting temperature. Lower hatch spacing increases the VED in the powder bed. Increasing the temperature beyond the melt point of the material results in evaporation of the powder [1], [2]. Rapid expansion of the evaporating particles creates an overpressure in the melted zone, resulting in material ejection from the powder bed. This occurrence leads to the formation of surface protrusions in single layer samples and could become prevalent where complete melting of the cemented carbide is desired. The choice in energy source in laser melting is an important factor influencing the consolidation of powders. This relates to 1) the energy absorptivity of materials being dependent on the laser wavelength and 2) powder densification being dependent on the incident laser energy on the powder bed [6]. Furthermore, the laser contact time determines the amount of laser energy transmitted to the powder bed. Contact time in SLM is usually between 0.5 and 25ms. This is dependent on the spot diameter and the scan speed. Fully molten powder particles cannot be achieved unless high laser power levels are used, due to the short exposure time. A particular difficulty associated with SLM is scan track formation and the

subsequent shrinkage behaviour observable. Individualised scan tracks promote uniform single layer formation. Part stability, the corresponding increased part density, and the associated mechanical properties are dependent on uniform single layers. Hatch spacing, scan speed, and laser power have been found to be the dominant factors affecting how well an individual scan track is formed [6], [14]–[17]. Specifically, hatch spacing relates to the amount of scan track overlap and determines the amount of energy dissipated into the substrate, previous scan tracks, and the raw powder [18], [19]. The incident energy reheats the previous layer and the substrate and conducts heat to the unmelted powder. The second scanned track appears lower than the first and the powder consolidation zone diminishes. The occurrence of this phenomenon relates to shrinkage phenomena. Shrinkage commonly occurs in conventional and novel sintering of cemented carbides [20]. Parts experience varying degrees of shrinkage, dependent on the nature and properties of the material used [1]. During SLM the material experiences thermal expansion upon heating of the powder bed. As the melted tracks cool and solidify, the particles rearrange and shrinkage occurs. The use of finer powder particles leads to faster onset of shrinkage. Catastrophic process failure by delamination was extensively studied by Yasa et al. [21] and noted to be a function of both shrinkage and the occurrence of elevated edges. The formation of elevated edges is explained as a consequence of surface tension. A scan track will assume a form minimising surface tension and maximising volume (i.e. a round cross section in a cylindrical shape). The first scan line is surrounded by unmelted powder with low thermal conductivity. As the melt pool changes, powder particles are drawn towards the melt volume, increasing the melt pool, and altering the solidification rate. This results in lower amounts of powder available for subsequent scan tracks. The result is lower adjacent scan tracks. Spheroidisation, and other defects, also result from the presence of oxide layers between powder particles and previously processed layers. Reduction of surface oxides is required to enable direct metal to metal interfaces [6]. This will encourage successful wetting in the SLM powder system. Oxidation is reduced or avoided by conducting AM processes in inert environments, such as argon gas. Even under extremely low partial pressure of oxygen, most metals form oxides at their respective melt temperatures. Li et al. [7] analysed W-Cu samples produced by SLM that showed lower part densities than for conventional PM. This is attributable to non-melting of the hard phase and limited liquid phase content under the investigated processing parameters. Part densities may be increased by a decrease in scan speed, using narrower hatch spacings, and material exposure at higher laser power [7], [13]. SLM is capable of producing high part densities; however the process develops residual stresses in the material, derived from the high

thermal gradients induced in the material. Part distortion, cracking, and/or delamination are but a few defects that could result from excessive residual stresses [3], [6]. Many authors specifically focus on the effects of changing laser power, scan speed, and layer thickness in a SLS/SLM process and how it influences the achievable single track, single layer, and multi-layer sample properties [15], [16]. Others investigate different hatch spacing values and the associated effects on each of these different production phases [18], [19]. Similarly, several works are presented on SLS/SLM using different materials and what the effect is of different material characteristics on achievable properties in single scan tracks and layers, as well as multi-layered samples. Finally, authors have also focused on determining the specific formation mechanisms associated with, for example, residual stress and balling [17]. From this it is clear that the production of cemented carbide parts using SLM technology is feasible and of great interest. The melt behaviour and associated defect formation during processing, however, remains a topic that requires further research. This work investigates single layer formation of a tool grade cemented tungsten carbide material in a SLM system. The influence that varying levels of laser power, scan speed, and hatch spacing have on the single layer formation is the primary focus of this work.

2 EXPERIMENTAL METHODOLOGY

2.1 Single layer sample production

The 16 test samples for this study are produced from WC-6.6wt.%Co with a M2 LaserCusing® SLM machine from Concept Laser GmbH according to the experimental design outlined in Table 1. The samples are 35x35mm squares. The geometry is used for simplicity and ease of analysis. Magics® software is used to prepare the Computer Aided Design (CAD) model and produce the 2D slice model data. The slice data are exported to the SLM machine which is then used to scan each layer, building the final 3D part. In this work only a single layer is scanned for each parameter set. A uniform powder layer is sieved onto the baseplate to a thickness of 150µm. The machine is sealed and the build chamber flooded with argon gas, thereby creating an inert environment. At oxygen levels below 0.9% the scanning process may commence. The machine is capable of processing multiple build parameters for multiple parts at once. As such, all 16 samples are created on the same build platform during a single experimental run.

2.2 Microscope analysis

The single layer test samples are analysed using an Olympus SZX7 Stereo-microscope System. The software used is Olympus Stream Essentials. Microscope images are captured at 1.25 and 3.20 times magnification. The observable differences in single layer formation, as a result of different production parameter sets, are studied by graphing the samples according to high-low, low-high, low-low,

and high-high combinations of power and scan speed. This is done for each hatch spacing value which is either 0.075mm, 0.100mm, 0.125mm, and 0.150mm.

3 RESULTS AND DISCUSSION

3.1 Microscope analysis

The microscope analysis is broken down into four primary focus points: 1) protrusion formation on the sample surface, 2) shrinkage activity present (i.e. valley formation), 3) scan track formation, and 4) balling present in the scan tracks.

3.1.1 Protrusion formation

All 16 samples exhibit protrusion formation on the surface. The extent of the formation depends on the combination of laser power, scan speed, and hatch spacing. This can be explained by the near-excessive VED levels developed in the powder bed during processing. In this work, as the layer thickness is held constant and the laser power and scan speed have only two levels (high and low), hatch spacing is the primary factor explaining the differences in the observable phenomena for each sample. Samples produced having a high VED (corresponding to a low hatch spacing) experience increased material ejection on the sample surface during processing. SLM is characterised by rapid melting and subsequent solidification of the material. The ejected material is thus trapped on the surface of the sample by the solidifying material. An increase in hatch spacing decreases VED which corresponds to a reduction in protrusion formation. This is shown in Figure 1 which shows all 16 samples produced. The protrusions appear as dark spots on each sample surface.

3.1.2 Shrinkage

The single layer samples in this work exhibit localised shrinkage near the island edges as well as the sample contours. This is explained by the rescanning of the island edge when an adjacent island is scanned. The rescanned area undergoes a second cycle of thermal expansion, particle rearrangement, and subsequent shrinkage. The process continues as the scan tracks are re-melted and reaches a plateau once particle rearrangement is no longer necessary or possible. It should be noted that shrinkage does not appear uniformly across any of the sample surfaces. The width, length, amount of shrinkage, and placement varies with the associated process parameter values. In some samples, the observable shrinkage increases as scan speed and hatch spacing increases. The occurrence of shrinkage at localised regions has the undesired effect of encouraging porosity formation. Uniform deposition of powdered material will create thicker layers in areas where shrinkage is pronounced. The incident laser energy doesn't penetrate the material far enough to fuse to the previously sintered layer, resulting in unmelted powder being trapped beneath the newly melted layer. Unmelted powder has a

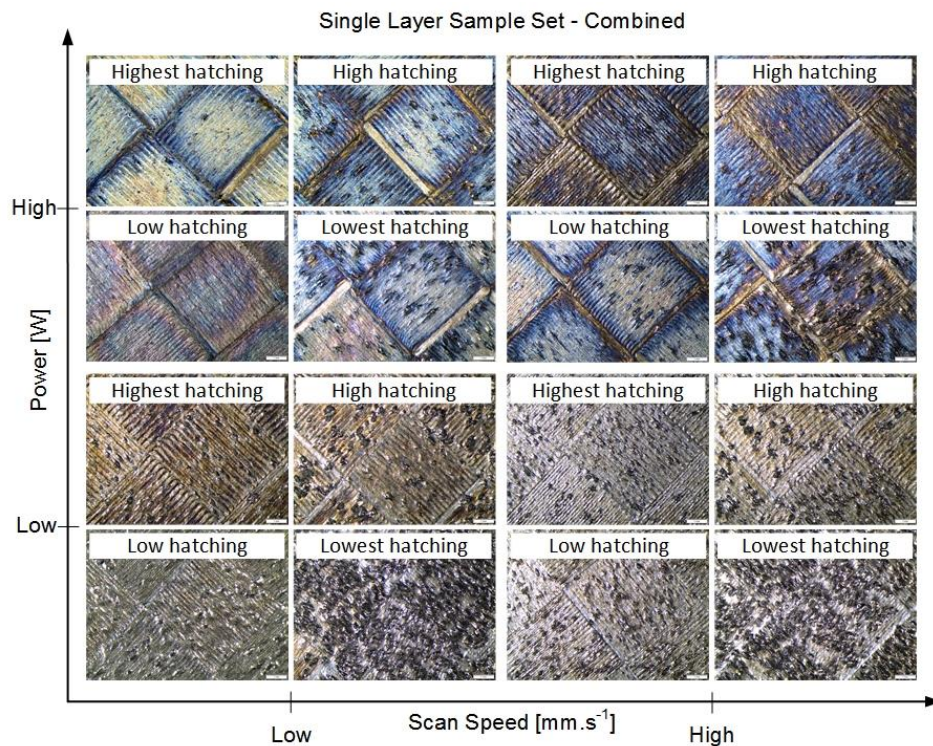


Figure 1 - Combined microscope images of single layer sample parameter sets, according to hatch spacing.

EXPERIMENT NAME	SCAN SPEED, v [mm/s]	LASER POWER, P [J/s]	HATCH SPACING, h [mm]	LAYER THICKNESS, d [mm]
E1	100	100	0,1	0,15
E2	200	100	0,1	0,15
E3	100	200	0,1	0,15
E4	200	200	0,1	0,15
E5	100	100	0,15	0,15
E6	200	100	0,15	0,15
E7	100	200	0,15	0,15
E8	200	200	0,15	0,15
E9	100	150	0,125	0,15
E10	150	100	0,125	0,15
E11	150	150	0,125	0,15
E12	100	100	0,125	0,15
E13	125	125	0,075	0,15
E14	175	175	0,075	0,15
E15	175	125	0,075	0,15
E16	125	175	0,075	0,15

Table 1 – Experimental design parameters and value combinations.

markedly lower density as opposed to the bulk material, which alters the mechanical properties of the built part. Furthermore, as unmelted powder is trapped between melted layers, unstable bonds are formed between these layers and delamination has a higher probability of occurring. The single layer samples produced in this work exhibit localised tendencies to form elevated edges at both island and part contours.

3.1.3 Scan track formation

In this work it is observed that an increase in hatch spacing results in well-defined scan tracks. This

follows since an increase in hatch spacing reduces the percentage overlap between adjacent scan tracks. Furthermore, it reduces the heat sink effect observable in single layer formation during SLM. Based on the experimental results observed here single layers with higher hatch spacing values yield favourable results. Samples with low hatch spacing exhibit obvious defects including pitting as a function of particle evaporation at low hatch spacing, balling as a result of low hatch spacing and moderate to high scan speed, and cracking as a result of low hatch spacing and high power.

3.1.4 Balling

Balling is visible in every sample, with the sample corresponding to $P = 200W$, $v = 100mm.s^{-1}$, and $h = 0.150mm$ showing the least amount of balling. Balling is more prominent at high scan speed for both low and high laser power, corresponding to the definition of 'shrinkage-induced balling'. This shows that lower scan speeds yield more favourable results. It can also be seen that low hatch spacing yields higher levels of balling in the sintered samples. The binder material melts incongruently over a range of temperatures, exhibiting a larger degree of melt activity as the temperature increases above the solidus point. Excessive liquid formation is accompanied by a prolonged liquid lifetime (resulting from a higher energy input into the powder material), leading to considerably lower melt viscosity. A higher degree of superheat of the low melting phase results, enhancing the Marangoni effect. This forms a large amount of individual spheres with the associated diminishing surface energy. At lower hatch spacing values, the amount of thermal energy in the sample layer will be higher due to a larger concentration of laser energy per unit area, thus leading to the formation of individual balls. This suggests that high values for hatch spacing yield more favourable results. Combinations of high laser power resulted in less balling in the test samples produced in this work. Coupled with high hatch spacing, significantly better scan tracks showing less balling or defect formation is achievable. Parameter combinations with low laser power show a higher concentration of balling and/or protrusion formation. This suggests that parameter combinations of low scan speed, high hatch spacing, and high laser power will result in favourable single layer formation.

3.2 Process windows

The results in the previous sections are used to create process windows describing the expected observable single layer formation phenomena when selectively melting WC-6.6wt.% Co powder. Here, the process windows incorporate the effect of various hatch spacing values on the formation of single layers, shown in Figure 1. It is clear that a high laser power, low scan speed, and high hatch spacing combination leads to the best results. The resultant samples are characterised by low levels of protrusion formation, little to no balling, limited micro-cracking, and almost no shrinkage. This processing region is defined as the baseline parameter set to describe the observable phenomena in the remaining three regions. In comparison to the baseline, low-low (P - v) combinations for the remaining hatch spacing values are characterised by prominent protrusion formation and other surface defects. These defects include indistinguishable scan track formation, pitting, localised shrinkage, and a certain degree of balling. A similar observation can be made for low-high and high-high combinations of laser power and scan speed. When compared to the baseline process region, again it is clear that single layer formation is

not as successful and surface defects are more pronounced. It is concluded that, for each combination (low-low, low-high, high-low, and high-high), as hatch spacing increases, the presence of surface defects decrease.

4 CONCLUSIONS

The following conclusions can be made from the results presented here:

1. Single layer samples were successfully produced using a SLM technology and tool grade cemented tungsten carbide powder.
2. Process windows were established to describe the expected melt activity observable for a given combination of laser power, scan speed, and hatch spacing.
3. Varying laser power, scan speed, and hatch spacing has a significant effect on single layer formation and results in different levels of surface defect formation.
4. The optimal processing region to produce single layers from a tool grade cemented tungsten carbide material corresponds to high laser power ($200W$), low scan speed ($100mm.s^{-1}$), and high hatch spacing ($0.15mm$). This corresponds to a $VED = 88.889 J.mm^{-3}$.

5 ACKNOWLEDGEMENTS

The authors wish to acknowledge the financial support received from the Department of Science and Technology and the National Research Foundation in South Africa, as well as the Engineering Departments of Stellenbosch University for the equipment and expertise required to make this work possible.

6 REFERENCES

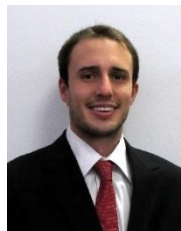
- [1] H.-C. Kim, I.-J. Shon, J. E. Garay, and Z. a. Munir, "Consolidation and Properties of Binderless Sub-Micron Tungsten Carbide by Field-Activated Sintering," *Int. J. Refract. Met. Hard Mater.*, vol. 22, no. 6, pp. 257–264, Nov. 2004.
- [2] C. Allen and A. Ball, "A Review of the Performance of Engineering Materials Under Prevalent Tribological and Wear Situations in South African Industries," *Tribol. Int.*, vol. 29, no. 2, pp. 105–116, Feb. 1996.
- [3] S. L. Campanelli, N. Contuzzi, A. Angelastro, and A. D. Ludovico, "Capabilities and Performances of the Selective Laser Melting Process," in *New Trends in Technologies: Devices, Computer, Communication and Industrial Systems*, M. J. Er, Ed. Sciyo, 2010, pp. 233–252.
- [4] J. P. Kruth, J. Deckers, E. Yasa, and R. Wauthle, "Assessing and comparing influencing factors of residual stresses in selective laser melting using a novel analysis method," *Proc. Inst. Mech. Eng. Part B J. Eng. Manuf.*, vol. 226, no. 6, pp. 980–991, 2012.

- [5] X. C. Wang, T. Laoui, J. Bonse, J. P. Kruth, B. Lauwers, and L. Froyen, "Direct Selective Laser Sintering of Hard Metal Powders: Experimental Study and Simulation," *Int. J. Adv. Manuf. Technol.*, vol. 19, no. 5, pp. 351–357, Mar. 2002.
- [6] D. D. Gu, W. Meiners, K. Wissenbach, and R. Poprawe, "Laser additive manufacturing of metallic components: materials, processes and mechanisms," *Int. Mater. Rev.*, vol. 57, no. 3, pp. 133–164, May 2012.
- [7] R. Li, Y. Shi, J. Liu, Z. Xie, and Z. Wang, "Selective Laser Melting W-10 wt.% Cu Composite Powders," *Int. J. Adv. Manuf. Technol.*, vol. 48, no. 5–8, pp. 597–605, Sep. 2010.
- [8] J. P. Kruth, B. Van der Schueren, J. E. Bonse, and B. Morren, "Basic Powder Metallurgical Aspects in Selective Metal Powder Sintering," *CIRP Ann. - Manuf. Technol.*, vol. 45, no. 1, pp. 183–186, 1996.
- [9] J. P. Kruth, P. Mercelis, J. Van Vaerenbergh, L. Froyen, and M. Rombouts, "Binding Mechanisms in Selective Laser Sintering and Selective Laser Melting," *Rapid Prototyp. J.*, vol. 11, no. 1, pp. 26–36, 2005.
- [10] N. K. Tolochko, S. E. Mozzharov, I. a. Yadroitsev, T. Laoui, L. Froyen, V. I. Titov, and M. B. Ignatiev, "Balling processes during selective laser treatment of powders," *Rapid Prototyp. J.*, vol. 10, no. 2, pp. 78–87, 2004.
- [11] D. Gu and Y. Shen, "Balling phenomena during direct laser sintering of multi-component Cu-based metal powder," *J. Alloys Compd.*, vol. 432, no. 1–2, pp. 163–166, 2007.
- [12] D. Zhang, Q. Cai, J. Liu, and R. Li, "Research on Process and Microstructure Formation of W-Ni-Fe Alloy Fabricated by Selective Laser Melting," *J. Mater. Eng. Perform.*, vol. 20, no. 6, pp. 1049–1054, Aug. 2010.
- [13] D. Zhang, Q. Cai, J. Liu, J. He, and R. Li, "Microstructural Evolvement and Formation of Selective Laser Melting W-Ni-Cu Composite Powder," *Int. J. Adv. Manuf. Technol.*, vol. 67, no. 9–12, pp. 2233–2242, Nov. 2012.
- [14] D. . Pham and R. . Gault, "A Comparison of Rapid Prototyping Technologies," *Int. J. Mach. Tools Manuf.*, vol. 38, no. 10–11, pp. 1257–1287, Oct. 1998.
- [15] D. Gu and Y. Shen, "Balling phenomena in direct laser sintering of stainless steel powder: Metallurgical mechanisms and control methods," *Mater. Des.*, vol. 30, no. 8, pp. 2903–2910, 2009.
- [16] I. Yadroitsev, P. Bertrand, and I. Smurov, "Parametric analysis of the selective laser melting process," *Appl. Surf. Sci.*, vol. 253, no. 19, pp. 8064–8069, 2007.
- [17] I. Yadroitsev, a. Gusarov, I. Yadroitsava, and I. Smurov, "Single track formation in selective laser melting of metal powders," *J. Mater. Process. Technol.*, vol. 210, no. 12, pp. 1624–1631, 2010.
- [18] M. Badrossamay and T. H. C. Childs, "Further studies in selective laser melting of stainless and tool steel powders," *Int. J. Mach. Tools Manuf.*, vol. 47, pp. 779–784, 2007.
- [19] I. Yadroitsev and I. Smurov, "Surface morphology in selective laser melting of metal powders," *Phys. Procedia*, vol. 12, pp. 264–270, 2011.
- [20] K. Senthilkumaran, P. M. Pandey, and P. V. M. Rao, "Influence of building strategies on the accuracy of parts in selective laser sintering," *Mater. Des.*, vol. 30, no. 8, pp. 2946–2954, 2009.
- [21] E. Yasa, J. Deckers, T. Craeghs, M. Badrossamay, and J. P. Kruth, "Investigation on occurrence of elevated edges in selective laser melting," in *Twentieth Annual International Solid Freeform Fabrication Symposium*, 2009, pp. 180–192.

7 BIOGRAPHY



Coetzee van Staden obtained his BEng (Ind) degree from the Department of Industrial Engineering, University of Stellenbosch. He is currently a Masters student at the Department of Industrial Engineering, Stellenbosch University, South Africa.



Devon Hagedorn-Hansen obtained his BEng (Mech) degree from the Department of Mechanical Engineering, University of Johannesburg. He is currently a Masters student at the Department of Industrial Engineering, Stellenbosch University, South Africa.



Gert Adriaan Oosthuizen obtained his PhD degree from Stellenbosch University. In 2011 he became a CIRP research affiliate and was appointed as senior lecturer and head of Rapid Product Development at Stellenbosch University, South Africa.



Natasha Sacks is an Associate Professor in Metallurgical and Materials Engineering at the University of the Witwatersrand in Johannesburg, South Africa, and a Member of the South African Institute of Mining and Metallurgy.